ELECTRONIC STRUCTURE METHODS FOR THE INVESTIGATION OF NONADIABATIC DYNAMICS

Ethan C. M. Alguire

A DISSERTATION

in

Chemistry

Presented to the Faculties of the University of Pennsylvania

in

Partial Fulfillment of the Requirements for the
Degree of Doctor of Philosophy

2015

Supervisor of Dissertation

Joseph E. Subotnik, Professor of Chemistry

Graduate Group Chairperson

Gary A. Molander, Hirschmann-Makineni Professor of Chemistry

Dissertation Committee:

Andrew M. Rappe, Professor of Chemistry
Marsha I. Lester, Professor of Chemistry
Zahra Fakhraai, Professor of Chemistry

ACKNOWLEDGMENT

If I've learned anything in my many years of schooling, most of the credit lies with the outstanding tutelage and mentorship of Joshua Schrier, Andrew Rappe and Joe Subotnik. One could not ask for better examples of intelligence, industry, and kindness. I would like to thank my thesis committee members, Marsha Lester, Robin Hochstrasser, and Zahra Fakhraai, for their help and guidance. Thanks also to Niels Damrauer and Jamie Snyder at the University of Colorado for initiating a very interesting and productive collaboration. Without the help of Yihan Shao and Zhengting Gan at Q-Chem, Inc., we would not have accomplished anything; I cannot thank them enough. Joe will be happy to know that I have learned his Socratic lesson: όλοι *είναι* χαζός.

I also have to thank the graduate students and postdocs I've had the pleasure of working with, who provided help and friendship along the way. All of the members of the Rappe and Subotnik group during my time here have my appreciation, but there are a few who have been particularly helpful. From the Subotnik group, I want to give special thanks to Shervin Fatehi, Qi Ou, Brian Landry, Wenjun Ouyang, Andrew Petit, and Amber Jain. From the Rappe group, Steve Young, Joe Bennett, Tingting Qi, John Brehm, Shi Liu, Dio Saldana-Greco, Lai Jiang, Mark Martirez, Hiro Takenaka, Nathan Koocher, and Fan Zheng have all been tremendously helpful. And of course there are my pals, Chris and Lali. You guys are okay by me.

Finally, I want to offer my sincerest thanks for the patience and support of my girlfriend Mitra, my brother Eben, and my parents, Barbara and Patrick. I was a real handful even before I started graduate school, and there's no reason to think that will change once I leave. So thanks in advance.

ABSTRACT

ELECTRONIC STRUCTURE METHODS FOR THE INVESTIGATION OF NONADIABATIC DYNAMICS

Ethan C. M. Alguire

Joseph E. Subotnik

A detailed understanding of the interface between nuclear dynamics and electronic structure is crucial for describing excited state dynamics in photoexcited systems, a key aspect of modelling the efficiency of photovoltaic devices, among other applications. There has been a proliferation of techniques for approaching the problem of electronic-nuclear interactions from the perspective of both electronic structure and nuclear dynamics; the work presented here focuses on the electronic part of the equation. Methods are developed for alternative electronic representations, called diabatic representations, that anticipate the effects of nuclear momentum and attempt to minimize it. Diabatic representations can also be used to describe the electronic states involved in charge transfer or energy transfer processes, providing couplings necessary for approximating rates using Marcus theory. In addition, analytic techniques are developed that measure the impact of nuclear motion on electronic states, which can be used in the context of a dynamics simulation to approximate rates of energy transfer, charge transfer, or other types of internal conversion in chemical systems for which Marcus theory is insufficient. These methods are then used to couplings and rates for triplet-triplet energy transfer and singlet fission systems.

TABLE OF CONTENTS

ACKNOWLEDGMENT ii

ABSTRACT iii

LIST OF TABLES ix

LIST OF ILLUSTRATIONS xxii

CHAPTER 1 : Outline 1

CHAPTER 2 : Introduction 4

2.1 The Born-Oppenheimer Approximation 4

2.2 The structure of electronic wavefunctions 8

2.3 Excited state methods 16

2.4 Adiabatic vs. diabatic representation 20

2.5 Diabatic state methodologies 22

CHAPTER 3 : Diabatic Coupling for Charge Recombination Via Boys Localization and Spin-Flip Configuration Interaction Singles 30

3.1 Introduction: modelling charge recombination 30

3.2 Theory and methodology 33

3.3 Results 36

3.4 Discussion 42

3.5 Conclusions 45

CHAPTER 4 : Optimal Diabatic States Based on Solvation Parameters 47

4.1 Introduction 47

4.2 Notation 49

4.3 Theory and methodology 49
4.4 Results 53
4.5 Conclusions and future directions 61
4.6 Acknowledgments 61

CHAPTER 5 : An Analysis of Localized Diabatic States Beyond the Condon Approximation for Excitation Energy Transfer Processes 62
5.1 Introduction 62
5.2 Notation 64
5.3 Theory 65
5.4 Results 70
5.5 Discussion: the strictly diabatic approximation 79
5.6 Conclusions and future work 81
5.7 Acknowledgments 81

CHAPTER 6 : Calculating Derivative Couplings between TDHF Excited States with Pseudo-Wavefunctions 82
6.1 Introduction 82
6.2 Notation and preliminary considerations 85
6.3 Theory 88
6.4 Results 101
6.5 Discussion and conclusions 102
6.6 Acknowledgments 107

CHAPTER 7 : Exploring Non-Condon Effects in a Covalent Tetracene Dimer: How Important are Vibrations in Determining the Electronic Coupling for Singlet Fission? 108
7.1 Introduction 108
7.2 Theory 112
7.3 Results and Discussion 117

7.4 Conclusions 134
7.5 Acknowledgements 137

CHAPTER 8 : Conclusion and future work 149

APPENDIX 151

BIBLIOGRAPHY 160

LIST OF TABLES

TABLE 5.1 : Magnitudes of DCs between the triplet-triplet energy transfer states of three different Closs molecules in the adiabatic and diabatic (BoysOV) representations at the configuration nearest to the avoided crossing along the linearly-defined reaction coordinate ζ. These configurations represent the maximum DC magnitudes among the configurations sampled for each system, suggesting that the diabatic DCs are negligible over all relevant portions of configuration space for these systems. 73

TABLE 5.2 : Analysis of change in diabatic coupling of C-1,4ee due to thermally-induced conformational fluctuations at T = 298 K along the normal modes which contribute most significantly to ΔH_{AB}. The curvature around each potential energy well on the T_1 surface is taken to be the same as that of the S_0 minimum, and is obtained from a ground-state Hessian calculation. Using this information, we are able to estimate how much this molecule can be expected to deviate (ΔL_η) from its stable configurations ($\zeta = 0$ and $\zeta = 1$) at room temperature. Multiplying this value by the projection of the diabatic coupling gradient ($|H_{AB}^{[\eta]}|$) tells us how much we can then expect the diabatic coupling to change ($\Delta H_{AB,\eta}$) both in absolute terms and as a fraction of its value at the respective reference configuration (H_{AB}). 77

TABLE 6.3 : Derivative coupling between the TDHF excited states S_1, S_4, and S_5 of formaldehyde using the 6-31G* basis set. Results presented for both the finite difference approximation ("FD", Eq. 6.67) and our analytic method (Eq. 6.65). All results are presented in a_0^{-1}. To match finite difference result, the non-translationally invariant term ($S^{A[Q]}G^{IJ}$, Eqs. 6.65 and A.29) was included. For the finite difference calculation, a step size of $\mathbf{h} = 1.89 * 10^{-4}$ a_0 was used. For all degrees of freedom (Q), the analytic result agrees with the finite difference approximation at least to the expected level of accuracy for finite difference, $\sim 10^{-4}$ a_0^{-1}. 103

TABLE 7.4 : Comparison of one-electron interchromophore coupling matrix elements (in meV) and various products of these elements (in meV^2) in noncovalent Tc dimer with Boys method versus previously-described Hartree-Fock method. The latter come from unpublished values calculated by Berkelbach.[1,2] Sign differences of orbital coupling components (t) are due to different orbital phase conventions; they are ultimately resolved in the final coupling expressions, $\sqrt{3/2}\,(t_{\mathrm{LH}}t_{\mathrm{LL}} - t_{\mathrm{HL}}t_{\mathrm{HH}})$ and $\sqrt{3/2}\,(t_{\mathrm{HL}}t_{\mathrm{LL}} - t_{\mathrm{LH}}t_{\mathrm{HH}})$. The only major difference in magnitudes of the orbital coupling components is for t_{HH}, for which the BHR-HF magnitude is more than twice as large as the Boys magnitude. This may be caused by the previously-reported tendency of HF to overestimate couplings.[2,3] 122

TABLE 7.5 : Coupling gradients for all normal modes of BT1, given in meV/Å. 141

TABLE 7.6 : One-electron couplings calculated at RMS deviation of the normal modes of BT1 at 298 K. 146

TABLE 7.7 : Couplings for BT1 using a geometry perturbed from the ωB97X-D minimum energy by 0.1 Å along mode 26. All couplings in meV. Note the monotonic increase in the coupling magnitudes with the portion of exact exchange included in the exchange-correlation functional. 146

TABLE 7.8 : Couplings for tetracene dimer using a geometry perturbed from the ωB97X-D minimum energy by 0.1 Å along mode 26. All couplings in meV. Note the monotonic increase in the coupling magnitudes with the portion of exact exchange included in the exchange-correlation functional. 146

LIST OF ILLUSTRATIONS

FIGURE 2.1 : Electronic state energies of a two-level alkali halide system in the adiabatic (solid lines) and diabatic (dotted lines) representations. Adiabatic states (S_0 and S_1) maintain a consistent energy ordering, but change character between ionic and covalent as the internuclear separation (R) becomes larger. Diabatic states (Ionic and Covalent) maintain consistent character, but alternate energy ordering. 21

FIGURE 3.2 : Energies of the twelve lowest electronic states of molecular LiF in a vacuum as a function of internuclear separation R. **(a)** Standard CIS adiabatic states, **(b)** SF-CIS adiabatic states, **(c)** standard CIS diabatic states and **(d)** SF-CIS diabatic states. States are ordered by energy in the adiabatic basis, and all states but the single CT state (state 0) are ordered by energy in the diabatic basis. All non-CT states have been block-diagonalized after diabatization. Values from the present work were constructed from an adiabatic space of the 12 lowest-energy eigenstates. 37

FIGURE 3.3 : Diabatic couplings to the CT state from lowest-energy covalent diabatic state as a function of Li and F internuclear separation R. Depicted are two quantities from the present work: LiF in a vacuum and LiF solvated by a single, frozen water molecule. Values from the present work were constructed from the 12 lowest states of the SF adiabatic eigenspace in the case of molecular LiF, and the 11 lowest states in the case of solvated LiF. The "WM" values are from Ref. 4, calculated for molecular LiF alone. 38

FIGURE 3.4 : Energy of 12 lowest electronic states for molecular LiF as a function of reaction coordinate R, which represents the separation between Li and F nuclei. All states but the single CT state (state 0) are ordered by energy. These are the energies of states that have not been block-diagonalized after undergoing diabatization, and consequently demonstrate some irregularities and the empirical need for rediagonalization of non-CT states. 39

FIGURE 3.5 : Diabatic couplings to the CT state from the 11 lowest-energy covalent diabatic states as a function of internuclear separation R. Because each calculation is independent, the signs of these quantities has been chosen to maximize continuity. The "WM" values are from Ref. 4. See Fig. 3.3 for a more limited and clearer subset of these results. 40

FIGURE 3.6 : Electric dipole along the internuclear axis of 12 lowest SF electronic states of molecular LiF as a function of internuclear separation R. Values obtained from **(a)** adiabatic states and **(b)** diabatic states are shown. States are ordered by energy in the adiabatic basis, and all states but the single CT state (state 0) are ordered by energy in the diabatic basis. Consider how much smoother the values are in the diabatic basis than in the adiabatic basis. These calculations highlight the changing electronic character of different adiabatic states at different nuclear geometries, and the power of a diabatic representation. 41

FIGURE 3.7 : Diabatic coupling to the CT state from the lowest-energy covalent diabatic state of molecular LiF as a function of reaction coordinate R, which represents nuclear separation between Li and F. Calculations were performed using a basis composed of the five lowest states, the eight lowest states, and the twelve lowest states of the SF adiabatic eigenbasis. We see from the deviation of the 5 state calculations that this quantity is sensitive to the number of adiabatic states used as a basis for the diabatization procedure. The "WM" values are from Ref. 4. 43

FIGURE 3.8 : $\langle S^2 \rangle$ for 12 lowest SF electronic states of molecular LiF as a function of internuclear separation R. SF-CIS results in the **(a)** adiabatic and **(b)** diabatic basis are shown. States are ordered by energy in the adiabatic basis, and all states but the single CT state (state 0) are ordered by energy in the diabatic basis. All non-CT states been block diagonalized after diabatization. These quantities demonstrate the high degree of spin purity of the CT state in the diabatic basis, and the high degree of spin contamination of all other states. 44

FIGURE 3.9 : Ground state adiabatic energy of molecular LiF as a function of internuclear separation R as calculated by both SF-CIS and SF-XCIS procedures. The spin-pure SF-XCIS energies shows a marked improvement in variational accuracy. Future work will explore and compare localized diabatization as applied to SF-XCIS adiabatic states. 46

FIGURE 4.10 :DBA molecule in which the 4-benzaldehydeyl donor and the 2-naphthyl acceptor groups are joined at 1,4-equitorial positions on a cyclohexane bridge, henceforth known as C-1,4ee. Here C-1,4ee is shown in the geometry optimized for the A*D configuration of the T_1 excited state. 53

FIGURE 4.11 :PES of the seven lowest-energy triplet states of C-1,4ee in three bases: **(a)** the adiabatic basis, **(b)** the ER diabatic basis, and **(c)** the ER-ε diabatic basis. The reaction coordinate ζ denotes a linear interpolation between two geometries: $\zeta = 0$ corresponds to the optimized A*D geometry, and $\zeta = 1$ corresponds to the optimized AD* geometry. While the two lowest-energy ER diabatic states are clearly over-mixed with higher-energy states, this is not a problem for ER-ε diabatic states. 54

FIGURE 4.12 :Diabatic coupling between the two lowest-energy triplet states of C-1,4ee: the reaction coordinate ζ denotes a linear interpolation between two geometries; $\zeta = 0$ corresponds to the optimized A*D geometry, and $\zeta = 1$ corresponds to the optimized AD* geometry. The diabatic coupling calculated by ER localization is nearly constant over the reaction coordinate, while that produced by ER-ε peaks at $\zeta = 0.85$, close to the avoided crossing at $\zeta = 0.887$. Notice also that the two ER-ε couplings are very similar, despite having been generated from adiabatic bases of different size, indicating that ER-ε localization is not prone to over-mixing. 55

FIGURE 4.13 :Magnitude of the approximate derivative coupling between the two lowest-energy triplet states of C-1,4ee: the reaction coordinate ζ denotes a linear interpolation between two geometries; $\zeta = 0$ corresponds to the optimized A*D geometry, and $\zeta = 1$ corresponds to the optimized AD* geometry. Derivative couplings in three bases are represented: the adiabatic basis, the ER diabatic basis, and the ER-ε diabatic basis. In the adiabatic basis, the derivative coupling becomes large close to the avoided crossing at $\zeta = 0.887$, as expected, reaching values as large as 750 a_0^{-1}. In the ER basis, the derivative couplings are consistently small, peaking at 0.05 a_0^{-1}. In the ER-ε basis, derivative couplings match adiabatic values for many nuclear geometries, and become as large as 0.17 a_0^{-1}. Close to the avoided crossing, however, this is not the case, and the enormous couplings present in the adiabatic basis are eliminated. The apparent 'kink' in the ER-ε derivative coupling is in fact a sign change (see Fig. 4.14). 56

FIGURE 4.14 :Approximate derivative coupling between the two lowest-energy triplet states of C-1,4ee: the reaction coordinate ζ denotes a linear interpolation between two geometries; $\zeta = 0$ corresponds to the optimized A*D geometry, and $\zeta = 1$ corresponds to the optimized AD* geometry. Derivative couplings in three bases are represented: the adiabatic basis, the ER diabatic basis, and the ER-ε diabatic basis. The derivative coupling values presented here are identical to those presented in Fig. 4.13, with the exception that sign information has been included in this figure. The 'kink' in the ER-ε derivative coupling near the avoided crossing in Fig. 4.13 is in fact a change of sign, as shown here. 58

FIGURE 4.15 :Localization phase diagram of S_1 and S_2 states of dibenzene: the degree of mixing between states S_1 and S_2 of the molecular system is presented via mixing angle θ as a function of Pekar factor C and temperature T. A mixing angle of $\theta = 0$ represents total delocalization (unchanged from adiabatic states), and $\theta = \frac{\pi}{4}$ represents total localization. The model predicts complete localization of these electronic states at room temperature for a sufficiently polar ($C \gtrapprox 0.6$) solvent. 59

FIGURE 4.16 :Attachment/detachment densities of the lowest-energy singlet excited state of the dibenzene system in in the ER-ε basis with three different sets of solvation parameters: **(a)** $C = 0.4$ and $T = 200$ K, (b) $C = 0.8$ and $T = 200$ K, and **(c)** $C = 0.8$ and $T = 300$ K. In each case, top figure is the attachment density, and the bottom figure is the detachment density. As solvent perturbations are applied, the delocalized excitation in the adiabatic basis begins to localize onto one ring. Increasing the polarity and temperature of the environment results in more rapid solvent fluctuations which further trap electron density. 60

FIGURE 5.17 :The DBA molecule C-1,4ee has two minima on the T_1 surface associated with a triplet-triplet EET system. In the higher-energy local minimum configuration, the excitation is localized on the benzaldehydeyl donor (the AD* state). In the global minimum configuration for this surface, the excitation is localized on the 2-naphthyl acceptor (the A*D state). Here C-1,4ee is shown in the geometry optimized for the A*D configuration of the T_1 excited state. . . . 71

FIGURE 5.18 :Magnitudes of the DC vector along the linearly-interpolated reaction pathway between A*D ($\zeta = 0$) and AD* ($\zeta = 1$) T_1 states of the C-1,4ee molecule. DC magnitudes are presented in both the adiabatic and diabatic (BoysOV) bases. While the DC magnitude is smaller in the BoysOV basis for every point sampled, the degree of reduction is greatest near the avoided crossing, where it peaks at 2.7×10^{3} a_0^{-1} in the adiabatic basis, and 3.6×10^{-2} a_0^{-1} in the diabatic basis. There is little difference between the adiabatic and diabatic representations far from the avoided crossing at $\zeta = 0$, where DC magnitudes are negligible in either representation. . . . 72

FIGURE 5.19 :Diabatic coupling along the linearly-interpolated reaction pathway between A*D ($\zeta = 0$) and AD* ($\zeta = 1$) T_1 states of the C-1,4ee molecule in the BoysOV representation. Among the points sampled, the maximum value (22.4 μE_h) and minimum value (20.8 μE_h) differ only by about 7% over the extent of the points sampled here; changing $\zeta = 0$ to $\zeta = 1$ constitutes a change of 0.88 a_0. . . . 74

FIGURE 5.20 :Magnitude of the diabatic coupling gradient ($|H_{AB}^{[Q]}|$) along the linearly-interpolated reaction pathway between A*D ($\zeta = 0$) and AD* ($\zeta = 1$) T_1 states of the C-1,4ee molecule in the BoysOV representation. The magnitude of the gradient alone suggests that the diabatic couplings change by as much as 140 μE_h over the reaction pathway defined here (total length 0.88 a_0); however, as the graph of the diabatic coupling makes clear (Fig. 5.19), the diabatic coupling gradient overlaps little with the degree of freedom defined by the reaction coordinate. 76

FIGURE 5.21 :Quiver plot of C-1,4ee depicting the **(A)** diabatic coupling gradient ($H_{AB}^{[Q]}$) at $\zeta = 0$, **(B)** normal mode 59 from the S_0 minimum-energy configuration, and **(C)** normal mode 57 from the S_0 minimum-energy configuration. Those modes are each moderately rigid, with characteristic lengths $\Delta L_{59} = 0.162$ a_0 and $\Delta L_{57} = 0.157$ a_0. At the $\zeta = 0$ geometry, the projection of the diabatic coupling gradient ($H_{AB}^{[\eta]}$) onto mode 59 is $H_{AB}^{[59]} = 45.7$ $\mu E_h/a_0$, and $H_{AB}^{[57]} = 34.8$ $\mu E_h/a_0$ for mode 57. At the $\zeta = 1$ geometry, $H_{AB}^{[59]} = 42.6$ $\mu E_h/a_0$, and $H_{AB}^{[57]} = 42.4$ $\mu E_h/a_0$. See Table 5.2 for a thorough description of how these quantities are determined. 78

FIGURE 5.22 :Error in the magnitude and direction of the diabatic coupling gradient ($H_{AB}^{[Q]}$) under the strictly diabatic approximation along the linearly-interpolated reaction pathway between A*D ($\zeta = 0$) and AD* ($\zeta = 1$) T_1 states of the C-1,4ee molecule. Magnitudinal error is calculated as the conventional relative change for scalar quantities (Eq. 5.30). Directional error is obtained by normalizing both the approximate and analytic vector quantities, then subtracting their inner product from unity (Eq. 5.31). While both magnitudinal and directional errors are very low near the avoided crossing (at $\zeta = 0.89$), they begin to diverge significantly for $\zeta < 0.6$. While the error in the magnitude has a maximum of around 25%, the directional error is nearly 50% and rising as $\zeta \to 0$. This strongly suggests that for diabatic couplings, this approximation is only reliable where diabatization can achieve significant reductions in DC magnitudes, i.e. near avoided crossings. 80

FIGURE 7.23 :Two representations of the tetracene dimer BT1. The molecular structure comes from a geometry optimization calculation using the ωB97X-D density functional, the 6-31G(d) basis set, and a polarizable continuum model of solvent parameterized for toluene.[5] For the group theory analyses that follow, the molecule (C_{2v} point group) is aligned with the xz plane as shown. 111
FIGURE 7.24 :Cartoon showing coupling pathways for SF from S_1S_0 to ^{1}TT and how these would relate to one-electron configurations in a frontier orbital active space consisting of HOMO and LUMO on chromophores A and B. This figure is adapted from Refs. 6,7. 113
FIGURE 7.25 :Frontier orbitals for monomeric tetracene. 117

FIGURE 7.26 :Localized frontier orbitals needed to calculate one-electron coupling matrix elements are obtained according to the depicted schematic. Starting with a four canonical-orbital basis set (left) consisting of two highest occupied orbitals ($|\mathrm{H}-1\rangle$ and $|\mathrm{H}\rangle$) and two lowest unoccupied orbitals ($|\mathrm{L}\rangle$ and $|\mathrm{L}+1\rangle$), Boys localization leads to four iso-energetic (in this symmetrical case) orbitals (middle) two of which are localized to the right side of the molecule ($|\mathrm{R1}\rangle$ and $|\mathrm{R2}\rangle$) and two of which are localized to the left ($|\mathrm{L1}\rangle$ and $|\mathrm{L2}\rangle$). Rediagonalization of subspaces relevant for the left and right sides of the molecule, respectively, leads (right) to the localized frontier orbitals $|\mathrm{h_A}\rangle$, $|\mathrm{l_A}\rangle$, $|\mathrm{h_B}\rangle$, and $|\mathrm{l_B}\rangle$, where A and B refer to the right and left sides of the molecule as depicted and where h and l refer to HOMO and LUMO. The representative Fock matrices for each of these three steps are also shown with the third one (right) showing orbital couplings relevant for the SF model that ignores two-electron terms. In the right-most Fock matrix, the black zeros are a result of the diagonalization whereas the red zeros are a manifestation of the symmetry. Orbital images were generated using the free visualization tool Avogadro (version 1.1.1).[8] 118

FIGURE 7.27 :Structure of non-covalent Tc dimer system used to test methods for calculating t_{HH}, t_{LL}, t_{HL}, and t_{LH}. The structure is one of three unique nearest neighbor pairs in the most common polymorph of crystalline Tc.[9] This structure comes from the ab plane of the experimental unit cell and corresponds to an [a b] translation vector of $[\frac{1}{2}\ \frac{1}{2}]$. 121

FIGURE 7.28 :Examples of patterns in the one-electron coupling gradients (in meV/Å) for each type of vibrational mode according to its irreducible representation (A_1, A_2, B_1, and B_2; relevant for the C_{2v} point group symmetry of the molecule). Those shown correspond to the lowest-frequency instances of each: A_1 at 21 cm^{-1}, A_2 at 81 cm^{-1}, B_1 at 44 cm^{-1}, and B_2 at 72 cm^{-1}. Of note, only A_2 and B_2 modes have non-zero values for $\frac{dt_{HL}}{dq_i}$ and $\frac{dt_{LH}}{dq_i}$. In all B_2 modes these have the same sign whereas in all A_2 modes these have opposite signs. 125

FIGURE 7.29 :Coupling gradient $\frac{dt_{LH}}{dq}$ shown for all frequencies and according to the irreducible representation of each mode: A_1 (red), A_2 (blue), B_1 (orange), and B_2 (green). For each frequency the corresponding gradient $\frac{dt_{HL}}{dq}$ can be inferred using the pattern according to Fig. 7.28. 126

FIGURE 7.30 :(a) Depiction of 1772 cm^{-1} B_2 normal mode of motion (no. 159) that has the highest magnitude coupling gradient $\frac{dt_{LH}}{dq}$. The viewpoint is in the $+z$ direction such that the central methylene group of the molecule is headed into the paper. (b) Cartoon rationalizing how t_{LH} coupling develops during this motion (in both $+q$ and $-q$ directions) with the focus on only part of the orbital (phase inferred from Fig. 7.26) for l_A and h_B (see text for details). (c) Depiction of A_2 1765 cm^{-1} normal mode of motion (no. 158) that has the second highest magnitude coupling gradient $\frac{dt_{LH}}{dq}$. (d) Cartoon rationalizing how t_{LH} coupling develops during this motion (in both $+q$ and $-q$ directions) with the focus on only part of the orbital for l_A and h_B (again, see text for details). 127

FIGURE 7.31 :This figure is analogous to Fig. 7.30 from the manuscript but works with h_A and l_B as opposed to l_A and h_B. (a) Depiction of 1772 cm^{-1} B_2 normal mode of motion (no. 159) that has the highest magnitude coupling gradient $\frac{dt_{HL}}{dq}$ (and $\frac{dt_{LH}}{dq}$). The viewpoint is in the $+z$ direction such that the central methylene group of the molecule is headed into the paper. (b) Cartoon rationalizing how t_{HL} coupling develops during this motion (in both $+q$ and $-q$ directions) with the focus on only part of the orbital (phase inferred from Fig. 7.26) for h_A and l_B. Note that the sign of the coupling that develops is the same here as it was in Fig. 7.30 which considered l_A and h_B. This similarity in sign is true of all B_2 motions. (c) Depiction of A_2 1765 cm^{-1} normal mode of motion (no. 158) that has the second highest magnitude coupling gradient $\frac{dt_{HL}}{dq}$ (and $\frac{dt_{LH}}{dq}$). (d) Cartoon rationalizing how t_{HL} coupling develops during this motion (in both $+q$ and $-q$ directions) with the focus on only part of the orbital for h_A and l_B (again, see text for details). Note here that the sign of the coupling that develops is the opposite of what it in Fig. 7.30 which considered l_A and h_B. This difference in sign is true of all A_2 motions. 147

FIGURE 7.32 :Electronic coupling (S_0S_1 to ^{1}TT; mediated via virtual CT states) calculated (Eq. 7.14) at RMS deviation in position (298 K) for each normal mode and plotted as a function of frequency and according to irreducible representation (A_1 (red), A_2 (blue), B_1 (orange), and B_2 (green)). The value for ΔE_{CT} is 659 meV as determined in previous work by the Damrauer group.[5] 148

FIGURE 7.33 :Effective SF coupling in BT1 for a range of reorganization energies as determined by the Stuchebrukhov formalism, for which we equate Eq. 7.22 with Eq. 7.23 and solve for $|V_{\text{eff}}|$, using $E_{^1\text{TT}} - E_{\text{S}_1\text{S}_0} = 30$ meV and $\Delta E_{\text{CT}} = 659$ meV.[5] The SF coupling terms c_α are inversely proportional to ΔE_{CT} within the frontier orbital model (cf. Eq. 7.19). 148

FIGURE 34 : **(A)** Potential energy surfaces of a spin boson system in the diabatic representation. The derivative coupling between the two diabatic states is zero by assumption, but the diabatic coupling (not pictured) is constant with respect to the reaction coordinate x. **(B)** Potential energy surfaces in the adiabatic representation. The two energy surfaces no longer cross, and the diabatic coupling is now zero. The derivative coupling (d_{12}) is small except for a peak near the avoided crossing. 151

CHAPTER 1 : Outline

In chapter 2, we briefly describe a basis for much of the electronic structure methods used in the following chapters. We begin with a description of the challenges in describing molecular wavefunctions: the presence of both nuclear and electronic components means that only a portion of the Hamiltonian may be diagonalized at once. The discussion includes a description of the Born-Oppenheimer approximation and associated quantities. Having established this, we introduce several methods for describing adiabatic electronic states, including the Hartree-Fock method, configuration interaction singles (CIS), and time-dependent Hartree-Fock (TDHF). This chapter concludes with a discussion of the adiabatic and various diabatic representations of the electronic subsystem, with a particular focus on localized diabatization methods.

In chapter 3, we describe a straightforward technique for obtaining diabatic couplings applicable to charge transfer (CT) from or charge recombination (CR) to the electronic ground state. Our method is nearly black box, requiring minimal chemical intuition from the user, and merges two well-established approaches in electronic structure theory: first, smooth and balanced adiabatic states are generated using spin-flip-configuration interaction singles (SF-CIS) based on a triplet HF state; second, Boys localization is applied to rotate all adiabatic states into charge-localized diabatic states. The method is computationally inexpensive, scaling only with the cost of CIS, and does not require a choice of active space, which is usually required for such intrinsically multiconfigurational problems. Molecular LiF in vacuum and LiF solvated by a single water molecule are examined as model systems. We find nearly smooth diabatic potential energy surfaces and couplings, and we find that the Condon approximation is obeyed approximately for this model problem.

In chapter 4, a new method for obtaining diabatic electronic states of a molecular system in a condensed environment is proposed and evaluated. This technique, which we denote ER-ε diabatization, forms diabatic states as a linear combination of adiabatic states by minimizing

an approximation to the total coupling between states in a medium with temperature T and with a characteristic Pekar factor C. ER-ε diabatization represents an improvement upon previous localized diabatization methods for two reasons: first, it is sensitive to the energy separation between adiabatic states, thus accounting for fluctuations in energy and effectively preventing over-mixing. Second, it responds to the strength of system-solvent interactions via parameters for the dielectric constant and temperature of the medium, which is physically reasonable. Here, we apply the ER-ε technique to both intramolecular and intermolecular excitation energy transfer systems. We find that ER-ε diabatic states satisfy three important properties: (1) they have small derivative couplings everywhere; (2) they have small diabatic couplings at avoided crossings, and (3) they have negligible diabatic couplings everywhere else. As such, ER-ε states are good candidates for so called 'optimal diabatic states.'

In chapter 5, we apply the techniques described in Ref. 10 for calculating the analytic derivative couplings of Boys diabatic states within the CIS formalism to the analysis of triplet-triplet energy transfer systems studied by Closs and collaborators.[11] For the systems examined, we are able to conclude that (i) the derivative coupling in the BoysOV diabatic representation is negligible, and (ii) the diabatic couplings will likely change little over the configuration space explored at room temperature. Furthermore, we propose and evaluate an approximation which allows for the inexpensive calculation of accurate diabatic energy gradients, called the 'strictly diabatic' approximation. This work highlights the effectiveness of diabatic state analytic gradient theory in realistic systems, and demonstrates that localized diabatic states can serve as an acceptable approximation to strictly diabatic states.

In chapter 6, a pseudo-wavefunction description of TDHF states is proposed and used to develop an analytic expression for derivative couplings between TDHF excited states based on the Hellmann-Feynman theorem. The resulting expression includes Pulay terms associated with using an atom-centered basis as well as a correction to ensure translational

invariance. We demonstrate that our formalism recovers the well-known Chernyak-Mukamel expression in the limit of a complete basis, and thus our approach is consistent with time-dependent response theory.

In chapter 7, we describe a method for investigating a component of the rates of singlet fission in molecular systems that incorporates the influence of molecular vibrations. Singlet fission (SF) offers opportunities for wavelength-selective processing of solar photons with an end goal of achieving higher efficiency inexpensive photovoltaic or solar-fuels-producing devices. In order to evaluate new molecular design strategies and for theoretical exploration of dynamics, it is important to put in place tools for efficient calculation of the electronic coupling between single-exciton reactant and multi-exciton product states. For maximum utility, the couplings should be calculated at multiple nuclear geometries (rather than assumed constant everywhere, i.e. the Condon approximation) and we must be able to evaluate couplings for covalently linked multichromophore systems. With these requirements in mind, in this chapter we describe the simplest methodology possible for rapid calculation of diabatic one-electron coupling matrix elements - based on Boys localization and rediagonalization of molecular orbitals. We focus on a covalent species called BT1 that juxtaposes two tetracene units in a partially cofacial geometry via a norbornyl bridge. In BT1, at the equilibrium C_{2v} structure, the non-horizontal couplings between HOMOs and LUMOs (t_{HL}, and t_{LH}) vanish by symmetry. We then explore the impact of molecular vibrations through the calculation of t_{AB} coupling gradients along 183 normal modes of motion. Rules are established for the types of motions (irreducible representations in the C_{2v} point group) that turn on t_{HL}, and t_{LH} values as well as for the patterns that emerge in constructive versus destructive interference of pathways to the SF product. For the best modes, calculated electronic coupling magnitudes for SF (at RMS deviation in position at 298 K), are within a factor of two of that seen for non-covalent tetracene dimers relevant to the molecular crystal. An overall "effective' electronic coupling is also given, based on the Stuchebrukhov formalism for non-Condon electron transfer rates.

CHAPTER 2 : Introduction

2.1. The Born-Oppenheimer Approximation[1]

The behavior of molecular systems is described entirely by the solution of the time-independent Schrödinger equation

$$\hat{H}\,|\Psi\rangle = \mathcal{E}\,|\Psi\rangle \tag{2.1}$$

where $\hat{H}$ is the molecular Hamiltonian, $|\Psi\rangle$ is the combined nuclear-electronic wavefunction and $\mathcal{E}$ is the corresponding energy. In atomic units, the Hamiltonian is given by

$$\begin{aligned}\hat{H} = &-\sum_{i=1}^{N_{\text{el}}}\frac{1}{2}\nabla_i^2 - \sum_{A=1}^{N_{\text{nuc}}}\frac{1}{2M_A}\nabla_A^2 - \sum_{i=1}^{N_{\text{el}}}\sum_{A=1}^{N_{\text{nuc}}}\frac{Z_A}{r_{iA}} \\ &+ \sum_{i=1}^{N_{\text{el}}}\sum_{j>i}^{N_{\text{el}}}\frac{1}{r_{ij}} + \sum_{A=1}^{N_{\text{nuc}}}\sum_{B>A}^{N_{\text{nuc}}}\frac{Z_A Z_B}{r_{AB}}\end{aligned} \tag{2.2}$$

where i and j index the N_{el} electrons of the system, A and B index the N_{nuc} nuclei, Z is a nuclear charge, M is a nuclear mass, and r is a scalar distance between two particles. Although the Hamiltonian is a conceptually simple summation of kinetic energy and Coulomb interaction terms, numerous approximations are necessary to find its eigenfunctions for nontrivial systems. In this chapter, we will focus on two of these: the first is the Born-Oppenheimer approximation, which takes electronic states to be independent of nuclear momentum, and allows the electronic and nuclear components of the wavefunction to be calculated separately. The second involves the many-body nature of the electronic wavefunction, which we address here using the Hartree-Fock approximation and associated methods. This second approximation will be discussed at greater length in section 2.2.

The conventional intuitive justification of the Born-Oppenheimer approximation is that electrons, which have mass several orders of magnitude less than that of nuclei, are expected to move much more quickly. Consequently, so the argument goes, the perturbation to the

[1] Unless otherwise cited, much of the material from sections 2.1 and 2.2 has been adapted from Ref. 12.

electronic subsystem caused by nuclear motion is applied very slowly on the electronic time scale, allowing the electronic wavefunction to remain in an instantaneous eigenstate; in this way, nuclear motion is approximated as being *adiabatic* with respect to the electronic subsystem. As such, nuclear momentum should not impact the behavior of the electrons, and hence the interactions between the corresponding term in the molecular Hamiltonian (Eq. 2.2) and the electronic part of the wavefunction can be neglected. Thus, the Schrödinger equation (Eq. 2.1) separates into electronic (Eq. 2.3) and nuclear (Eq. 2.4) components. In practice, the electronic part is solved first, using the nuclear positions ($\{\mathbf{R}_A\}$) as parameters. The eigenfunctions of the resulting electronic Hamiltonian constitute the *adiabatic basis* of electronic states. Next, the slow-moving nuclei are are treated on a set of *potential energy surfaces* (PESs) formed by adding the electronic energies plus the nuclear-nuclear Coulombic repulsion energy.

$$\hat{H}^{\text{el}} = -\sum_{i=1}^{N_{\text{el}}} \frac{1}{2}\nabla_i^2 - \sum_{i=1}^{N_{\text{el}}}\sum_{A=1}^{N_{\text{nuc}}} \frac{Z_A}{r_{iA}} + \sum_{i=1}^{N_{\text{el}}}\sum_{j>i}^{N_{\text{el}}} \frac{1}{r_{ij}} \tag{2.3}$$

$$\hat{H}^{\text{nuc}} = -\sum_{A=1}^{N_{\text{nuc}}} \frac{1}{2M_A}\nabla_A^2 + E_{\text{el}} + \sum_{A=1}^{N_{\text{nuc}}}\sum_{B>A}^{N_{\text{nuc}}} \frac{Z_A Z_B}{R_{AB}} \tag{2.4}$$

While the adiabaticity of nuclear perturbations is often a good assumption in molecular systems, the Born-Oppenheimer approximation is not always valid, and so it would be useful to more precisely describe the conditions under which it fails. In order to do so, we briefly return to the full molecular Schrödinger equation. For simplicity, $\mathbf{R}$ will refers to all $3N_{\text{nuc}}$ nuclear spatial coordinates:

$$\mathbf{R} = \{\mathbf{R}_A\} = \{R_{A\mu}\}, \tag{2.5}$$

for $\mu = \{x, y, z\}$ and $A = \{1, \ldots, N_{\text{nuc}}\}$. Similarly, $\mathbf{r}$ will refer to all $3N_{\text{el}}$ electronic spatial coordinates. Given a complete basis for nuclear states ($\{|\Theta(\mathbf{R})\rangle\}$) and electronic

states ($\{|\Phi(\mathbf{r};\mathbf{R})\rangle\}$), we can write (without loss of generality) the full nuclear-electronic wavefunction introduced in Eq. 2.1 as

$$|\Psi(\mathbf{R},\mathbf{r})\rangle = \sum_{\Gamma I} C_{\Gamma I} \, |\Theta_{\Gamma I}(\mathbf{R})\rangle \, |\Phi_I(\mathbf{r};\mathbf{R})\rangle \tag{2.6}$$

If we then allow the full molecular Hamiltonian (Eq. 2.1) to act on this wavefunction and compare the result to the product of the electronic and nuclear parts of the Hamiltonian acting on their respective wavefunctions, we can recover the Hamiltonian matrix elements (here, between electronic states I and J) neglected under the Born-Oppenheimer approximation:

$$\begin{aligned} &\sum_{A\Gamma\Sigma} -\frac{1}{2M_A} \left(\langle \Theta_{\Gamma I} | \langle \Phi_I | \nabla_A \Phi_J \rangle | \nabla_A \Theta_{\Sigma J} \rangle + \langle \Theta_{\Gamma I} | \langle \Phi_I | \nabla_A^2 \Phi_J \rangle | \Theta_{\Sigma J} \rangle \right) \\ &= \sum_{A\Gamma\Sigma} -\frac{1}{2M_A} \left(d_{IJ}^{[Q_{A\mu}]} \langle \Theta_{\Gamma I} | \nabla_A | \Theta_{\Sigma J} \rangle + g_{IJ}^{[Q_{A\mu}]} \langle \Theta_{\Gamma I} | \Theta_{\Sigma J} \rangle \right) \end{aligned} \tag{2.7}$$

Two new terms have been introduced in Eq. 2.7: the derivative coupling,

$$d_{IJ}^{[\mathbf{Q}]} = \langle \Phi_I | \, \nabla_{\mathbf{Q}} \, | \Phi_J \rangle \, , \tag{2.8}$$

and the second derivative coupling,

$$g_{IJ}^{[\mathbf{Q}]} = \langle \Phi_I | \, \nabla_{\mathbf{Q}}^2 \, | \Phi_J \rangle \, , \tag{2.9}$$

each indexed by all nuclear degrees of freedom $\mathbf{Q} = \{A\mu\}$, where A indexes the nuclei and μ indexes the three Cartesian coordinates. Second derivative couplings are nearly always neglected in the adiabatic representation because they tend to be small.[13] In contrast, the derivative coupling (DC, also known as the nonadiabatic or dynamic coupling) vector can become quite large under certain conditions, and for this reason it will be the focus of much of this dissertation.

Note that for every pair of electronic states, the DC is a vector of size $3N_{\text{nuc}}$. In the context of nonadiabatic dynamics, coupling between electronic states is induced by the dot product

of the DC with the nuclear momentum vector ($\mathbf{P}$).[127] Thus if one assumes that nuclei are completely stationary ($\mathbf{P} = \mathbf{0}$), the derivative cannot contribute to interstate coupling. Obviously, this is never the case in real systems, and in fact the DC can diverge so that even miniscule nuclear velocities can generate large perturbations to the Hamiltonian. In the adiabatic representation, it is easy to show that the DC magnitude $|d_{IJ}^{[\mathbf{Q}]}|$ is inversely proportional to the energy difference between states in a special case of the Hellmann-Feynman theorem. We first note that, as eigenfunctions of a Hermitian operator, adiabatic states (or *adiabats*) can be chosen to be orthonormal,

$$\langle \Phi_I | \Phi_J \rangle = \delta_{IJ}. \tag{2.10}$$

By applying the nuclear gradient operator and remembering the product rule, we find

$$\begin{aligned} \nabla_{\mathbf{Q}} \langle \Phi_I | \Phi_J \rangle = \langle \nabla_{\mathbf{Q}} \Phi_I | \Phi_J \rangle + \langle \Phi_I | \nabla_{\mathbf{Q}} \Phi_J \rangle = 0 \\ \Rightarrow \langle \nabla_{\mathbf{Q}} \Phi_I | \Phi_J \rangle = - \langle \Phi_I | \nabla_{\mathbf{Q}} \Phi_J \rangle . \end{aligned} \tag{2.11}$$

Next, noting that adiabatic wavefunctions diagonalize the Born-Oppenheimer Hamiltonian, we can show that for $I \neq J$,

$$\begin{aligned} 0 =& \nabla_{\mathbf{Q}} \langle \Phi_I | \hat{H}^{\mathrm{el}} | \Phi_J \rangle \\ =& \langle \nabla_{\mathbf{Q}} \Phi_I | \hat{H}^{\mathrm{el}} | \Phi_J \rangle + \langle \Phi_I | \nabla_{\mathbf{Q}} \hat{H}^{\mathrm{el}} | \Phi_J \rangle + \langle \Phi_I | \hat{H}^{\mathrm{el}} | \nabla_{\mathbf{Q}} \Phi_J \rangle \\ =& E_J \langle \nabla_{\mathbf{Q}} \Phi_I | \Phi_J \rangle + \langle \Phi_I | \nabla_{\mathbf{Q}} \hat{H}^{\mathrm{el}} | \Phi_J \rangle + E_I \langle \Phi_I | \nabla_{\mathbf{Q}} \Phi_J \rangle \end{aligned} \tag{2.12}$$

Applying Eq. 2.11, we further obtain

$$0 = (E_I - E_J) \langle \Phi_I | \nabla_{\mathbf{Q}} \Phi_J \rangle + \langle \Phi_I | \nabla_{\mathbf{Q}} \hat{H}^{\mathrm{el}} | \Phi_J \rangle \tag{2.13}$$

$$\Rightarrow \langle \Phi_I | \nabla_{\mathbf{Q}} \Phi_J \rangle = \frac{\langle \Phi_I | \nabla_{\mathbf{Q}} \hat{H}^{\mathrm{el}} | \Phi_J \rangle}{E_J - E_I} \tag{2.14}$$

It is clear from this expression that the Born-Oppenheimer approximation can be badly violated when electronic states become close in energy, for example near avoided crossings,

or precisely degenerate, e.g. at conical intersections. For systems in which these degeneracies are accessible, DCs can no longer be thought of as a small perturbation to the adiabatic states, and a separate *diabatic* basis may be called for. This topic is discussed further in section 2.4.

2.2. The structure of electronic wavefunctions

2.2.1. The variational method

Given a system for which the Born-Oppenheimer approximation is viable, the next step is to describe the electronic wavefunction. An essential guiding principle in this process is the *variational principle*, which states that the true wavefunction minimizes the expectation value of the energy (Eq. 2.15).

$$\langle E \rangle \leq \langle E_{\text{trial}} \rangle = \frac{\langle \phi_{\text{trial}} | \, \hat{H} \, | \phi_{\text{trial}} \rangle}{\langle \phi_{\text{trial}} | \phi_{\text{trial}} \rangle} \tag{2.15}$$

In other words, if we have an arbitrary set of "test" wavefunctions, the one with the lowest energy should be closest to the true solution to the Schrödinger equation. The variational principle can be exploited by defining a wavefunction that depends on any number of continuous, adjustable parameters and changing those parameters so as to minimize $\langle E_{\text{trial}} \rangle$, thus obtaining the best possible solution of the given form. A number of different forms for one-electron wavefunctions have been published and are widely available in electronic structure packages as *basis sets*.

2.2.2. One-electron wavefunctions

For one-electron systems, the time-independent wavefunction $\phi(x, y, z)$ is called an *orbital*, and is easy to conceptualize as a scalar-valued function of three spatial variables. In the absence of other electrons, the wavefunction can be obtained by solving the time-independent

electronic Schrödinger equation (Eq. 2.1) for a much simpler Hamiltonian, given by

$$\hat{H} = -\frac{1}{2}\nabla^2 - \sum_{A=1}^{N_{\text{nuc}}} \frac{Z_A}{r_A}, \tag{2.16}$$

where r_A is the distance between the electron and nucleus A. Only a few such systems can be solved analytically, so we must rely on numerical solutions obtained via approaches such as the variational method (vide supra).

A reasonable question to ask might be: what is the best choice for the form of a parameterized one-electron wavefunction that can be subsequently optimized in accordance with the variational principle? For computational expediency, such orbitals are usually described by a linear combination of static functions

$$\phi(x, y, z; \{C_\mu\}) = \sum_{\mu=1}^{N_{\text{basis}}} C_\mu \zeta_\mu(x, y, z), \tag{2.17}$$

where C_μ are the variable parameters and ζ_μ is a Gaussian ($e^{-\alpha_\mu r^2}$ for $r = \sqrt{x^2 + y^2 + z^2}$) *basis function* centered around an atomic nucleus.[2] The value of α_μ is typically fixed before the calculation begins, and its value depends on the atom on which it is located and the nature of the basis set being employed. Although we know that the analytic form of atomic orbitals (AOs) near nuclei resemble Slater functions ($e^{-\alpha r}$), Gaussian functions are still used for reasons of computational efficiency: it is much easier to calculate the overlap between two Gaussian functions centered on different nuclei than to perform the same calculation for two Slater functions.[14–20] The efficiency gains are so great that many more Gaussian functions can be included in a basis set than Slater functions, ultimately resulting in more accurate descriptions of the orbitals for a given computational cost.

It should be noted that when minimizing the energy of orbitals of the form given in Eq. 2.17, the only parameter that is allowed to change is the coefficient (C_μ) of each basis

[2]The basis function itself may be a contracted sum of several Gaussians. These are almost always augmented with additional functions, such as spherical harmonics which describe the angular dependence of the atomic orbitals.

function. This allows the minimization to be solved with linear algebra methods, which is computationally expedient. If we wish to find the optimal orbital of the form Eq. 2.17, we must minimize the expectation value of the energy ($\langle\phi|\hat{H}|\phi\rangle$) as a function of the coefficients ($\{C_\mu\}$), subject to the constraint that the orbital be normalized ($\langle\phi|\phi\rangle = 1$). Using the method of Lagrange multipliers, we define a functional called the Lagrangian (L),

$$\begin{aligned} L(\{C\}) =& \langle\phi|\hat{H}|\phi\rangle - \epsilon(\langle\phi|\phi\rangle - 1) \\ =& \sum_{\mu\nu} C_\mu^* C_\nu \langle\xi_\mu|\hat{H}|\xi_\nu\rangle - \epsilon\left(\sum_{\mu\nu} C_\mu^* C_\nu \langle\xi_\mu|\xi_\nu\rangle - 1\right) \\ =& \sum_{\mu\nu} C_\mu^* C_\nu H_{\mu\nu} - \epsilon\left(\sum_{\mu\nu} C_\mu^* C_\nu S_{\mu\nu} - 1\right) \end{aligned} \tag{2.18}$$

where ϵ is a Lagrange multiplier (which will ultimately be revealed to be the orbital energy). We have also introduced the matrix form of the Hamiltonian $H_{\mu\nu} = \langle\xi_\mu|\hat{H}|\xi_\nu\rangle$ and the AO overlap $S_{\mu\nu} = \langle\xi_\mu|\xi_\nu\rangle$ in the basis of atomic orbitals $\{|\xi_\mu\rangle\}$). Minimizing the orbital energy subject to the normalization constraint can now be achieved by performing an unconstrained minimization of L using variational calculus. To minimize L, we set its first variation equal to 0,

$$\begin{aligned} \delta L =& \sum_{\mu\nu} \left(\delta C_\mu^* C_\nu + C_\mu^* \delta C_\nu\right) H_{\mu\nu} - \epsilon \sum_{\mu\nu} \left(\delta C_\mu^* C_\nu + C_\mu^* \delta C_\nu\right) S_{\mu\nu} = 0 \\ =& \sum_\mu \delta C_\mu^* \left(\sum_\nu H_{\mu\nu} C_\nu - \epsilon S_{\mu\nu} C_\nu\right) + \sum_\nu \delta C_\nu \left(\sum_\mu H_{\mu\nu} C_\mu - \epsilon S_{\mu\nu} C_\mu\right) = 0 \end{aligned} \tag{2.19}$$

and after relabeling the indices $\mu \leftrightarrow \nu$ in the second term, noting that H and S are symmetric, and recalling that the basis set and coefficients can all be chosen to be real, we find that the Lagrangian is minimized when

$$\sum_\nu H_{\mu\nu} C_\nu - \epsilon S_{\mu\nu} C_\nu = 0, \tag{2.20}$$

or in other words, the optimal one-electron wavefunction can be described by a linear

combination of AOs whose coefficients $\mathbf{C} = \{C_\mu\}$ satisfy

$$\mathbf{HC} = \mathbf{SC}\epsilon. \tag{2.21}$$

2.2.3. Accounting for spin

Having established in Section 2.2.2 how to numerically solve for a one-electron wavefunction, we now seek to generalize this solution to systems of two or more electrons. Before proceeding, it will be necessary to introduce the concept of spin angular momentum. Electrons, like other fermions, have an intrinsic angular momentum that, if measured relative to some preferred spatial direction, can be found to have eigenvalues of $\pm\frac{1}{2}$ (in atomic units). In the context of many calculations, magnetic interactions with electron spins from external fields or orbital angular momentum are small enough to ignore, so it is usually sufficient to choose an arbitrary reference axis for all spins and only keep track of the spin with respect to this axis, given as one of two spin functions: α ('up') or β ('down'). Using these designations, spatial orbitals (ϕ) can be augmented to form spin orbitals (χ); for example, a spin-up orbital with spatial component ϕ is given by

$$\chi(\mathbf{x}) = \chi(\mathbf{r};\omega) = \phi(\mathbf{r})\alpha(\omega), \tag{2.22}$$

where we have introduced the composite variable $\mathbf{x} = \{\mathbf{r}, \omega\}$, where ω is just a dummy spin variable (there is no functional form of $\alpha(\omega)$ or $\beta(\omega)$) meant to maintain a consistent formalism. The two spin functions are orthonormal ($\langle\alpha|\alpha\rangle = \langle\beta|\beta\rangle = 1$, $\langle\alpha|\beta\rangle = 0$), so that even if two electrons share the same spatial orbital, the spin orbitals they occupy may not overlap, as in Eq. 2.23.

$$\int d\mathbf{x}\chi_\mu^*(\mathbf{x})\chi_\nu(\mathbf{x}) = \int d\mathbf{r} \int d\omega\phi^*(\mathbf{r})\alpha^*(\omega)\phi(\mathbf{r})\beta(\omega) = \langle\phi|\phi\rangle\langle\alpha|\beta\rangle = (1)(0) = 0 \tag{2.23}$$

Spin is a crucial factor in forming many-electron wavefunctions, and the treatment provided here is only the minimum necessary to provide context for understanding the ground-state structure of a simple multi-electron wavefunction, in which a spin-up and spin-down electron can shrae a spatial orbital without violating the Pauli exclusion principle.

2.2.4. Many-electron wavefunctions and Hartree-Fock theory

Given a set of spin orbitals, the simplest form for the wavefunction of two electrons is the product of two such orbitals,

$$\Phi(\mathbf{x}_1, \mathbf{x}_2) = \chi_1(\mathbf{x}_1)\chi_2(\mathbf{x}_2) \tag{2.24}$$

where $\mathbf{x}_1$ and $\mathbf{x}_2$ correspond to the coordinates of electrons 1 and 2, and χ_1 and χ_2 are arbitrary spin orbitals (which do not necessarily correspond to electrons 1 and 2). This simple product must be ruled out immediately, however, because it does not respect antisymmetry under exchange: the wavefunction describing a system of fermions (such as electrons) must be antisymmetric under the exchange of particles, i.e.

$$\Psi(\ldots, \mathbf{x}_i, \ldots, \mathbf{x}_j, \ldots) = -\Psi(\ldots, \mathbf{x}_j, \ldots, \mathbf{x}_i, \ldots), \tag{2.25}$$

which cannot be satisfied for a simple function of the form of Eq. 2.24, except in the trivial case ($\chi_1(\mathbf{x}) = \chi_2(\mathbf{x}) = 0$).[3] In order to exhibit exchange antisymmetry, our two-electron wavefunction must be written as a *Slater determinant*, i.e.

$$\Phi(\mathbf{x}_1, \mathbf{x}_2) = \frac{1}{\sqrt{2}}\left(\chi_1(\mathbf{x}_1)\chi_2(\mathbf{x}_2) - \chi_1(\mathbf{x}_2)\chi_2(\mathbf{x}_1)\right) = \frac{1}{\sqrt{2}}\begin{vmatrix} \chi_1(\mathbf{x}_1) & \chi_2(\mathbf{x}_1) \\ \chi_1(\mathbf{x}_2) & \chi_2(\mathbf{x}_2) \end{vmatrix}, \tag{2.26}$$

where the factor of $\frac{1}{\sqrt{2}}$ is added as a normalization constant. Notice that in the determinant on the RHS of Eq. 2.26, each row corresponds to a different electron and each column

[3]The Pauli exclusion principle, which states that no two electrons can occupy the same orbital simultaneously, follows directly from this fact.

corresponds to a different spin orbital. The row-switching operation is therefore equivalent to exchanging electrons. Because switching any two rows of a determinant inverts its sign, this wavefunction is antisymmetric under exchange. Generalizing to a system with an arbitary number of electrons, the wavefunction can be written as a $N_{\mathrm{el}} \times N_{\mathrm{el}}$ determinant of the form

$$|\Phi\rangle = |\chi_1\chi_2\dots\chi_{N_{el}}\rangle = \frac{1}{\sqrt{N_{\mathrm{el}}!}} \begin{vmatrix} \chi_1(\mathbf{x}_1) & \chi_2(\mathbf{x}_1) & \dots & \chi_{N_{\mathrm{el}}}(\mathbf{x}_1) \\ \chi_1(\mathbf{x}_2) & \chi_2(\mathbf{x}_2) & \dots & \chi_{N_{\mathrm{el}}}(\mathbf{x}_2) \\ \vdots & \vdots & \ddots & \dots \\ \chi_1(\mathbf{x}_{N_{\mathrm{el}}}) & \chi_2(\mathbf{x}_{N_{\mathrm{el}}}) & \dots & \chi_{N_{\mathrm{el}}}(\mathbf{x}_{N_{\mathrm{el}}}) \end{vmatrix}. \tag{2.27}$$

It can be shown, given a set of wavefunctions that obey exchange antisymmetry, that any linear combination of these functions must also have this property, so it is easy to construct wavefunctions that contain contributions from many configurations (i.e. Slater determinants).

Although we now have a method of compute many-electron wavefunctions from orbitals, we have not yet addressed how to construct those orbitals. A popular approach is to use the Hartree-Fock method, which describes the ground-state wavefunction of a system as a single determinant. Broadly, the Hartree-Fock method extends the method for constructing one-electron wavefunctions described in Section 2.2.2 to systems containing many electrons while preserving the simplicity of the one-electron calculation.

Given a test wavefunction consisting of a single determinant $|\tilde{\Phi}\rangle = |\chi_1\chi_2\dots\chi_{N_{\mathrm{el}}}\rangle$, its total energy is

$$\begin{aligned} \tilde{E} = \langle\tilde{\Phi}|\hat{H}|\tilde{\Phi}\rangle &= \sum_i \langle\chi_i|\hat{h}|\chi_i\rangle + \frac{1}{2}\sum_{ij}\langle\chi_i\chi_j||\chi_i\chi_j\rangle \\ &= \sum_i \langle\chi_i|\hat{h}|\chi_i\rangle + \frac{1}{2}\sum_{ij}\langle\chi_i\chi_j|\chi_i\chi_j\rangle - \frac{1}{2}\sum_{ij}\langle\chi_i\chi_j|\chi_j\chi_i\rangle \end{aligned} \tag{2.28}$$

where $\hat{H}$ is the electronic Hamiltonian (Eq. 2.3), composed of the one-electron integrals

$$\langle \chi_i | \hat{h} | \chi_j \rangle = \langle \chi_i | \left(-\frac{1}{2}\nabla^2 + \sum_A \frac{1}{r_A} \right) | \chi_j \rangle \tag{2.29}$$

and two-electron integrals, given in physicists' notation by

$$\langle \chi_i \chi_j | \chi_k \chi_l \rangle = \int d\mathbf{x}_1 d\mathbf{x}_2 \chi_i^*(\mathbf{x}_1) \chi_j^*(\mathbf{x}_2) \frac{1}{r_{12}} \chi_k(\mathbf{x}_1) \chi_l(\mathbf{x}_2). \tag{2.30}$$

In particular, there are two kinds of two electron integrals: the first is called the *Coulomb integral*,

$$\langle \chi_i \chi_j | \chi_i \chi_j \rangle = \int d\mathbf{x}_1 d\mathbf{x}_2 \chi_i^*(\mathbf{x}_1) \chi_j^*(\mathbf{x}_2) \frac{1}{r_{12}} \chi_i(\mathbf{x}_1) \chi_j(\mathbf{x}_2) = \int d\mathbf{x}_1 d\mathbf{x}_2 |\chi_i(\mathbf{x}_1)|^2 \frac{1}{r_{12}} |\chi_j(\mathbf{x}_2)|^2 \tag{2.31}$$

which is the classical Coulomb repulsion between the charge densities associated with orbitals χ_i and χ_j. The second is the *exchange integral*,

$$\langle \chi_i \chi_j | \chi_j \chi_i \rangle = \int d\mathbf{x}_1 d\mathbf{x}_2 \chi_i^*(\mathbf{x}_1) \chi_j^*(\mathbf{x}_2) \frac{1}{r_{12}} \chi_j(\mathbf{x}_1) \chi_i(\mathbf{x}_2), \tag{2.32}$$

which has no classical analog, and is a result of the antisymmetric structure of the wavefunction.

The Coulomb and exchange integrals make it impossible to optimize the orbitals for a many-electron determinant using the same methodology described in Section 2.2.2 because these terms depend on the behavior of more than one electron. The Hartree-Fock method addresses this problem by writing the two-electron terms as one-electron operators, called the Coulomb ($\hat{J}$) and exchange ($\hat{K}$) operators, shown by their effects on a spin orbital χ_j in Eqs. 2.33 and 2.34.

$$\hat{J}_i(\mathbf{x}_1) \chi_j(\mathbf{x}_1) = \left[\int d\mathbf{x}_2 \chi_i^*(\mathbf{x}_2) \frac{1}{r_{12}} \chi_i(\mathbf{x}_2) \right] \chi_j(\mathbf{x}_1) \tag{2.33}$$

$$\hat{K}_i(\mathbf{x}_1)\chi_j(\mathbf{x}_1) = \left[\int d\mathbf{x}_2 \chi_i^*(\mathbf{x}_2)\frac{1}{r_{12}}\chi_j(\mathbf{x}_2)\right]\chi_i(\mathbf{x}_1) \tag{2.34}$$

It is important to note two things about both operators: first, they each have an orbital index as a subscript, because there is a distinct operator for each orbital, e.g., $\hat{J}_i$ only contains information about the Coulomb potential from orbital χ_i. Second, they are functions of a particular position/spin variable (e.g. $\mathbf{x}_1$), indicating that they only interact with other operators or functions of that variable.

Despite the unusual structure of $\hat{J}$ and $\hat{K}$, it is easy to show that their expectation values return the exact Coulomb and exchange energy:

$$\langle\chi_i|\hat{J}_j|\chi_i\rangle = \langle\chi_i\chi_j|\chi_i\chi_j\rangle \tag{2.35}$$

and

$$\langle\chi_i|\hat{K}_j|\chi_i\rangle = \langle\chi_i\chi_j|\chi_j\chi_i\rangle. \tag{2.36}$$

Combining the original one-electron operator $\hat{h}$ with these new operators, we define the Fock operator

$$\hat{f}(\mathbf{x}_1) = \hat{h}(\mathbf{x}_1) + \sum_{i=1}^{N_{\text{el}}}\hat{J}_i(\mathbf{x}_1) - \sum_{i=1}^{N_{\text{el}}}\hat{K}_i(\mathbf{x}_1), \tag{2.37}$$

where the index i is summed over all occupied orbitals. Individual orbital energies are given by the eigenvalue equation

$$\hat{f}|\chi\rangle = \epsilon|\chi\rangle. \tag{2.38}$$

Note that given a set of N_{basis} basis functions, there are N_{basis} solutions to Eq. 2.38: the lowest-energy N_{el}-orbitals correspond to occupied orbitals, and the remainder are unoccupied or *virtual* orbitals. Ultimately, the optimal orbitals for the Hartree-Fock wavefunction can be obtained by solving for these orbitals self-consistently: an initial guess value for the set of orbitals is used to define $\hat{J}$ and $\hat{K}$, which are then used to solve for an improved set of orbitals, and so on, until the orbitals change very little from one iteration to the next and the calculation is said to be converged. This type of approach is called a *mean-field* ap-

proximation, because it accounts for the interactions between each electron and the average of the field created by all of the other electrons. The shortcomings of this approximation can be seen if we examine the probability of two electrons occupying the same physical space: the Hartree-Fock determinant (and any single-determinant wavefunction) assumes electron locations are uncorrelated, yet our physical intuition tells us that if one electron is at a given position, its electric field will repel other electrons, reducing the probability of a second electron occupying a nearby space. Thus any improvements on the Hartree-Fock wavefunction is described as *correlation*, and the difference between the Hartree-Fock energy and the true energy of an electronic system is caled the *correlation energy*.

2.3. Excited state methods

2.3.1. Configuration interaction

The Hartree-Fock method is a useful tool for describing ground state wavefunctions, but it can also be a foundation for building more complicated state descriptions, for both the ground and excited states. Given some basis of orbitals, the best possible description of an N_{el}-electron wavefunction must be some linear combination of all possible N_{el} orbital configurations of the N_{basis} orbital basis, i.e.

$$|\Phi\rangle = \sum_{q=1}^{N_{\text{config}}} c_q \, |\Phi_q\rangle \tag{2.39}$$

where $|\Phi_q\rangle$ is one of N_{config} configurations, and c_q is its corresponding coefficient. Unfortunately, the number of possible orbital combinations (Eq. 2.40) scales combinatorially with basis size, so describing wavefunctions in this way is intractable for all but the smallest systems. The basis of determinants must therefore be truncated.

$$N_{\text{config}} = \binom{2N_{\text{basis}}}{N_{\text{el}}} = \frac{(2N_{\text{basis}})!}{N_{\text{el}}!(2N_{\text{basis}} - N_{\text{el}})!} \tag{2.40}$$

Using the Hartree-Fock method, we have been able to find a small (single-configuration) truncated description of the ground state; in fact, it is the best description of the wavefunction for a given basis using only a single determinant. A comparably simple excited state description would be to choose the lowest-energy excited determinant, e.g. the HOMO $\rightarrow$ LUMO excitation, to represent the first excited state. Naïvely, this one-determinant wavefunction seems like the best representation for the first excited state within the Hartree-Fock orbital framework. However, contributions from other determinants can reduce the energy of the state dramatically due to interactions between the various configurations. This is particularly important for excited states within the Hartree-Fock framework, since the orbitals were constructed exclusively to minimize the ground-state energy, and may not represent excited states as accurately.

It would be useful if there were a systematic way to determine which configurations are the most important to include in the description of an electronic state. One such partitioning is the *configuration interaction* (CI) expansion. To describe such an expansion one must obtain an orbital representation that allows for a partitioning between a set of N_{el} low-energy reference orbitals and the remaining higher-energy orbitals. Typically, this is done with Hartree-Fock theory, so that the reference orbitals correspond to the HF occupied orbitals, while the remaining orbitals are the virtual orbitals; for the remainder of the description of this method, we will assume that this is the case, although it need not be.[21–23] The CI expansion of the wavefunction is then written as the sum of the reference determinant ($|\Phi_0\rangle$), the reference determinant with single excitations ($|\Phi_i^a\rangle$), double excitations ($|\Phi_{ij}^{ab}\rangle$, and so on (Eq. 2.41).

$$|\Phi\rangle = c_0 |\Phi_0\rangle + \sum_{ai} c_i^a |\Phi_i^a\rangle + \sum_{abij} c_{ij}^{ab} |\Phi_{ij}^{ab}\rangle + \dots \tag{2.41}$$

Note here that we make use of a convention in which $\{i, j, k, \dots\}$ index occupied orbitals, while $\{a, b, c, \dots\}$ index virtual orbitals. Because the occupied orbitals are lower in energy than the virtual orbitals, we expect configurations with fewer excitations are lower in energy

than those with more excitations, and thus according to the variational principle they ought to contribute less (i.e., have smaller coefficients c) to the final expressions for low-energy wavefunctions. Different levels of truncated CI are thus identified by how many excitations are included in the *ansatz* (wavefunction description).

The least expensive truncated CI method is called CI with single excitations (CIS).[24] The CIS method uses a linear combination of all possible single excitations of the HF determinant to describe excited-state wavefunctions (Eq. 2.42).

$$|\Phi\rangle = \sum_{ia} c_i^a \, |\Phi_i^a\rangle \tag{2.42}$$

Solving for CIS wavefunctions is a straightforward process of diagonalizing the Hamiltonian in the space of single excitations,

$$\sum_{ai} A_{aibj} c_i^a = E_{\mathrm{CIS}} c_j^b, \tag{2.43}$$

where E_{CIS} is the CIS state energy and $A_{aibj} = \langle \Phi_i^a | \hat{H} | \Phi_j^b \rangle$. Of course, one is not typically interested in all $N_{\mathrm{occ}} \times N_{\mathrm{virt}}$ CIS states. In particular, high-energy excited states are likely poorly represented by this ansatz, as the low-level CI truncation is only expected to be reasonably accurate for low-energy states. Consequently, for actual CIS calculations, only the lowest n states are calculated for some small value of n, and the diagonalization is performed by iteratively solving for the smallest eigenvectors until n such states are determined.

Despite being a simple and inexpensive ansatz, CIS performs relatively well in general,[25] and has the added advantage of describing the correct behavior for charge transfer (CT) states at large separations (r) of the charged fragments, i.e. $E \propto -r^{-1}$.[26,27] Although the excitation energies of CIS states are crude, the energy difference among CIS states is generally much more reliable, with one exception: CIS dramatically overestimates the excitation energies of CT states.[27] This bias can be attributed to the fact that the CIS ansatz does not allow for orbital relaxation in excited states. If the electron density in the

CIS state is not very different from that of the reference (HF) state (such as for non-CT states), the error resulting from a lack of orbital relaxation should be small (perhaps due to cancellation of errors); for excited states that have dissimilar densities from the reference state (e.g. CT states), the error is much larger.

2.3.2. Time-Dependent Hartree-Fock

In addition to defining an ansatz using a truncated version of the CI expansion, there are many techniques for describing electronic states that arise from perturbation theory. One of these, called time-dependent Hartree-Fock (TDHF) or the random phase approximation (RPA),[28–32] can loosely be considered an extension of CIS, although formally it is nothing of the sort. TDHF is derived by examining the orbital response of a single-determinant wavefunction to an oscillatory electric field, although in practice the amplitudes and energies can be obtained by solving an eigenvalue equation for a non-Hermitian matrix.

Assuming real orbitals and amplitudes, the TDHF eigenvalue equation is given by

$$\begin{pmatrix} \mathbf{A} & \mathbf{B} \\ -\mathbf{B} & -\mathbf{A} \end{pmatrix} \begin{pmatrix} \mathbf{X} \\ \mathbf{Y} \end{pmatrix} = E_{\mathrm{TDHF}} \begin{pmatrix} \mathbf{X} \\ \mathbf{Y} \end{pmatrix}, \tag{2.44}$$

where $\mathbf{A}$ is the single-excitation space Hamiltonian matrix (Eq. 2.43), $\mathbf{B}$ is the subspace of the Hamiltonian between the HF ground state and the space of doubly-excited states,

$$B_{aibj} = \langle \Phi | \hat{H} | \Phi_{ij}^{ab} \rangle, \tag{2.45}$$

and $\mathbf{X} = \{X_i^a\}$ and $\mathbf{Y} = \{Y_i^a\}$ are the TDHF amplitudes that describe the state. If we allow $\mathbf{B} \to \mathbf{0}$, then the solutions to Eq. 2.44 are identical to the solutions of the CIS eigenvalue equation: $E_{\mathrm{CIS}} \to E_{\mathrm{TDHF}}$, $X_i^a \to c_i^a$, and $Y_i^a \to 0$. TDHF has several advantages over CIS, including slightly improved excitation energies and more accurate transition moments.[32,33] Despite having no ansatz, it is possible to assign pseudo-wavefunctions to each pair of TDHF states and thereby derive an approximate expression for DCs between TDHF states, as

described in Chapter 6.

2.4. Adiabatic vs. diabatic representation

Given the shortcomings of the Born-Oppenheimer approximation (section 2.1), the obvious question becomes: is there an alternative way to formulate a description of electronic states? In the strictly diabatic representation, the derivative coupling between electronic states is exactly zero.[34–36] In other words, while adiabatic states are defined by the diagonalization of the Born-Oppenheimer Hamiltonian (all terms except the first and second derivative coupling), diabatic states (or *diabats*) are defined by only diagonalizing the first derivative coupling (Eq. 2.8). One obvious consequence of a non-adiabatic representation is that the remaining terms in the Hamiltonian are not necessarily diagonalized, resulting in off-diagonal elements called *diabatic couplings*.

For those who are used to the more conventional adiabatic representation, it is not clear what form such diabatic states would take. Perhaps surprisingly, the nature of diabatic states is more intuitive than adiabatic states: while adiabats are ordered by the somewhat arbitrary criterion of their energy ranking, diabats can be thought of as being consistent in terms of their electronic character. As an example, consider an alkali halide molecule with two electronic states (Fig. 2.1). In the diabatic representation, these states can be characterized as ionic and covalent, and they maintain this character regardless of internuclear separation (R). In the adiabatic representation, the two states (which we will refer to as S_0 and S_1) are consistent in their energy ordering ($E(S_0) < E(S_1)$) for all values of R, but the character of each state changes with the internuclear separation: for small R, S_0 is ionic and S_1 is covalent, but the reverse is true for large R.

If we compare the concept of diabatic states as those states which preserve character throughout configuration space to the concept of strictly diabatic states (those with vanishing derivative couplings), we can establish a more intuitive understanding of what derivative couplings are. When the DC between two states is small in magnitude, these states main-

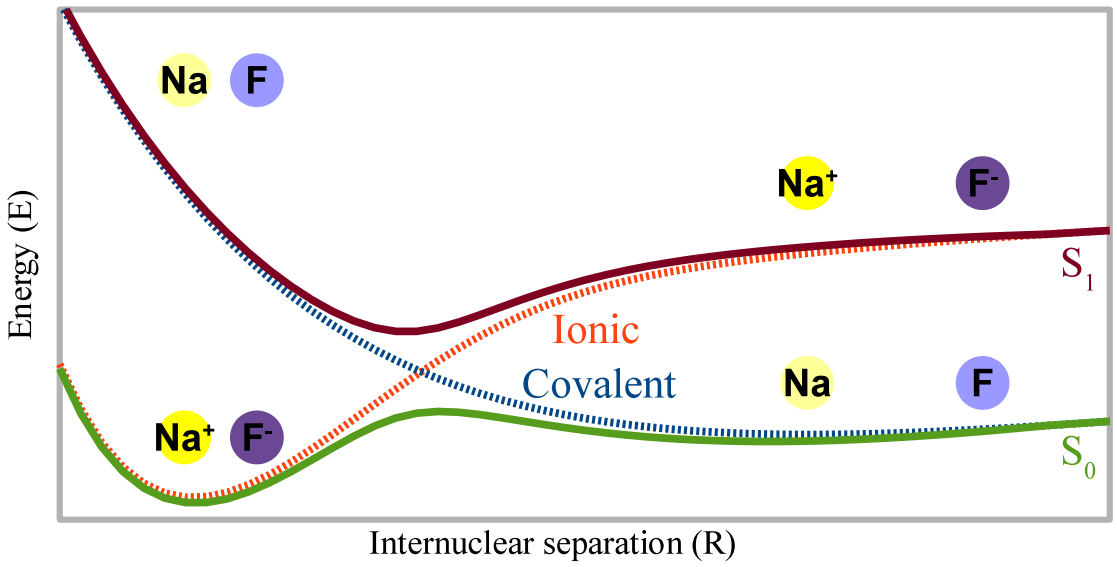

Figure 2.1: Electronic state energies of a two-level alkali halide system in the adiabatic (solid lines) and diabatic (dotted lines) representations. Adiabatic states (S_0 and S_1) maintain a consistent energy ordering, but change character between ionic and covalent as the internuclear separation (R) becomes larger. Diabatic states (Ionic and Covalent) maintain consistent character, but alternate energy ordering.

tain consistent character with respect to one another. Taking Fig. 2.1 as an example, the consistent ionic or covalent character of each diabatic state implies that the DC between those states is small, and vice versa. Conversely, if the DC between two states is large in magnitude, the two states exchange character significantly as the nuclei are moved in the direction of the DC vector. Examining the adiabatic states in Fig. 2.1, we conclude that the DC must be large for intermediate values of R, where the adiabats transition between ionic and covalent character. A small perturbation in the internuclear separation at this point might result in a large change in the electronic makeup (i.e., the ionic and covalent character) of both adiabats. Although the magnitude of the DC is not illustrated in Fig. 2.1, a similar model can be found in Appendix A.1 that numerically demonstrates the relationship between the adiabats, the diabats, and the derivative and diabatic couplings.

2.5. Diabatic state methodologies

While the strict definition of diabatic states is conceptually useful, it is not practical. It can be demonstrated[37,38] that obtaining electronic states with zero derivative coupling for real systems is impossible without an infinitely large basis set. Numerous alternative quasi-diabatic (or simply "diabatic") representations have been proposed as alternatives. The most obvious approximation to a strictly diabatic representation is to construct states that by some measure minimize DCs.[34,39–41] However, performing a direct minimization requires that one first calculate the derivative coupling at each nuclear configuration, which is computationally demanding.

One may still build a basis of diabats with small DCs, even without directly calculating the derivative coupling during construction. One approach is to force the diabatic wavefunctions to maintain a similar composition throughout configuration space. In block diagonalization,[42,43] this is accomplished by mixing a subspace of adiabats to maximize overlap with a set of reference (quasi-diabatic) states. Another strategy, called configurational uniformity,[44] is to identify the dominant electronic configurations associated with the desired diabats (over some limited region of coordinate space), and then mix an adiabatic subspace of states until such a composition is obtained. To ensure that the chosen configurations retain their character, a set of consistent MOs can also be defined.[45–47]

Another type of approach is to exploit the heuristic that diabats, in contrast to diffuse adiabats, often have local character. This is particularly true for diabats involved in charge transfer (CT) or excitation energy transfer (EET) processes, for which the "before" and "after" states are necessarily localized. This can be done directly with constrained density functional theory (CDFT),[48–51] in which distinct diabatic densities are produced subject to the constraint that the density be localized to a set of atomic centers with some manually-specified weighting. A related approach, the fragment charge difference (FCD) method,[52] produces diabatic states as a mixture of an adiabatic basis such that the manually-defined charge difference function is maximized. Similar methods have been proposed to tackle

energy transfer systems.[53,54]

2.5.1. Localized diabatization

A shared downside of many of the heuristic approaches to diabatic state formation is that they are not "black box"; i.e., they rely on a large number of situation-specific modifications in order to work correctly. If the final set of adiabats rely sensitively on potentially arbitrary choices, the method itself cannot be reliable. For example, consider a CDFT approach to an intermolecular CT system: if the electron donor and acceptor have no through-bond connections, there is likely little ambiguity in how to partition the donor and acceptor densities. If, on the other hand, the process is intramolecular, the choice is no longer so clear. For a diabatization method to be truly robust, it should not rely on any arbitrary human-defined parameters. This is largely the case for the generalized Mulliken-Hush (GMH) method,[55,56] which, like many diabatization algorithms, produces diabats ($|\Xi_A\rangle$, indexed by $\{A, B, C, \ldots\}$) from a basis of N_{states} adiabats ($|\Phi_I\rangle$, indexed by $\{I, J, K, \ldots\}$) by applying a unitary transformation (described by the unitary matrix $\mathbf{U}$) to the adiabatic basis,

$$|\Xi_A\rangle = \sum_{I=1}^{N_{\text{states}}} |\Phi_I\rangle\, U_{IA} \tag{2.46}$$

so that each resulting diabat is a linear combination of adiabats. The transformation is chosen so that GMH diabats diagonalize the electronic dipole matrix in the direction of charge transfer.[4] This effectively localizes the resulting states by maximizing the difference between the charge centers along the CT axis without requiring the user to define the charge distribution.

Another approach to producing diabatic states is called Boys localization,[57] a technique based on the orbital-localizing algorithm developed by Boys, Foster, Edmiston, and Ruedenberg.[58–62] Like GMH, Boys localization produces diabatic states by mixing together a basis of adiabatic states with a unitary matrix $\mathbf{U}$ as in Eq. 2.46. Instead of producing

[4] See also the earlier work of Werner and Meyer.[4]

states which diagonalize a dipole matrix, however, Boys localization produces states that maximize the diabatization function f_{Boys},

$$f_{\text{Boys}}\left(\mathbf{U}\right) = \sum_{AB} \left| \langle \Xi_A | \, \hat{X} \, | \Xi_A \rangle - \langle \Xi_B | \, \hat{X} \, | \Xi_B \rangle \right|^2, \tag{2.47}$$

where $\hat{X}$ is the electronic dipole operator. Maximizing f_{Boys} produces diabatic states with dissimilar dipole moments, a criterion that is very similar to that described for GMH. In fact, for two-state systems, the two methods produce identical results under certain symmetry conditions.[57] While GMH is less computationally demanding in principle — GMH requires only a diagonalization of a small matrix, while Boys requires the iterative minimization of a quartic function of adiabatic states — Boys localization has two notable advantages over GMH. First, it requires even less input: the user must only define the adiabatic subspace that will form the basis for the adiabatic-to-diabatic transformation. Second, it can handle systems for which there is no well-defined axis of charge transfer.

Because both GMH and Boys localization rely on producing states with different dipole moments, they are only appropriate to use for CT systems. In energy transfer systems, however, there is no large redistribution of electron density and so the dipole moments of the "before" and "after" states should be nearly identical. This hurdle can be overcome with a small modification to Boys localization called BoysOV localization.[63] The only difference between Boys and BoysOV is the description of the diabatization function: while f_{Boys} (Eq. 2.47) is the sum of the squares of the dipole moment differences between states, f_{BoysOV} considers the occupied and virtual contributions to the dipole moments separately,

$$f_{\text{BoysOV}}\left(\mathbf{U}\right) = \sum_{AB} \left| \langle \Xi_A | \, \hat{X}_{\text{occ}} \, | \Xi_A \rangle - \langle \Xi_B | \, \hat{X}_{\text{occ}} \, | \Xi_B \rangle \right|^2 + \sum_{AB} \left| \langle \Xi_A | \, \hat{X}_{\text{virt}} \, | \Xi_A \rangle - \langle \Xi_B | \, \hat{X}_{\text{virt}} \, | \Xi_B \rangle \right|^2 \tag{2.48}$$

where $\hat{X} = \hat{X}_{\text{occ}} + \hat{X}_{\text{virt}}$. In the same way that Boys diabatic states localize charge, BoysOV states localize excitation.

GMH, Boys, and BoysOV localization belong to a family of techniques called localized diabatization. Each localized diabatization method starts with a subspace of adiabats and

combines them via a constrained optimization procedure into a set of diabatic states. The constraints are always the same: because the resulting states ought to be orthonormal, the transformation matrix is chosen to be unitary. The difference between each localized diabatization method is the diabatization function (e.g., f_{Boys} e.g. f_{BoysOV}) to be optimized. Another method is Edmiston-Ruedenberg (ER) localization,[63,64] a technique based on earlier work on orbital localization[61] which approximately maximizes the Coulombic self-repulsion of the electronic states, localizing the wavefunction (Eq. 2.49).

$$\begin{aligned} f_{\text{ER}}(\mathbf{U}) &= \sum_{A=1}^{N_{\text{states}}} \int d\mathbf{r}_1 \int d\mathbf{r}_2 \frac{\langle \Xi_A | \hat{\rho}(\mathbf{r}_1) | \Xi_A \rangle \langle \Xi_A | \hat{\rho}(\mathbf{r}_2) | \Xi_A \rangle}{|\mathbf{r}_1 - \mathbf{r}_2|} \\ &\equiv \sum_{A=1}^{N_{\text{states}}} R_{AAAA} \end{aligned} \tag{2.49}$$

In Eq. 2.49, we have defined the self-interaction tensor R_{ABCD}, and introduced the density operator $\hat{\rho}$, which is given by

$$\hat{\rho}(\mathbf{r}) = \sum_{i=1}^{N_{\text{el}}} \delta(\mathbf{r} - \mathbf{r}_i), \tag{2.50}$$

where $\mathbf{r}_i$ is the position operator for the i^{th} electron. The form of f_{ER} arises from intuition about electronic states in realistic physical systems. Adiabatic states calculated for an isolated molecule using the Born-Oppenheimer approximation explicitly lack the kinds of perturbations that would encourage electronic wavefunctions to localize, e.g. a polar solvent. The purpose of ER localization is to mimic the localizing effect of such external perturbations by maximizing the system-solvent interaction energy, which is approximated by R_{AAAA}.

2.5.2. Choosing an adiabatic subspace

Both Boys and ER localization are meant to approximate the behavior of electronic states under the influence of a condensed environment. Although no such environment is explicitly modelled, the localized nature of these states can be thought of as a response to, for example, a polar solvent. It is reasonable to ask whether the maximal localization condition

of Boys localization or the maximal self-interaction condition of ER localization are realistic descriptions for electronic states in such an environment. The answer is that it depends on the size of the system-solvent interaction energy compared to the energy gap between states in the adiabatic subspace: if the system-solvent interaction energy is small, the true stationary states of the system are likely little different from the adiabatic states. If the system-solvent interactions are large, then it is possible for the true stationary states to be quite different from the adiabatic states. However, as the form of f_{Boys} (Eq. 2.47) and f_{ER} (Eq. 2.49) make clear, state energy is never taken into account in these methods; the solvent interaction is implicitly assumed to be dominant. Thus, if the adiabatic basis for diabatization has a wide energy spectrum, it is possible for these methods to produce unrealistic diabatic states that are composed of contributions from adiabats so well-separated in energy that no reasonable solvent perturbation could coerce them to mix. It is therefore necessary that the subspace of adiabatic states used as the basis for localized diabatization be chosen with care. First, the adiabats included in the subspace should constitute a narrow energy spectrum; if, on the contrary, the energy difference between adiabatic states is greater than the potential system-solvent interaction energy, little mixing should occur. Second, there should be a large energy gap between the states included in the subspace and the states not included in the subspace. Excluding adiabatic states that are close in energy to the selected subspace could produce inaccurate results, as they have the potential to mix with the subspace in the presence of solvent perturbations.

For some systems, it is impossible to select a subspace that adheres to these conditions. The spectrum of adiabats may be too dense, or the adiabats may have energies that change dramatically across the relevant region of nuclear coordinate space. In such cases, the spurious over-mixing can sometimes be addressed by enforcing local adiabaticity. Introduced as a criterion for GMH,[55] local adiabaticity dictates that any subspace of diabatic states localized on the same center (such as a single atom or a chromophore) should be locally adiabatic, i.e., the diabatic couplings within the subspace should be zero. This can be accomplished by performing a rediagonalization of the Hamiltonian within the selected subspace. Such

rediagonalization eliminates unphysical states that, for example, are localized to one half of a benzene molecule or to one side of an atom. This criterion is justified on the grounds that it eliminates states that are high in energy according to the system Hamiltonian but which would not make commensurate gains in solvent interaction energy. By performing such rediagonalizations judiciously, one may produce realistic diabats from an adiabatic subspace that fails to conform to the two selection rules described previously. This is demonstrated clearly for an alkalhi halide system in Chapter 3.

Of course, while there are clear benefits to enforcing local adiabaticity, it is a procedure that must be performed manually, thereby introducing potentially arbitrary user inputs and reducing the black box nature of these diabatization procedures. Ideally, the diabatization function itself should weigh the energetic gains and losses from solvent interaction and localization, and produce diabatic states that converge with respect to the size of the adiabatic subspace (N_{states}) and eschew over-localization. One step in this direction is the ER-ε localization method,[65] described in Chapter 4, that produces diabats by maximizing the diabatization function

$$f_{\text{ER}-\varepsilon}(\mathbf{U}) = \sum_A \exp\left[-\beta\left(E_A - \frac{C}{2}R_{AAAA}\right)\right], \tag{2.51}$$

where E_A is the diabatic state energy, $\beta = \frac{1}{k_B T}$, and C is the Pekar factor

$$C = \frac{1}{\varepsilon_e} - \frac{1}{\varepsilon_s}, \tag{2.52}$$

with ε_e and ε_s the high-frequency and static dielectric permittivities of the environment, respectively. By introducing two variable parameters — the temperature T and Pekar factor C — this function was designed to remove some of the subjective nature of localized diabatization procedures. In principle, once these parameters are specified based on solvent conditions, the diabatization should no longer sensitively depend on subjective user inputs. For example, high-energy excited states will be discouraged from mixing with low-energy

states due to the exponential state energy penalty built into the function. More generally, any adiabatic-to-diabatic mixing that increases state energy E_A must reduce solvent interaction energy given by $-\frac{C}{2}R_{AAAA}$ by an equivalent amount, which should eliminate spurious over-mixing and therefore the need for local rediagonalization and other sorts of extraneous user inputs.

2.5.3. The validity of localized diabatic states

While localized diabatic states may have many of the properties conventionally associated with diabatic states, i.e. uniform, local character, the question remains whether such states correspond in any real way to the historical conception of diabatic states. Specifically: are the derivative couplings between localized diabatic states small? We have reason to think that for at least some localized diabatization methods, this is the case: it can be shown[66] that state pairs which diagonalize any symmetric operator (e.g., dipole moment) can completely remove the singularity in the DC near a conical intersection. This result is not surprising in the sense that diagonalizing a (non-energy) observable is one approach to maintaining consistent character. Consequently, this proof must also apply to the Boys representation, at least in the limit where it is equivalent to GMH.[57]

While there is no rigorous proof demonstrating that diabatic DCs must be consistently small, they can be calculated directly in some circumstances. Because localized diabatic states are simply unitary transformations of a set of adiabatic states, the DC between localized diabatic states can be written as a sum of two terms: the unitary transformation of the adiabatic DC plus the gradient of the rotation term itself (Eq. 2.53).

$$\begin{aligned} d_{AB}^{[\mathbf{Q}]} &= \langle \Xi_A | \nabla_{\mathbf{Q}} | \Xi_B \rangle \\ &= \sum_{IJ} U_{IA} \langle \Phi_I | \nabla_{\mathbf{Q}} | \Phi_J \rangle U_{JB} + \sum_{IJ} U_{IA} \langle \Phi_I | \Phi_J \rangle \nabla_{\mathbf{Q}} U_{JB} \\ &= \sum_{IJ} U_{IA} d_{IJ}^{[\mathbf{Q}]} U_{JB} + \sum_{I} U_{IA} \nabla_{\mathbf{Q}} U_{IB}. \end{aligned} \tag{2.53}$$

We have developed analytic expressions for both the adiabatic DC[67] and the Boys/BoysOV

rotation matrix gradient [10] $\nabla_{\mathbf{Q}}\mathbf{U}$ within the CIS formalism. As described in Chapter 5, we are able to use these expressions to demonstrate that a pair of BoysOV states maintains a small DC magnitude even near an avoided crossing on the corresponding adiabatic PES.

CHAPTER 3 : Diabatic Coupling for Charge Recombination Via Boys Localization and Spin-Flip Configuration Interaction Singles

This chapter was adapted from Ref. 68.

3.1. Introduction: modelling charge recombination

Charge transfer (CT) processes come in several varieties. In charge separation (CS), the magnitude of the difference of local charge between donor and acceptor fragments is increased, typically involving electron transfer between initially neutral donor and acceptor fragments. In charge recombination (CR), the reverse occurs, usually resulting in the system returning to its ground electronic state. Charge shift (CSh) processes are those in which electron density is exchanged, but the magnitude of the difference difference of local charge is constant; for example, an electron may be transferred from a neutral (anionic) donor to a cationic (neutral) acceptor. Of particular interest to us is the case of dye-sensitized solar cells. Here, a certain fraction of sunlight is absorbed by organic molecules, provoking photoinduced CS which can be harnessed to drive a current which powers a load. Of course, one can lose a lot of power if the organic molecule returns to its ground electronic state before permanent charge separation, generating heat via CR. Understanding and predicting the rates of CS and CR in candidate dye molecules is therefore essential for determining the potential efficiency of such a device.

The very simplest means to calculate CT rates in a condensed environment is the Marcus equation in the limit of thermal activation,

$$k_{ET} = \frac{2\pi}{\hbar}|H_{AB}|^2 \frac{1}{\sqrt{4\pi\lambda k_b T}} \exp\left(-\frac{(\lambda + \Delta G^\circ)^2}{4\lambda k_b T}\right). \tag{3.1}$$

Here, λ is the reorganization energy, ΔG° is the change in Gibbs free energy for the reaction, and H_{AB} is the diabatic coupling. Among λ, ΔG, and H_{AB}, the former two quantities can be obtained by geometric optimization of adiabatic state energies using traditional elec-

tronic structure packages, assuming weak coupling. As its signifier (H_{AB}) suggests, the diabatic coupling is the off-diagonal Hamiltonian matrix element between the initial and final electronic states of the system, which enters all perturbation or golden rule expressions. Moreover, H_{AB} is the key matrix element which drives all nonadiabatic electronic transitions and thus figures prominently both in Marcus theory and all higher order perturbation theories and complicated rate expressions. Because the electronic states produced by conventional wavefunction methods are approximations to the full CI adiabatic solutions of the Schrödinger equation, which by definition have no off-diagonal position-local Hamiltonian elements, non-standard techniques are required to compute these important quantities, as described below.

With that in mind, suppose we now seek to model a CT event for a particular molecule or molecular environment, and we begin with standard electronic structure calculations. In general, the initial and final electronic states for ET processes of model systems will not be adiabatic eigenstates for one of the following reasons: (i) the effect of external perturbations including solvent, which are often ignored due to computational cost, (ii) the effect of intramolecular motion, which is ignored when we consider frozen nuclei, or (iii) the initial experimental preparation of states. In each case, H_{AB} represents the energetic coupling between wave functions that are non-stationary with regard to the *in vacuo* electronic Hamiltonian.

Several computational techniques for approximating the diabatic couplings have been proposed in the literature.[34–36,38,44–51,53–57,69–88] For reviews on this topic, see Refs. 38 and 69. One approach for determining couplings is constrained density functional theory (CDFT), developed by Van Voorhis *et al.*[48–51] This method computes diabatic states directly by minimizing the energy of a system using Kohn-Sham density functional theory with the constraint that either spin or electronic density must be localized on some set of atomic centers. On the one hand, CDFT has the advantages of being physically motivated and computationally inexpensive. On the other hand, because CDFT constraints are applied manually,

different results can be obtained for different choices of how to localize charge. In particular, CDFT may be less trustworthy for intramolecular CT, including for donor-bridge-acceptor (DBA) molecules, and as such, CDFT is often not ideal. Another direct approach developed by Newton, and later Larsson, Dupuis and coworkers, involves symmetry-broken self-consistent field (SCF) calculations, in which an SCF calculation with relaxed symmetry constraints finds localized states as solutions.[70–79] Biorthogonalization of these states produces diabatic states.

A separate approach for diabatization is to first construct adiabatic states and then rotate these states together to form diabatic states. Several techniques have been proposed for generating this so-called adiabatic-to-diabatic rotation matrix, **U**. Some focus on minimizing the derivative couplings[34–36,80,81], other focus on keeping a constant electronic character over configuration space[82,83], such as those proposed by Ruedenberg *et al.*[44,45] and Truhlar *et al.*[46,47,84] We will use localized diabatization techniques, where **U** is chosen to imitate the localizing effects of some external perturbation, such as solvent or nuclear motion. Whereas CDFT forces the electron density to localize around arbitrary atomic centers, localized diabatization techniques can generate a set of diabatic states without any parametrization.

Notwithstanding the advantage of being parameter-free, methods that generate diabatic states by transforming adiabatic states have a particular difficulty with the specific case of CT reactions involving the ground state. The reason has nothing to do with localized diabatization and everything to do with basic electronic structure theory. CR reactions as well as certain CS and CSh reactions involve transitions to or from the ground electronic state. Unfortunately, the standard practice in quantum chemistry is to compute a ground state first and subsequently generate excited states using the same ground state as a reference. The above procedure is true for CIS, equation of motion coupled-cluster singles and doubles (EOM-CCSD), or time-dependent DFT (TD-DFT). As such, most wavefunction methods do not form ground and excited states equivalently or in a balanced manner; any diabati-

zation scheme that produces diabatic states from such an unbalanced combination of such ground and excited adiabatic states cannot be expected to be accurate or smooth. To that end, most calculations of such CT reactions require complete active space self-consistent field (CASSCF) calculations to produce the initial adiabatic eigenspace. (For some examples of such in the context of generalized Mulliken-Hush (GMH), see Refs. 89–93.) To reiterate, when modelling certain CT events, there is a basic electronic structure problem in computing stable and well-balanced adiabatic states.

With this background in mind, and a desire to compute diabatic states without too much user input, in this chapter we construct diabatic states applicable to CR by merging (1) Boys localization and (2) spin-flip CIS (SF-CIS). Both of these methods are black box and require no chemical intuition. In the first part of this chapter, we describe in further detail each of these methods. We then present the results of the application of this method to a model system of molecular LiF and LiF solvated by a single water molecule. There follows a discussion of these results and future directions for this research.

3.2. Theory and methodology

3.2.1. Localized diabatization techniques

As discussed above, there are many ways to define diabatic states [34,42,44–47,55,56,64,80–84,94–96]; no single definition is appropriate for all situations. However, for the purposes of this chapter, 'diabatic states' will refer to electronic states generated by the Boys diabatization procedure as described below. These states can be thought of as approximating the 'before' and 'after' states of a CT reaction in which an external perturbation, such as solvent or nuclear motion, acts to localize the electronic states.

Boys localization [57] is one example of a general class of localized diabatization techniques. [63,64] Localization procedures similar to these were originally applied to single-electron orbitals; these diabatization methods can be thought of as the state-space analogues of the localized molecular orbital methods originally described by Boys, Foster, Edmiston and Rueden-

berg.[58–62] For molecules with arbitrary molecular geometry, localized diabatization techniques create a set of diabatic states $\{|\Xi_I\rangle\}$ as linear combinations of adiabatic states $\{|\Phi_I\rangle\}$ through the action of a rotation matrix $\mathbf{U}$. Note that states are labeled by capital letters (I, J) and orbitals are labelled by lowercase letters (i, j, a, b). For N adiabatic states, we can write

$$|\Xi_I\rangle = \sum_{J=1}^{N} |\Phi_J\rangle U_{JI}. \tag{3.2}$$

The rotation matrix $\mathbf{U}$ is chosen to maximize a given function, and it is in the specification of this function that the various diabatization techniques differ. In Boys localization, an extension of Cave and Newton's GMH procedure[55,56,97] to multiple charge centers, the diabatic states are maximally separated by optimizing the sum of the differences between the dipole moments of the states,

$$f_{Boys}(\mathbf{U}) = \sum_{I,J=1}^{N} |\langle \Xi_I|\vec{\mu}|\Xi_I\rangle - \langle \Xi_J|\vec{\mu}|\Xi_J\rangle|^2. \tag{3.3}$$

Although Boys localization is used exclusively in this chapter, a separate method is the Edmiston-Ruedenberg (ER) procedure[64], which generates localized states by maximizing the sum of electronic self-repulsion energies,

$$f_{ER}(\mathbf{U}) = \sum_{I=1}^{N} \int d\mathbf{r_1} \int d\mathbf{r_2} \frac{\langle \Xi_I|\hat{\rho}(\mathbf{r_1})|\Xi_I\rangle\langle \Xi_I|\hat{\rho}(\mathbf{r_2})|\Xi_I\rangle}{|\mathbf{r_1} - \mathbf{r_2}|}, \tag{3.4}$$

where $\hat{\rho}(\mathbf{r})$ is the density operator, defined as

$$\hat{\rho}(\mathbf{r}) = \sum_{j}^{\text{all electrons}} \delta(\mathbf{r} - \mathbf{r_j}), \tag{3.5}$$

for $\mathbf{r_j}$ the position of the jth electron. These methods have already been used to successfully predict the triplet-triplet energy transfer rate in donor-bridge-acceptor (DBA) molecules.[63]

3.2.2. Spin-flip

The spin-flip family of techniques, developed by Krylov, Head-Gordon *et al.* use a triplet ($M_s = 1$) electronic state as a reference from which other states may be constructed.[21–23,98–101] The simplest model, SF-CIS, uses a Hartree-Fock-based reference triplet state and adds single spin-flipping excitations to generate both singlet and triplet $M_s = 0$ states. Formally, the SF-CIS wavefunction ansatz is

$$|\Phi_{SF-CIS}\rangle = \sum_{i,\bar{a}} t_i^{\bar{a}} |\Phi_i^{\bar{a}}\rangle, \tag{3.6}$$

where the i is an occupied alpha orbital, $\bar{a}$ is a virtual beta orbital, $|\Phi_i^{\bar{a}}\rangle$ is the SF reference state after having undergone an $i \rightarrow \bar{a}$ excitation.

For our purposes, spin-flip CIS has several advantages over standard CIS. First and most importantly, SF-CIS generates the singlet ground state and all excited states equivalently. More precisely, the ground and excited singlet states are all generated as linear combinations of single excitations from the reference triplet state, and therefore have the same functional form. Consequently, the ground singlet state can be rotated into the diabatic basis on equal footing with the excited singlet states and as such we expect that localization routines based on SF-CIS will offer more balanced and meaningful diabatic states. By contrast, standard CIS excited states are generated directly from linear combinations of singly excited determinants of the ground state. Subsequently mixing the HF ground state and CIS excited states isn't expected to yield either meaningful or smooth diabatic states.

Second, in cases of bond forming and breaking, and in cases of charge transfer where there are avoided crossings between the ground state and excited states, SF-CIS has a better chance of success than standard CIS. Provided the triplet electronic ground state is well-defined and well-separated from triplet excited states, the reference state for SF-CIS will be smooth. All singlet states will then be automatically constructed with multireference character to allow for static correlation. Whereas standard CIS will certainly fail in these

cases, the odds are reasonable that SF-CIS will solve the Schrödinger equation at least qualitatively correctly. Hsu *et al.* have previously taken advantage of these features by using SF-CIS to calculate diabatic coupling terms from energy splittings in the symmetric case.[87,88]

3.2.3. Boys-localized SF-CIS states

A method for applying Boys localization to CIS excited states has been described previously.[63] In the present context, the application to SF-CIS requires nominal adjustments. Because Boys localization requires only the dipole moments between adiabatic states, we need only compute the dipole moments between SF-CIS states and then apply the standard Jacobi sweeps algorithm.[61]

For SF-CIS states (Eq. 3.6), we find

$$\langle \Phi_I | X | \Phi_J \rangle = \sum_i \delta_{IJ} X_{ii} - \sum_{ij\bar{a}} t_i^{I\bar{a}} t_j^{J\bar{a}} X_{ij} + \sum_{i\bar{a}\bar{b}} t_i^{I\bar{a}} t_i^{J\bar{b}} X_{\bar{a}\bar{b}}. \tag{3.7}$$

This quantity has the nearly the same functional form as the equivalent quantity calculated for standard CIS states; the only difference is that we now include $\alpha \rightarrow \beta$ excitations in place of $\alpha \rightarrow \alpha$ and $\beta \rightarrow \beta$ excitations.

3.3. Results

In order to test the method suggested above, we examine the potential energy surfaces of two model systems: molecular LiF and molecular LiF solvated with a single water molecule. To make a good comparison, values were obtained with standard CIS and SF-CIS with Boys diabatization. A modified version of the Q-CHEM software package[102] was used with a 6-31G* basis for all calculations. Single-point calculations were performed along a reaction coordinate R representing the Li-F internuclear separation. For the solvated system, the nuclear geometries were optimized and then frozen in place with the exception of the fluorine atom. Finally, note that because independent calculations are needed for each point along

the reaction coordinate, arbitrary phases are introduced that affect the sign of the diabatic coupling. Consequently, the sign of this quantity is chosen to maximize continuity.

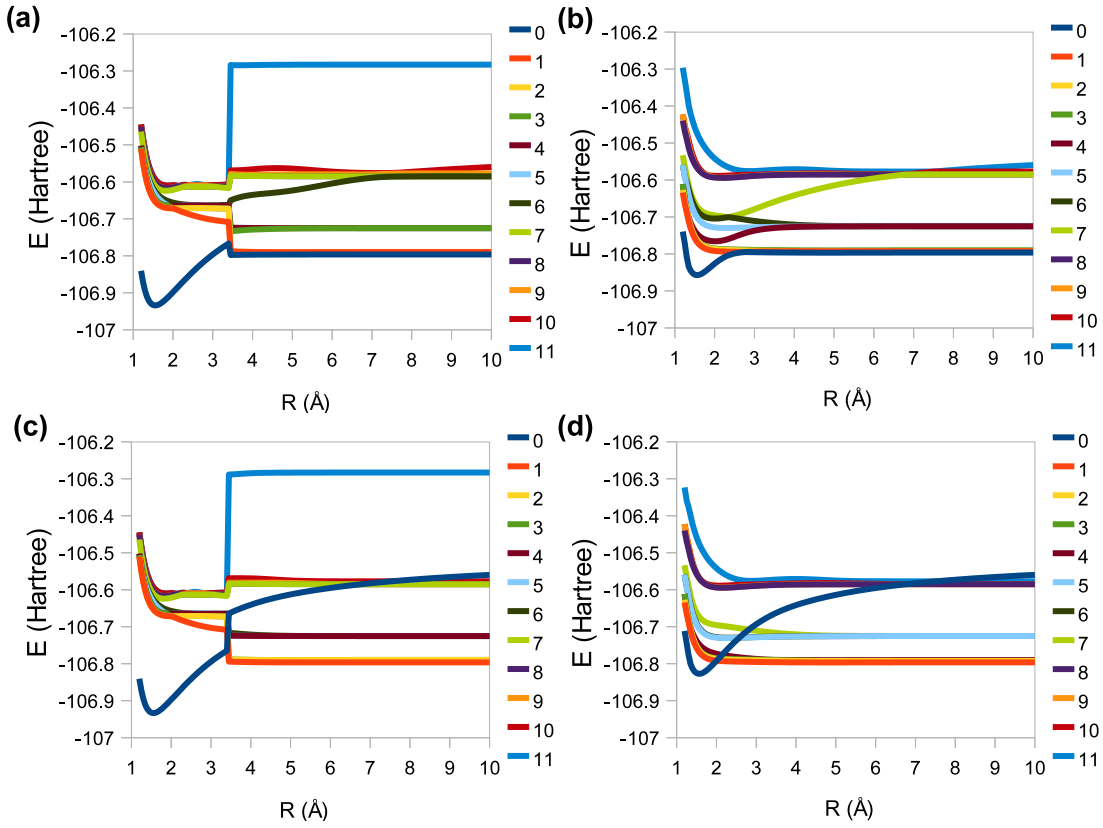

Figure 3.2: Energies of the twelve lowest electronic states of molecular LiF in a vacuum as a function of internuclear separation R. **(a)** Standard CIS adiabatic states, **(b)** SF-CIS adiabatic states, **(c)** standard CIS diabatic states and **(d)** SF-CIS diabatic states. States are ordered by energy in the adiabatic basis, and all states but the single CT state (state 0) are ordered by energy in the diabatic basis. All non-CT states have been block-diagonalized after diabatization. Values from the present work were constructed from an adiabatic space of the 12 lowest-energy eigenstates.

3.3.1. Adiabatic states

Before considering diabatic representations of LiF, we first consider adiabatic energies. The most pronounced difference between quantities generated by the standard CIS and SF-CIS calculations is the lack of the closed-shell/open-shell discontinuity in the latter case (Fig. 3.2). This irregularity appears immediately in the adiabatic energies shown in Fig. 3.2a. The UHF adiabatic energy has a large kink at R = 3.4 Å. This irregularity is propagated

into other quantities as well, including the electric dipoles, the average of the squared total spin, and the diabatic couplings. By contrast, the SF adiabatic energies are smooth in Fig. 3.2b, as are all other quantities obtained using a SF-CIS basis (Figs. 3.3, 3.6, and 3.8).

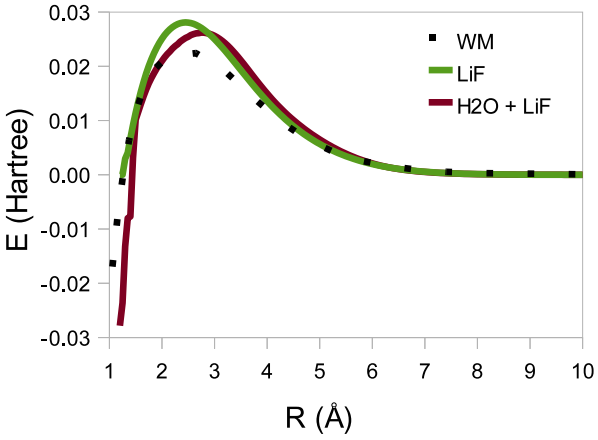

Figure 3.3: Diabatic couplings to the CT state from lowest-energy covalent diabatic state as a function of Li and F internuclear separation R. Depicted are two quantities from the present work: LiF in a vacuum and LiF solvated by a single, frozen water molecule. Values from the present work were constructed from the 12 lowest states of the SF adiabatic eigenspace in the case of molecular LiF, and the 11 lowest states in the case of solvated LiF. The "WM" values are from Ref. 4, calculated for molecular LiF alone.

3.3.2. Diabatic states

We now turn to the diabatic state energies and couplings (Fig. 3.3). *Ab initio* calculations have been used to determine the diabatic coupling of LiF for several decades.[4,103–106] As a comparison for the diabatic couplings obtained from the present work, we include results obtained by Werner and Meyer.[4] In their analysis of the system, the two lowest $^1\Sigma^+$ states were calculated using multi-configurational SCF with the optimized valence configuration method and a hand-picked active space. They then produced diabatic states via rotation with the 2×2 unitary matrix that diagonalizes the dipole along the reaction coordinate. The present work is nearly black box, and appears to overestimate the peak coupling value by $\sim$0.005 Hartree with respect to Werner and Meyer's results. However, the peaks are located at the same internuclear separation and the behavior of our curves largely replicates that of Werner and Meyer.

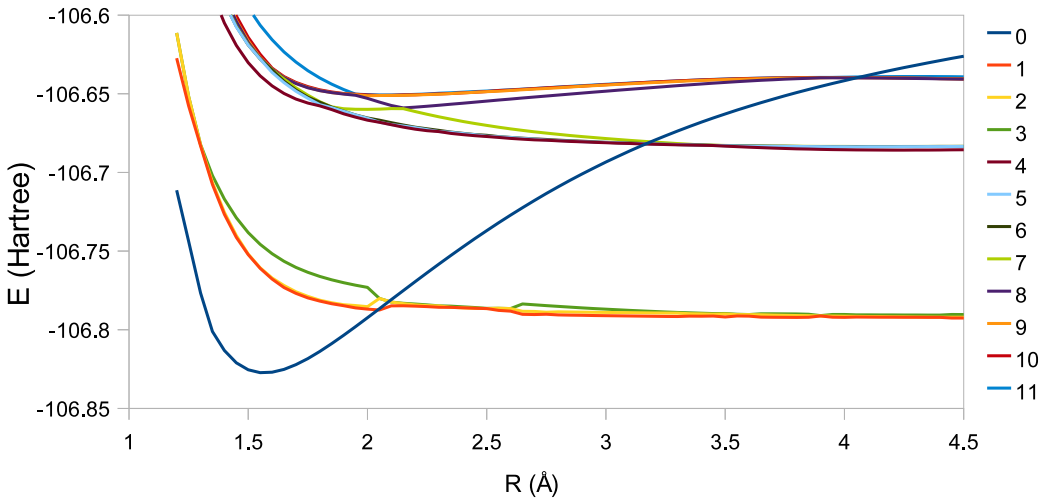

Figure 3.4: Energy of 12 lowest electronic states for molecular LiF as a function of reaction coordinate R, which represents the separation between Li and F nuclei. All states but the single CT state (state 0) are ordered by energy. These are the energies of states that have not been block-diagonalized after undergoing diabatization, and consequently demonstrate some irregularities and the empirical need for rediagonalization of non-CT states.

It should be noted that the diabatic states from the present work have been calculated using more than two adiabatic states. Instead, we use 12 adiabatic states, so $\mathbf{U}$ is 12×12. For a discussion of subspace choice, see section 3.5. We emphasize that all diabatic states have been block-diagonalized after the extraction of the CT state. This is in keeping with the constraints imposed by Cave and Newton for GMH.[55] Block diagonalization allows for the states associated with a particular charge center to be locally adiabatic while retaining diabatic coupling terms to electronic states localized elsewhere. LiF diabatic energies generated without the benefit of block diagonalization (Fig. 3.4) are notably less smooth; in particular, the diabatization procedure appears to create an unnatural discontinuity between states 1-3 in the region R $\cong$ 2.0-2.6 Å. These apparent discontinuities are caused by the fact that there is no unique set of Boys localized states for this model problem–the Boys function appears to have a zero eigenvalue for the Hessian at the optimal point. This seems logical, because one can only localize down to the atom; when there are multiple states all with the same excitation character on the same atom center, further localization is not unique. As such, block localization would appear very important.

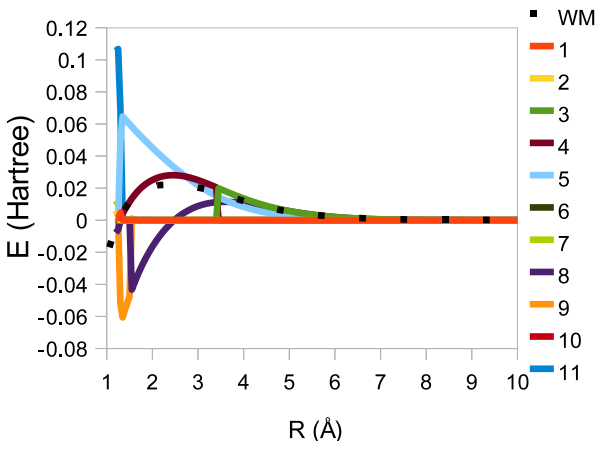

Figure 3.5: Diabatic couplings to the CT state from the 11 lowest-energy covalent diabatic states as a function of internuclear separation R. Because each calculation is independent, the signs of these quantities has been chosen to maximize continuity. The "WM" values are from Ref. 4. See Fig. 3.3 for a more limited and clearer subset of these results.

All 11 diabatic couplings from covalent states to the CT state of molecular LiF in the SF adiabatic basis can be seen in Fig. 3.5. In order to make this figure clear, in Figs. 3.3 and 3.7 we plot the diabatic coupling for a smaller subset of diabatic states: only the couplings from the lowest-energy covalent state with non-zero coupling to the CT state are shown. For R $\leq$ 3.4 Å, these couplings are between the CT state and state 4, but for R $>$ 3.4 Å, the identity of the appropriate coupling state abruptly changes to state 3. States 3 and 4 happen to be nearly degenerate in the SF adiabatic basis; this irregularity arises from an incidental switching of their identities at this point. Our SF calculations impose no symmetry constraints, and only one of these states has $^1\Sigma^+$ symmetry at each R value.

3.3.3. Solvation effects and Condon Principle

Marcus theory assumes the "Condon approximation," namely that the diabatic coupling is independent of nuclear coordinates. When modelling CR in a condensed environment, we would like to compute the diabatic coupling in vacuum and ignore CR to solvent for computational savings. As such, ideally the diabatic coupling between the covalent and ionic states of LiF should not depend on water position or orientation. When a solvent

molecule is introduced to the system, modest changes in the diabatic coupling are apparent (Fig. 3.3). The peak of 0.028 Hartree in the isolated case is reduced to 0.026 Hartree with the introduction of the water molecule. Solvation also induces a peak shift, from 2.45 Å separation to 2.75 Å. This model suggests that coupling is weakened by solvation with one monomer, although only slightly. The ability of solvent-induced non-Condon effects to reduce diabatic coupling has been reported previously using dielectric continuum solvation.[107] In that case, the reduction was determined to be caused by an increase in the separation between centroids of the relevant donor and acceptor electronic states; a similar effect might be possible here. Finally, we see that in both the solvated and non-solvated cases, the diabatic coupling is sensitive to movement along the reaction coordinate. At large internuclear separations the expected exponential decay $H_{AB} \propto e^{-\frac{1}{2}\beta R}$ is observed. In the future, it might be interesting to explore the veracity of the Condon approximation in larger systems, e.g. by adding a larger solvation shell, although this introduces a new set of problems, including CT to solvent and long-range Coulomb interaction.

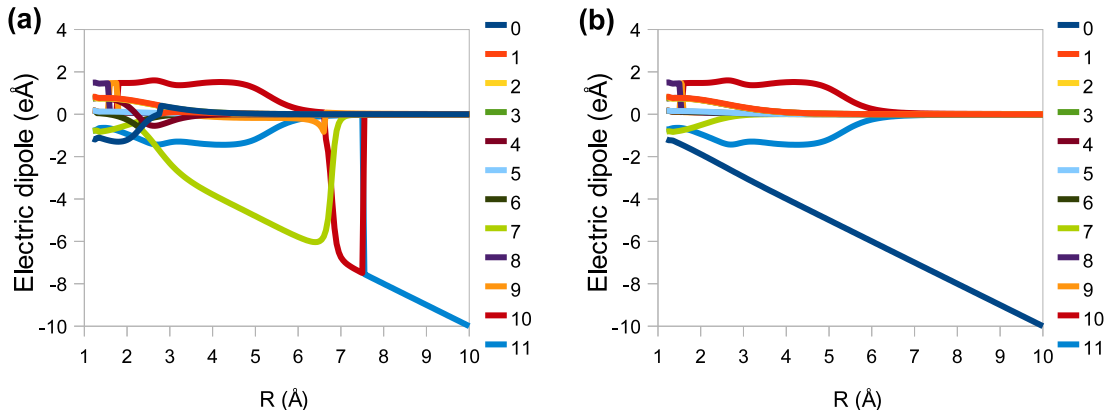

Figure 3.6: Electric dipole along the internuclear axis of 12 lowest SF electronic states of molecular LiF as a function of internuclear separation R. Values obtained from **(a)** adiabatic states and **(b)** diabatic states are shown. States are ordered by energy in the adiabatic basis, and all states but the single CT state (state 0) are ordered by energy in the diabatic basis. Consider how much smoother the values are in the diabatic basis than in the adiabatic basis. These calculations highlight the changing electronic character of different adiabatic states at different nuclear geometries, and the power of a diabatic representation.

3.3.4. Electric dipole moment

In order to highlight the meaning of localized diabatic states, we now look at dipole moments. The changing character of the adiabatic basis is clear if one examines the electronic dipole moment as a function of internuclear separation, i.e. our choice of reaction coordinate (Fig. 3.6a). This picture makes clear how many avoided crossings there are in the adiabatic basis and why a diabatic basis is useful. The dramatic changes in the dipole moment of the adiabatic states is almost entirely resolved in the diabatic basis (Fig. 3.6b), suggesting that this procedure preserves the character of states across configuration space at least for those states with non-zero dipole moment. The CT state in particular has been isolated over the entire range of nuclear separations examined.

3.4. Discussion

We have shown that the Boys diabatization method successfully isolates the CT state using both standard CIS and SF-CIS adiabatic bases. For the standard CIS case, however, irregularities and discontinuities in the potential energy surface arise from single-reference character of the reference HF state and are propagated into other quantities, including diabatic coupling values. By contrast, quantities generated from SF-CIS states contain none of these features: we have shown that Boys-localized SF-CIS diabatic states can have smooth energies, diabatic couplings, electric dipoles, and total spin squared angular momentum. This approach is nearly black box and does not require much user input or chemical intuition. It also applies to arbitrarily many adiabatic states, as demonstrated here with 12 electronic states. Thus localized diabatization of SF-CIS electronic states appears to be a promising, low-cost method of obtaining CT rates. That being said, we now address a few concerns and unexplored issues.

3.4.1. Choice of adiabatic subspace

Because the adiabatic states form a basis for the construction of the diabatic states, the choice of supspace is essential for localized diabatization. Errors associated with choosing

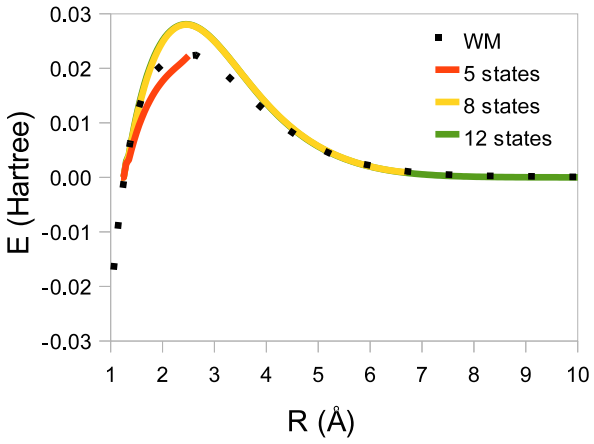

Figure 3.7: Diabatic coupling to the CT state from the lowest-energy covalent diabatic state of molecular LiF as a function of reaction coordinate R, which represents nuclear separation between Li and F. Calculations were performed using a basis composed of the five lowest states, the eight lowest states, and the twelve lowest states of the SF adiabatic eigenbasis. We see from the deviation of the 5 state calculations that this quantity is sensitive to the number of adiabatic states used as a basis for the diabatization procedure. The "WM" values are from Ref. 4.

too small of an adiabatic basis can be demonstrated in the current system (Fig. 3.7). Failure occurs in both the 5- and 8-state calculations when the internuclear distance removes the ionic state from the adiabatic basis (at 2.6 Å and 6.9 Å, respectively). It is clear in the 5-state calculation that the diabatic couplings have not converged with respect to adiabatic basis size even before this point. This alone may not be problematic, as recent work shows more states may not always be better for describing initial and final CT states.[108] Moreover, the block diagonalization criterion resolves some problems caused by too large an adiabatic basis. In choosing a subspace, one criterion is certain, however. Because it can be shown that the degree of mixing between adiabatic states due to nuclear motion is inversely proportional to their difference in energy, typically all excited states below a certain energy cutoff are chosen as the basis. This cutoff must be selected to include a converged adiabatic basis, i.e. one which does not exclude any states that are close in energy to any state included in the basis and which therefore might contribute significantly to the diabatic states in a real system. Consequently, the basis is typically chosen to include states below some large energy gap in CIS spectrum. In the current work, a 12-state basis was chosen because the

states included are separated from the next-lowest-energy state by ∼0.3 Hartree. However, there is no reason to think that such a gap will exist between a convenient set of adiabatic states in all systems. As this work progresses, a more general procedure for determining the state cutoff should be explored.

3.4.2. Black box block diagonalization

Block diagonalization after localization is important because one must relax electronic states with charge or excitation character on the same "fragment." In the present work, it was known that only one CT state exists in the state space explored. Selecting the appropriate subspaces for block diagonalization was a simple matter of identifying the electronic state with the largest electric dipole along the internuclear axis. However, that approach requires user input to implement, and as such SF-CIS/Boys localization cannot yet be considered a wholly black box algorithm. Constructing an algorithm that can automatically relax diabatic states with charge or excitation character on the same fragment is a key objective in the future development of this method.

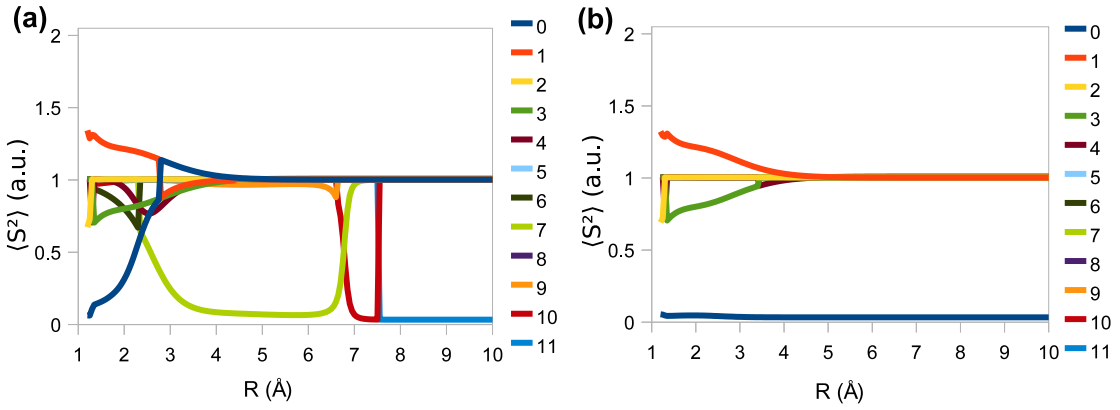

Figure 3.8: $\langle S^2 \rangle$ for 12 lowest SF electronic states of molecular LiF as a function of internuclear separation R. SF-CIS results in the **(a)** adiabatic and **(b)** diabatic basis are shown. States are ordered by energy in the adiabatic basis, and all states but the single CT state (state 0) are ordered by energy in the diabatic basis. All non-CT states been block diagonalized after diabatization. These quantities demonstrate the high degree of spin purity of the CT state in the diabatic basis, and the high degree of spin contamination of all other states.

3.4.3. Spin contamination and energetic accuracy

Finally, both the standard and SF-CIS results presented here possess a high degree of spin contamination (Fig. 3.8). Ideally, we should find singlets ($S^2 = 0$) and triplets ($S^2 = 2$). Instead, we find that most states have $\langle S^2 \rangle = 1$. That being said, the charge transfer state in both cases has been made nearly spin-pure by the diabatization process, further suggesting that this method enforces a sort of uniformity of character across phase space in spite of the unrestricted nature of the adiabatic basis. However, this cannot be accomplished in general for every diabatic state in the SF-CIS basis. This problem can likely be addressed by use of the SF extended single excitation configuration interaction (SF-XCIS) method.[99–101] SF-XCIS improves the SF-CIS description of states by including the use of singly- and certain doubly-excited states to produce less spin-contaminated adiabatic states. In principle, this should provide a more accurate depiction of the potential energy surface with a marginal increase in computational cost. As demonstrated previously by Casanova *et al.* in the similar HF system, SF-XCIS also produces a much more accurate ground state energy for the dissociation of this type of molecule.[99] These results are born out in LiF as well, as shown in Fig. 3.9. Our next step is to apply localized diabatization methods to the SF-XCIS algorithm, and model the effects of the newly added double excitations on the resulting diabatic states. Following the work of Larsson[109], we don't expect correlation effects to be large, but this will be checked explicitly.

3.5. Conclusions

In this chapter, we have presented a general method for obtaining off-diagonal Hamiltonian coupling elements for intramolecular and intermolecular CT reactions. In contrast to other available techniques, this method is nearly black box and applicable to multiple charge centers. Using a model LiF system, it was shown that the diabatization procedure is capable of producing a set of smoothly varying states that include an isolated CT state. Furthermore, diabatic couplings are calculated which (1) are only weakly impacted by the presence of solvent, confirming the Condon approximation, and (2) are comparable

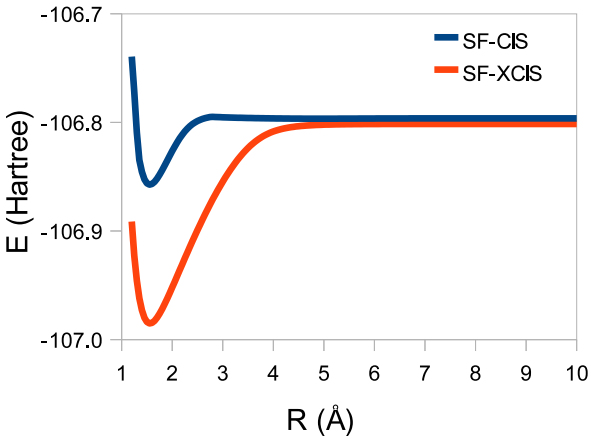

Figure 3.9: Ground state adiabatic energy of molecular LiF as a function of internuclear separation R as calculated by both SF-CIS and SF-XCIS procedures. The spin-pure SF-XCIS energies shows a marked improvement in variational accuracy. Future work will explore and compare localized diabatization as applied to SF-XCIS adiabatic states.

to previously reported values calculated using MCSCF. The SF/Boys localization method relies on a level of theory no higher than CIS and does not require a hand-picked active space. As such, we believe that this combination of algorithms offers a meaningful and computationally accessible approach for calculating diabatic couplings.

CHAPTER 4 : Optimal Diabatic States Based on Solvation Parameters

This chapter was adapted from Ref. 65.

4.1. Introduction

Conventional electronic structure calculations generate orthonormal adiabatic states, for which the electronic charge and excitation are usually delocalized near avoided crossings. Within the construct of time-dependent quantum mechanics, however, a more interesting question is: what are the initial and final electronic states of a physical system undergoing electron transfer (ET) or excitation energy transfer (EET)? These electronic states are usually denoted diabatic states (in contrast with the 'historical' definition of diabatic states as those with minimal derivative couplings[34–36]), and for these states, electronic charge or excitation is necessarily localized, even at an avoided crossing. In principle, diabatic states should be stationary with respect to perturbations from nuclear motion (Born-Oppenheimer coupling) or, as we have argued,[63,64] to fluctuations in solvent structure. Methods that construct such diabatic states do so by (i) imposing constraints on wavefunctions[42,46,47,70–74,76–78,84] or density,[110] such as constrained density functional theory,[48–51,111] or (ii) rotating a basis of adiabatic states, either to diagonalize an observable,[52–54,85,112] a technique most notably used in the generalized Mulliken-Hush method developed by Cave and Newton,[55,56] or more generally, to optimize some diabatization function.[57,63,64,68]

Now, supposing we can generate a set of reasonable diabatic states, we can imagine two different uses for such an electronic basis. First, one might use such states in the context of Marcus theory to model ET[38,48–52,55–57,64,68–74,76–78,110,111] or EET[53,54,63,64,85,112–114] according to golden rule perturbation theory. This scenario only makes sense if (i) the electronic coupling is small; (ii) the electronic coupling doesn't depend on nuclear constraints (in accordance with the Condon approximation), which effectively restricts the usefulness of such couplings to rigid molecules (for example, see Ref. 63); (iii) the derivative couplings

between such diabatic states must be mostly negligible. In this context and the activated crossing limit, diabatic potential energy surfaces (PESs) are unnecessary; one needs only an approximate value for the electronic coupling (H_{IF}) for the Marcus rate of ET,[113,114]

$$k_{IF} = \frac{2\pi}{\hbar}|H_{IF}|^2\sqrt{\frac{1}{4\pi\lambda k_B T}}e^{-(\Delta G^\circ+\lambda)^2/4\lambda k_B T}, \tag{4.1}$$

in which the indices I and F refer to the initial and final electronic states of the system, λ is the solvent reorganization energy, and ΔG° is the change in free energy between the fully relaxed initial and final states.

Of course, there is a second scenario wherein one needs diabatic potential energy surfaces in addition to the diabatic and derivative couplings, all as a function of nuclear coordinates ζ. Namely, if one of the three conditions above is not satisfied, and thus one cannot simply apply Marcus theory. In this case, one must run some version of nonadiabatic dynamics for a more comprehensive picture of ET/EET.[115] To do so, a good first step is to develop optimal smooth diabatic PESs, which should optimally have small diabatic *and* derivative couplings, along the lines of Michael Herman's suggestion.[116,117]

To that end, in this chapter we propose to generate such diabatic states using an implicit solvent (with Pekar factor C) to model environmental effects that are absent in our electronic structure calculations. Certainly solvent can play a role in understanding diabatic states.[89] In fact, a strong motivation for this chapter is the work of Yeganeh and Van Voorhis,[118] who incorporated temperature and system-solvent coupling parameters into a new method for evaluating diabatic states for a model spin-boson Hamiltonian. In this chapter we report a localized diabatization method that is both sensitive to environmental conditions and which produces diabatic states for arbitrary systems, in a sense extending the approach used in Ref. 118. All of this is done within the framework of conventional electronic structure calculations. Armed with such a new tool, we will explore whether one should expect diabatic states with localized electronic charge, excitation, or couplings, and the subsequent consequences for predicted ET/EET rates.

4.2. Notation

The uppercase letters $\{I, J, K, L\}$ index adiabatic electronic states, while A will be used to index diabatic electronic states. The lowercase letters $\{i, a, p, q, r, s\}$ index molecular orbitals, with i and a indexing occupied and virtual orbitals, respectively. An uppercase italic E denotes a diagonal element of the Hamiltonian H. Electronic states are denoted Φ, and diabatic states in particular are denoted Ξ. All other terms are explained as they arise.

4.3. Theory and methodology

In order to generate our optimal diabatic states, we use some variation of localized diabatization: a basis of N adiabatic electronic states is mixed together via an adiabatic-to-diabatic rotation matrix $\mathbf{U}$, such that

$$\Xi_A = \sum_{I=1}^{N} \Phi_I U_{IA}. \tag{4.2}$$

This rotation matrix is chosen by optimizing some diabatization function $f(\mathbf{U})$. Because N is generally small, the computational cost of any such procedure is minimal compared to that of the electronic structure technique used to generate the adiabatic basis. Previously, our research group has explored ER (Edmiston-Ruedenberg) diabatization [64] as a means to create localized electronic states for golden rule ET/EET rates. In principle, ER diabatic states are derived by including electrostatic interactions from a homogeneous linear dielectric solvent. The relevant diabatization function, f_{ER} (Eq. 4.3), accounts for system-solvent interactions by summing the solvation energies of the diabatic states (up to a constant).

$$f_{\mathrm{ER}}(\mathbf{U}) = \sum_{A=1}^{N} \int d\mathbf{r_1} \int d\mathbf{r_2} \frac{\langle \Xi_A | \hat{\rho}(\mathbf{r_1}) | \Xi_A \rangle \langle \Xi_A | \hat{\rho}(\mathbf{r_2}) | \Xi_A \rangle}{|\mathbf{r_1} - \mathbf{r_2}|} \tag{4.3}$$

$$\equiv \sum_{A=1}^{N} R_{AAAA} \tag{4.4}$$

In f_{ER}, the diabatic self-interaction term R_{AAAA} can be obtained from the adiabatic self-interaction tensor via the transformation

$$R_{AAAA} = \sum_{I,J,K,L=1}^{N} U_{IA}U_{JA}U_{KA}U_{LA}R_{IJKL}, \tag{4.5}$$

and the density operator $\hat{\rho}$ is defined

$$\hat{\rho}(\mathbf{r}) = \sum_{i=1}^{\text{all electrons}} \delta(\mathbf{r} - \mathbf{r_i}), \tag{4.6}$$

where $\mathbf{r_i}$ is the position operator for the i^{th} electron.

Although ER localization has many advantages, there are two drawbacks to the procedure: (i) ER diabatization does not take the energy difference between states into account, and will therefore mix states together even when such states are separated by a large energy gap, provided there is enough gain in solvation energy. In other words, ER diabatization 'over-mixes' adiabatic states because it ignores the off-diagonal fluctuations in the electronic Hamiltonian. Consequently, diabatic states constructed by maximizing f_{ER} can strongly depend on the choice of adiabatic basis (in particular, the number of adiabatic states), which is not optimal. (ii) The localization function f_{ER} is independent of temperature or any kind of solvent parameter, and therefore is insensitive to environmental conditions, which is not always realistic. The original justification for ER[64] was based on a strong polar solvent, which limits the generality of the algorithm.

To correct these deficiencies and ideally generate optimal PESs for surface hopping, we propose a new localization function, $f_{\mathrm{ER}-\varepsilon}$ (Eq. 4.7). This function uses the same approximation of a linear dielectric solvent as f_{ER}, but now mediates its effect on the system through the inclusion of diabatic state energies in addition to the temperature and polarity

of the medium. We define $f_{\mathrm{ER}-\varepsilon}$ as

$$f_{\mathrm{ER}-\varepsilon}(\mathbf{U}) = \sum_{A=1}^{N} \exp\left(-\beta\left(E_A - \frac{C}{2}R_{AAAA}\right)\right), \tag{4.7}$$

where the diabatic state energies can be obtained from the adiabatic Hamiltonian via the transformation

$$E_A = \sum_{I,J=1}^{N} U_{IA}U_{JA}H_{IJ} = \sum_{I=1}^{N} U_{IA}^2 E_I, \tag{4.8}$$

where $\beta = \frac{1}{k_B T}$ (see also Appendix A.4), and where C is the Pekar factor,

$$C = \frac{1}{\varepsilon_e} - \frac{1}{\varepsilon_s}, \tag{4.9}$$

with ε_e and ε_s the high-frequency and static dielectric permittivities of the environment, respectively. The Pekar factor was chosen as a coefficient to this term so that only the permanent dipole contributions are taken into account when calculating the system-bath interaction energy. Although the electronic contributions from the solvent are important, these cannot be adequately accounted for without treating the solvent at a much higher level of theory.[119] Consequently, this method assumes that the solvent is only able to reorient slowly with respect to the system, allowing nuclei to be treated classically. Both this system-solvent interaction term and the electronic state energy are incorporated into the ER-ε function (Eq. 4.7) in such a way that maximizing $f_{\mathrm{ER}-\varepsilon}$ is approximately analogous to minimizing the Helmholtz free energy A (Eq. 4.10) for an electronic Hamiltonian perturbed by solvent interactions, with $H = H_{\mathrm{el}} + H_{\text{system-bath}}$. See Appendix A.5 for a more detailed description of how $f_{\mathrm{ER}-\epsilon}$ is maximized in practice.

$$A = -\beta^{-1} \ln \mathrm{Tr}\left(e^{-\beta H}\right) = -\beta^{-1} \ln\left(\sum_{I} e^{-\beta E_I}\right) \tag{4.10}$$

The new ER-ε function addresses the shortcomings of ER diabatization in two ways. First, by including state energies in the expression for $f_{\mathrm{ER}-\varepsilon}$, this method discourages mixing be-

tween states that have different energies, i.e., where the energy difference between adiabatic states is larger than any possible gain in solvation energy. Second, this function introduces parameters for temperature and solvent polarity, which can account for the different degrees of localization resulting from changing the solvent environment.

Furthermore, $f_{\mathrm{ER}-\varepsilon}$ behaves appropriately in the required limiting cases. For example, in the high temperature limit, the function becomes

$$\lim_{\beta\to 0} f_{\mathrm{ER}-\varepsilon}(\mathbf{U}) \approx 1 - \beta \mathrm{Tr}(H) + \beta \frac{C}{2} \sum_{A=1}^{N} R_{AAAA}. \tag{4.11}$$

Because the trace of the Hamiltonian is invariant under unitary transformation, maximizing $f_{\mathrm{ER}-\varepsilon}$ becomes equivalent to maximizing f_{ER}. Thus, $f_{\mathrm{ER}-\varepsilon}$ recovers the expected behavior in the high temperature limit, i.e. the localization of charge or excitation density in response to rapid nuclear motion, and subsequent electronic decoherence (in the localized basis).[120–122] Conversely, at lower temperatures nuclei become effectively frozen, therefore allowing electronic tunneling to dominate, resulting in delocalized excitations[121,122] and coherent oscillations between diabatic electronic states.[120] As a result, there is a well-known transition between band and hopping descriptions of electron transfer as a function of increasing temperature.[121,122]

Similarly, in the case of a very small Pekar factor (which is equivalent to removing the solvent), the ER-ε function becomes

$$\lim_{C\to 0} f_{\mathrm{ER}-\varepsilon}(\mathbf{U}) = \sum_{A=1}^{N} \exp\left(-\beta E_A\right). \tag{4.12}$$

Maximizing this expression is equivalent to diagonalizing the Hamiltonian, therefore recovering adiabatic states in a vacuum. By increasing C, the system-solvent interaction term can be 'turned on,' thus continuously increasing the amount of state localization. The strength of the ER-ε approach is that by altering these parameters, we can walk between maximally localized and delocalized electronic states as a function of solvent polarity (C)

and temperature (T).

4.4. Results

We have modified the Q-CHEM 3.2 package[102] to implement ER-ε diabatization, and tested the procedure on both intramolecular and intermolecular model systems. All excited state calculations were performed using standard configuration interaction singles (CIS) with a 6-31G* basis. ER-ε states are computed assuming benzene solvent ($C = 0.5$[123–125]) at room temperature ($T = 298$ K) unless otherwise specified. All visualizations were generated using VMD.[126]

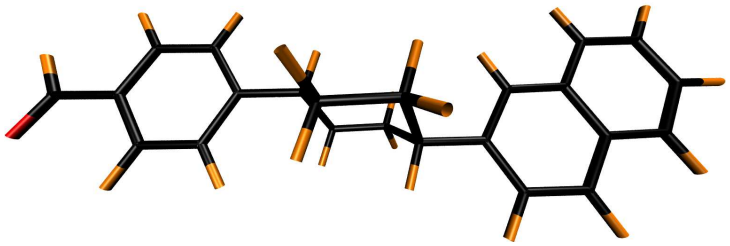

Figure 4.10: DBA molecule in which the 4-benzaldehydeyl donor and the 2-naphthyl acceptor groups are joined at 1,4-equitorial positions on a cyclohexane bridge, henceforth known as C-1,4ee. Here C-1,4ee is shown in the geometry optimized for the A*D configuration of the T_1 excited state.

4.4.1. Multi-state mixing and total coupling minimization

As discussed in section 4.3, according to many modern diabatization algorithms, diabatic states are constructed without reference to the energy differences between adiabatic states, thereby generating over-mixed diabatic states which must be remedied by block diagonalization of charge centers after mixing.[55,56,68] The ER-ε diabatization function was designed in part to remedy such unphysical behavior. In order to evaluate the new function's tendency to over-mix, we will compare ER-ε with ER diabatic states along an EET reaction coordinate using a large ($N = 7$) adiabatic basis, including states separated by both large and small energy gaps. In particular, we have modelled the lowest-energy triplet states of the system identified as C-1,4ee by Closs *et al.* in Ref. 11: a donor-bridge-acceptor (DBA)

molecule in which the donor and acceptor are joined to a cyclohexane bridge at 1,4 equatorial positions (Fig. 4.10). In Ref. 11, the donor is a 4-benzophenoneyl group, and the acceptor is a 2-naphthyl group, but in the current work we substitute 4-benzaldehydeyl as the donor for simplicity (as in Ref. 63). The surfaces and diabatic couplings are calculated over a set of nuclear geometries interpolated linearly between optimized A*D and AD* minimum-energy configurations of the T_1 state.

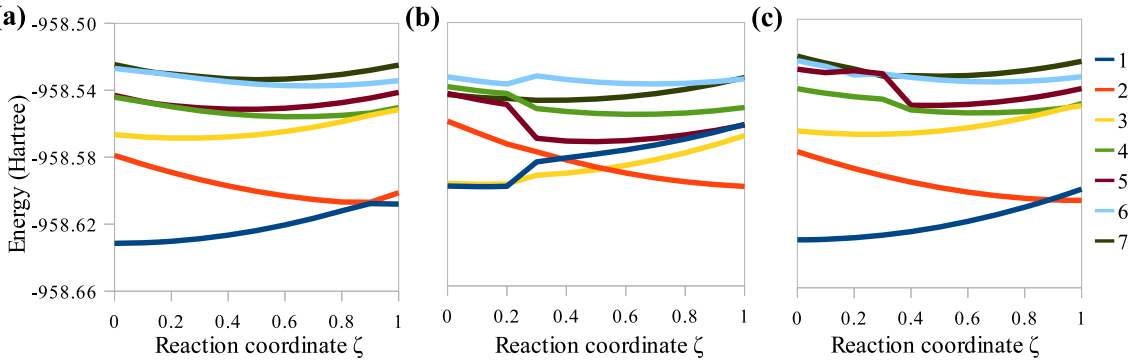

Figure 4.11: PES of the seven lowest-energy triplet states of C-1,4ee in three bases: **(a)** the adiabatic basis, **(b)** the ER diabatic basis, and **(c)** the ER-ε diabatic basis. The reaction coordinate ζ denotes a linear interpolation between two geometries: $\zeta = 0$ corresponds to the optimized A*D geometry, and $\zeta = 1$ corresponds to the optimized AD* geometry. While the two lowest-energy ER diabatic states are clearly over-mixed with higher-energy states, this is not a problem for ER-ε diabatic states.

The diabatic state energies for the DBA system are presented in Fig. 4.11. Although ER has been shown to perform well on this system with a smaller ($N = 2$) adiabatic basis,[63] it clearly fails if a larger basis is employed. Of particular concern is the over-mixing of T_1 and T_2 with higher-energy states, as these states are energetically well-separated from the remainder of the basis set. Admittedly, this over-mixing is not entirely unexpected, as the ER diabatization function does not take state energies into account, as discussed in section 4.3. Nevertheless, the ER-ε states do not appear to be over-mixed (Fig. 4.11c). Although there is mixing among the closely-spaced, high-energy states (T_4-T_7), the energies of T_1 and T_2 are virtually identical to that of their adiabatic counterparts, indicating minimal mixing between these states and higher-energy states. However, it is clear that mixing does occur between states T_1 and T_2 in this basis, as evidenced by the diabatic couplings shown in Fig.

4.12. This result suggests that given enough adiabatic states (with high enough energy), one can construct meaningful diabatic states without having to cherry-pick an adiabatic subspace or manually block-diagonalize after diabatization.[68]

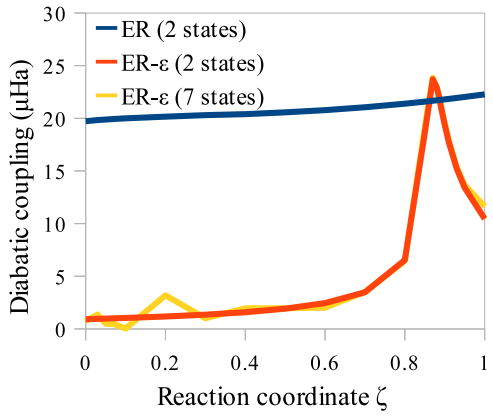

Figure 4.12: Diabatic coupling between the two lowest-energy triplet states of C-1,4ee: the reaction coordinate ζ denotes a linear interpolation between two geometries; $\zeta = 0$ corresponds to the optimized A*D geometry, and $\zeta = 1$ corresponds to the optimized AD* geometry. The diabatic coupling calculated by ER localization is nearly constant over the reaction coordinate, while that produced by ER-ε peaks at $\zeta = 0.85$, close to the avoided crossing at $\zeta = 0.887$. Notice also that the two ER-ε couplings are very similar, despite having been generated from adiabatic bases of different size, indicating that ER-ε localization is not prone to over-mixing.

Another way to determine the effect of basis set size on diabatic states is to calculate the diabatic coupling between states, as shown in in Fig. 4.12. The first thing to note is that whether we include two or seven states in the adiabatic basis, ER-ε yields nearly the same diabatic couplings between states T_1 and T_2, providing further corroboration that this method is resistant to over-mixing. The second salient feature of Fig. 4.12 is the ζ-dependence of the diabatic couplings. On the one hand, the ER diabatic coupling is essentially constant with respect to the reaction coordinate, suggesting the Condon approximation should hold, and ER diabatic states can be used in the context of Marcus theory.[113,114] On the other hand, the ER-ε diabatic coupling is maximized close to the avoided crossing and is small elsewhere. While the latter behavior does not take full advantage of the Condon approximation, these data suggest a reason why diabatic states from ER-ε may be useful for semiclassical dynamics: both the derivative and the diabatic couplings for the

ER-ε diabatic states should be negligible outside a small volume of configuration space, thus simplifying and localizing certain kinds of dynamics calculations. For example, such states were originally suggested [116,117] to be optimal for surface-hopping [127] calculations. We wonder if these 'optimal diabatic states' might also be helpful in the context of multiple spawning. [128–131]

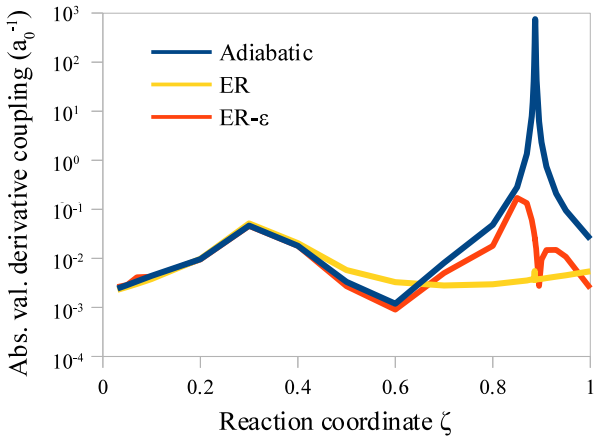

Figure 4.13: Magnitude of the approximate derivative coupling between the two lowest-energy triplet states of C-1,4ee: the reaction coordinate ζ denotes a linear interpolation between two geometries; $\zeta = 0$ corresponds to the optimized A*D geometry, and $\zeta = 1$ corresponds to the optimized AD* geometry. Derivative couplings in three bases are represented: the adiabatic basis, the ER diabatic basis, and the ER-ε diabatic basis. In the adiabatic basis, the derivative coupling becomes large close to the avoided crossing at $\zeta = 0.887$, as expected, reaching values as large as 750 a_0^{-1}. In the ER basis, the derivative couplings are consistently small, peaking at 0.05 a_0^{-1}. In the ER-ε basis, derivative couplings match adiabatic values for many nuclear geometries, and become as large as 0.17 a_0^{-1}. Close to the avoided crossing, however, this is not the case, and the enormous couplings present in the adiabatic basis are eliminated. The apparent 'kink' in the ER-ε derivative coupling is in fact a sign change (see Fig. 4.14).

Although an analytical method for calculating the derivative coupling between localized diabatic CIS states is not yet available, an estimate of this quantity may be obtained via finite difference approximation,

$$\langle \Phi_I | \frac{\mathrm{d}}{\mathrm{d}\zeta} \Phi_J \rangle \approx \frac{\langle \Phi_I(\zeta) | \Phi_J(\zeta + h) \rangle - \langle \Phi_I(\zeta) | \Phi_J(\zeta - h) \rangle}{2h}, \tag{4.13}$$

where $|\Phi_I\rangle$ and $|\Phi_J\rangle$ are CIS states that are functions of an arbitrary reaction coordinate ζ. In the present work, changes in molecular orbitals are neglected in calculating cross-state overlap, so that CIS states can be expressed

$$|\Phi_I\rangle \approx \sum_{i,a} t_i^{I,a}(\zeta)|\Phi_i^a\rangle. \tag{4.14}$$

In this approximation, overlaps are determined solely by CIS amplitudes t, so that

$$\langle\Phi_I(\zeta)|\Phi_J(\zeta+h)\rangle = \sum_{i,a} t_i^{I,a}(\zeta)t_i^{J,a}(\zeta+h). \tag{4.15}$$

A more detailed desription of how to obtain finite difference derivative couplings is described in Appendix A.3.

The approximate magnitudes of the derivative couplings with respect to movement along the triplet-triplet energy transfer reaction coordinate are shown in Figs. 4.13 and 4.14. While the adiabatic derivative coupling becomes large near the avoided crossing ($\zeta = 0.887$), the derivative couplings in both diabatic bases remain small across all geometries explored. In the ER basis, derivative couplings are reliably small, peaking at 0.05 a_0^{-1}. While the derivative coupling in the ER-ε is often larger than that in the ER basis, it does not suffer from the enormous couplings present near the avoided crossing in the adiabatic basis. This behavior results from the penalties incurred in $f_{\text{ER-}\varepsilon}$ when adiabatic state energies differ by too great an amount: mixing is discouraged everywhere but near the avoided crossing. Although this property of $f_{\text{ER-}\varepsilon}$ results in generally larger derivative couplings than in the ER basis, the very large derivative couplings in the adiabatic basis are nonetheless avoided, and this is achieved without accumulating a consistently large diabatic coupling (see Fig. 4.12). As our goal is to minimize the total couplings between states (both diabatic and derivative), this is a promising initial result.

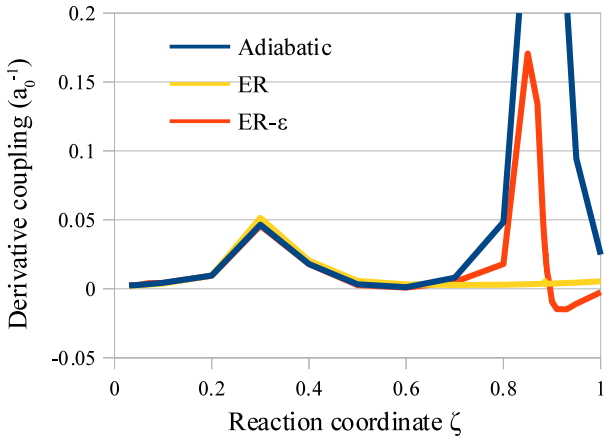

Figure 4.14: Approximate derivative coupling between the two lowest-energy triplet states of C-1,4ee: the reaction coordinate ζ denotes a linear interpolation between two geometries; $\zeta = 0$ corresponds to the optimized A*D geometry, and $\zeta = 1$ corresponds to the optimized AD* geometry. Derivative couplings in three bases are represented: the adiabatic basis, the ER diabatic basis, and the ER-ε diabatic basis. The derivative coupling values presented here are identical to those presented in Fig. 4.13, with the exception that sign information has been included in this figure. The 'kink' in the ER-ε derivative coupling near the avoided crossing in Fig. 4.13 is in fact a change of sign, as shown here.

4.4.2. Localization phase diagrams

Because ER-ε includes measurable solvation parameters, it is essential that the behavior of the function responds to these parameters in a realistic way. In order to investigate the influence of these parameters on ER-ε diabatic states, we have calculated the magnitude of mixing as a function of T and C. For simplicity, a two state adiabatic basis was used, and therefore the mixing information from the rotation matrix

$$\mathbf{U} = \begin{pmatrix} \cos(\theta) & -\sin(\theta) \\ \sin(\theta) & \cos(\theta) \end{pmatrix} \tag{4.16}$$

can be condensed into a single mixing angle θ. In our model system, as must be true, the electronic excitation density is completely delocalized in the adiabatic basis at the crossing point, so any subsequent mixing between these states can only serve to localize the excitation density.

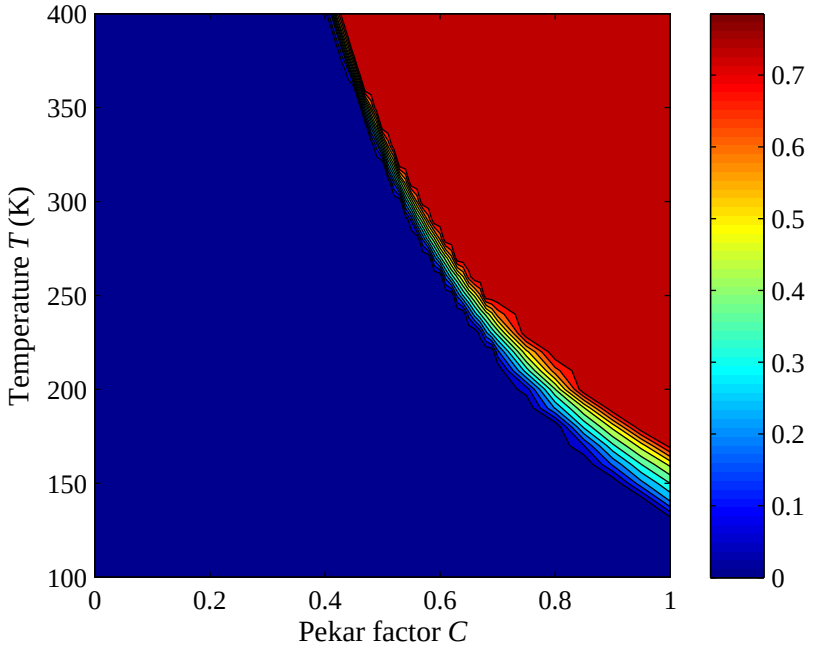

Figure 4.15: Localization phase diagram of S_1 and S_2 states of dibenzene: the degree of mixing between states S_1 and S_2 of the molecular system is presented via mixing angle θ as a function of Pekar factor C and temperature T. A mixing angle of $\theta = 0$ represents total delocalization (unchanged from adiabatic states), and $\theta = \frac{\pi}{4}$ represents total localization. The model predicts complete localization of these electronic states at room temperature for a sufficiently polar ($C \gtrapprox 0.6$) solvent.

To evaluate the effects of external environment and solvation parameters on state localization, we chose as our model system the two lowest-energy excited singlet states of two adjacent benzene molecules. For our calculations, the two rings are oriented in a clamshell configuration, rotated $\frac{7\pi}{16}$ radians with respect to one another, and are separated at their closest point by 2.54 Å. Our results are summarized in Fig. 4.15. We see a dramatic shift from fully delocalized ($\theta = 0$) to fully localized ($\theta = \frac{\pi}{4}$) as C and T are increased beyond a certain threshold. To illustrate this effect, we have included attachment/detachment densities of the bimolecular system at three points on the phase diagram (Fig. 4.16). These results correspond nicely with our intuitive understanding of electronic behavior in a condensed environment: higher temperatures reflect rapid solvent motion, which encourages the electronic states to localize.[121,122] As discussed previously, $f_{\mathrm{ER}-\varepsilon}$ enforces maximal lo-

calization in the high-temperature limit (Eq. 4.11). However, no localization was observed in this system for small Pekar factor ($C \lessapprox 0.4$) below 400 K. It is clear that the localization effects of temperature can be strongly mediated by the polarity of the solvent.

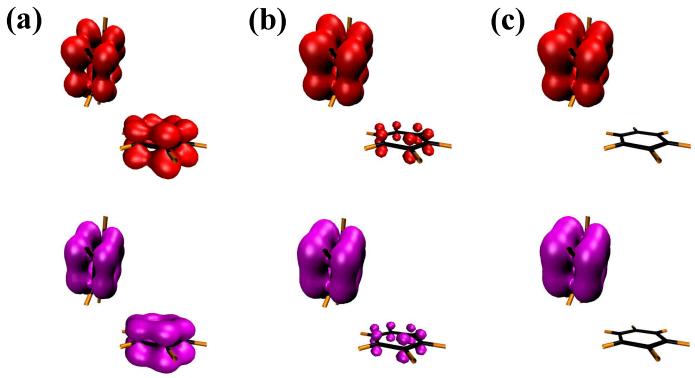

Figure 4.16: Attachment/detachment densities of the lowest-energy singlet excited state of the dibenzene system in in the ER-ε basis with three different sets of solvation parameters: **(a)** $C = 0.4$ and $T = 200$ K, (b) $C = 0.8$ and $T = 200$ K, and **(c)** $C = 0.8$ and $T = 300$ K. In each case, top figure is the attachment density, and the bottom figure is the detachment density. As solvent perturbations are applied, the delocalized excitation in the adiabatic basis begins to localize onto one ring. Increasing the polarity and temperature of the environment results in more rapid solvent fluctuations which further trap electron density.

As shown above, the degree of localization determined by $f_{\mathrm{ER}-\varepsilon}$ responds in an appropriate way to changes in T and C, and our method allows a very rough qualitative prediction of electronic properties of bichromophores in solution. To test our predictions, it would be interesting to see an experimental evaluation of state localization as a function of solvent and temperature, perhaps via time-dependent fluorescence anisotropy measurements. Choosing an appropriate model system would be key to the success of such an endeavor; in our model of localized diabatization, we account for nuclear motion only through a dielectric parameter, never explicitly, so systems with strong intramolecular vibronic coupling likely cannot be represented accurately by the electronic structure at only one nuclear geometry (the crossing point); instead, some nuclear dynamics calculations are probably necessary.

4.5. Conclusions and future directions

We have introduced the ER-ε localization function as a simple, low-cost method for obtaining diabatic states of molecules in a condensed environment. Not only is this method more realistically independent of adiabatic basis than previous methods (section 4.4.1), but it also makes qualitative predictions about state localization as a function of the dielectric constant and solvent temperature (section 4.4.2).

As previously mentioned, a principle application of this method is to generate potential energy surfaces for semiclassical surface hopping calculations. Our preliminary results strongly support the proposition that ER-ε diabatic states offer a decent approximation to the optimal diabatic basis in which total coupling (diabatic and derivative) between electronic surfaces is minimized. However, we have only determined the couplings along a single reaction coordinate; a more thorough exploration of configuration space is needed to confirm that the couplings between surfaces in the ER-ε basis are consistently small over the all accessible geometries. In order to efficiently accomplish this goal, an analytic evaluation of the derivative couplings of ER-ε states is necessary. As such, we will soon derive and implement such an algorithm. In the end, if the ER-ε basis succeeds in minimizing interstate coupling, it may prove to be a valuable tool in performing tractable surface-hopping calculations and pushing the limits of nonadiabatic dynamics simulations. As a side note, ER-ε orbitals could be interesting as well, in the context of local correlation theory, as such valence orbitals may have sparse electron-electron correlations.

4.6. Acknowledgments

The authors would like to thank David Reichman and Robin Hochstrasser for helpful discussions. This work was supported by NSF CAREER Grant CHE-1150851. J.E.S. also acknowledges an Alfred P. Sloan Research Fellowship.

CHAPTER 5 : An Analysis of Localized Diabatic States Beyond the Condon Approximation for Excitation Energy Transfer Processes

This chapter was adapted from Ref. 132.

5.1. Introduction

The ability to properly model nonadiabatic dynamics is essential for understanding innumerable chemical systems.[133] Problems in the field of nonadiabatic dynamics are commonly approached, at least in a conceptual framework, from the perspective of the strictly diabatic electronic representation. Strictly diabatic wavefunctions ($\{|\Xi_A\rangle\}$) are defined by the characteristic that they are not coupled to each other by nuclear momentum, or in other words, that the derivative couplings (DCs) are zero,

$$d_{AB}^{[Q]} = \langle \Xi_A | \nabla_Q | \Xi_B \rangle = 0, \tag{5.1}$$

where Q indexes a nuclear degree of freedom. While they are not coupled by nuclear momentum, diabatic states are coupled by elements of the electronic Hamiltonian (H_{AB}) called diabatic couplings. If this Hamiltonian is diagonalized, of course, one obtains the adiabatic basis of electronic states. The cost of this transformation is that the derivative couplings in the new basis are inversely proportional to the energy difference between the states that they couple ($d_{IJ}^{[Q]} \propto (E_J - E_I)^{-1}$), and can therefore become large near avoided crossings and diverge near conical intersections. For a brief review of the representation dependence of derivative couplings within the spin boson model, see Appendix A.1.

While a strictly diabatic basis would be useful, in practice it is impossible to obtain.[37,38] In its place, numerous approximations (called simply 'diabatic' states) have been proposed. One approach is to directly minimize DCs along a given reaction path.[34] In more recent years, Yarkony has proposed a method that can minimize derivative couplings for small- to medium-sized systems.[134,135] Other methods approximate diabatic states by construct-

ing a basis in which the states change little with respect to nuclear motion; such methods include Pacher, Cederbaum, and Köppel's block diagonalization,[43] Atchity, Ruedenberg, *et al.*'s configurational uniformity,[44,45] and Nakamura and Truhlar's fourfold way.[46,47,84] Still other techniques approach the problem more obliquely; the Generalized Mulliken-Hush (GMH) algorithm of Cave and Newton[55,56] approximates diabatic states as eigenstates of a component of the dipole operator, utilizing the heuristic property that diabatic states for electron transfer (ET) processes tend to be localized in space. The idea that singular derivative couplings could be removed by obtaining the eigenstates of an observable was later formally demonstrated by Yarkony.[66,136,137] Lastly, there are a plethora of techniques which produce diabatic states by localizing wavefunctions, including Voityuk's fragment charge difference (FCD) method;[52] Hsu's extension of FCD to excitation energy transfer (EET) systems, fragment excitation difference (FED);[53,54,85] and Boys and ER localization.[57,63,64] The concept of charge localization in ET states was also applied to the construction of diabatic densities in the context of density functional theory (DFT) by Van Voorhis *et al.*[49–51] For comprehensive reviews on this topic, see Refs. 38 and 69. The current work is concerned with localized diabatization schemes,[57,63–65] for which diabatic ET and EET states can be approximated by a linear combination of adiabatic states determined by minimizing a functional of the electronic subspace. Hereafter, any reference to diabatic states will refer to localized diabatic states.

As discussed in previous publications,[10,65] localized diabatic states could potentially be used with several nonadiabatic dynamics methods,[138,139] especially those that are agnostic to electronic representation.[127,140–142] In order to propagate dynamics in a localized diabatic representation, it is necessary to have an efficient way to determine diabatic gradient quantities; it would be even better to establish that derivative couplings in such a representation are negligible for a particular system. Additionally, localized diabatization methods have been used in the context of Marcus theory to accurately model[63] the rate of triplet-triplet EET in systems studied by Closs *et al.*[11,143] While theoretical and experimental results agreed reasonably well, until now we have not been able to prove beyond doubt that

this success was not coincidental. After all, Marcus theory is formally applicable only to strictly diabatic states.

In this manuscript, we use our newly-developed analytic gradient theory for diabatic states [10] to reexamine the validity of locally diabatic states and to ascertain definitively whether the Closs systems conform to the approximations of Marcus theory. With these considerations in mind, first, we compare the DCs of these molecules in the adiabatic and diabatic representations. If the diabatic states are similar to the strictly diabatic states postulated by Marcus, one should expect that their DCs are insignificant even near avoided crossings. Second, we use diabatic Hamiltonian gradients to estimate how much the diabatic coupling changes within the configuration space available to these systems at room temperature. In addition to assuming strictly diabatic states, Marcus theory assumes the Condon approximation, which posits that the diabatic couplings do not change significantly, and we show that it holds true here. Third and finally, in the discussion section, we will present and evaluate an approximation which can produce diabatic state gradient quantities at the cost of producing adiabatic derivative couplings.

5.2. Notation

The upper case letters $\{I, J, K, L\}$ index adiabatic electronic states, while $\{A, B, C\}$ are used to index diabatic electronic states. The lower case letters $\{i, j\}$ index occupied molecular orbitals, while $\{a, b\}$ index virtual molecular orbitals. Following the convention established in Ref. 67, nuclear degrees of freedom in the Cartesian basis are indexed by the letter Q, and gradients with respect to such degrees of freedom are denoted by a superscript Q enclosed in square brackets, such as $f^{[Q]}$. Nuclear degrees of freedom in the basis of normal modes are indexed by the letter η, and gradients are similarly represented as superscripts enclosed in brackets, e.g. $f^{[\eta]}$. Diabatic states are denoted $|\Xi\rangle$, adiabatic states are denoted $|\Phi\rangle$, and derivative couplings are denoted $d_{IJ}^{[Q]}$. All other terms are explained as they arise.

5.3. Theory

5.3.1. Localized diabatization

The localized diabatization method is an inexpensive, black-box method for generating a diabatic electronic basis as a linear combination of adiabatic states. Localized diabatic states are obtained by mixing a basis of M adiabatic states via an adiabatic-to-diabatic transformation matrix $\mathbf{U}$, such that

$$|\Xi_A\rangle = \sum_{I=1}^{M} U_{AI}|\Phi_I\rangle, \tag{5.2}$$

where $\mathbf{U}$ is chosen (1) to be unitary, ensuring orthonormal diabats, and (2) to maximize some diabatization function. Three such functions, GMH, Boys, and BoysOV, are defined in terms of state dipole operators, so their respective analytic gradient expressions have many similarities, which will be described below. Diabatic states in the GMH representation must have a dipole operator that is diagonalized in the direction of charge transfer.[55] Boys diabatization represents an extension of this method to multiple centers of charge, and in fact reduces to GMH for two-state systems.[57] In principle, Boys diabatic states can be thought of as adiabatic states perturbed by the approximate effects of a strongly localizing solvent bath, one which exerts a linear electrostatic potential on the electronic system being diabatized. Consequently, maximizing this interaction is equivalent to maximizing the localization function f_{Boys}, given by

$$f_{\text{Boys}}(\mathbf{U}) = f_{\text{Boys}}(\{\Xi_A\}) \tag{5.3}$$

$$= \sum_{A,B=1}^{M} |\langle\Xi_A|\boldsymbol{\mu}|\Xi_A\rangle - \langle\Xi_B|\boldsymbol{\mu}|\Xi_B\rangle|^2, \tag{5.4}$$

where $\boldsymbol{\mu}$ is the electronic dipole operator. Boys diabatic states are useful for localizing ET states, but are subject to certain limitations. In particular, the Boys method is unable to localize the electronic states of an EET system, in which electronic excitation, not

charge, becomes localized. An alternative method, called BoysOV localization,[63] uses a diabatization function given by

$$f_{\text{BoysOV}}(\mathbf{U}) = \sum_{A,B=1}^{M} |\langle \Xi_A | \boldsymbol{\mu}^{\text{occ}} | \Xi_A \rangle - \langle \Xi_B | \boldsymbol{\mu}^{\text{occ}} | \Xi_B \rangle|^2 \tag{5.5}$$

$$+ \sum_{A,B=1}^{M} |\langle \Xi_A | \boldsymbol{\mu}^{\text{virt}} | \Xi_A \rangle - \langle \Xi_B | \boldsymbol{\mu}^{\text{virt}} | \Xi_B \rangle|^2, \tag{5.6}$$

where the dipole operators $\boldsymbol{\mu}^{\text{occ}}$ and $\boldsymbol{\mu}^{\text{virt}}$ only interact with occupied and virtual orbital densities, respectively. For CIS states, this means

$$\langle \Xi_A | \boldsymbol{\mu}^{\text{occ}} | \Xi_B \rangle = \boldsymbol{\mu}^{\text{occ}}_{AB} = -\sum_{i,j,a} t_i^{A,a} t_j^{B,a} \boldsymbol{\mu}_{ij} \tag{5.7}$$

and

$$\langle \Xi_A | \boldsymbol{\mu}^{\text{virt}} | \Xi_B \rangle = \boldsymbol{\mu}^{\text{virt}}_{AB} = \sum_{i,a,b} t_i^{A,a} t_i^{B,b} \boldsymbol{\mu}_{ab}, \tag{5.8}$$

where we have introduced CIS amplitudes $\{t\}$. By separately localizing these two types of electron densities, BoysOV allows for the localization of excitations for a given set of states, even if charge cannot be localized for the same subspace. Formally, BoysOV can be easily applied to CIS or time-dependent density functional theory under the Tamm-Dancoff approximation (TD-DFT/TDA), but further generalizations are possible (see Appendix A.2).

5.3.2. Derivative couplings between localized diabatic states

The formal expression for derivative couplings between localized diabatic states can be written simply as

$$d^{[Q]}_{AB} = \sum_{IJ} U_{AI} d^{[Q]}_{IJ} U_{BJ} + \sum_{I} U_{AI} U^{[Q]}_{BI}. \tag{5.9}$$

Expressions for the derivative couplings[144–152] and gradients[153–157] of CI adiabatic states are available, and we have described methods for obtaining analytic derivative couplings between adiabatic states within the CIS formalism.[67] To calculate any gradient quantity

within a diabatic representation also requires the transformation matrix gradient, $\mathbf{U}^{[Q]}$. The process for calculating $\mathbf{U}^{[Q]}$ for Boys diabatic states is described in detail in Ref. 10. Here, we will broadly describe the process for the three localized diabatization schemes that make use of dipole operators: GMH, Boys, and BoysOV localization. In each case, there are two groups of constraints on the diabatic states which can be used to construct a supermatrix equation,

$$\sum_{CK} \begin{bmatrix} \mathcal{A}_{ABCK} \\ \mathcal{B}_{ABCK} \end{bmatrix} U^{[Q]}_{CK} = - \begin{bmatrix} \mathbf{0} \\ \mathcal{C}^{[Q]}_{AB} \end{bmatrix}, \tag{5.10}$$

which can subsequently be solved to obtain $\mathbf{U}^{[Q]}$. The first set of constraints,

$$\sum_{CK} \mathcal{A}_{ABCK} U^{[Q]}_{CK} = \mathbf{0}, \tag{5.11}$$

arises from the condition that diabatic states must be orthonormal,

$$\sum_{I} U_{AI} U_{BI} = \delta_{AB}. \tag{5.12}$$

If we take the gradient of Eq. 5.12 with respect to nuclear degrees of freedom Q, we obtain

$$\sum_{I} U^{[Q]}_{AI} U_{BI} + \sum_{I} U_{AI} U^{[Q]}_{BI} = 0, \tag{5.13}$$

which holds for all state pairs $A \geq B$. This result can be rearranged in the form of Eq. 5.11, where $\mathcal{A}_{ABCK} = \delta_{AC} U_{BK} + \delta_{BC} U_{AK}$.

While the unitarity condition is true for all localized diabatization schemes, in order to fully define the M^2 elements of $\mathbf{U}^{[Q]}$ we must turn to the second set of constraints,

$$\sum_{CK} \mathcal{B}_{ABCK} U^{[Q]}_{CK} = -\mathcal{C}^{[Q]}_{AB}, \tag{5.14}$$

which involve conditions specific to each scheme. By definition,[55] GMH states must be

constructed such that for $M = 2$,

$$\boldsymbol{\mu}_{AB} \cdot (\boldsymbol{\mu}_{11} - \boldsymbol{\mu}_{22}) = 0 \tag{5.15}$$

where $\boldsymbol{\mu}_{11}$ and $\boldsymbol{\mu}_{22}$ are diagonal elements of the dipole operator in the adiabatic basis, localized on the two different charge centers associated with the ET reaction. Taking the gradient of Eq. 5.15 with respect to nuclear degrees of freedom Q again allows us to express $\mathbf{U}^{[Q]}$ in the context of a supermatrix equation (Eq. 5.14), for which

$$\begin{aligned} \mathcal{B}^{\mathrm{GMH}}_{ABCK} =& \delta_{AC}\boldsymbol{\mu}_{BK} \cdot (\boldsymbol{\mu}_{11} - \boldsymbol{\mu}_{22}) && (5.16)\\ &+\delta_{BC}\boldsymbol{\mu}_{AK} \cdot (\boldsymbol{\mu}_{11} - \boldsymbol{\mu}_{22}) && (5.17) \end{aligned}$$

and

$$\mathcal{C}^{\mathrm{GMH}[Q]}_{AB} = \sum_{IJ} \left[\boldsymbol{\mu}^{[Q]}_{IJ} \cdot (\boldsymbol{\mu}_{11} - \boldsymbol{\mu}_{22}) + \boldsymbol{\mu}_{IJ} \cdot \left(\boldsymbol{\mu}^{[Q]}_{11} - \boldsymbol{\mu}^{[Q]}_{22} \right) \right] U_{AI} U_{BJ}. \tag{5.18}$$

A similar approach is used to define the constraints on $\mathbf{U}^{[Q]}$ for the Boys representation. It can be shown[57] that the condition

$$\boldsymbol{\mu}_{AB} \cdot (\boldsymbol{\mu}_{AA} - \boldsymbol{\mu}_{BB}) = 0 \tag{5.19}$$

must be obeyed for all state pairs such that $A > B$. The gradient of this expression can then be taken and the result can be written in the form of Eq. 5.14 with

$$\begin{aligned} \mathcal{B}^{\mathrm{Boys}}_{ABCK} =& \delta_{AC} \left[2\boldsymbol{\mu}_{AB} \cdot \boldsymbol{\mu}_{KA} + (\boldsymbol{\mu}_{AA} - \boldsymbol{\mu}_{BB}) \cdot \boldsymbol{\mu}_{KB} \right] && (5.20)\\ &-\delta_{BC} \left[2\boldsymbol{\mu}_{AB} \cdot \boldsymbol{\mu}_{KB} - (\boldsymbol{\mu}_{AA} - \boldsymbol{\mu}_{BB}) \cdot \boldsymbol{\mu}_{KA} \right] && (5.21) \end{aligned}$$

and

$$\mathcal{C}^{\mathrm{Boys}[Q]}_{AB} = \sum_{IJKL} \left[\boldsymbol{\mu}^{[Q]}_{IJ} \cdot \boldsymbol{\mu}_{KL} + \boldsymbol{\mu}_{IJ} \cdot \boldsymbol{\mu}^{[Q]}_{KL} \right] U_{AI} U_{BJ} \left(U_{BK} U_{BL} - U_{AK} U_{AL} \right). \tag{5.22}$$

We can easily extend the form of this supermatrix expression to BoysOV localization if we instead require that the condition

$$\boldsymbol{\mu}_{AB}^{\mathrm{occ}} \cdot (\boldsymbol{\mu}_{AA}^{\mathrm{occ}} - \boldsymbol{\mu}_{BB}^{\mathrm{occ}}) + \boldsymbol{\mu}_{AB}^{\mathrm{virt}} \cdot \left(\boldsymbol{\mu}_{AA}^{\mathrm{virt}} - \boldsymbol{\mu}_{BB}^{\mathrm{virt}}\right) = 0 \tag{5.23}$$

must be satisfied. This 'BoysOV condition' is simply the Boys condition divided into separate parts for the occupied and virtual contributions to the dipole operator. The resulting supermatrices, represented as functions of the dipole operators, can be written

$$\mathcal{B}^{\mathrm{BoysOV}} = \mathcal{B}^{\mathrm{Boys}}\left(\boldsymbol{\mu}^{\mathrm{occ}}\right) + \mathcal{B}^{\mathrm{Boys}}\left(\boldsymbol{\mu}^{\mathrm{virt}}\right), \tag{5.24}$$

and

$$\mathcal{C}^{\mathrm{BoysOV}[Q]} = \mathcal{C}^{\mathrm{Boys}[Q]}\left(\boldsymbol{\mu}^{\mathrm{occ}}\right) + \mathcal{C}^{\mathrm{Boys}[Q]}\left(\boldsymbol{\mu}^{\mathrm{virt}}\right). \tag{5.25}$$

The supermatrices necessary for obtaining $\mathbf{U}^{[Q]}$ exist in a small-dimensional state space, so inverting Eq. 5.10 is computationally trivial. The costly part of obtaining diabatic gradient quantities is filling in the constraint matrix $\mathcal{C}^{[Q]}$ with adiabatic dipole gradients $\boldsymbol{\mu}^{[Q]}$. Note that although the cost of calculating $\mathcal{C}^{[Q]}$ for GMH is equivalent to the same procedure for Boys diabatic states, the cost for BoysOV is twice as great, as each quantity must be calculated once for virtual densities and once for occupied densities. Consequently, for a two-state calculation, the cost of this procedure for BoysOV states should be approximately twenty times the cost of a CIS gradient.[10]

5.3.3. Diabatic Hamiltonian gradient and the strictly diabatic approximation

In addition to producing diabatic-basis derivative couplings, the transformation matrix gradient $\mathbf{U}^{[Q]}$ can be used to produce any diabatic gradient quantity. Among these quantities, the diabatic Hamiltonian gradient $H^{[Q]}$ is of primary interest. As with the expression for

the derivative coupling (Eq. 5.9), the expression for the Hamiltonian gradient is simple,

$$H_{AB}^{[Q]} = \sum_{IJ} \left(U_{AI} H_{IJ}^{[Q]} U_{BJ} + U_{AI}^{[Q]} H_{IJ} U_{BJ} + U_{AI} H_{IJ} U_{BJ}^{[Q]} \right). \tag{5.26}$$

From Eq. 5.26, one can calculate both energy gradients (diagonal elements) and diabatic coupling derivatives (off-diagonal elements). The gradients of any other observable can be represented by the same expression, by simply replacing the Hamiltonian with the Hermitian operator of interest.

As for derivative couplings, the most costly step in evaluating Eq. 5.26 is the calculation of $\mathbf{U}^{[Q]}$. Reducing the cost of building the transformation matrix gradient would make building the energy gradients much less expensive, and therefore practical for larger molecules. One shortcut, which we dub the 'strictly diabatic' approximation, takes advantage of one of the principal desired property of diabatic states: negligible derivative couplings. Formally assuming the strictly diabatic condition (Eq. 5.1) allows us to solve Eq. 5.9 for $\mathbf{U}^{[Q]}$,

$$U_{AI}^{[Q]} = \sum_{J} U_{AJ} d_{JI}^{[Q]}. \tag{5.27}$$

If it can be demonstrated that localized diabatic states have small enough derivative couplings to make this a viable approximation, diabatic gradient quantities could be obtained for the cost of adiabatic derivative couplings, which would reduce calculation time by an order of magnitude. Furthermore, because it does not require any information about the diabatic basis beyond the transformation matrix, it can be trivially applied to any localized diabatization method.

5.4. Results

All results were calculated using a development version of the Q-CHEM software package.[102,158] Excited states were generated using the restricted Hartree-Fock configuration interaction singles (RHF-CIS) formalism with a 6-31G** basis set. The systems under

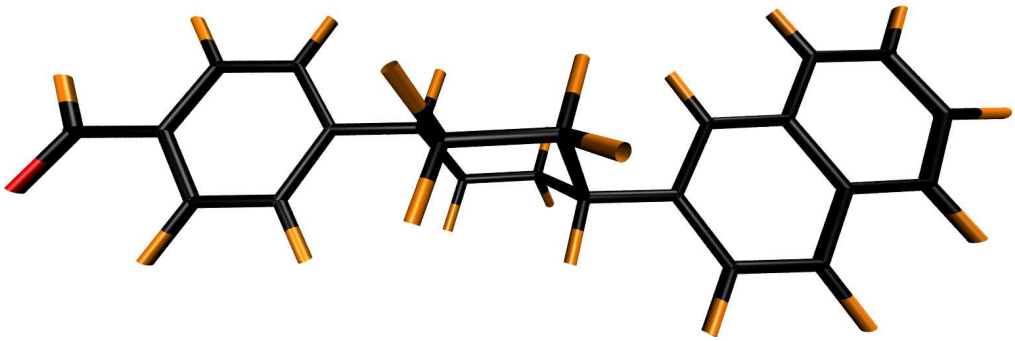

Figure 5.17: The DBA molecule C-1,4ee has two minima on the T_1 surface associated with a triplet-triplet EET system. In the higher-energy local minimum configuration, the excitation is localized on the benzaldehydeyl donor (the AD* state). In the global minimum configuration for this surface, the excitation is localized on the 2-naphthyl acceptor (the A*D state). Here C-1,4ee is shown in the geometry optimized for the A*D configuration of the T_1 excited state.

consideration are similar to those used in Ref. 11: each is a donor-bridge-acceptor (DBA) molecule in which a 4-benzaldehydeyl donor and a 2-naphthyl acceptor are joined to a variable bridge. Note that in the actual experiments, the donor is a benzophenoneyl group instead of a benzaldehydeyl group. We designate these molecules using the same naming scheme employed in Ref. 11; for example, C-1,3ea signifies a cyclohexane bridge to which the donor group is attached at carbon 1 equatorially, and to which the acceptor group is attached to carbon 3 axially. One such molecule, C-1,4ee, is pictured in Fig. 5.17. The electronic subspace is restricted to the T_1 and T_2 excited states for each molecule. The space of configurations considered is a reaction coordinate ζ defined as a linear interpolation between the 'before' and 'after' configurations of a triplet-triplet EET reaction, i.e. the A*D ($\zeta = 0$) and AD* ($\zeta = 1$) energy-minimized geometries of the T_1 state. Diabatic states are constructed in the BoysOV representation. Normal modes are indexed by frequency, where mode 1 is the lowest-frequency mode.

5.4.1. Derivative coupling in the BoysOV representation

While the derivative coupling is of course a 3N-vector, for the purposes of analyzing the validity of Eq. 5.1 for localized diabatic states, it is sufficient to discuss the derivative

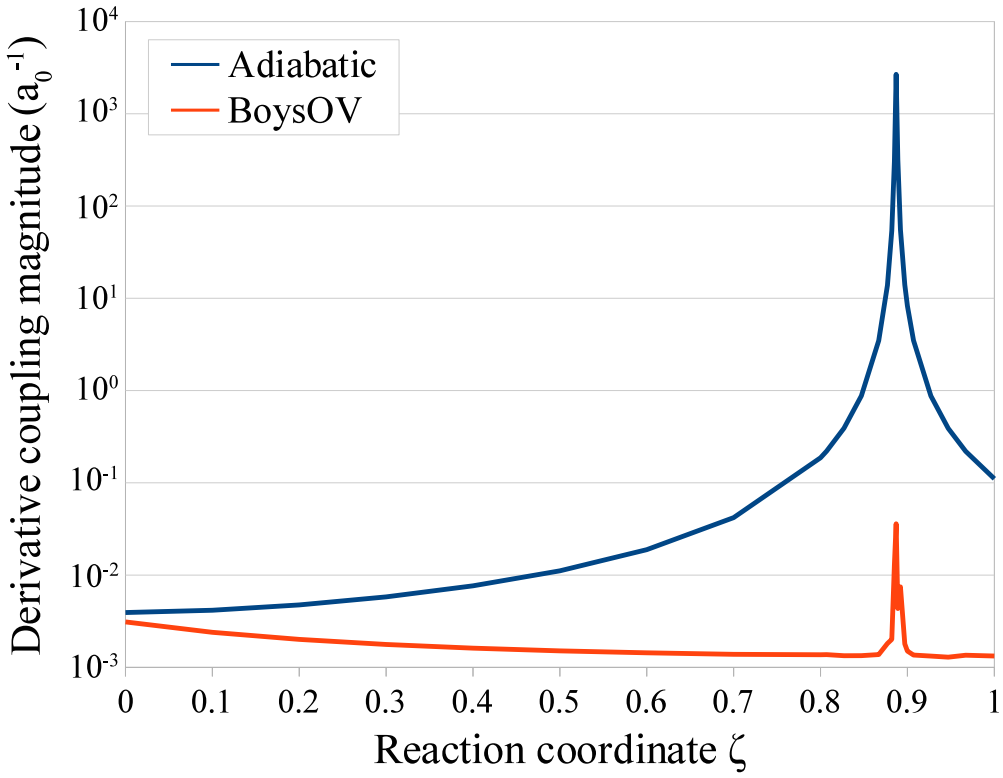

Figure 5.18: Magnitudes of the DC vector along the linearly-interpolated reaction pathway between A*D ($\zeta = 0$) and AD* ($\zeta = 1$) T_1 states of the C-1,4ee molecule. DC magnitudes are presented in both the adiabatic and diabatic (BoysOV) bases. While the DC magnitude is smaller in the BoysOV basis for every point sampled, the degree of reduction is greatest near the avoided crossing, where it peaks at 2.7×10^3 a_0^{-1} in the adiabatic basis, and 3.6×10^{-2} a_0^{-1} in the diabatic basis. There is little difference between the adiabatic and diabatic representations far from the avoided crossing at $\zeta = 0$, where DC magnitudes are negligible in either representation.

coupling magnitudes alone. Because the systems under consideration are involved in energy transfer and not charge transfer, the only localized diabatization method considered here is BoysOV. DC magnitudes in the adiabatic and BoysOV representations for C-1,4ee are shown in Fig. 5.18. This system is typical of the molecules considered in this study: the adiabatic DC magnitudes tend to be negligible near the endpoints of the reaction coordinate, but peak sharply near the avoided crossing. For a model with a harmonic approximation and the Condon approximation, the form of these derivative couplings is computed exactly in Appendix A.1.

Table 5.1: Magnitudes of DCs between the triplet-triplet energy transfer states of three different Closs molecules in the adiabatic and diabatic (BoysOV) representations at the configuration nearest to the avoided crossing along the linearly-defined reaction coordinate ζ. These configurations represent the maximum DC magnitudes among the configurations sampled for each system, suggesting that the diabatic DCs are negligible over all relevant portions of configuration space for these systems.

	DC magnitude at avoided crossing point (a_0^{-1})		
Representation	C-1,3ea	C-1,3ee	C-1,4ee
Adiabatic	2500	970	2700
Diabatic	0.066	0.0078	0.036
A/D ratio	3.8×10^4	1.2×10^5	7.4×10^4

By contrast, in the case of diabatic states, the DC magnitude is universally smaller in the BoysOV representation than it is in the adiabatic representation, particularly near the avoided crossing, where it is smaller by a factor of nearly 10^5. Just like the corresponding adiabatic quantity, the BoysOV DC magnitude peaks near the avoided crossing. However, it is not clear whether this peak is an accurate reflection of the BoysOV wavefunction behavior in this region: the coupled-perturbed CIS (CPCIS) equations necessary for calculating BoysOV derivative couplings are particularly unstable here, requiring relaxed convergence criteria. Furthermore, the final expression for the diabatic DC near an avoided crossing involves two very large terms of opposite sign, the conjugated adiabatic DC and the rotation matrix gradient (*cf.* Eq. 5.9). As a result, numerical noise may become significant when the adiabatic DC magnitude becomes large. However, it should be noted that the expression for the adiabatic derivative couplings is not affected by the same instabilities, so these can be generated at full precision near the avoided crossing. Even with the higher error associated with calculating the diabatic DC, their magnitude is still universally small, peaking at a value of 0.036 a_0^{-1}.

For a more general comparison, we have collected the magnitudes of the derivative couplings for several Closs systems near the avoided crossing point along the chosen reaction coordinate. This information is presented in Table 5.1. As in the case of C-1,4ee, the avoided crossing point is where the DC magnitude peaks in each representation. In the

diabatic representation, DC magnitude is reduced from the corresponding adiabatic value by at least four orders of magnitude in each case, and is never greater than 0.1 a_0^{-1}. As mentioned for the C-1,4ee system, it seems likely that the true DC magnitudes for BoysOV states are even smaller than the values presented here, as instabilities in the orbital response calculations and finite precision error have likely inflated the size of this quantity near the avoided crossings.

5.4.2. Evaluating fluctuations in the diabatic coupling

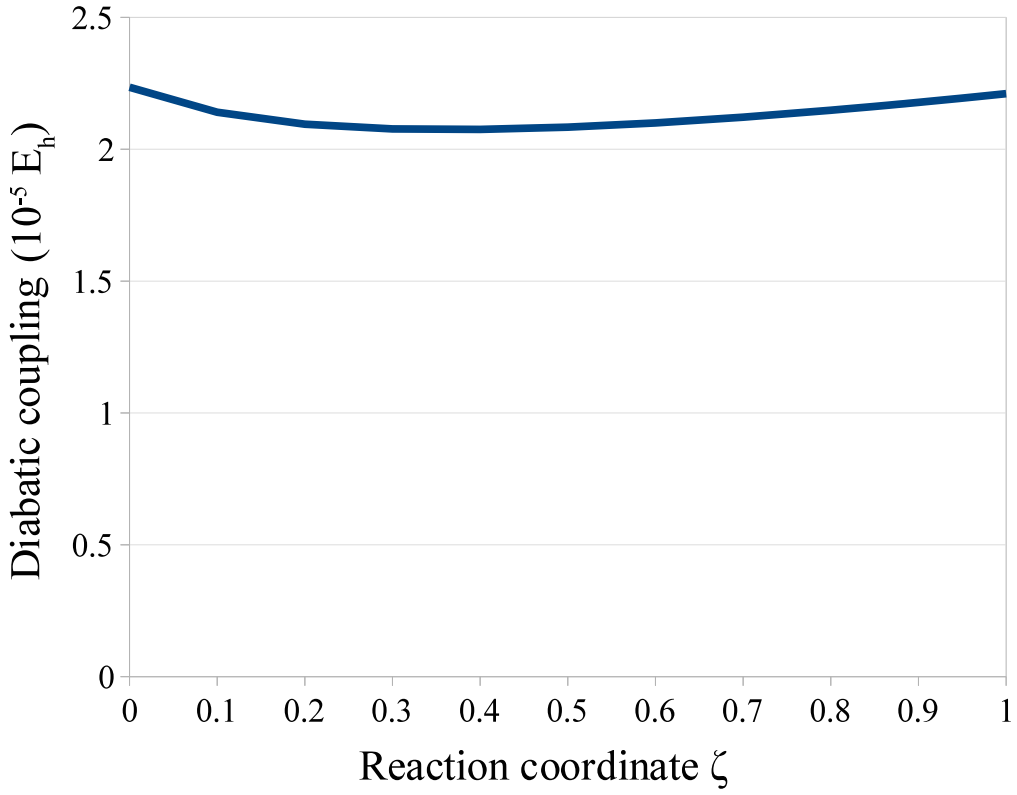

Figure 5.19: Diabatic coupling along the linearly-interpolated reaction pathway between A*D ($\zeta = 0$) and AD* ($\zeta = 1$) T_1 states of the C-1,4ee molecule in the BoysOV representation. Among the points sampled, the maximum value (22.4 μE_h) and minimum value (20.8 μE_h) differ only by about 7% over the extent of the points sampled here; changing $\zeta = 0$ to $\zeta = 1$ constitutes a change of 0.88 a_0.

While the derivative couplings in the adiabatic representation appear to be tightly localized in space for these systems, the same is not necessarily true for the diabatic coupling in

the BoysOV representation. On the contrary, in the BoysOV representation, the diabatic coupling varies little along the reaction coordinate sampled in our study (Fig. 5.19); the difference between its maximum and minimum values is only 7%. At first glance, Fig. 5.19 would seem to conform to the Condon approximation for this molecular system, and thus to the assumptions of Marcus theory (as explained in Refs. 114 and 113). Nevertheless, Fig. 5.19 is only a one-dimensional representation of the diabatic coupling. To understand multidimensional effects, in Fig. 5.20 we plot the norm of the diabatic coupling gradient ($|H_{AB}^{[Q]}|$, for $A \neq B$) as a function of the reaction coordinate. Although $|H_{AB}^{[Q]}|$ overlaps little with the reaction coordinate, should the molecule be displaced into some orthogonal mode, the diabatic coupling will not necessarily remain stable. Thus, it is worthwhile to explore whether this molecule is rigid enough at room temperature to avoid such conformational fluctuations as might change its diabatic coupling significantly.

To determine how much the diabatic coupling of this molecule might deviate due to conformational fluctuations, we must first estimate the probable conformational changes accessible to it at room temperature, and then combine this information with the diabatic coupling gradient. We can accomplish this goal in three steps: (1) for each minimum-energy geometry on the T_1 surface, we approximate the shape of the potential well as that of the minimum-energy ground state configuration. We can then use a Hessian calculation at the S_0 minimum-energy configuration to describe the normal modes and corresponding vibrational frequencies (ν_η) of the system. (2) Approximate the magnitude of configurational fluctuations (ΔL_η) with respect to this degree of freedom by taking the square root of the thermal average of the squared displacement operators along these modes,

$$\Delta L_\eta = \sqrt{\sum_m P_m \Delta X_{\eta,m}^2} = \sqrt{\sum_m P_m \langle \phi_m | \hat{X}_\eta^2 | \phi_m \rangle}, \tag{5.28}$$

where ϕ_m is the m^{th} harmonic oscillator stationary state, and P_m is the corresponding Boltzmann-weighted probability at T = 298 K. (3) We estimate the change in diabatic coupling with respect to this degree of freedom ($\Delta H_{AB,\eta}$) as the product of the component

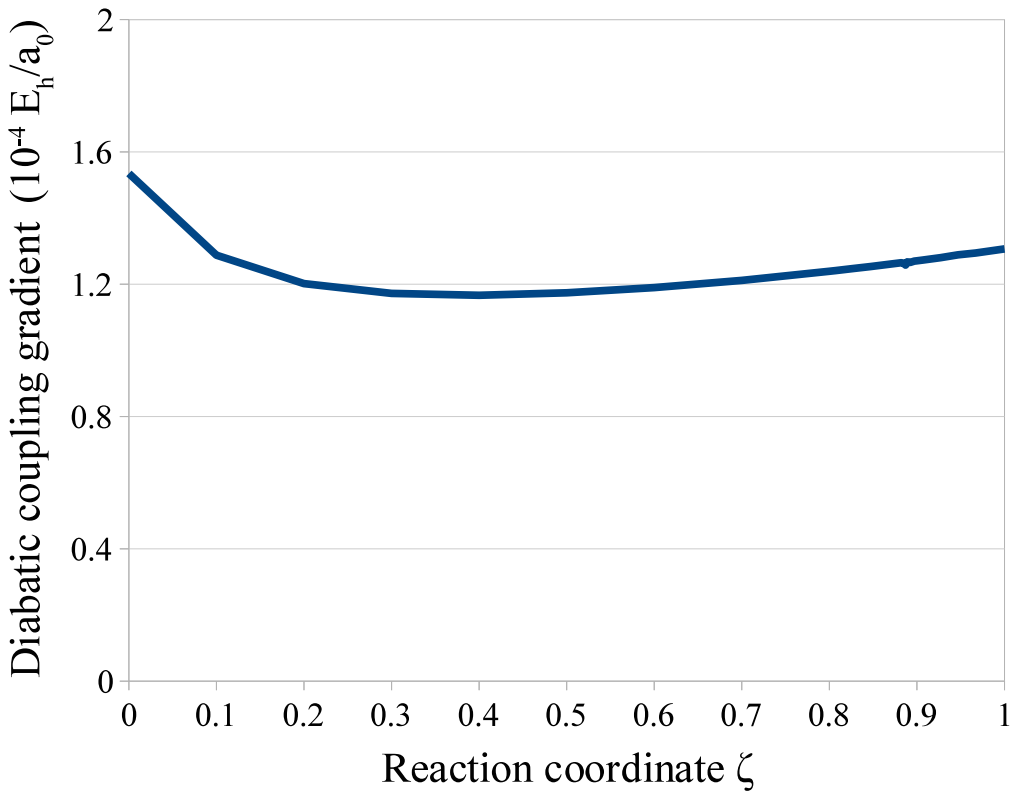

Figure 5.20: Magnitude of the diabatic coupling gradient ($|H_{AB}^{[Q]}|$) along the linearly-interpolated reaction pathway between A*D ($\zeta = 0$) and AD* ($\zeta = 1$) T_1 states of the C-1,4ee molecule in the BoysOV representation. The magnitude of the gradient alone suggests that the diabatic couplings change by as much as 140 μE_h over the reaction pathway defined here (total length 0.88 a_0); however, as the graph of the diabatic coupling makes clear (Fig. 5.19), the diabatic coupling gradient overlaps little with the degree of freedom defined by the reaction coordinate.

of the gradient along this degree of freedom with the magnitude of the fluctuation along this degree of freedom, $\Delta H_{AB,\eta} = \Delta L_\eta H_{AB}^{[\eta]}$.

Using this procedure, we can calculate $\Delta H_{AB,\eta}$ across all degrees of freedom by examining the projection of the gradient vectors onto each normal mode of the ground state. For the $\zeta = 0$ configuration, we find that there are 5 modes along which the diabatic coupling could change by more than 20% of its reference value. The most significant of these is mode 59; our analysis suggests that the diabatic coupling could change by 33% if the molecule were to move along this degree of freedom at room temperature. For the $\zeta = 1$ configuration,

Table 5.2: Analysis of change in diabatic coupling of C-1,4ee due to thermally-induced conformational fluctuations at T = 298 K along the normal modes which contribute most significantly to ΔH_{AB}. The curvature around each potential energy well on the T_1 surface is taken to be the same as that of the S_0 minimum, and is obtained from a ground-state Hessian calculation. Using this information, we are able to estimate how much this molecule can be expected to deviate (ΔL_η) from its stable configurations ($\zeta = 0$ and $\zeta = 1$) at room temperature. Multiplying this value by the projection of the diabatic coupling gradient ($|H_{AB}^{[\eta]}|$) tells us how much we can then expect the diabatic coupling to change ($\Delta H_{AB,\eta}$) both in absolute terms and as a fraction of its value at the respective reference configuration (H_{AB}).

Geometry	H_{AB} (μE_h)	Mode	$\lvert H_{AB}^{[\eta]}\rvert$ ($\mu E_h/a_0$)	ΔL_η (a_0)	$\Delta H_{AB,\eta}$ (μE_h)	$\Delta H_{AB,\eta}$ (%)
$\zeta = 0$	22.4	59	45.7	0.162	7.39	33.1
		57	34.8	0.157	5.48	24.5
		77	34.4	0.145	4.99	22.3
		106	67.8	0.072	4.91	22.0
		65	30.5	0.149	4.55	20.4
$\zeta = 1$	22.1	59	42.6	0.162	6.89	31.1
		57	42.4	0.157	6.67	30.2
		109	72.3	0.074	5.35	24.2
		73	22.1	0.177	3.91	17.7
		82	21.5	0.181	3.88	17.5

there are only 3 modes which the diabatic coupling could change by more than 20%; mode 59 is also the most significant in this case, along which the diabatic coupling can change by 31%. For a visual representation of the normal modes which correspond to the greatest change in the diabatic coupling, see Fig. 5.21.

Under the approximation described in this section, one can calculate the total change in diabatic coupling ($\Delta H_{AB}^{\text{total}}$) as the 2-norm of its component parts,

$$\Delta H_{AB}^{\text{total}} = \sqrt{\sum_\eta (\Delta H_{AB,\eta})^2}. \tag{5.29}$$

For the $\zeta = 0$ configuration, $\Delta H_{AB}^{\text{total}} = 19$ μE_h, or a 87% change from the reference value. For the $\zeta = 1$ configuration, $\Delta H_{AB}^{\text{total}} = 17$ μE_h, a 78% change. Because of these fluctuations in the electronic coupling alone, we can expect our calculated Marcus rates to be off by up to a factor of 3 or 4 from the experimental rates. In our view, however, such small effects do

not represent a significant breakdown of the Condon approximation; indeed, as a practical matter, the original calculations in Ref. 63 were also off by a factor of 2 to 3 from the experimental results. In the end, while there may be some fluctuations of the diabatic coupling, the molecule is rigid enough at room temperature that non-Condon effects will be relatively small.

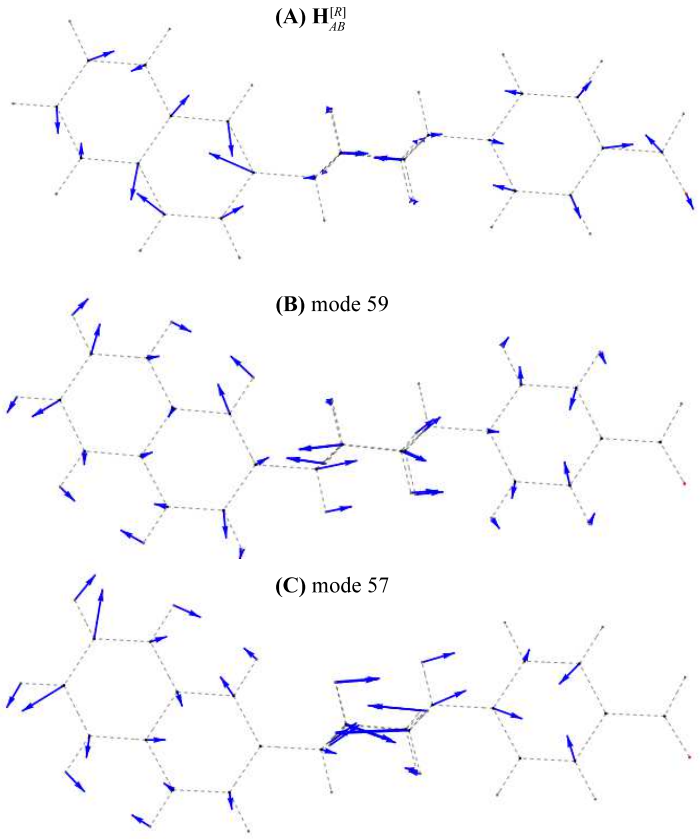

Figure 5.21: Quiver plot of C-1,4ee depicting the **(A)** diabatic coupling gradient ($H_{AB}^{[Q]}$) at $\zeta = 0$, **(B)** normal mode 59 from the S_0 minimum-energy configuration, and **(C)** normal mode 57 from the S_0 minimum-energy configuration. Those modes are each moderately rigid, with characteristic lengths $\Delta L_{59} = 0.162$ a_0 and $\Delta L_{57} = 0.157$ a_0. At the $\zeta = 0$ geometry, the projection of the diabatic coupling gradient ($H_{AB}^{[\eta]}$) onto mode 59 is $H_{AB}^{[59]} = 45.7$ $\mu E_h/a_0$, and $H_{AB}^{[57]} = 34.8$ $\mu E_h/a_0$ for mode 57. At the $\zeta = 1$ geometry, $H_{AB}^{[59]} = 42.6$ $\mu E_h/a_0$, and $H_{AB}^{[57]} = 42.4$ $\mu E_h/a_0$. See Table 5.2 for a thorough description of how these quantities are determined.

5.5. Discussion: the strictly diabatic approximation

To test the viability of the strictly diabatic approximation described in section 5.3.3, we have used it to calculate the Hamiltonian gradient in the BoysOV basis for C-1,4ee. To more clearly assess this approximation of a vector quantity, error analysis has been split into two components: magnitude and direction. Magnitudinal error is calculated as the conventional error for scalar quantities,

$$\varepsilon_{\text{mag}} = \frac{|H^{[Q]}_{AB,\text{approx.}}| - |H^{[Q]}_{AB,\text{analytic}}|}{|H^{[Q]}_{AB,\text{analytic}}|}. \tag{5.30}$$

Directional error is obtained by normalizing both the approximate and analytic vector quantities, then subtracting their inner product from unity,

$$\varepsilon_{\text{dir}} = 1 - \left(\frac{H^{[Q]}_{AB,\text{approx.}}}{|H^{[Q]}_{AB,\text{approx.}}|} \right) \cdot \left(\frac{H^{[Q]}_{AB,\text{analytic}}}{|H^{[Q]}_{AB,\text{analytic}}|} \right). \tag{5.31}$$

First, we discuss diabatic coupling gradients ($H^{[Q]}_{AB}$, $A \neq B$). A comparison between these results and those found for direct analytic evaluation of the diabatic coupling gradient can be found in Fig. 5.22.

Under the strictly diabatic approximation, the diabatic coupling gradient is accurately approximated near the avoided crossing at $\zeta = 0.89$. For the region $0.8 < \zeta < 1.0$, the magnitudinal error in the diabatic coupling vector diverges linearly away from the avoided crossing, ultimately rising to 4%. In this same region, the directional error is generally much smaller; with the exception of a spike to 2% at the geometry nearest to the avoided crossing, the directional error is not greater than 0.2%. Further away from the avoided crossing, the approximation fares much worse: for $\zeta < 0.5$, the magnitudinal error is greater than 10%, and the directional error rises to nearly 50% for $\zeta = 0$. Of course, the relatively large error at the $\zeta = 0$ configuration compared to the $\zeta = 1$ configuration reflects only the relative distance from the avoided crossing. These data strongly suggest, as one might

expect, that the strictly diabatic approximation should be used only at configurations where the derivative coupling in the localized diabatic basis is significantly smaller than in the adiabatic basis, i.e., near avoided crossings (see Fig. 5.18).

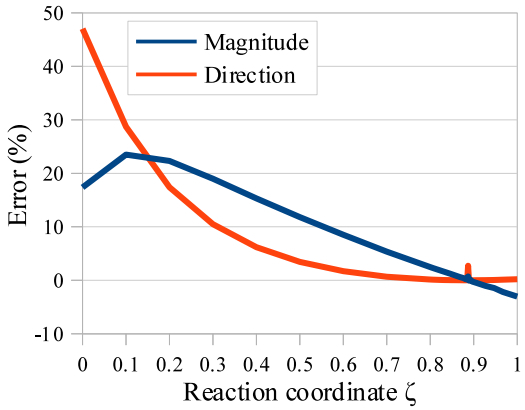

Figure 5.22: Error in the magnitude and direction of the diabatic coupling gradient ($H_{AB}^{[Q]}$) under the strictly diabatic approximation along the linearly-interpolated reaction pathway between A*D ($\zeta = 0$) and AD* ($\zeta = 1$) T_1 states of the C-1,4ee molecule. Magnitudinal error is calculated as the conventional relative change for scalar quantities (Eq. 5.30). Directional error is obtained by normalizing both the approximate and analytic vector quantities, then subtracting their inner product from unity (Eq. 5.31). While both magnitudinal and directional errors are very low near the avoided crossing (at $\zeta = 0.89$), they begin to diverge significantly for $\zeta < 0.6$. While the error in the magnitude has a maximum of around 25%, the directional error is nearly 50% and rising as $\zeta \to 0$. This strongly suggests that for diabatic couplings, this approximation is only reliable where diabatization can achieve significant reductions in DC magnitudes, i.e. near avoided crossings.

Second, we study diabatic energy gradients ($H_{AA}^{[Q]}$). In contrast to the results for the diabatic coupling gradients, the approximate diabatic state energy gradients are essentially identical to the analytic result for every point sampled. For much of configuration space, this be attributed to the fact that the dominant contribution to the diabatic energy gradient comes from the first term on the right hand side of Eq. 5.26, which does not depend on $\mathbf{U}^{[Q]}$, and is therefore unchanged by the approximation. Near the avoided crossing, however, $\mathbf{U}$ changes rapidly, and the remaining terms in this expression can no longer be neglected. In this region, however, the derivative couplings in the diabatic representation are smallest, so the strictly diabatic approximation is the most well-founded. Thus, in two complementary limits, it seems that the strictly diabatic approximation for energy gradients can be expected

to be accurate. As it turns out, the error in the approximate magnitude of the gradient is never much greater than $10^{-4}\%$, and directional error never rises above $10^{-9}\%$. For energy gradients, at least, the strictly diabatic approximation appears to be extremely robust.

5.6. Conclusions and future work

The recent advent and implementation of analytic gradient methods for localized diabatic states has been tremendously helpful in both evaluating the reliability of these quasi-diabatic representations, and increasing the functionality of these transformations. In this work, we used methods introduced in Ref. 10 to evaluate the properties of diabatic states of triplet-triplet energy transfer systems, finding that the derivative couplings were negligible and that diabatic couplings were largely stable. Furthermore, we extended these methods to encompass BoysOV and GMH states. Finally, we used the knowledge that derivative couplings in the diabatic basis are reliably small to propose an approximation that allows diabatic gradient quantities to be calculated at greatly reduced cost. We were able to show that this 'strictly diabatic' approximation was successful at accurately calculating diabatic coupling gradients near avoided crossings, and diabatic energy gradients everywhere. We fully expect that these results are transferable to the gradients of other observables.

Looking forward, we anticipate that the strictly diabatic approximation may make several new applications of these diabatic gradient methods more attractive. One such application is diabatic state energy minimization: because local minima on an adiabatic potential energy surface may correspond to global minima on a diabatic potential energy surface, performing a geometry optimization on diabatic surfaces may offer a more reliable way to find such configurations. We plan to implement and make available this technique in the coming months.

5.7. Acknowledgments

This work was supported by NSF CAREER Grant CHE-1150851. J.E.S. acknowledges an Alfred P. Sloan Research Fellowship and a David & Lucile Packard Fellowship.

CHAPTER 6 : Calculating Derivative Couplings between TDHF Excited States with Pseudo-Wavefunctions

This chapter was adapted from Ref. 159.

6.1. Introduction

Derivative couplings, or DCs, describe the coupling between electronic states induced by nuclear motion,

$$d_{IJ}^{[Q]} = \langle \Psi_I | \nabla_Q | \Psi_J \rangle, \tag{6.1}$$

where Q indexes a nuclear degree of freedom. Given an orthonormal basis of electronic states $\{|\Psi_I\rangle\}$, we expect this quantity to be largest when a small change in the nuclear configuration results in a large change in the electronic states. In many cases, adiabatic electronic states change little as the molecular nuclear arrangement is perturbed, and therefore $d_{IJ}^{[Q]}$ can be safely ignored. Neglect of such terms forms the basis of the Born-Oppenheimer or adiabatic approximation, which posits the separability of the nuclear and electronic parts of the molecular wavefunction. However, there are numerous examples for which the adiabatic approximation breaks down; even for diatomic systems, there are nuclear configurations for which the probability of a non-radiative transition is high.[160,161] Such configurations become more pervasive for systems with more nuclear degrees of freedom.

A great deal of effort has been spent calculating DCs within the multi-reference configuration interaction (MRCI) formalism by Lengsfield, Saxe, Yarkony, Lischka, Shepard, and coworkers.[146,148,149,151] Going forward, many researchers are keen to explore excited state dynamics for even larger systems. As such, there is growing demand for analytic DCs by means of a less expensive formalism, such as configuration interaction singles (CIS),[67] and time-dependent Hartree-Fock (TDHF), or equivalently time-dependent density functional theory under the Tamm-Dancoff approximation (TDDFT-TDA),[162–164] and full time-dependent density functional theory.[165–175]

In this manuscript, our goal is to calculate a reasonable expression for derivative couplings between excited states within the TDHF formalism. Rather than use time-dependent response theory, we will construct DCs via a wavefunction-based Hellmann-Feynman expression with a projector-modified Hamiltonian. This approach is analogous to that described in Ref. 67 for CIS, and matches exactly the DCs as constructed by Li and Liu from a time-independent equation of motion.[176] It is worth mentioning that our final answer does not match the result from the Tavernelli group,[162] who proposed DCs based on Casida's assignment of TDHF states.[177] As in the work of Send and Furche,[175] our approach includes Pulay terms that account for a finite, atom-centered basis.[178] In addition, we note that while the expression in the current work contains terms that violate translational invariance, the use of electron translation factors (ETFs)[67,179] allow us to recover translationally invariant DCs without any additional computational cost. To justify our approach, we will show that near an excited state crossing we recover the Chernyak-Mukamel formula, in which the DC is described as a function of the transition density (as calculated by response theory).[165,166,180]

The structure of this manuscript is as follows: in section 6.16.1.1, we briefly introduce the TDHF formalism. After establishing notational conventions in section 6.2, we propose a Hellmann-Feynman approach for TDHF DCs in section 6.3. In section 6.4, we compare our results to those obtained from a finite difference approximation. In section 6.5, we show that our proposed expression for DCs match the exact Chernyak-Mukamel formalism and is thus completely consistent with time-dependent response theory near an excited state crossing. In Ref. 181, we extend the approach here to include TDDFT and show that the theory explored in this chapter produces DCs with the correct behavior around a conical intersection.

6.1.1. Time-dependent Hartree-Fock

While the first appearance of TDHF[28–32] (also known as the random phase approximation, or RPA) predates configuration interaction singles,[24] TDHF can be considered (loosely)

an extension to CIS. The CIS formalism is defined by a wavefunction

$$|\Phi_I^{\mathrm{CIS}}\rangle = \sum_{ia} t_i^{Ia} |\Phi_i^a\rangle \tag{6.2}$$

and the set of eigenvalue equations

$$\mathbf{A}\mathbf{t}^I = \sum_{jb} A_{aibj} t_j^{Ib} = E_I^{\mathrm{CIS}} \mathbf{t}^I. \tag{6.3}$$

Here, $\mathbf{t}^I$ is a set of amplitudes for state I, E_I is the corresponding excitation energy, and $\mathbf{A}$ is the single-excitation subspace of the Hamiltonian

$$A_{aibj} = \langle \Phi_i^a | \hat{H} | \Phi_j^b \rangle = \delta_{ab}\delta_{ij}(\varepsilon_a - \varepsilon_i) + \langle ib||aj\rangle. \tag{6.4}$$

In Eq. 6.4, ε_p is the Fock energy of orbital p, and $\langle pq||rs\rangle$ is the antisymmetrized two-electron integral in physicists' notation.

While TDHF does not correspond to a static wavefunction ansatz, the TDHF formalism is governed by an eigenvalue equation which is similar to Eq. 6.3,

$$\begin{pmatrix} \mathbf{A} & \mathbf{B} \\ -\mathbf{B} & -\mathbf{A} \end{pmatrix} \begin{pmatrix} \mathbf{X}^I \\ \mathbf{Y}^I \end{pmatrix} = E_I \begin{pmatrix} \mathbf{X}^I \\ \mathbf{Y}^I \end{pmatrix}. \tag{6.5}$$

Here, we assume real orbitals and amplitudes, and $\mathbf{B}$ is the subspace of the Hamiltonian associated with coupling between the Hartree-Fock ground state and doubly-excited states

$$B_{aibj} = \langle \Phi_{ij}^{ab} | \hat{H} | \Phi_{\mathrm{HF}} \rangle = \langle ab||ij\rangle. \tag{6.6}$$

$\mathbf{X}^I$ is a set of amplitudes indexed by X_i^{Ia} that are analogous to $\mathbf{t}^I$, and $\mathbf{Y}^I$ is a set of amplitudes that is associated with the energy contribution from $\mathbf{B}$ and captures electronic correlation in the ground state. TDHF amplitudes associated with different electronic states

have an orthonormality relationship given as

$$\left(\mathbf{X}^{I\dagger} - \mathbf{Y}^{I\dagger}\right) \begin{pmatrix} \mathbf{X}^{J} \\ \mathbf{Y}^{J} \end{pmatrix} = \mathbf{X}^{I\dagger}\mathbf{X}^{J} - \mathbf{Y}^{I\dagger}\mathbf{Y}^{J} = \delta_{IJ}. \tag{6.7}$$

Compared to CIS, TDHF produces slightly improved excited state energies. It also obeys the Thomas-Reiche-Kuhn sum rule for oscillator strengths, and as such usually produces more accurate transition moments.[32,33]

It is well-known that in order for TDHF to be accurate, the Y amplitudes must have small magnitude.[33,182] Consequently, our goal in this manuscript is to determine DCs up to $O(\mathbf{Y}^2)$. For these purposes, note that Eq. 6.7 can be rewritten

$$\mathbf{X}^{I\dagger}\mathbf{X}^{J} = \delta_{IJ} + O(\mathbf{Y}^2). \tag{6.8}$$

The relative magnitude of the X and Y amplitudes should reflect the fact that TDHF must offer only a small correction to CIS; if we let $\mathbf{B} \to \mathbf{0}$ in Eq. 6.5, then we recover the CIS energies and amplitudes.

6.2. Notation and preliminary considerations

The uppercase letters $\{I, J\}$ index adiabatic electronic states. The lowercase letters $\{i, j, \ldots\}$ index occupied molecular orbitals (MOs), while $\{a, b, \ldots\}$ index virtual MOs, $\{p, q, \ldots\}$ index general MOs, and Greek letters $\{\alpha, \beta, \mu, \nu, \lambda, \sigma\}$ index atomic orbitals (AOs). MO coefficients are denoted $C_{\mu p}$. Following the convention established in Ref. 67, nuclear degrees of freedom in the Cartesian basis are indexed by the letter Q, and gradients with respect to such degrees of freedom are denoted by a superscript Q enclosed in square brackets, such as $f^{[Q]}$. The Hartree-Fock ground state is denoted $|\Phi_{\text{HF}}\rangle$, and derivative couplings are denoted $d_{IJ}^{[Q]}$.

Configuration interaction projection operators are denoted $\mathcal{P}_n$, where n indicates the level

of excitation to which the projection operator corresponds; for example,

$$\mathcal{P}_0 \equiv |\Phi_{\mathrm{HF}}\rangle\langle\Phi_{\mathrm{HF}}| \tag{6.9}$$

$$\mathcal{P}_1 \equiv \sum_{ia} |\Phi_i^a\rangle\langle\Phi_i^a| \tag{6.10}$$

$$\mathcal{P}_2 \equiv \frac{1}{4}\sum_{ijab} |\Phi_{ij}^{ab}\rangle\langle\Phi_{ij}^{ab}| \tag{6.11}$$

and so forth, so that the full configuration interaction resolution of the identity is given by

$$\mathbf{1} = \mathcal{P}_0 + \mathcal{P}_1 + \mathcal{P}_2 + \mathcal{P}_3 + ... \tag{6.12}$$

We define the Hartree-Fock density matrix

$$P_{\mu\nu} \equiv \sum_i C_{\mu i} C_{\nu i} \tag{6.13}$$

and a related quantity,

$$\widetilde{P}_{\mu\nu} \equiv \sum_p C_{\mu p} C_{\nu p} = P_{\mu\nu} + \sum_a C_{\mu a} C_{\nu a}. \tag{6.14}$$

TDHF transition density matrices from the ground to an excited state are given by

$$R_{\mu\nu}^{XI} \equiv \sum_{ia} C_{\mu a} X_i^{Ia} C_{\nu i} \tag{6.15}$$

and

$$R_{\mu\nu}^{YI} \equiv \sum_{ia} C_{\mu a} Y_i^{Ia} C_{\nu i}, \tag{6.16}$$

where X_i^{Ia} and Y_i^{Ia} are the TDHF amplitudes associated with state I. Generalized differ-

ence density matrices between excited states are given by

$$D^{IJ}_{\mu\nu} \equiv \sum_{iab} C_{\mu a} \left(X^{Ia}_i X^{Jb}_i + Y^{Ja}_i Y^{Ib}_i \right) C_{\nu b} - \sum_{ija} C_{\mu i} \left(X^{Ja}_i X^{Ia}_j + Y^{Ia}_i Y^{Ja}_j \right) C_{\nu j}. \tag{6.17}$$

We define the "right" molecular orbital overlap gradient

$$O^{R[Q]}_{pq} \equiv \langle p | q^{[Q]} \rangle = \sum_{\alpha\beta} C_{\mu p} S^{A[Q]}_{\alpha\beta} C_{\nu q} - \Theta^{[Q]}_{pq}, \tag{6.18}$$

where the second equality is derived in Ref. 67. Here, $\Theta^{[Q]}_{pq}$ is the orbital response term describing the mixing between MOs p and q.[1] $S^{A[Q]}_{\mu\nu}$ is the antisymmetrized atomic orbital overlap gradient

$$S^{A[Q]}_{\mu\nu} \equiv \frac{1}{2} \left(\langle \mu | \nu^{[Q]} \rangle - \langle \mu^{[Q]} | \nu \rangle \right) \tag{6.19}$$

Similarly, the symmetric AO overlap gradient is written

$$S^{[Q]}_{\mu\nu} \equiv \frac{1}{2} \left(\langle \mu | \nu^{[Q]} \rangle + \langle \mu^{[Q]} | \nu \rangle \right). \tag{6.20}$$

Terms containing $S^{A[Q]}$ arise from the inability of real-valued basis functions to account for translational momentum of the electrons as they follow the perturbed nuclei. Ultimately, this contribution to the derivative coupling can lead to a lack of translational invariance, i.e., systems can acquire some overall translational motion from electronic relaxation that violates conservation of momentum. These nonphysical terms are small, and can be neglected to first order if we include atomic electronic translational factors.[67] Finally, terms containing $S^{[Q]}$ are the so-called Pulay terms that account for the effect of an atom-centered basis on nuclear gradients.

Throughout the text, we will make use of orbital creation ($\hat{a}^\dagger_p$) and annihilation ($\hat{a}_p$) oper-

[1] Any quantity that is traced against $\Theta^{[Q]}_{pq}$ contributes to the orbital response Lagrangian, and is ultimately resolved using standard coupled-perturbed Hartree-Fock theory.[183,184] The contributions to the DC arising from orbital response will end up 'relaxing' the generalized difference density matrices $D^{IJ}_{\mu\nu}$ that appear in the final expression in exactly the same manner as in the corresponding density matrices from the CIS DCs described in Ref. 67. In what follows, we will neglect intra-subspace (or 'redundant') orbital response terms, as all such terms ultimately vanish from the final expression, just as they do for CIS derivative couplings.[67]

ators; e.g., for the Hamiltonian, we write

$$\hat{H} = \sum_{pq} h_{pq} \hat{a}_p^\dagger \hat{a}_q + \frac{1}{4} \sum_{pqrs} \Pi_{pqrs} \hat{a}_p^\dagger \hat{a}_q^\dagger \hat{a}_s \hat{a}_r \tag{6.21}$$

where h_{pq} is the single electron Hamiltonian matrix element, and Π_{pqrs} is an antisymmetrized two-electron integral,[2] which is given in physicists' notation by

$$\Pi_{pqrs} = \langle pq||rs\rangle. \tag{6.22}$$

6.3. Theory

6.3.1. Hellmann-Feynman derivative coupling expression

Let $|\Psi_I^{\mathrm{Ex}}\rangle$ and E_I^{Ex} be exact eigenstates and eigenvalues of the electronic Hamiltonian $\hat{H}$. The Hellmann-Feynman expression for derivative couplings is

$$d_{IJ}^{\mathrm{Ex}[Q]} = \langle \Psi_I^{\mathrm{Ex}} | \nabla_Q | \Psi_J^{\mathrm{Ex}} \rangle = \frac{\langle \Psi_I^{\mathrm{Ex}} | \hat{H}^{[Q]} | \Psi_J^{\mathrm{Ex}} \rangle}{E_J^{\mathrm{Ex}} - E_I^{\mathrm{Ex}}}, \tag{6.23}$$

where $I \neq J$.

As we have shown,[67] one can obtain an analogous expression for the derivative couplings between CIS states ($|\Phi_I^{\mathrm{CIS}}\rangle$). Noting that these states have the properties

$$\mathcal{P}_1 \hat{H} \mathcal{P}_1 |\Phi_I^{\mathrm{CIS}}\rangle = \sum_{ia} A_{aibj} t_i^{Ia} |\Phi_j^b\rangle = E_I^{\mathrm{CIS}} \sum_{jb} t_j^{Ib} |\Phi_j^b\rangle = E_I^{\mathrm{CIS}} |\Phi_I^{\mathrm{CIS}}\rangle \tag{6.24}$$

and

$$\langle \Phi_I^{\mathrm{CIS}} | \mathcal{P}_1 \hat{H} \mathcal{P}_1 | \Phi_J^{\mathrm{CIS}} \rangle = \sum_{ijab} t_i^{Ia} t_j^{Jb} A_{aibj} = \delta_{IJ} E_I^{\mathrm{CIS}} \tag{6.25}$$

(cf. Eqs. 6.2 and 6.3), we can obtain an exact Hellmann-Feynman expression for CIS DCs

[2] Explicitly, $\Pi_{pqrs} = \iint \mathrm{d}\mathbf{x}_1 \mathrm{d}\mathbf{x}_2 \chi_p^*(\mathbf{x}_1) \chi_q^*(\mathbf{x}_2) r_{12}^{-1} \chi_r(\mathbf{x}_1) \chi_s(\mathbf{x}_2) - \iint \mathrm{d}\mathbf{x}_1 \mathrm{d}\mathbf{x}_2 \chi_p^*(\mathbf{x}_1) \chi_q^*(\mathbf{x}_2) r_{12}^{-1} \chi_s(\mathbf{x}_1) \chi_r(\mathbf{x}_2)$, where χ is a molecular spin orbital, and r_{12} is the distance between electrons 1 and 2.

by replacing the Hamiltonian $\hat{H}$ in Eq. 6.23 with a modified operator

$$\widetilde{A} = \mathcal{P}_1 \hat{H} \mathcal{P}_1 \tag{6.26}$$

Here, $\mathcal{P}_1$ is a projection operator onto singly-excited states (Eq. 6.10). In this case,

$$\begin{aligned} d_{IJ}^{\mathrm{CIS}[Q]} =& \langle \Phi_I^{\mathrm{CIS}} | \nabla_Q | \Phi_J^{\mathrm{CIS}} \rangle = \frac{\langle \Phi_I^{\mathrm{CIS}} | \widetilde{A}^{[Q]} | \Phi_J^{\mathrm{CIS}} \rangle}{E_J^{\mathrm{CIS}} - E_I^{\mathrm{CIS}}} \\ =& \frac{1}{E_J^{\mathrm{CIS}} - E_I^{\mathrm{CIS}}} \sum_{ijab} t_i^{Ia} t_j^{Jb} \langle \Phi_i^a | \widetilde{A}^{[Q]} | \Phi_j^b \rangle. \end{aligned} \tag{6.27}$$

Eq. 6.27 can be resolved into a gradient of the Hamiltonian, which represents the naïve Hellmann-Feynman result, plus the gradient of the projection operators. This second term contributes to the orbital response, reflecting the fact that the CIS wavefunctions are restricted to sums of singly-excited determinants.

In this chapter, we would like to find an analogous approach to derive DCs for the TDHF formalism. However, because the Hellmann-Feynman method clearly depends on the existence of wavefunctions, we must define a "wavefunction" that corresponds to the TDHF states.

6.3.2. TDHF pseudo-wavefunctions

Unlike CIS, the TDHF formalism is derived as a response theory without a static wavefunction ansatz. That being said, for a *pair* of TDHF solutions, we can write TDHF pseudo-wavefunctions that exhibit certain desired behaviors upon inner product. For a pair of states I and J, these pseudo-wavefunctions are given by

$$|\Psi_I\rangle \equiv \left(\hat{X}^I + \hat{X}^I \hat{X}^J \hat{Y}^J \right) |\Phi_{\mathrm{HF}}\rangle \tag{6.28}$$

and

$$|\Psi_J\rangle \equiv \left(\hat{X}^J + \hat{X}^J \hat{X}^I \hat{Y}^I \right) |\Phi_{\mathrm{HF}}\rangle. \tag{6.29}$$

Here we define the TDHF excitation operators

$$\hat{X}^I \equiv \sum_{ia} X_i^{Ia} \hat{a}_a^\dagger \hat{a}_i \tag{6.30}$$

and

$$\hat{Y}^I \equiv \sum_{ia} Y_i^{Ia} \hat{a}_a^\dagger \hat{a}_i. \tag{6.31}$$

Notice that these wavefunctions are not entirely independent; the wavefunction for state I depends on state J, and vice-versa.

Assuming the HF energy is zero ($E_{\mathrm{HF}} = 0$), the Hamiltonian matrix element between two of these pseudo-wavefunctions can be written as

$$\langle \Psi_I | \hat{H} | \Psi_J \rangle = \langle \Phi_{\mathrm{HF}} | \left(\hat{X}^{I\dagger} + \hat{Y}^{J\dagger} \hat{X}^{J\dagger} \hat{X}^{I\dagger} \right) \hat{H} \left(\hat{X}^J + \hat{X}^J \hat{X}^I \hat{Y}^I \right) | \Phi_{\mathrm{HF}} \rangle. \tag{6.32}$$

The TDHF eigenvalue equation (Eq. 6.5) can be approximately derived from Eq. 6.32 by discarding all terms but a single disconnected component. To arrive at this result, we employ the following reasoning: given that TDHF X amplitudes are nearly orthonormal (Eq. 6.8), any term containing $\mathbf{X}^{I\dagger}\mathbf{X}^I$ will dominate the following expressions. Using Wick's theorem, we can write

$$\begin{aligned} \left\langle \Phi_{\mathrm{HF}} \hat{Y}^{J\dagger} \hat{X}^{J\dagger} \hat{X}^{I\dagger} \middle| \hat{H} \middle| \hat{X}^J \Phi_{\mathrm{HF}} \right\rangle &= \left\langle \Phi_{\mathrm{HF}} \hat{Y}^{J\dagger} \hat{X}^{I\dagger} \middle| \hat{H} \middle| \Phi_{\mathrm{HF}} \right\rangle \mathbf{X}^{I\dagger}\mathbf{X}^I + \dots \\ &\approx \left\langle \Phi_{\mathrm{HF}} \hat{Y}^{J\dagger} \hat{X}^{I\dagger} \middle| \hat{H} \middle| \Phi_{\mathrm{HF}} \right\rangle \\ &= \mathbf{X}^{I\dagger}\mathbf{B}\mathbf{Y}^J \end{aligned} \tag{6.33}$$

and

$$\left\langle \Phi_{\mathrm{HF}}\hat{Y}^{J\dagger}\hat{X}^{J\dagger}\hat{X}^{I\dagger}\middle|\,\hat{H}\,\middle|\hat{X}^{J}\hat{X}^{I}\hat{Y}^{I}\Phi_{\mathrm{HF}}\right\rangle = \left\langle \Phi_{\mathrm{HF}}\hat{Y}^{J\dagger}\middle|\hat{H}\middle|\,\hat{Y}^{I}\Phi_{\mathrm{HF}}\right\rangle \left(\mathbf{X}^{I\dagger}\mathbf{X}^{I}\right)\left(\mathbf{X}^{J\dagger}\mathbf{X}^{J}\right) + \ldots \tag{6.34}$$

$$\begin{aligned} &\approx \left\langle \Phi_{\mathrm{HF}}\hat{Y}^{J\dagger}\middle|\hat{H}\middle|\,\hat{Y}^{I}\Phi_{\mathrm{HF}}\right\rangle \\ &= \mathbf{Y}^{I\dagger}\mathbf{A}\mathbf{Y}^{J} \end{aligned}$$

so that we obtain

$$\begin{aligned} \langle\Psi_I|\hat{H}|\Psi_J\rangle \approx& \mathbf{X}^{I\dagger}\mathbf{A}\mathbf{X}^{J} + \mathbf{X}^{I\dagger}\mathbf{B}\mathbf{Y}^{J} + \mathbf{Y}^{I\dagger}\mathbf{B}\mathbf{X}^{J} + \mathbf{Y}^{I\dagger}\mathbf{A}\mathbf{Y}^{J} \\ &= \left(\mathbf{X}^{I\dagger} - \mathbf{Y}^{I\dagger}\right)\begin{pmatrix} \mathbf{A} & \mathbf{B} \\ -\mathbf{B} & -\mathbf{A} \end{pmatrix}\begin{pmatrix} \mathbf{X}^{J} \\ \mathbf{Y}^{J} \end{pmatrix} \\ &= \delta_{IJ}E_I. \end{aligned} \tag{6.35}$$

Eq. 6.35 shows that the TDHF pseudo-wavefunctions sandwiched around the Hamiltonian approximately reproduce the TDHF eigenvalue equation (Eq. 6.5). From the same perspective, the overlap between TDHF pseudo-wavefunctions,

$$\begin{aligned} \langle\Psi_I|\Psi_J\rangle \approx& \langle\Phi_{\mathrm{HF}}|\hat{X}^{I\dagger}\hat{X}^{J}|\Phi_{\mathrm{HF}}\rangle + \langle\Phi_{\mathrm{HF}}|\hat{Y}^{J\dagger}\hat{Y}^{I}|\Phi_{\mathrm{HF}}\rangle \\ &= \mathbf{X}^{I\dagger}\mathbf{X}^{J} + \mathbf{Y}^{I\dagger}\mathbf{Y}^{J} \\ &\approx \mathbf{X}^{I\dagger}\mathbf{X}^{J} \approx \delta_{IJ}, \end{aligned} \tag{6.36}$$

approximately recovers Eq. 6.8.

Now, our heuristic derivation of TDHF requires that the X amplitudes be nearly orthonormal, and equivalently, that Y amplitudes remain below a certain magnitude. In particular, we would like to ignore all terms on the order of $O(\mathbf{Y}^2)$ if possible. In this case, we require

that if $\mathbf{Y}^{J\dagger}\mathbf{Y}^{I} \approx 0$,

$$\begin{aligned}\langle\Phi_{\mathrm{HF}}\hat{Y}^{J\dagger}|\left(|\hat{Y}^{I}\Phi_{\mathrm{HF}}\rangle\right)^{[Q]} &\approx -\left(\langle\Phi_{\mathrm{HF}}\hat{Y}^{J\dagger}|\right)^{[Q]}|\hat{Y}^{I}\Phi_{\mathrm{HF}}\rangle \\ &= -\langle\Phi_{\mathrm{HF}}\hat{Y}^{I\dagger}|\left(|\hat{Y}^{J}\Phi_{\mathrm{HF}}\rangle\right)^{[Q]}.\end{aligned} \tag{6.37}$$

In Eq. 6.37, we note that even though Y is small, the gradients of Y amplitudes need not be small: $Y^{[Q]}$ terms cannot be neglected in a gradient expression.

We are finally prepared to examine the derivative couplings between TDHF pseudo-wavefunctions. By evaluating the overlap between pseudo-wavefunction $|\Psi_I\rangle$ and the nuclear gradient of pseudo-wavefunction $|\Psi_J\rangle$, we find

$$\begin{aligned}\langle\Psi_I|\nabla_Q|\Psi_J\rangle \approx&\langle\Phi_{\mathrm{HF}}\hat{X}^{I\dagger}|\left(|\hat{X}^{J}\Phi_{\mathrm{HF}}\rangle\right)^{[Q]} + \langle\Phi_{\mathrm{HF}}\hat{Y}^{J\dagger}|\left(|\hat{Y}^{I}\Phi_{\mathrm{HF}}\rangle\right)^{[Q]} \\ \approx&\langle\Phi_{\mathrm{HF}}\hat{X}^{I\dagger}|\left(|\hat{X}^{J}\Phi_{\mathrm{HF}}\rangle\right)^{[Q]} - \langle\Phi_{\mathrm{HF}}\hat{Y}^{I\dagger}|\left(|\hat{Y}^{J}\Phi_{\mathrm{HF}}\rangle\right)^{[Q]} \\ =&\sum_{ijab}\left(X_i^{Ia}X_j^{Jb} - Y_i^{Ia}Y_j^{Jb}\right)\langle\Phi_i^a|\Phi_j^{b[Q]}\rangle + \sum_{ia}\left(X_i^{Ia}X_i^{Ja[Q]} - Y_i^{Ia}Y_i^{Ja[Q]}\right),\end{aligned} \tag{6.38}$$

where we have used Eq. 6.37 to obtain the second approximate equality. Eq. 6.38 for DCs will be explored in Ref. 181.

In this manuscript we note that Eq. 6.38 can be transformed into an effective Hellmann-Feynman expression for TDHF DCs analogous to Eq. 6.27

$$\begin{aligned}d_{IJ}^{\mathrm{TDHF}[Q]} = \frac{1}{E_J - E_I}\sum_{ijab}\Big[&(X_i^{Ia}X_j^{Jb} + Y_i^{Ia}Y_j^{Jb})\langle\Phi_i^a|\widetilde{A}^{[Q]}|\Phi_j^b\rangle \\ &+(X_i^{Ia}Y_j^{Jb} + Y_i^{Ia}X_j^{Jb})\langle\Phi_{ij}^{ab}|\widetilde{B}^{[Q]}|\Phi_{\mathrm{HF}}\rangle\Big],\end{aligned} \tag{6.39}$$

where $\widetilde{A}$ is defined in Eq. 6.26, and

$$\widetilde{B} = \mathcal{P}_2\hat{H}\mathcal{P}_0. \tag{6.40}$$

To better see the correspondence between the CIS and TDHF Hellmann-Feynman DC equations, compare the relationship between Eqs. 6.25 and 6.27 to that of Eqs. 6.35 and 6.39. We will now show how to evaluate Eq. 6.39 in practice, and in A.6, we will show that our final result matches the result obtained working directly from Eq. 6.38

6.3.3. Evaluating the Hellmann-Feynman derivative coupling

The first step in evaluating the Hellmann-Feynman DC is to expand Eq. 6.39 and apply the product rule. To simplify the resulting expression, we partition it into four terms:

$$d_{IJ}^{\mathrm{TDHF}[Q]} = \frac{1}{E_J - E_I}\left(W_1 + W_2 + W_3 + W_4\right), \tag{6.41}$$

where

$$\begin{aligned} W_1 = &\sum_{ijab}\left(X_i^{Ia}X_j^{Jb} + Y_i^{Ia}Y_j^{Jb}\right)\langle\Phi_i^a|\Big[H^{[Q]} \\ &+ \left(\sum_{kc}|\Phi_k^c\rangle\langle\Phi_k^{c[Q]}|\right)H + H\left(\sum_{kc}|\Phi_k^{c[Q]}\rangle\langle\Phi_k^c|\right) \\ &+ \left(\sum_{kc}|\Phi_k^{c[Q]}\rangle\langle\Phi_k^c|\right)H + H\left(\sum_{kc}|\Phi_k^c\rangle\langle\Phi_k^{c[Q]}|\right)\Big]|\Phi_j^b\rangle, \end{aligned} \tag{6.42}$$

$$W_2 = \sum_{ijab}\left(X_i^{Ia}Y_j^{Jb} + Y_i^{Ia}X_j^{Jb}\right)\langle\Phi_{ij}^{ab}|H^{[Q]}|\Phi_{\mathrm{HF}}\rangle, \tag{6.43}$$

$$W_3 = \sum_{ijab}\left(X_i^{Ia}Y_j^{Jb} + Y_i^{Ia}X_j^{Jb}\right)\langle\Phi_{ij}^{ab}|H|\Phi_{\mathrm{HF}}^{[Q]}\rangle, \tag{6.44}$$

and

$$\begin{aligned} W_4 = &\frac{1}{4}\sum_{ijab}\left(X_i^{Ia}Y_j^{Jb} + Y_i^{Ia}X_j^{Jb}\right)\langle\Phi_{ij}^{ab}|\left[\hat{H}\left(|\Phi_{\mathrm{HF}}\rangle\langle\Phi_{\mathrm{HF}}^{[Q]}|\right) + \left(\sum_{klcd}|\Phi_{kl}^{cd}\rangle\langle\Phi_{kl}^{cd[Q]}|\right)\hat{H}\right. \\ &\left. + \left(\sum_{klcd}|\Phi_{kl}^{cd[Q]}\rangle\langle\Phi_{kl}^{cd}|\right)\hat{H}\right]|\Phi_{\mathrm{HF}}\rangle. \end{aligned} \tag{6.45}$$

Beginning with W_4, we see that the first term in square brackets in Eq. 6.45 involves the derivative coupling between the HF state and itself, $\langle\Phi_{\mathrm{HF}}^{[Q]}|\Phi_{\mathrm{HF}}\rangle$, which is easily shown to

be zero. The second term involves the Hartee-Fock ground state coupled via a Hamiltonian to the gradient of a doubly-excited state, $\langle \Phi_{kl}^{cd[Q]} | \hat{H} | \Phi_{\mathrm{HF}} \rangle$. In order to evaluate this term, we insert the configuration interaction resolution of the identity (Eq. 6.12) between the Hamiltonian and the gradient term. Because the Hamiltonian is a two-electron operator, it can only couple the Hartree-Fock state on the left-hand side of the term to another Hartree-Fock state, a singly-excited state, or a doubly-excited state. By Brillouin's theorem, however, the Hamiltonian cannot couple the Hartree-Fock state to a singly-excited state. This leaves only

$$\langle \Phi_{kl}^{cd[Q]} | \left(|\Phi_{\mathrm{HF}}\rangle\langle\Phi_{\mathrm{HF}}| + \frac{1}{4} \sum_{mnef} |\Phi_{mn}^{ef}\rangle\langle\Phi_{mn}^{ef}| \right) \hat{H} | \Phi_{\mathrm{HF}} \rangle \tag{6.46}$$

When the gradient operator ($^{[Q]}$) acts on states, it behaves like a single electron operator. As such, it cannot couple doubly-excited states to the Hartree-Fock state. Finally, the only remaining terms include expressions of the form $\left\langle \Phi_{kl}^{cd[Q]} | \Phi_{mn}^{ef} \right\rangle$. Applying the gradient and resolving the second quantization operators, we find

$$\begin{aligned} \sum_{mnef} \left\langle \Phi_{kl}^{cd[Q]} | \Phi_{mn}^{ef} \right\rangle = \sum_{mnef} \Big[(\delta_{mk}\delta_{nl} - \delta_{ml}\delta_{nk}) \left(\delta_{fd} O_{ce}^{R[Q]} - \delta_{ed} O_{cf}^{R[Q]} + \delta_{ec} O_{df}^{R[Q]} - \delta_{fc} O_{de}^{R[Q]} \right) \\ (\delta_{ec}\delta_{fd} - \delta_{ed}\delta_{fc}) \left(\delta_{mk} O_{ln}^{R[Q]} - \delta_{nk} O_{lm}^{R[Q]} + \delta_{nl} O_{km}^{R[Q]} - \delta_{ml} O_{kn}^{R[Q]} \right) \Big] . \end{aligned} \tag{6.47}$$

It is trivial to show by relabeling the indices that Eq. 6.47 is equal to zero. Thus, both remaining terms in W_4 evaluate to zero, and no part of W_4 contributes to the final DC expression: $W_4 = 0$.

Turning our attention to W_1 (Eq. 6.42), inspection reveals that it is nearly identical to the CIS derivative coupling expression (cf. Eq. 17 of Ref. 67), with the CIS amplitudes $t_i^{Ia} t_j^{Jb}$ replaced by TDHF amplitudes $X_i^{Ia} X_j^{Jb} + Y_i^{Ia} Y_j^{Jb}$. The derivation for CIS derivative couplings can be followed to obtain an expression for W_1 that is very similar to the final

expression for CIS derivative couplings (Ref. 67, Eqs. 81-83) once the amplitude substitution is made. In the AO basis, W_1 becomes

$$
\begin{aligned}
W_1 = & \sum_{\mu\nu} h^{[Q]}_{\mu\nu} D^{IJ}_{\mu\nu} + \sum_{\mu\nu\lambda\sigma} \Pi^{[Q]}_{\mu\lambda\nu\sigma} \left(R^{XI}_{\mu\nu} R^{XJ}_{\sigma\lambda} + R^{YI}_{\mu\nu} R^{YJ}_{\sigma\lambda} + D^{IJ}_{\mu\nu} P_{\sigma\lambda} \right) \\
& - \frac{1}{2} \sum_{\mu\nu\alpha\beta} S^{[Q]}_{\mu\nu} \tilde{P}_{\mu\alpha} \left(D^{IJ}_{\beta\nu} + D^{IJ}_{\nu\beta} \right) F_{\alpha\beta} - \frac{1}{2} \sum_{\mu\nu\alpha\beta\lambda\sigma} S^{[Q]}_{\mu\nu} \tilde{P}_{\mu\alpha} P_{\nu\beta} \left(D^{IJ}_{\sigma\lambda} + D^{IJ}_{\lambda\sigma} \right) \Pi_{\alpha\lambda\beta\sigma} \\
& - \frac{1}{2} \sum_{\mu\nu\alpha\beta\lambda\sigma} S^{[Q]}_{\mu\nu} \tilde{P}_{\mu\alpha} \left(R^{XI}_{\nu\beta} R^{XJ}_{\sigma\lambda} + R^{XI}_{\sigma\lambda} R^{XJ}_{\nu\beta} + R^{XI}_{\beta\nu} R^{XJ}_{\lambda\sigma} + R^{XI}_{\lambda\sigma} R^{XJ}_{\beta\nu} \right) \Pi_{\alpha\lambda\beta\sigma} \\
& - \frac{1}{2} \sum_{\mu\nu\alpha\beta\lambda\sigma} S^{[Q]}_{\mu\nu} \tilde{P}_{\mu\alpha} \left(R^{YI}_{\nu\beta} R^{YJ}_{\sigma\lambda} + R^{YI}_{\sigma\lambda} R^{YJ}_{\nu\beta} + R^{YI}_{\beta\nu} R^{YJ}_{\lambda\sigma} + R^{YI}_{\lambda\sigma} R^{YJ}_{\beta\nu} \right) \Pi_{\alpha\lambda\beta\sigma} \\
& - \sum_{ck} L^{\mathrm{A},IJ}_{ck} \Theta^{[Q]}_{ck} + (E_J - E_I) \sum_{\mu\nu} S^{A[Q]}_{\mu\nu} G^{\mathrm{A}}_{\mu\nu},
\end{aligned}
\tag{6.48}
$$

where L^{A} is the W_1 contribution to the orbital response Lagrangian, given by

$$
\begin{aligned}
L^{\mathrm{A},IJ}_{ck} = & \sum_{\mu\nu\lambda\sigma} C_{\lambda c} C_{\sigma k} \left(D^{IJ}_{\mu\nu} + D^{IJ}_{\nu\mu} \right) \Pi_{\mu\lambda\nu\sigma} \\
& + \sum_{a\mu\nu\lambda\sigma} C_{\lambda c} C_{\sigma a} \left(R^{XI}_{\mu\nu} X^{Ja}_{k} + X^{Ia}_{k} R^{XJ}_{\mu\nu} + R^{YI}_{\mu\nu} Y^{Ja}_{k} + Y^{Ia}_{k} R^{YJ}_{\mu\nu} \right) \Pi_{\mu\lambda\nu\sigma} \\
& - \sum_{i\mu\nu\lambda\sigma} C_{\lambda i} C_{\sigma k} \left(R^{XI}_{\mu\nu} X^{Jc}_{i} + X^{Ic}_{i} R^{XJ}_{\mu\nu} + R^{YI}_{\mu\nu} Y^{Jc}_{i} + Y^{Ic}_{i} R^{YJ}_{\mu\nu} \right) \Pi_{\mu\lambda\nu\sigma}
\end{aligned}
\tag{6.49}
$$

and $G^{\mathrm{A},IJ}$ contains the translationally variant contributions from W_1 (Eq. 6.50).

$$
\begin{aligned}
G^{\mathrm{A},IJ}_{\mu\nu} = \frac{1}{E_J - E_I} \Bigg[& \sum_{ijabc} C_{\mu c} C_{\nu a} \Pi_{ibaj} \left(X_i^{Ic} X_j^{Jb} + X_j^{Ib} X_i^{Jc} + Y_i^{Ic} Y_j^{Jb} + Y_j^{Ib} Y_i^{Jc} \right) \\
& - \sum_{ijkab} C_{\mu i} C_{\nu k} \Pi_{abij} \left(X_k^{Ia} X_j^{Jb} + X_j^{Ib} X_k^{Ja} + Y_k^{Ia} Y_j^{Jb} + Y_j^{Ib} Y_k^{Ja} \right) \\
& + \sum_{iac} C_{\mu c} C_{\nu a} \varepsilon_a \left(X_i^{Ia} X_i^{Jc} + X_i^{Ic} X_i^{Ja} + Y_i^{Ia} Y_i^{Jc} + Y_i^{Ic} Y_i^{Ja} \right) \\
& + \sum_{ika} C_{\mu i} C_{\nu k} \varepsilon_i \left(X_i^{Ia} X_k^{Ja} + X_k^{Ia} X_i^{Ja} + Y_i^{Ia} Y_k^{Ja} + Y_k^{Ia} Y_i^{Ja} \right) \\
& - \sum_{ijkab} C_{\mu i} C_{\nu k} \Pi_{iakb} \left(X_j^{Ia} X_j^{Jb} + X_j^{Ib} X_j^{Ja} + Y_j^{Ia} Y_j^{Jb} + Y_j^{Ib} Y_j^{Ja} \right) \\
& + \sum_{ijkla} C_{\mu i} C_{\nu k} \Pi_{ilkj} \left(X_l^{Ia} X_j^{Ja} + X_j^{Ia} X_l^{Ja} + Y_l^{Ia} Y_j^{Ja} + Y_j^{Ia} Y_l^{Ja} \right) \Bigg]
\end{aligned}
\tag{6.50}
$$

6.3.4. Evaluating the TDHF cross-terms

We now turn our attention to a contribution that is unique to TDHF, W_2 (Eq. 6.43). The second-quantization expression for the Hamiltonian is given in Eq. 6.21, so that its gradient is

$$
\begin{aligned}
\hat{H}^{[Q]} = & \sum_{pq} \left(h^{[Q]}_{pq} \hat{a}^\dagger_p \hat{a}_q + h_{pq} \hat{a}^{\dagger[Q]}_p \hat{a}_q + h_{pq} \hat{a}^\dagger_p \hat{a}^{[Q]}_q \right) \\
& + \frac{1}{4} \sum_{pqrs} \Big(\Pi^{[Q]}_{pqrs} \hat{a}^\dagger_p \hat{a}^\dagger_q \hat{a}_s \hat{a}_r + \Pi_{pqrs} \hat{a}^{\dagger[Q]}_p \hat{a}^\dagger_q \hat{a}_s \hat{a}_r + \Pi_{pqrs} \hat{a}^\dagger_p \hat{a}^{\dagger[Q]}_q \hat{a}_s \hat{a}_r \\
& \qquad + \Pi_{pqrs} \hat{a}^\dagger_p \hat{a}^\dagger_q \hat{a}^{[Q]}_s \hat{a}_r + \Pi_{pqrs} \hat{a}^\dagger_p \hat{a}^\dagger_q \hat{a}_s \hat{a}^{[Q]}_r \Big)
\end{aligned}
\tag{6.51}
$$

As demonstrated in Ref. 67 (Eq. 28), the gradient of creation/annihilation operators is given by

$$
\hat{a}^{[Q]}_p = - \sum_q O^{R[Q]}_{pq} \hat{a}_q, \tag{6.52}
$$

for the "right" molecular orbital overlap gradient $O_{pq}^{R[Q]}$ (Eq. 6.18). This expression makes it clear that the one-electron operator component of the Hamiltonian remains a one-electron operator after the application of the gradient. As such, all one-electron terms cannot couple the Hartree-Fock state to a doubly-excited state and can be discarded. The remaining contributions, from the two-electron integral, yield

$$\langle \Phi_{\mathrm{HF}} | \hat{H}^{[Q]} | \Phi_{ij}^{ab} \rangle = \Pi_{abij}^{[Q]} - \sum_{p} \left(O_{pa}^{R[Q]} \Pi_{pbij} + O_{pb}^{R[Q]} \Pi_{apij} + O_{pi}^{R[Q]} \Pi_{abpj} + O_{pj}^{R[Q]} \Pi_{abip} \right). \tag{6.53}$$

After reassigning some indices and utilizing the symmetry properties of the two-electron integral ($\Pi_{pqrs} = -\Pi_{qprs} = \Pi_{rspq}$) and the molecular overlap gradient ($O_{pq}^{R[Q]} = -O_{qp}^{R[Q]}$), we obtain the expression

$$\begin{aligned} W_2 = & \sum_{ijab} \Pi_{abij}^{[Q]} \left(X_i^{Ia} Y_j^{Jb} + Y_i^{Ia} X_j^{Jb} \right) \\ & - \sum_{acijk} O_{pk}^{R[Q]} \left(X_i^{Ia} Y_k^{Jb} + Y_i^{Ia} X_k^{Jb} + X_k^{Ib} Y_i^{Ja} + Y_k^{Ib} X_i^{Ja} \right) \Pi_{bapi} \\ & + \sum_{abcik} O_{cp}^{R[Q]} \left(X_i^{Ia} Y_j^{Jc} + Y_i^{Ia} X_j^{Jc} + X_j^{Ic} Y_i^{Ja} + Y_j^{Ic} X_i^{Ja} \right) \Pi_{paji}. \end{aligned} \tag{6.54}$$

The MO overlap gradient $O_{pq}^{R[Q]}$ can be further decomposed according to Eq. 6.18, and the two-electron integral can be expanded in terms of MO coefficients

$$\Pi_{abij} = \sum_{\mu\nu\lambda\sigma} \Pi_{\mu\lambda\nu\sigma} C_{\mu a} C_{\lambda b} C_{\nu i} C_{\sigma j}, \tag{6.55}$$

so that

$$\begin{aligned} \Pi_{abij}^{[Q]} = \sum_{\mu\nu\lambda\sigma} \Big(& \Pi_{\mu\lambda\nu\sigma}^{[Q]} C_{\mu a} C_{\lambda b} C_{\nu i} C_{\sigma j} \\ & + \Pi_{\mu\lambda\nu\sigma} C_{\mu a}^{[Q]} C_{\lambda b} C_{\nu i} C_{\sigma j} + \Pi_{\mu\lambda\nu\sigma} C_{\mu a} C_{\lambda b}^{[Q]} C_{\nu i} C_{\sigma j} \\ & + \Pi_{\mu\lambda\nu\sigma} C_{\mu a} C_{\lambda b} C_{\nu i}^{[Q]} C_{\sigma j} + \Pi_{\mu\lambda\nu\sigma} C_{\mu a} C_{\lambda b} C_{\nu i} C_{\sigma j}^{[Q]} \Big) \end{aligned} \tag{6.56}$$

As a function of AO overlap (S) and orbital rotation (Θ), the MO coefficient gradient is given by Eq. 63 of Ref. 67

$$\begin{aligned} C_{\mu p}^{[Q]} =& \sum_{\alpha\beta} \frac{\partial C_{\mu p}}{\partial S_{\alpha\beta}} S_{\alpha\beta}^{[Q]} + \sum_{ck} \frac{\partial C_{\mu p}}{\partial \Theta_{ck}} \Theta_{ck}^{[Q]} \\ =& -\frac{1}{2} \sum_{\alpha\beta} \tilde{P}_{\mu\alpha} C_{\beta p} S_{\alpha\beta}^{[Q]} + \sum_{ck} \left(C_{\mu k} \Theta_{cp}^{[Q]} - C_{\mu c} \Theta_{pk}^{[Q]} \right). \end{aligned} \tag{6.57}$$

After substituting these expressions into Eq. 6.54 and rearranging the indices, the response terms cancel entirely and the expression becomes

$$\begin{aligned} W_2 =& \sum_{ijbcp\alpha\beta} S_{\alpha\beta}^{A[Q]} C_{\alpha c} C_{\beta p} \left(X_i^{Ic} Y_j^{Jb} + X_j^{Ib} Y_i^{Jc} + Y_i^{Ic} X_j^{Jb} + Y_j^{Ib} X_i^{Jc} \right) \Pi_{pbij} \\ &- \sum_{jkabp\alpha\beta} S_{\alpha\beta}^{A[Q]} C_{\alpha p} C_{\beta k} \left(X_k^{Ia} Y_j^{Jb} + X_j^{Ib} Y_k^{Ja} + Y_k^{Ia} X_j^{Jb} + Y_j^{Ib} X_k^{Ja} \right) \Pi_{abpj} \\ &- \frac{1}{2} \sum_{\mu\nu\alpha\beta\lambda\sigma} S_{\mu\nu}^{[Q]} \tilde{P}_{\mu\alpha} \left(R_{\beta\nu}^{XI} R_{\sigma\lambda}^{YJ} + R_{\sigma\lambda}^{XI} R_{\beta\nu}^{YJ} + R_{\nu\beta}^{XI} R_{\lambda\sigma}^{YJ} + R_{\lambda\sigma}^{XI} R_{\nu\beta}^{YJ} \right) \Pi_{\alpha\lambda\beta\sigma} \\ &- \frac{1}{2} \sum_{\mu\nu\alpha\beta\lambda\sigma} S_{\mu\nu}^{[Q]} \tilde{P}_{\mu\alpha} \left(R_{\beta\nu}^{YI} R_{\sigma\lambda}^{XJ} + R_{\sigma\lambda}^{YI} R_{\beta\nu}^{XJ} + R_{\nu\beta}^{YI} R_{\lambda\sigma}^{XJ} + R_{\lambda\sigma}^{YI} R_{\nu\beta}^{XJ} \right) \Pi_{\alpha\lambda\beta\sigma} \\ &+ \sum_{\mu\nu\lambda\sigma} \Pi_{\mu\lambda\nu\sigma}^{[Q]} C_{\mu a} C_{\lambda b} C_{\nu i} C_{\sigma j} \left(X_i^{Ia} Y_j^{Jb} + Y_i^{Ia} X_j^{Jb} \right). \end{aligned} \tag{6.58}$$

Finally, we turn to W_3, Eq. 6.44. The gradient operating on the Hartree-Fock state couples the Hartree-Fock ground state to singly-excited states, so that

$$\begin{aligned} \langle \Phi_{\mathrm{HF}}^{[Q]} | \hat{H} | \Phi_{ij}^{ab} \rangle =& \langle \Phi_{\mathrm{HF}}^{[Q]} | \left(\mathcal{P}_0 + \mathcal{P}_1 + \mathcal{P}_2 + ... \right) | \hat{H} | \Phi_{ij}^{ab} \rangle \\ =& \langle \Phi_{\mathrm{HF}}^{[Q]} | \left(\sum_{kc} | \Phi_k^c \rangle \langle \Phi_k^c | \right) | \hat{H} | \Phi_{ij}^{ab} \rangle \\ =& \sum_{kc} O_{ck}^{R[Q]} \langle \Phi_k^c | \hat{H} | \Phi_{ij}^{ab} \rangle, \end{aligned} \tag{6.59}$$

where we have taken $\langle \Phi_{\mathrm{HF}}^{[Q]} | \Phi_k^c \rangle = O_{ck}^{R[Q]}$ due to the orthogonality of the molecular orbital basis. Furthermore, if we expand the Hamiltonian matrix element and make use of the

orthogonality of the Fock matrix

$$h_{pq} + \sum_{m} \Pi_{pmqm} = F_{pq} = \delta_{pq}\epsilon_p, \tag{6.60}$$

we obtain, after the rearrangement of the indices and the use of Eq. 6.18,

$$\begin{aligned} W_3 = &- \sum_{ijkbc\alpha\beta} S^{A[Q]}_{\alpha\beta} C_{\alpha c} C_{\beta k} \left(X^{Ic}_i Y^{Jb}_j + X^{Ib}_j Y^{Jc}_i + Y^{Ic}_i X^{Jb}_j + Y^{Ib}_j X^{Jc}_i \right) \Pi_{kbij} \\ &+ \sum_{jkabc\alpha\beta} S^{A[Q]}_{\alpha\beta} C_{\alpha c} C_{\beta k} \left(X^{Ia}_k Y^{Jb}_j + X^{Ib}_j Y^{Ja}_k + Y^{Ia}_k X^{Jb}_j + Y^{Ib}_j X^{Ja}_k \right) \Pi_{abcj} \\ &+ \sum_{ijkbc} \Theta^{[Q]}_{ck} \left(X^{Ic}_i Y^{Jb}_j + X^{Ib}_j Y^{Jc}_i + Y^{Ic}_i X^{Jb}_j + Y^{Ib}_j X^{Jc}_i \right) \Pi_{kbij} \\ &- \sum_{jkabc} \Theta^{[Q]}_{ck} \left(X^{Ia}_k Y^{Jb}_j + X^{Ib}_j Y^{Ja}_k + Y^{Ia}_k X^{Jb}_j + Y^{Ib}_j X^{Ja}_k \right) \Pi_{abcj}. \end{aligned} \tag{6.61}$$

By inspection, it is clear that when p indexes an occupied orbital, the first term of W_2 (Eq. 6.58) is the additive inverse of the first term of W_3 (Eq. 6.61), thus negating these contributions to the final derivative coupling expression. The same is true for the respective second terms of Eqs. 6.58 and 6.61 in the case that p indexes a virtual orbital. Noting this, we obtain the sum $W_{2+3} = W_2 + W_3$,

$$\begin{aligned} W_{2+3} = &-\frac{1}{2} \sum_{\mu\nu\alpha\beta\lambda\sigma} S^{[Q]}_{\mu\nu} \tilde{P}_{\mu\alpha} \left(R^{XI}_{\beta\nu} R^{YJ}_{\sigma\lambda} + R^{XI}_{\sigma\lambda} R^{YJ}_{\beta\nu} + R^{XI}_{\nu\beta} R^{YJ}_{\lambda\sigma} + R^{XI}_{\lambda\sigma} R^{YJ}_{\nu\beta} \right) \Pi_{\alpha\lambda\beta\sigma} \\ &-\frac{1}{2} \sum_{\mu\nu\alpha\beta\lambda\sigma} S^{[Q]}_{\mu\nu} \tilde{P}_{\mu\alpha} \left(R^{YI}_{\beta\nu} R^{XJ}_{\sigma\lambda} + R^{YI}_{\sigma\lambda} R^{XJ}_{\beta\nu} + R^{YI}_{\nu\beta} R^{XJ}_{\lambda\sigma} + R^{YI}_{\lambda\sigma} R^{XJ}_{\nu\beta} \right) \Pi_{\alpha\lambda\beta\sigma} \\ &+ \sum_{ijab\mu\nu\lambda\sigma} \Pi^{[Q]}_{\mu\lambda\nu\sigma} C_{\mu a} C_{\lambda b} C_{\nu i} C_{\sigma j} \left(X^{Ia}_i Y^{Jb}_j + Y^{Ia}_i X^{Jb}_j \right) \\ &- \sum_{kc} \Theta^{[Q]}_{ck} L^{\mathrm{B},IJ}_{ck} + (E_J - E_I) \sum_{\mu\nu} S^{A[Q]}_{\mu\nu} G^{\mathrm{B},IJ}_{\mu\nu}, \end{aligned} \tag{6.62}$$

where the CPHF Lagrangian $L^{\mathrm{B},IJ}$ is

$$\begin{aligned} L_{ck}^{\mathrm{B},IJ} = &\sum_{jab} \Pi_{abcj} \left(X_k^{Ia} Y_j^{Jb} + X_j^{Ib} Y_k^{Ja} + Y_k^{Ia} X_j^{Jb} + Y_j^{Ib} X_k^{Ja} \right) \\ &- \sum_{ijb} \Pi_{kbij} \left(X_i^{Ic} Y_j^{Jb} + X_j^{Ib} Y_i^{Jc} + Y_i^{Ic} X_j^{Jb} + Y_j^{Ib} X_i^{Jc} \right) \end{aligned} \tag{6.63}$$

and $G^{\mathrm{B},IJ}$ is given by

$$\begin{aligned} G_{\mu\nu}^{\mathrm{B},IJ} = \frac{1}{E_J - E_I} \Bigg[&\sum_{ijabc} C_{\mu c} C_{\nu a} \Pi_{abij} \left(X_i^{Ic} Y_j^{Jb} + X_j^{Ib} Y_i^{Jc} + Y_i^{Ic} X_j^{Jb} + Y_j^{Ib} X_i^{Jc} \right) \\ &- \sum_{ijkab} C_{\mu i} C_{\nu k} \Pi_{abij} \left(X_k^{Ia} Y_j^{Jb} + X_j^{Ib} Y_k^{Ja} + Y_k^{Ia} X_j^{Jb} + Y_j^{Ib} X_k^{Ja} \right) \Bigg] \end{aligned} \tag{6.64}$$

If W_1 corresponds to CIS-like contributions to the DC, W_{2+3} constitutes the non-CIS-like contributions. Just as for the CIS DCs in Ref. 67, the non-translationally invariant term (here, $G^{IJ} = G^{\mathrm{A},IJ} + G^{\mathrm{B},IJ}$) can be simplified into an expression that has no explicit dependence on the energy difference between states. This is described in detail in A.6. Combining Eqs. 6.48 and 6.62 while fully converting the latter to the AO representation, we arrive at our final expression

$$\begin{aligned} d_{IJ}^{\mathrm{TDHF}[Q]} = &\frac{1}{E_J - E_I} \Bigg[\sum_{\mu\nu} h_{\mu\nu}^{[Q]} D_{\mu\nu}^{IJ} + \sum_{\mu\nu\lambda\sigma} \Pi_{\mu\lambda\nu\sigma}^{[Q]} \left(R_{\mu\nu}^{XI} R_{\sigma\lambda}^{XJ} + R_{\mu\nu}^{YI} R_{\sigma\lambda}^{YJ} + R_{\mu\nu}^{XI} R_{\lambda\sigma}^{YJ} + R_{\mu\nu}^{YI} R_{\lambda\sigma}^{XJ} + D_{\mu\nu}^{IJ} P_{\sigma\lambda} \right) \\ &- \frac{1}{2} \sum_{\mu\nu\alpha\beta} S_{\mu\nu}^{[Q]} \tilde{P}_{\mu\alpha} \left(D_{\beta\nu}^{IJ} + D_{\nu\beta}^{IJ} \right) F_{\alpha\beta} - \frac{1}{2} \sum_{\mu\nu\alpha\beta\lambda\sigma} S_{\mu\nu}^{[Q]} \tilde{P}_{\mu\alpha} P_{\nu\beta} \left(D_{\sigma\lambda}^{IJ} + D_{\lambda\sigma}^{IJ} \right) \Pi_{\alpha\lambda\beta\sigma} \\ &- \frac{1}{2} \sum_{\mu\nu\alpha\beta\lambda\sigma} S_{\mu\nu}^{[Q]} \tilde{P}_{\mu\alpha} \left(R_{\nu\beta}^{XI} R_{\sigma\lambda}^{XJ} + R_{\sigma\lambda}^{XI} R_{\nu\beta}^{XJ} + R_{\beta\nu}^{XI} R_{\lambda\sigma}^{XJ} + R_{\lambda\sigma}^{XI} R_{\beta\nu}^{XJ} \right) \Pi_{\alpha\lambda\beta\sigma} \\ &- \frac{1}{2} \sum_{\mu\nu\alpha\beta\lambda\sigma} S_{\mu\nu}^{[Q]} \tilde{P}_{\mu\alpha} \left(R_{\nu\beta}^{YI} R_{\sigma\lambda}^{YJ} + R_{\sigma\lambda}^{YI} R_{\nu\beta}^{YJ} + R_{\beta\nu}^{YI} R_{\lambda\sigma}^{YJ} + R_{\lambda\sigma}^{YI} R_{\beta\nu}^{YJ} \right) \Pi_{\alpha\lambda\beta\sigma} \\ &- \frac{1}{2} \sum_{\mu\nu\alpha\beta\lambda\sigma} S_{\mu\nu}^{[Q]} \tilde{P}_{\mu\alpha} \left(R_{\beta\nu}^{XI} R_{\sigma\lambda}^{YJ} + R_{\sigma\lambda}^{XI} R_{\beta\nu}^{YJ} + R_{\nu\beta}^{XI} R_{\lambda\sigma}^{YJ} + R_{\lambda\sigma}^{XI} R_{\nu\beta}^{YJ} \right) \Pi_{\alpha\lambda\beta\sigma} \\ &- \frac{1}{2} \sum_{\mu\nu\alpha\beta\lambda\sigma} S_{\mu\nu}^{[Q]} \tilde{P}_{\mu\alpha} \left(R_{\beta\nu}^{YI} R_{\sigma\lambda}^{XJ} + R_{\sigma\lambda}^{YI} R_{\beta\nu}^{XJ} + R_{\nu\beta}^{YI} R_{\lambda\sigma}^{XJ} + R_{\lambda\sigma}^{YI} R_{\nu\beta}^{XJ} \right) \Pi_{\alpha\lambda\beta\sigma} \Bigg] \\ &- \frac{1}{E_J - E_I} \sum_{ck} L_{ck}^{IJ} \Theta_{ck}^{[Q]} + \sum_{\mu\nu} S_{\mu\nu}^{A[Q]} G_{\mu\nu}^{IJ} \end{aligned} \tag{6.65}$$

where L^{IJ} is the full orbital response Lagrangian, composed of the contributions from $L^{\mathrm{A},IJ}$ (Eq. 6.49) and $L^{\mathrm{B},IJ}$ (Eq. 6.63). In the basis of atomic orbitals, this term is

$$\begin{aligned} L_{ck}^{IJ} = & \sum_{\mu\nu\lambda\sigma} C_{\lambda c} C_{\sigma k} \left(D_{\mu\nu}^{IJ} + D_{\nu\mu}^{IJ} \right) \Pi_{\mu\lambda\nu\sigma} \\ & + \sum_{a\mu\nu\lambda\sigma} C_{\lambda c} C_{\sigma a} \left(R_{\mu\nu}^{XI} X_k^{Ja} + X_k^{Ia} R_{\mu\nu}^{XJ} + R_{\mu\nu}^{YI} Y_k^{Ja} + Y_k^{Ia} R_{\mu\nu}^{YJ} \right) \Pi_{\mu\lambda\nu\sigma} \\ & - \sum_{i\mu\nu\lambda\sigma} C_{\lambda i} C_{\sigma k} \left(R_{\mu\nu}^{XI} X_i^{Jc} + X_i^{Ic} R_{\mu\nu}^{XJ} + R_{\mu\nu}^{YI} Y_i^{Jc} + Y_i^{Ic} R_{\mu\nu}^{YJ} \right) \Pi_{\mu\lambda\nu\sigma} \\ & + \sum_{a\mu\nu\lambda\sigma} C_{\lambda a} C_{\sigma c} \left(R_{\mu\nu}^{XI} Y_k^{Ja} + X_k^{Ia} R_{\mu\nu}^{YJ} + R_{\mu\nu}^{YI} X_k^{Ja} + Y_k^{Ia} R_{\mu\nu}^{XJ} \right) \Pi_{\mu\lambda\nu\sigma} \\ & - \sum_{i\mu\nu\lambda\sigma} C_{\lambda k} C_{\sigma i} \left(R_{\mu\nu}^{XI} Y_i^{Jc} + X_i^{Ic} R_{\mu\nu}^{YJ} + R_{\mu\nu}^{YI} X_i^{Jc} + Y_i^{Ic} R_{\mu\nu}^{XJ} \right) \Pi_{\mu\lambda\nu\sigma} \end{aligned} \tag{6.66}$$

Eqs. 6.65 and 6.66 represent our final expression for the DC. With the exception of the $S^{A[Q]}$ term, this expression is identical to that obtained from direct differentiation, as shown in Eq. 50 of Ref. 181. Note that the terms containing the antisymmetrized AO overlap gradients ($S^{A[Q]}$) are responsible for a lack of translational invariance in Eq. 6.65. As Ref. 67 shows, by including electron translation factors to account for the momentum experienced by electrons as they follow moving nuclei, we find that $S^{A[Q]}$ terms are entirely eliminated, restoring translational invariance. However, the antisymmetrized overlap gradients are present in finite difference approximations to the derivative coupling, and so must be included for purposes of debugging (though they may be neglected otherwise). For details on how the $S^{A[Q]}$ term in the present work is reconciled with the direct differentiation result, see A.6.

6.4. Results

Eqs. 6.65, 6.66 and A.29 were implemented in a development version of the Q-CHEM software package.[102,158] To evaluate the analytic solution, the direct coupling expression

(Eq. 6.38) was approximated via finite difference (Eq. 6.67).

$$\begin{aligned} d_{IJ}^{\mathrm{TDHF}[Q]} \approx & \langle \Phi_{\mathrm{HF}} \hat{X}^{I\dagger} | \left(| \hat{X}^J \Phi_{\mathrm{HF}} \rangle \right)^{[Q]} - \langle \Phi_{\mathrm{HF}} \hat{Y}^{I\dagger} | \left(| \hat{Y}^J \Phi_{\mathrm{HF}} \rangle \right)^{[Q]} \\ \approx & \frac{\langle \mathcal{X}^I(\mathbf{x}) | \mathcal{X}^J(\mathbf{x}+\mathbf{h}) \rangle - \langle \mathcal{X}^I(\mathbf{x}) | \mathcal{X}^J(\mathbf{x}-\mathbf{h}) \rangle}{2\,|\mathbf{h}|} \\ & - \frac{\langle \mathcal{Y}^I(\mathbf{x}) | \mathcal{Y}^J(\mathbf{x}+\mathbf{h}) \rangle - \langle \mathcal{Y}^I(\mathbf{x}) | \mathcal{Y}^J(\mathbf{x}-\mathbf{h}) \rangle}{2\,|\mathbf{h}|} \end{aligned} \tag{6.67}$$

Here, $\mathbf{x}$ is reference nuclear configuration, and $\mathbf{h}$ is a small perturbation with respect to the degree of freedom Q. We have defined $|\mathcal{X}^I\rangle \equiv |\hat{X}^I \Phi_{\mathrm{HF}}\rangle$ and $|\mathcal{Y}^I\rangle \equiv |\hat{Y}^I \Phi_{\mathrm{HF}}\rangle$ for simplicity.

For our test case, we calculated the derivative couplings between TDHF states S_1, S_4, and S_5 of formaldehyde. Results were generated using the 6-31G* basis set and the HF minimum-energy geometry. Both analytic and finite difference results are summarized in Table 6.3. The analytic results agree with the finite difference values to within $\sim 10^{-4}$ a_0^{-1}, which is the expected precision of the finite difference approximation. It is clear by inspection that these derivative coupling components lack translational invariance. The non-translationally invariant term ($S^{A[Q]}G^{IJ}$, Eqs. 6.65 and A.29) was included in this calculation to match the finite-difference result.

6.5. Discussion and conclusions

By defining pseudo-wavefunctions that approximately correspond to TDHF states, we have been able to develop an analytic expression for derivative couplings between TDHF states in the form of a Hellmann-Feynman expression. Our final expression is similar in form to the corresponding CIS derivative couplings,[67] though there are important differences. In particular, XY coupling appears in the orbital response Lagrangian (Eq. 6.66) that has no CIS counterpart. The derivative couplings calculated according to Eqs. 6.65-6.66 and A.29 agree exactly with a direct differentiation expression (Eq. 6.38), and numerical results match finite difference results to a high degree of precision in practice.

Table 6.3: Derivative coupling between the TDHF excited states S_1, S_4, and S_5 of formaldehyde using the 6-31G* basis set. Results presented for both the finite difference approximation ("FD", Eq. 6.67) and our analytic method (Eq. 6.65). All results are presented in a_0^{-1}. To match finite difference result, the non-translationally invariant term ($S^{A[Q]}G^{IJ}$, Eqs. 6.65 and A.29) was included. For the finite difference calculation, a step size of $\mathbf{h} = 1.89 * 10^{-4}$ a_0 was used. For all degrees of freedom (Q), the analytic result agrees with the finite difference approximation at least to the expected level of accuracy for finite difference, $\sim 10^{-4}$ a_0^{-1}.

Q	S_1-S_4		S_1-S_5		S_4-S_5	
	FD	Analytic	FD	Analytic	FD	Analytic
C_x	0.00000	0.00000	0.00000	0.00000	-0.00005	0.00000
C_y	0.00000	0.00000	-0.76790	-0.76790	0.00000	0.00000
C_z	-0.15739	-0.15741	0.00001	0.00000	1.99752	1.99721
H_{1x}	0.00002	0.00000	0.04297	0.04299	0.00023	0.00000
H_{1y}	0.00001	0.00000	0.08164	0.08162	0.00008	0.00000
H_{1z}	0.07660	0.07660	-0.00001	0.00000	-0.66402	-0.66410
H_{2x}	0.00000	0.00000	-0.04297	-0.04299	-0.00001	0.00000
H_{2y}	0.00000	0.00000	0.08164	0.08162	-0.00003	0.00000
H_{2z}	0.07659	0.07660	0.00000	0.00000	-0.66407	-0.66410
O_x	0.00000	0.00000	0.00000	0.00000	0.00000	0.00000
O_y	0.00000	0.00000	0.35603	0.35599	0.00000	0.00000
O_z	0.02519	0.02514	0.00009	0.00000	-0.65012	-0.65073

6.5.1. Comparison with Chernyak-Mukamel and time-dependent response theory

To further justify our approach to DCs, we would like to compare our expression (Eq. 6.65) with the exact Chernyak-Mukamel formula (Eq. 6.73),[165] which expresses DCs as a function of the transition density matrix in the limit of exact wavefunctions. In such a limit, the basis set is complete, so we may naturally dispense with the Pulay terms ($S^{[Q]}$) and the antisymmetrized AO overlap gradients ($S^{A[Q]}$). Additionally, as noted by Send and Furche,[175,185] the only component of the Hamiltonian that depends on nuclear position (and therefore a finite atom-centered basis) is the nuclear-electronic potential, v; the electron kinetic energy and two-electron operators can therefore also be eliminated. Consequently, in the MO basis, we can write our complete basis DC expression

$$d_{IJ}^{\mathrm{CB}[Q]} = \frac{1}{E_J - E_I} \sum_{pq} v_{pq}^{[Q]} D_{pq}^{IJ} - \frac{1}{E_J - E_I} \sum_{ck} \Theta_{ck}^{[Q]} L_{ck}^{IJ}, \tag{6.68}$$

where the MO-basis difference density matrix[3] is

$$D_{pq}^{IJ} = \begin{cases} -\sum_a \left(X_p^{Ja} X_q^{Ia} + Y_p^{Ia} Y_q^{Ja} \right) & \text{for } p,q \in \text{ Occ} \\ \sum_i \left(X_i^{Ip} X_i^{Jq} + Y_i^{Jp} Y_i^{Iq} \right) & \text{for } p,q \in \text{ Virt} \\ 0 & \text{otherwise} \end{cases} \tag{6.69}$$

and the MO-basis orbital response Lagrangian is

$$\begin{aligned} L_{ck}^{IJ} = & \sum_{pq} \Pi_{pcqk} \left(D_{pq}^{IJ} + D_{qp}^{IJ} \right) \\ & + \sum_{jab} \Big[\Pi_{bcja} \left(X_k^{Ia} X_j^{Jb} + X_j^{Ib} X_k^{Ja} + Y_k^{Ia} Y_j^{Jb} + Y_j^{Ib} Y_k^{Ja} \right) \\ & \qquad + \Pi_{baja} \left(X_k^{Ia} Y_j^{Jb} + X_j^{Ib} Y_k^{Ja} + Y_k^{Ia} X_j^{Jb} + Y_j^{Ib} X_k^{Ja} \right) \Big] \\ & - \sum_{ijb} \Big[\Pi_{bijk} \left(X_i^{Ic} X_j^{Jb} + X_j^{Ib} X_i^{Jc} + Y_i^{Ic} Y_j^{Jb} + Y_j^{Ib} Y_i^{Jc} \right) \\ & \qquad + \Pi_{bkji} \left(X_i^{Ic} Y_j^{Jb} + X_j^{Ib} Y_i^{Jc} + Y_i^{Ic} X_j^{Jb} + Y_j^{Ib} X_i^{Jc} \right) \Big] . \end{aligned} \tag{6.70}$$

Equivalently, we can write

$$d_{IJ}^{\mathrm{CB}[Q]} = \frac{1}{E_J - E_I} \sum_{pq} v_{pq}^{[Q]} \Gamma_{pq}^{IJ}, \tag{6.71}$$

for a matrix $\mathbf{\Gamma}^{IJ}$ given by

$$\Gamma_{pq}^{IJ} = \begin{cases} D_{pq}^{IJ} & \text{for } p,q \in \text{ Occ or } p,q \in \text{ Virt} \\ -\frac{1}{2} \sum_{ai} (A+B)_{pqai}^{-1} L_{ai} & \text{for } p \in \text{ Virt}, q \in \text{ Occ} \\ -\frac{1}{2} \sum_{ai} (A+B)_{qpai}^{-1} L_{ai} & \text{for } p \in \text{ Occ}, q \in \text{ Virt}. \end{cases} \tag{6.72}$$

If we now compare our complete basis DC expression to the Chernyak-Mukamel formula,

$$d_{IJ}^{\mathrm{CM}[Q]} = \frac{1}{E_J - E_I} \sum_{pq} v_{pq}^{[Q]} \gamma_{pq}^{IJ}, \tag{6.73}$$

[3]This matrix can be recovered using the pseudo-wavefunctions described in Section 6.36.3.2 acting on a single-electron density operator, $D_{pq}^{IJ} \approx \langle \Psi_I | \hat{a}_p^\dagger \hat{a}_q | \Psi_J \rangle$.

it is clear that, if our pseudo-wavefunction approach is meaningful, $\mathbf{\Gamma}^{IJ}$ from Eq. 6.72 should correspond to γ^{IJ}, the exact transition density matrix. According to response theory [186,187] the exact transition density matrix between states I and J is

$$\gamma_{pq}^{IJ} = \begin{cases} D_{pq}^{IJ} & \text{for } p,q \in \text{ Occ or } p,q \in \text{ Virt} \\ \gamma_{pq}^{(1),IJ} & \text{for } p \in \text{ Virt, } q \in \text{ Occ} \\ \gamma_{pq}^{(2),IJ} & \text{for } p \in \text{ Occ, } q \in \text{ Virt.} \end{cases} \tag{6.74}$$

The occupied-virtual components of γ^{IJ} are obtained by solving

$$\left[\begin{pmatrix} \mathbf{A} & \mathbf{B} \\ \mathbf{B} & \mathbf{A} \end{pmatrix} + (E_J - E_I) \begin{pmatrix} \mathbf{I} & 0 \\ 0 & -\mathbf{I} \end{pmatrix} \right] \begin{pmatrix} \gamma^{(1),IJ} \\ \gamma^{(2),IJ} \end{pmatrix} = - \begin{pmatrix} \mathbf{L}^{(1),IJ} \\ \mathbf{L}^{(2),IJ} \end{pmatrix}, \tag{6.75}$$

where $\mathbf{I}$ is the identity matrix,

$$\begin{aligned} L_{ck}^{(1),IJ} = & \sum_{pq} \Pi_{pcqk} D_{pq}^{IJ} \\ & + \sum_{jab} \left[\Pi_{bcja} \left(X_k^{Ia} X_j^{Jb} + Y_j^{Ib} Y_k^{Ja} \right) + \Pi_{bajc} \left(X_j^{Ib} Y_k^{Ja} + X_k^{Ia} Y_j^{Jb} \right) \right] \\ & - \sum_{ijb} \left[\Pi_{bijk} \left(X_i^{Ic} X_j^{Jb} + Y_j^{Ib} Y_i^{Jc} \right) + \Pi_{bkji} \left(X_j^{Ib} Y_i^{Jc} + X_i^{Ic} Y_j^{Jb} \right) \right], \end{aligned} \tag{6.76}$$

and

$$\begin{aligned} L_{ck}^{(2),IJ} = & \sum_{pq} \Pi_{pcqk} D_{qp}^{IJ} \\ & + \sum_{jab} \left[\Pi_{bcja} \left(X_j^{Ib} X_k^{Ja} + Y_k^{Ia} Y_j^{Jb} \right) + \Pi_{bajc} \left(Y_j^{Ib} X_k^{Ja} + Y_k^{Ia} X_j^{Jb} \right) \right] \\ & - \sum_{ijb} \left[\Pi_{bijk} \left(X_j^{Ib} X_i^{Jc} + Y_i^{Ic} Y_j^{Jb} \right) + \Pi_{bkji} \left(Y_j^{Ib} X_i^{Jc} + Y_i^{Ic} X_j^{Jb} \right) \right]. \end{aligned} \tag{6.77}$$

The key point to notice is that $L_{ck}^{IJ} = L_{ck}^{(1),IJ} + L_{ck}^{(2),IJ}$. Furthermore, in the limit of an excited state crossing, where $(E_J - E_I) \to 0$, it follows that

$$\left(\gamma_{ai}^{(1),IJ} + \gamma_{ia}^{(2),IJ}\right) = -\sum_{jb} (A+B)_{aibj}^{-1} L_{jb}^{IJ}. \tag{6.78}$$

Thus, in the end, we may conclude that whenever the state energy difference $(E_J - E_I) \ll E_1$, where E_1 is the lowest TDHF/TDDFT excitation energy, we recover the Chernyak-Mukamel formula, $d_{IJ}^{\mathrm{CB}[Q]} = d_{IJ}^{\mathrm{CM}[Q]}$. Therefore our DCs agree with response theory in the limit of an excited state crossing. Altogether, this analysis provides further evidence of the reliability of the approximations made in the present work.

6.5.2. Future work

Although our approach is able to recover the Chernyak-Mukamel formula for TDHF DCs, the reader may still ask him or herself whether our intuitive pseudo-wavefunctions can be entirely trusted in practice. After all, we have made several approximations along the way, most notably the assumption of small Y amplitudes. To convince the reader of the reliability of Eqs. 6.65-6.66, in Ref. 181 we show that our derivative coupling expression displays the correct behavior near conical intersections. In particular, the DCs in Eqs. 6.65-6.66 recover the correct branching plane and Berry's phase behavior, which provide yet another crucial piece of empirical evidence that our approach captures the correct physics underlying the derivative couplings between TDHF or, equivalently, TDDFT states. In the future, it will be interesting to compare our derivative couplings with derivative couplings derived entirely from response theory. Li and Liu[176] have recently made such a comparison in the abstract, but no practical or numerical examples have yet been published. Looking forward, there are many possible applications for our model of pseudo-wavefunctions, including the construction of locally diabatized states[52,55,57,64,85] and nonadiabatic dynamics.

6.6. Acknowledgments

This work was supported by NSF CAREER Grant CHE-1150851. J.E.S. acknowledges an Alfred P. Sloan Research Fellowship and a David & Lucile Packard Fellowship. JES thanks Filipp Furche for very stimulating conversations and his suggestion to compare our results with the Chernyak-Mukamel formalism.

CHAPTER 7 : Exploring Non-Condon Effects in a Covalent Tetracene Dimer: How Important are Vibrations in Determining the Electronic Coupling for Singlet Fission?

This chapter was adapted from Ref. 188.

7.1. Introduction

Interest in achieving third-generation solar energy conversion[189] – where the ratio of efficiency versus cost would exceed that achieved in single junction crystalline and thin-film devices – has reinvigorated the exploration of organic material photophysics characterized by the fission of photo-produced singlet exciton states into singlet-coupled pairs of triplets.[6,7] This so-called singlet fission (SF) offers opportunities to process bluer solar photons into charge carriers with a quantum yield larger than one and properly designed devices that exploit SF may in principle exceed the Shockley-Quiesser limit[190] that bounds single junction devices.[191] While significant constraints on state energetics – where most importantly $E_{\text{singlet}} \approx 2E_{\text{triplet}}$ – limit the space of available chromophores that can engage in SF, it is nonetheless the case that marked advances have occurred in recent years within several chromophore platforms that include polyacenes,[192–199] isobenzofurans,[200–203] carotenoids and polyenes,[204,205] and diimides,[206] as well as within device settings.[197,207,208] Recent advances have also occurred in theoretical treatments of SF mechanism and state energetics although important debates remain.[1–3,7,209–221] It is in this mechanistic landscape that attention is focused in this current study.

The role of nuclear conformation as well as dynamics in the process of SF remains a topic of great interest and significant discussion. Nuclear conformation is central to electronic coupling between states involved in the initial photoreaction[196,202,203,205,206,222] and arises naturally in electronic structure explorations of SF as electronic couplings can vary greatly due to orbital phase and constructive or destructive interference (that depends on nuclear geometry).[5–7,214,215,219,223] Dynamics have been explored directly[1,2,209,215,223–225] under

the approximation that all fluctuations (modulating the energy of relevant states as well as the coupling between them) are harmonic and can be captured by a spectral density. Dynamical effects can also be inferred indirectly in electronic structure work that attempts to calculate global potential energy surfaces along relevant nuclear coordinates for states involved in the photoreaction.[3,214,216,220,226–228]

In some systems, such as crystalline tetracene (Tc), the role of nuclear motions in the mechanism of SF, particularly the initial events following photoexcitation, remains debated despite the long history of exploration for SF. We have observed, using laser pulse shaping experiments, significant sensitivity of fission yield to low frequency intermolecular phonon modes.[229] On the one hand, these experimental observations might be partly supported by restricted-active-space (RAS) calculations by Zimmerman and coworkers who have observed evidence for endoergic SF and a decreasing of the energy gap between the lowest energy adiabatic bright singlet exciton state and the dark multi-exciton state along an intermolecular (between Tc monomers) coordinate.[216,227] Assuming that C-C stretches are also a meaningful nuclear coordinate promoting state mixing, one might then conclude that there are at least two important motions in the SF process – it is possible that fluctuations in the intermolecular coordinate are experimentally observed. On the other hand, recent electronic structure work by Yost and coworkers[211] that attempts to tie together a broad swath of experimental data, suggests electronic coupling is well above k_BT at room temperature and that SF in crystalline Tc should occur in the adiabatic Marcus limit. In such a case, the dependence of electronic coupling on nuclear coordinates is weak and one might argue that one reaction coordinate is sufficient.[1] [230–232] Finally however, recent high level electronic structure calculations by Parker and coworkers[210] find electronic coupling between diabatic reactants and products states that is smaller than Yost and coworkers[211]

[1] Interestingly, this work as well as the work mentioned above by Zimmerman and co-workers (cf. Ref 227) is at odds with interpretations of temperature-independent spectroscopic data (cf. Refs. 230–232) where, for example based on transient absorption studies, it has been suggested that SF in Tc occurs between isoenergetic reactant and product states via vibronic tunneling in the limit of small electronic coupling (cf. Ref. 230). We will not consider such vibronic tunneling here, but in this context intermolecular motions might play some role mediating a tunneling barrier.

but still significantly larger than one might expect for a low coupling limit.[230] As we will discuss briefly, although not the main focus of this manuscript, our simple methods allow for calculation of electronic coupling with good agreement to Parker and coworkers.[210] This may be useful in future calculations of dynamics in the vein of theory by Berkelbach, Hybertson, and Reichman[1,2] and in this context, it would be interesting to take into account – via the spectral density – how phonon modes impact yields of single fission.

Molecular dimers for SF, that are of interest to our group, are expected to have significant sensitivity towards molecular vibration in their photoreaction rates. In very general terms, dimers present useful platforms for the study of SF mechanism[5,222,233] (a key point in this manuscript) but may also play an important role in future devices based on dye-sensitized solar cell technologies.[6,191] We have been interested in a series of dimers that juxtapose Tc monomer units in partially co-facial orientation via norbornyl bridges of varying size (see Fig. 7.23 for the smallest of these). The dimers are inspired by naphthalene analogues explored by Paddon-Row and coworkers that show elegant control of exciton splitting as a function of bridge size.[234] In recent DFT and TD-DFT computational work by the Damrauer group, it was established that these systems have excited state energetic properties suitable for SF.[5] Further, the molecules[5] show, particularly the dimer BT1 with the smallest bridge, significant electronic communication between tetracene units as measured by calculation of Davydov splitting and quantification of so-called electron transfer integrals that impact splittings of canonical orbitals (HOMO versus HOMO-1 and LUMO versus LUMO+1; vide infra). To achieve efficient SF, however, there are stringent demands on inter-chromophore electronic coupling beyond what is needed for energy or electron transfer. As we have shown previously[5] and explore more extensively in this chapter, orbital symmetry arguments show us that SF pathways will vanish in the limit that certain symmetry elements of these molecules[5] are preserved.

The essence of this manuscript is to establish – with BT1 as a test case – the order of magnitude of electronic coupling for singlet fission that will arise as molecular vibrations

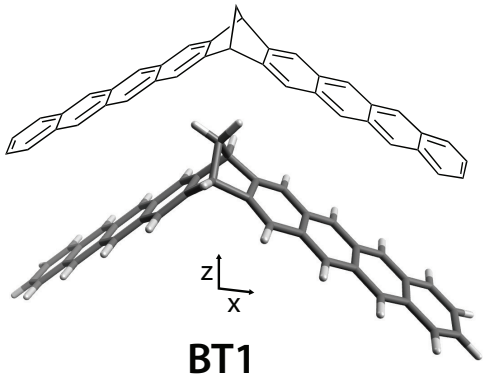

Figure 7.23: Two representations of the tetracene dimer BT1. The molecular structure comes from a geometry optimization calculation using the ωB97X-D density functional, the 6-31G(d) basis set, and a polarizable continuum model of solvent parameterized for toluene.[5] For the group theory analyses that follow, the molecule (C_{2v} point group) is aligned with the xz plane as shown.

occur and to speculate on the possibility of SF. To approach this we first establish the basis of a frontier orbital model that we will use to approximate coupling magnitudes in section 7.2.1. In section 7.2.2, we describe protocols for converting delocalized canonical orbitals within dimer molecules into a set of diabatic one-electron wave functions. These localized orbitals are in essence frontier orbitals on each chromophore of the dimer. Such functions and their couplings are essential ingredients in approximate expressions for electronic coupling between reactant and product excited states during SF. In section 7.3.1, we first illustrate the orbital localization procedure for the case of BT1, and then establish that the couplings that arise from this description of the orbitals are comparable to those produced with Berkelbach et al. in the case of a non-covalent Tc dimer. In section 7.3.2, we calculate gradients for these one-electronic couplings and look at projections into the directions of the normal modes of vibrational motion for BT1. Rules emerge about the types of motion (irreducible representations in C_{2v} symmetry) that permit electronic coupling necessary for SF. We then calculate the magnitude of electronic coupling that emerges during root-mean-squared (RMS) motions of the molecule at room temperature along these relevant modes. In section 7.3.3, we give a very rough error analysis of our diabatization formalism. Finally, in section 7.3.4, we estimate an overall effective coupling value for SF in BT1 based on

Stuchebrukhov's model Hamiltonian for inelastic tunneling in a fluctuating medium. We summarize our findings and conclude in section 7.4.

7.2. Theory

7.2.1. Frontier molecular orbital theory for singlet fission

In recent electronic structure treatments of SF in Class I systems, it has been common to focus on dimer structures relevant to crystalline systems and to utilize a simple frontier-orbital basis set (HOMO and LUMO on each of the two chromophores A and B; referred to later as $|h_A\rangle$, $|l_A\rangle$, $|h_B\rangle$, and $|l_B\rangle$) to describe the electronic states that are involved in the nascent photoreaction within the singlet manifold, prior to dissociation and dephasing of the two triplets (see cartoon in Fig. 7.24).[1–3,6,213–215,219,224,233] The four-orbital basis is able to capture the essential electronic structure of five relevant diabatic states: the Frenkel exciton reactant states (S_1S_0 and S_0S_1 or superpositions of these), the charge transfer states (^{1}CA and ^{1}AC; where A refers to anion and C refers to cation), and the multiexciton product state (^{1}TT).[2] Further, the use of this basis is justified, particularly in polyacene systems, by a significant energy gap between the HOMO-1 and lower energy occupied molecular orbitals and between the LUMO+1 and higher energy unoccupied orbitals.[3]

The process of constructing the HOMO and LUMO for each chromophore can be accomplished by using the corresponding molecular orbitals of the chromophores as isolated molecules, as in the Hartree-Fock method described by Berkelbach, Hybertson, and Reichman (HF-BHR).[2] In bridged systems, however, obtaining a MO description of the isolated chromophores is no longer trivial. In the current manuscript, we instead apply a unitary transformation to the canonical MOs of the entire system to produce a localized frontier orbital representation, a process that can be equivalently applied to both intermolecular

[2]The notation that is used here for diabatic states relates to the monomer units A and B in that order. So, for example, S_1S_0 means that unit A is in the first excited singlet state while B is in the ground state. As a further example, ^{1}CA means that monomer A is oxidized (cationic) while monomer B is reduced (anionic).

[3]Of course, such an orbital description ignores any and all effects of electron correlation so that, for accuracy, this approach will necessary rely on a fortuitous cancellation of errors, which holds quite often.

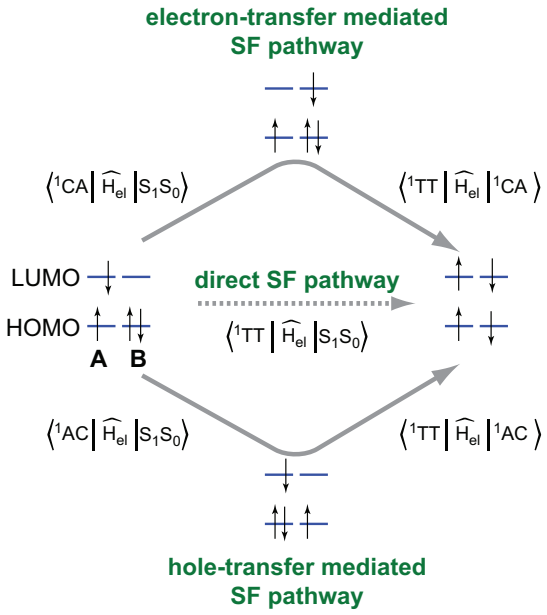

Figure 7.24: Cartoon showing coupling pathways for SF from S_1S_0 to ^{1}TT and how these would relate to one-electron configurations in a frontier orbital active space consisting of HOMO and LUMO on chromophores A and B. This figure is adapted from Refs. 6,7.

and intramolecular systems. This procedure is described in greater detail in section 7.2.2.

In generalized rate expressions that emerge from the frontier orbital description,[2,6,7] the electronic coupling (squared) between reactants and product states (from S_1S_0 or S_0S_1 to ^{1}TT) is an essential ingredient. These states may, in principle, couple directly via a Coulomb operator, however, in many systems the matrix elements describing this are small in magnitude and direct pathways (see Fig. 7.24) for SF are expected to have limited mechanistic importance.[2,7,209] We will test this assumption for BT1 as described more later. An alternative route for reactant and product electronic coupling is so-called mediated via participation of charge transfer (CT) excited states (again see Fig. 7.24). In crystalline polyacene systems[3,210,211,214] as well as within our series of dimers,[5] the CT states are higher in energy than either the singlet exciton reactant or the ^{1}TT product. The CT states may therefore participate in coupling for SF via superexchange.[2] Berkelbach and coworkers have shown an expression for a Frenkel exciton to first order in coupling to CT states as well as for the ^{1}TT to first order in coupling to CT states.[2] From these, under the assumptions that (i) direct singlet exciton to ^{1}TT coupling (either S_1S_0 or S_0S_1 to ^{1}TT) can

be ignored, that (ii) $E(\mathrm{CT}) - E(\mathrm{S_1S_0}$ or $\mathrm{S_0S_1}) \approx E(\mathrm{CT}) - E(^1\mathrm{TT}) = \Delta E_{\mathrm{CT}}$, and that (iii) we are in the nonadiabatic regime, a Marcus-like rate constant expression for conversion to $\left|^1\mathrm{TT}\right\rangle$ from a singlet exciton $\left|^1\mathrm{EX}\right\rangle$ (equal to either $|\mathrm{S_1S_0}\rangle$ or $|\mathrm{S_0S_1}\rangle$) can be written in the following way:

$$k_{\mathrm{SF}} \approx \frac{2\pi}{\sqrt{4\pi\hbar^2\lambda k_{\mathrm{B}}T}} \frac{1}{\Delta E_{\mathrm{CT}}^2} \left| \left\langle {}^1\mathrm{TT}|\hat{H}_{\mathrm{el}}|{}^1\mathrm{CA}\right\rangle \left\langle {}^1\mathrm{CA}|\hat{H}_{\mathrm{el}}|{}^1\mathrm{EX}\right\rangle + \left\langle {}^1\mathrm{TT}|\hat{H}_{\mathrm{el}}|{}^1\mathrm{AC}\right\rangle \left\langle {}^1\mathrm{AC}|\hat{H}_{\mathrm{el}}|{}^1\mathrm{EX}\right\rangle \right|^2 \times \exp\left(-\frac{(\Delta G_{\mathrm{rxn}} + \lambda)^2}{4\lambda k_{\mathrm{B}}T}\right) \tag{7.1}$$

$$\begin{aligned}
\left\langle {}^1\mathrm{TT}\right| \hat{H}_{\mathrm{el}} \left|{}^1\mathrm{CA}\right\rangle &= \sqrt{\frac{3}{2}} \left(\langle \mathrm{l_A}| \hat{F} |\mathrm{h_B}\rangle + \langle \mathrm{l_A l_B}|\mathrm{h_B l_B}\rangle - \langle \mathrm{l_A h_A}|\mathrm{h_B h_A}\rangle \right) \\
\left\langle {}^1\mathrm{TT}\right| \hat{H}_{\mathrm{el}} \left|{}^1\mathrm{AC}\right\rangle &= \sqrt{\frac{3}{2}} \left(\langle \mathrm{h_A}| \hat{F} |\mathrm{l_B}\rangle + \langle \mathrm{l_B l_A}|\mathrm{h_A l_A}\rangle - \langle \mathrm{l_B h_B}|\mathrm{h_A h_B}\rangle \right) \\
\left\langle {}^1\mathrm{CA}\right| \hat{H}_{\mathrm{el}} |\mathrm{S_1S_0}\rangle &= \langle \mathrm{l_A}| \hat{F} |\mathrm{l_B}\rangle + 2\langle \mathrm{h_A l_A}|\mathrm{l_B h_A}\rangle - \langle \mathrm{h_A l_A}|\mathrm{h_A l_B}\rangle \\
\left\langle {}^1\mathrm{CA}\right| \hat{H}_{\mathrm{el}} |\mathrm{S_0S_1}\rangle &= -\langle \mathrm{h_A}| \hat{F} |\mathrm{h_B}\rangle + 2\langle \mathrm{h_B l_B}|\mathrm{l_B h_A}\rangle - \langle \mathrm{h_B l_B}|\mathrm{h_A l_B}\rangle \\
\left\langle {}^1\mathrm{AC}\right| \hat{H}_{\mathrm{el}} |\mathrm{S_1S_0}\rangle &= -\langle \mathrm{h_A}| \hat{F} |\mathrm{h_B}\rangle + 2\langle \mathrm{h_A l_A}|\mathrm{l_A h_B}\rangle - \langle \mathrm{h_A l_A}|\mathrm{h_B l_A}\rangle \\
\left\langle {}^1\mathrm{AC}\right| \hat{H}_{\mathrm{el}} |\mathrm{S_0S_1}\rangle &= \langle \mathrm{l_A}| \hat{F} |\mathrm{l_B}\rangle + 2\langle \mathrm{h_B l_B}|\mathrm{l_A h_B}\rangle - \langle \mathrm{h_B l_B}|\mathrm{h_B l_A}\rangle \\
\left\langle {}^1\mathrm{TT}\right| \hat{H}_{\mathrm{el}} |\mathrm{S_1S_0}\rangle &= \sqrt{\frac{3}{2}} \left(\langle \mathrm{l_A l_B}|\mathrm{h_B l_A}\rangle - \langle \mathrm{h_A h_B}|\mathrm{l_B h_A}\rangle \right) \\
\left\langle {}^1\mathrm{TT}\right| \hat{H}_{\mathrm{el}} |\mathrm{S_0S_1}\rangle &= \sqrt{\frac{3}{2}} \left(\langle \mathrm{l_B l_A}|\mathrm{h_A l_B}\rangle - \langle \mathrm{h_B h_A}|\mathrm{l_A h_B}\rangle \right)
\end{aligned} \tag{7.2}$$

The matrix elements within the square coupling component of this rate constant may be expressed in the frontier orbital basis with one-electron off-diagonal elements of the Fock matrix and with two-electron Coulomb repulsion terms. The full expressions have been previously derived[1,6] and are shown in Eq. 7.2. For many systems described in the literature, for example crystalline polyacenes, the two-electron Coulomb terms are small and reasonably neglected.[2,7,235] We will take the same approach here and justify this

approximation later in the chapter. Neglecting these terms according to Eq. 7.3,[2,6]

$$\begin{aligned}
\left\langle {}^1\mathrm{TT}|\hat{H}_{\mathrm{el}}|{}^1\mathrm{CA}\right\rangle &\approx \sqrt{3/2}\left\langle l_{\mathrm{A}}|\hat{F}|h_{\mathrm{B}}\right\rangle = \sqrt{3/2}t_{\mathrm{LH}} \\
\left\langle {}^1\mathrm{TT}|\hat{H}_{\mathrm{el}}|{}^1\mathrm{AC}\right\rangle &\approx \sqrt{3/2}\left\langle h_{\mathrm{A}}|\hat{F}|l_{\mathrm{B}}\right\rangle = \sqrt{3/2}t_{\mathrm{HL}} \\
\left\langle {}^1\mathrm{CA}|\hat{H}_{\mathrm{el}}|\mathrm{S_0S_1}\right\rangle &\approx -\left\langle h_{\mathrm{A}}|\hat{F}|h_{\mathrm{B}}\right\rangle = -t_{\mathrm{HH}} \\
\left\langle {}^1\mathrm{AC}|\hat{H}_{\mathrm{el}}|\mathrm{S_1S_0}\right\rangle &\approx -\left\langle h_{\mathrm{A}}|\hat{F}|h_{\mathrm{B}}\right\rangle = -t_{\mathrm{HH}} \\
\left\langle {}^1\mathrm{AC}|\hat{H}_{\mathrm{el}}|\mathrm{S_0S_1}\right\rangle &\approx \left\langle l_{\mathrm{A}}|\hat{F}|l_{\mathrm{B}}\right\rangle = t_{\mathrm{LL}} \\
\left\langle {}^1\mathrm{CA}|\hat{H}_{\mathrm{el}}|\mathrm{S_1S_0}\right\rangle &\approx \left\langle l_{\mathrm{A}}|\hat{F}|l_{\mathrm{B}}\right\rangle = t_{\mathrm{LL}}
\end{aligned} \tag{7.3}$$

expressions for electronic coupling emerge that are relevant for conversion from $|\mathrm{S_0S_1}\rangle$ to $\left|{}^1\mathrm{TT}\right\rangle$ (Eq. 7.4) and from $|\mathrm{S_1S_0}\rangle$ to $\left|{}^1\mathrm{TT}\right\rangle$ (Eq. 7.5).

$$\begin{aligned}
&\frac{1}{\Delta E_{\mathrm{CT}}}\left|\left\langle {}^1\mathrm{TT}|\hat{H}_{\mathrm{el}}|{}^1\mathrm{AC}\right\rangle\left\langle {}^1\mathrm{AC}|\hat{H}_{\mathrm{el}}|\mathrm{S_0S_1}\right\rangle + \left\langle {}^1\mathrm{TT}|\hat{H}_{\mathrm{el}}|{}^1\mathrm{CA}\right\rangle\left\langle {}^1\mathrm{CA}|\hat{H}_{\mathrm{el}}|\mathrm{S_0S_1}\right\rangle\right| \\
&\qquad = \sqrt{\frac{3}{2}}\frac{|t_{\mathrm{HL}}t_{\mathrm{LL}} - t_{\mathrm{LH}}t_{\mathrm{HH}}|}{\Delta E_{\mathrm{CT}}}
\end{aligned} \tag{7.4}$$

$$\begin{aligned}
&\frac{1}{\Delta E_{\mathrm{CT}}}\left|\left\langle {}^1\mathrm{TT}|\hat{H}_{\mathrm{el}}|{}^1\mathrm{CA}\right\rangle\left\langle {}^1\mathrm{CA}|\hat{H}_{\mathrm{el}}|\mathrm{S_1S_0}\right\rangle + \left\langle {}^1\mathrm{TT}|\hat{H}_{\mathrm{el}}|{}^1\mathrm{AC}\right\rangle\left\langle {}^1\mathrm{AC}|\hat{H}_{\mathrm{el}}|\mathrm{S_1S_0}\right\rangle\right| \\
&\qquad = \sqrt{\frac{3}{2}}\frac{|t_{\mathrm{HL}}t_{\mathrm{LL}} - t_{\mathrm{LH}}t_{\mathrm{HH}}|}{\Delta E_{\mathrm{CT}}}
\end{aligned} \tag{7.5}$$

These matrix elements will be used in what follows for comparative discussions of electronic coupling in a Tc dimer system relevant for the molecular crystal and in BT1 under conditions relevant for vibrational motion.

7.2.2. Computational details: Boys localization

All vibrational analyses and coupling element calculations employed a modified version of the Q-CHEM software package,[102,158] were performed with the ωB97X-D density functional,[236] and utilized the 6-31G(d) basis set. This functional was chosen to be consistent with our previous work where we note that ωB97X-D outperforms B3LYP particularly in describing singlet excited state energies.[5] For a comparison of coupling values obtained

with different functionals for two different systems (BT1 and a noncovalent Tc dimer) see Tables 7.7 and 7.8. Orbital couplings were calculated by applying Boys localization [58,59,61] to the HOMO-1, ..., LUMO+1 subspace of molecular orbitals. The resulting Boys-localized molecular orbital coefficients (C') are the result of a unitary transformation of the canonical molecular orbital subspace (C),

$$C'_{\mu p} = \sum_r C_{\mu r} U_{rp} \tag{7.6}$$

where the transformation matrix $\mathbf{U}$ is chosen such that it maximizes the Boys function (f_{Boys}), given by

$$f_{\text{Boys}}(\mathbf{U}) = \sum_{pq} \left| \left\langle \phi_p | \hat{X} | \phi_p \right\rangle - \left\langle \phi_q | \hat{X} | \phi_q \right\rangle \right|^2 \tag{7.7}$$

where $\hat{X}$ is the vectorized dipole operator and $|\phi_p\rangle$ is the p^{th} molecular orbital. The four resulting Boys-localized orbitals are then block diagonalized, so that the two-orbital subspaces on each chromophore are not coupled by the Fock operator. The orbitals resulting from this last transformation correspond to two HOMO/LUMO pairs, each localized to a single chromophore. Using this transformed molecular orbital basis, the Fock matrix is obtained according to

$$F'_{pq} = \sum_{\mu\nu} C'_{\mu p} F_{\mu\nu} C'_{\nu q} = \sum_{rs} U_{pr} F_{rs} U_{sq} \tag{7.8}$$

The Coulombic repulsion terms were obtained by contracting the full AO-basis two-electron integral ($\langle \mu\lambda | \nu\sigma \rangle$) with densities given by $D'^{pr}_{\lambda\sigma} = C'_{\lambda a} C'_{\sigma s}$, so that a single element of the two-electron integral tensor is obtained in the desired basis,

$$\langle pq | rs \rangle' = \sum_{\mu\nu\lambda\sigma} D'^{pr}_{\mu\nu} \langle \mu\lambda | \nu\sigma \rangle D'^{qs}_{\lambda\sigma} \tag{7.9}$$

It is worth emphasizing that the resulting localized MO coefficients are obtained entirely from the transformation of the canonical MO coefficients from the full-system calculation; separate calculations for isolated chromophores are not necessary. Furthermore, this approach is identical for covalent and non-covalent systems.

7.3. Results and Discussion

7.3.1. Demonstrations of the Boys Method for Calculating One-Electron Coupling Matrix Elements

The covalently-bridged dimer BT1

In BT1 we take a four-orbital active space approach as described in section 7.2.2. The starting place is four canonical Kohn-Sham orbitals for this system: $|H-1\rangle$, $|H\rangle$, $|L\rangle$, and $|L+1\rangle$. As expected, each is delocalized over the full π system of the molecule (Fig. 7.26 (left)). The energy gap from $|H-1\rangle$ to$|H-2\rangle$ (not shown) is 1280 meV and the energy gap from $|L+1\rangle$ to $|L+2\rangle$ (not shown) is 1390 meV. It is natural to consider BT1 as being comprised of two covalently coupled Tc subunits and from this perspective $|H-1\rangle$ and $|H\rangle$ give the appearance, respectively, of in-phase and out-of-phase superpositions of the familiar nodal pattern of the Tc monomer HOMO (see Fig. 7.25). An analogous statement can be made for and in reference to the Tc LUMO.

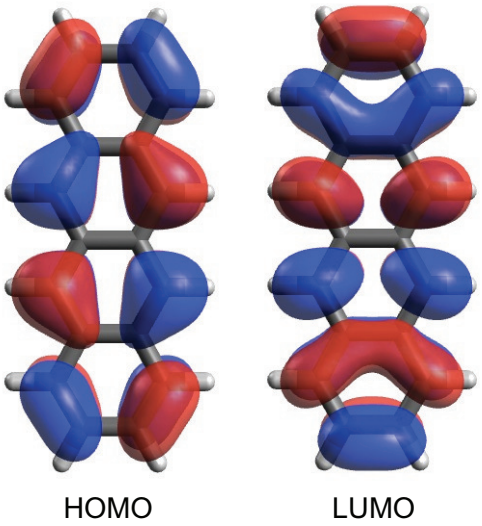

Figure 7.25: Frontier orbitals for monomeric tetracene.

Also shown in Fig. 7.26 (left) is a subset of the Fock matrix inclusive of the frontier orbital basis with values reported in meV. For symmetric systems, in the limit where a one-electron

Hamiltonian is accurate, one half the energy splitting between occupied orbitals and between unoccupied orbitals is exactly equal to the electron transfer integrals T_{HT} and T_{ET}, respectively, as has been described extensively in literature focusing on donor/acceptor interactions between alkyl-separated π systems.[237,238] The quantities $|T_{HT}| = 63.5$ meV and $|T_{ET}| = 141$ meV are relevant for hole-transfer and electron-transfer pathways, respectively, coupling the two tetracene subunits in BT1.[5]

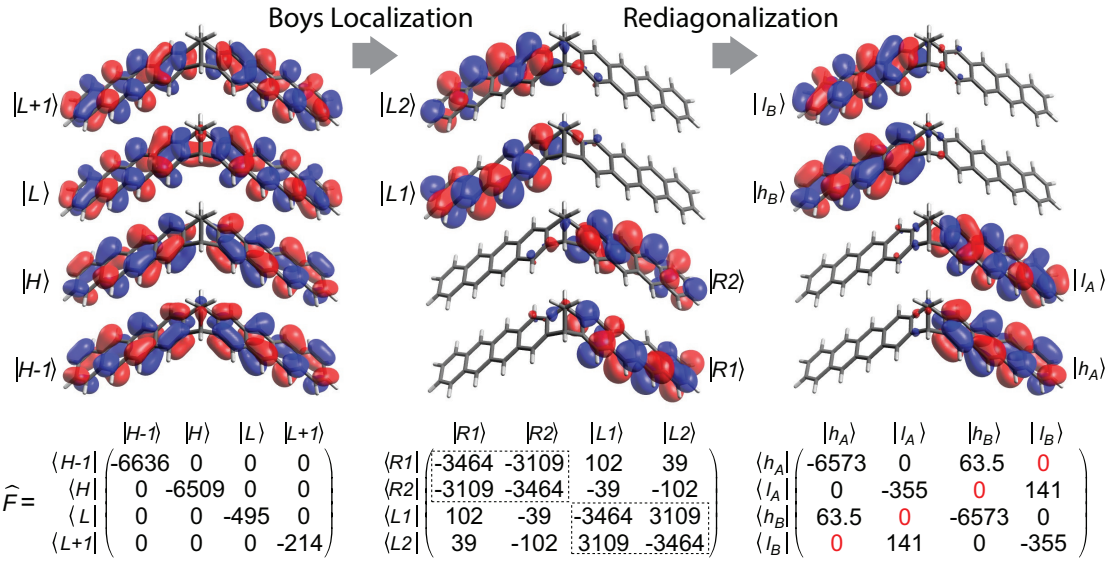

Figure 7.26: Localized frontier orbitals needed to calculate one-electron coupling matrix elements are obtained according to the depicted schematic. Starting with a four canonical-orbital basis set (left) consisting of two highest occupied orbitals ($|\mathrm{H}-1\rangle$ and $|\mathrm{H}\rangle$) and two lowest unoccupied orbitals ($|\mathrm{L}\rangle$ and $|\mathrm{L}+1\rangle$), Boys localization leads to four iso-energetic (in this symmetrical case) orbitals (middle) two of which are localized to the right side of the molecule ($|\mathrm{R1}\rangle$ and $|\mathrm{R2}\rangle$) and two of which are localized to the left ($|\mathrm{L1}\rangle$ and $|\mathrm{L2}\rangle$). Rediagonalization of subspaces relevant for the left and right sides of the molecule, respectively, leads (right) to the localized frontier orbitals $|\mathrm{h_A}\rangle$, $|\mathrm{l_A}\rangle$, $|\mathrm{h_B}\rangle$, and $|\mathrm{l_B}\rangle$, where A and B refer to the right and left sides of the molecule as depicted and where h and l refer to HOMO and LUMO. The representative Fock matrices for each of these three steps are also shown with the third one (right) showing orbital couplings relevant for the SF model that ignores two-electron terms. In the right-most Fock matrix, the black zeros are a result of the diagonalization whereas the red zeros are a manifestation of the symmetry. Orbital images were generated using the free visualization tool Avogadro (version 1.1.1).[8]

As discussed in the introductory comments, we have sought the simplest method for calculating one-electron matrix elements describing orbital couplings between chromophoric

subunits within dimeric molecules. To construct localized diabatic orbitals starting from the canonical frontier orbitals, we apply a unitary transformation based on Boys localization, (as described in section 7.2.2.[58,59,61]). As can be seen in Fig. 7.26 (middle) this produces a set of four orthonormal MOs of identical energy, two of which, $|R1\rangle$ and $|R2\rangle$ are localized to the right side of BT1 and two of which, $|L1\rangle$ and $|L2\rangle$, are localized to the left side. As can be seen in the Fock matrix, there are very significant off-diagonal energy couplings between pairs of orbitals on either side of the molecule (e.g., $\left|\left\langle R1|\hat{F}|R2\right\rangle\right| = \left|\left\langle L1|\hat{F}|L2\right\rangle\right| = 3109$ meV) whereas off-diagonal couplings between left and right orbitals are small and of order 100 meV.

With these localized MOs it is now straightforward to obtain a HOMO/LUMO set for each of the chromophoric sides of the molecule by focusing on diagonalization in the two 2×2 subspaces that are represented by the dotted-line boxes in Fig. 7.26 (middle), as suggested in a very similar context by Cave and Newton.[55] This is achieved by the application of two Givens rotation matrices, each with a dimension NBasis $\times$ NBasis (where, NBasis = 4) but each as the identity other that the 2×2 subspace on which it is acting. The procedure results in four new MOs as seen in Fig. 7.26 (right). For each side of the dimer (labeled A versus B) a HOMO/LUMO set is generated with the expected nodal patterns relative to monomeric Tc (again, see Fig. 7.25) and with no energy couplings between HOMO and LUMO – e.g., $\left\langle h_{\mathrm{A}}|\hat{F}|l_{\mathrm{A}}\right\rangle = \left\langle h_{\mathrm{B}}|\hat{F}|l_{\mathrm{B}}\right\rangle = 0$. Critically, however, off-diagonal matrix elements exposing energy couplings between orbitals across the dimer are permitted. As shown in the Fock matrix of Fig. 7.26 (right), $\left\langle h_{\mathrm{A}}|\hat{F}|h_{\mathrm{B}}\right\rangle = t_{\mathrm{HH}} = 63.5$ meV and $\left\langle l_{\mathrm{A}}|\hat{F}|l_{\mathrm{B}}\right\rangle = t_{\mathrm{LL}} = 141$ meV, both values identical to the magnitudes $|T_{\mathrm{HT}}|$ and $|T_{\mathrm{ET}}|$ obtained from splittings within the canonical orbitals (vide supra). As expected from symmetry considerations, both matrix elements $\left\langle h_{\mathrm{A}}|\hat{F}|l_{\mathrm{B}}\right\rangle = t_{\mathrm{HL}}$ and $\left\langle l_{\mathrm{A}}|\hat{F}|h_{\mathrm{B}}\right\rangle = t_{\mathrm{LH}}$ are zero. Note that for asymmetric systems, one cannot use HOMO/HOMO-1 or LUMO/LUMO+1 splittings to calculate electron transfer integrals; one is forced to use a more general approach, e.g., the Boys approach described above.

Digression: A non-covalent tetracene dimer

To quantitatively benchmark the overall procedure just described against other known methods we have considered a non-covalent Tc dimer system where the electronic coupling for SF is expected to be large both by literature precedent [210,211,214] and by inference to a structurally and electronically related pentacene dimer for which values of t_{HH}, t_{LL}, t_{HL}, and t_{LH} have been previously reported. [2] The structure considered here (Fig. 7.27) represents one of three unique nearest neighbor pairs in the most common polymorph of crystalline Tc. [9] The choice of this dimer amongst the three is somewhat arbitrary as each is expected to have significant inter-chromophore orbital couplings particularly the two that have the general herringbone arrangement of the Tc monomers. [2,210] We choose this structure, in part, so that comparisons can be made (vide infra) with reported high level calculations. [210] Using Hartree-Fock methods identical to those applied previously to pentacene dimers by Berkelbach, Hybertson and Reichman (BHR-HF), [2] values were calculated for t_{HH}, t_{LL}, t_{HL}, and t_{LH}[4] and are shown in Table 7.4. The Boys methodology was then applied for purposes of comparison.

The sign differences observed between the two methods originate from differing orbital phase conventions that were used. Such a sign difference is unimportant as can be seen in the various products of one-electron matrix elements (terms such as $\sqrt{3/2}t_{\mathrm{HL}}t_{\mathrm{LL}}$) that are listed in Table 7.4: in all cases the two products whose difference is relevant for the electronic coupling (Eqs. 7.4 or 7.5) needed for rate expressions have a common sign indicating there will be a destructive interference between hole-transfer and electron transfer pathways leading from the singlet exciton state to the ^{1}TT. In general there is reasonably good agreement in the magnitude of the coupling values calculated with the two methods. It is noted that in the case of t_{HH}, the Boys method predicts a value less than half the magnitude of the HF method. This may be a manifestation of a previously noted overestimation of coupling using HF. [2,3] Along these lines, if HF exchange is used with the current Boys

[4] These calculations pertaining to the noncovalent Tc dimer that were made using BHR-HF method were generously provided to us by Dr. T. Berkelbach.

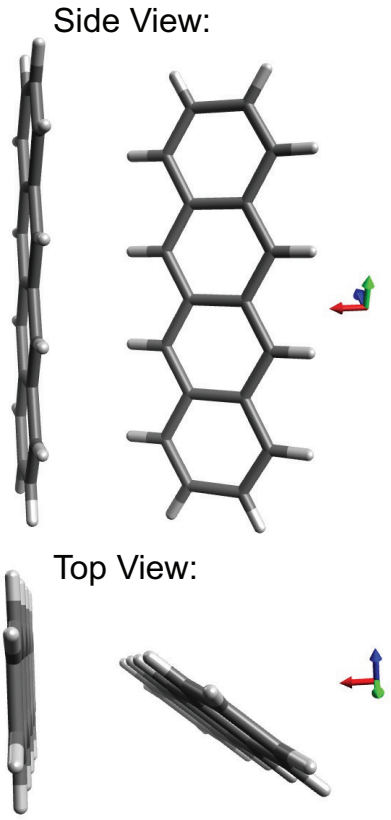

Figure 7.27: Structure of non-covalent Tc dimer system used to test methods for calculating t_{HH}, t_{LL}, t_{HL}, and t_{LH}. The structure is one of three unique nearest neighbor pairs in the most common polymorph of crystalline Tc.[9] This structure comes from the ab plane of the experimental unit cell and corresponds to an [a b] translation vector of $[\frac{1}{2}\ \frac{1}{2}]$.

method intead of ωB97X-D, universally larger couplings are obtained for the Tc dimer (Table 7.8 as well as for BT1 (Table 7.7.) We note a general increase in coupling as the extent of exact exchange is increased in the functional from PBE where there is none) to B3LYP, to ωB97X-D, and finally to HF (which contains all exact exchange). However, it is pointed out that the magnitude of t_{HH} that we calculate for the Tc dimer with HF exchange is still approximately half that calculated by Berkelbach. It is noted that factor of 2 discrepancy between couplings from single molecule and supramolecular calculations has been seen previously for excitonic couplings.[239]

It is worthwhile to consider some measure of electronic coupling between diabatic states

	BHR-HF	Boys
t_{HH}	-204	-91
t_{LL}	113	-83.5
t_{HL}	79	-74
t_{LH}	-88	-107
$\sqrt{3/2}t_{\mathrm{LH}}t_{\mathrm{LL}}$	-12179	10942
$\sqrt{3/2}t_{\mathrm{HL}}t_{\mathrm{HH}}$	-19738	8247
$\sqrt{3/2}\left(t_{\mathrm{LH}}t_{\mathrm{LL}} - t_{\mathrm{HL}}t_{\mathrm{HH}}\right)$	7559	2695
$\sqrt{3/2}t_{\mathrm{HL}}t_{\mathrm{LL}}$	10933	7553
$\sqrt{3/2}t_{\mathrm{LH}}t_{\mathrm{HH}}$	21987	11923
$\sqrt{3/2}\left(t_{\mathrm{HL}}t_{\mathrm{LL}} - t_{\mathrm{LH}}t_{\mathrm{HH}}\right)$	-11054	-4370

Table 7.4: Comparison of one-electron interchromophore coupling matrix elements (in meV) and various products of these elements (in meV^2) in noncovalent Tc dimer with Boys method versus previously-described Hartree-Fock method. The latter come from unpublished values calculated by Berkelbach.[1,2] Sign differences of orbital coupling components (t) are due to different orbital phase conventions; they are ultimately resolved in the final coupling expressions, $\sqrt{3/2}\left(t_{\mathrm{LH}}t_{\mathrm{LL}} - t_{\mathrm{HL}}t_{\mathrm{HH}}\right)$ and $\sqrt{3/2}\left(t_{\mathrm{HL}}t_{\mathrm{LL}} - t_{\mathrm{LH}}t_{\mathrm{HH}}\right)$. The only major difference in magnitudes of the orbital coupling components is for t_{HH}, for which the BHR-HF magnitude is more than twice as large as the Boys magnitude. This may be caused by the previously-reported tendency of HF to overestimate couplings.[2,3]

involved in SF in order to connect to other theoretical treatments in the literature. As discussed in section 7.2, quantities such as $\left|\sqrt{3/2}\left(t_{\mathrm{HL}}t_{\mathrm{LL}} - t_{\mathrm{LH}}t_{\mathrm{HH}}\right)\right|$ and $\left|\sqrt{3/2}\left(t_{\mathrm{LH}}t_{\mathrm{LL}} - t_{\mathrm{HL}}t_{\mathrm{HH}}\right)\right|$ serve as useful approximations to relevant superpositions of superexchange coupling pathways in SF from either $\mathrm{S_0S_1}$ (Eq. 7.4) or $\mathrm{S_1S_0}$ (Eq. 7.5), respectively. We highlight in Table 7.4 the quantity $\left|\sqrt{3/2}\left(t_{\mathrm{HL}}t_{\mathrm{LL}} - t_{\mathrm{LH}}t_{\mathrm{HH}}\right)\right|$ relevant for $\mathrm{S_0S_1} \rightarrow {}^1\mathrm{TT}$ (Eq. 7.4) as opposed to $\left|\sqrt{3/2}\left(t_{\mathrm{LH}}t_{\mathrm{LL}} - t_{\mathrm{HL}}t_{\mathrm{HH}}\right)\right|$ relevant for $\mathrm{S_1S_0} \rightarrow {}^1\mathrm{TT}$ (Eq. 7.5) as the magnitude is larger for the former quantity using both methods. With the Boys method, $\left|\sqrt{3/2}\left(t_{\mathrm{HL}}t_{\mathrm{LL}} - t_{\mathrm{LH}}t_{\mathrm{HH}}\right)\right|$ = 4370 meV^2. This is within 30% of values extracted from diabatic state couplings obtained in a high level calculation of a model Hamiltonian for a tetracene dimer by Parker and Shiozaki where $\left|\left\langle {}^1\mathrm{TT}|\hat{H}_{\mathrm{el}}|{}^1\mathrm{AC}\right\rangle\left\langle {}^1\mathrm{AC}|\hat{H}_{\mathrm{el}}|\mathrm{S_0S_1}\right\rangle + \left\langle {}^1\mathrm{TT}|\hat{H}_{\mathrm{el}}|{}^1\mathrm{CA}\right\rangle\left\langle {}^1\mathrm{CA}|\hat{H}_{\mathrm{el}}|\mathrm{S_0S_1}\right\rangle\right|$ = 3233 meV^2.[210] Working backwards from the individual state coupling matrix elements in this model Hamiltonian, again under the assumption that Coulomb terms due to two-electron overlap densities are small, it is possible to extract one-electron terms where t_{HH} = 100 meV, t_{LL} = 88 meV, t_{HL} = 45 meV, and t_{LH} = 66 meV. These are also in reasonably good

agreement with values obtained by the simpler methods listed in Table 7.4.

Before leaving this model non-covalent dimer and returning to discussions of BT1, we note that all methods discussed in this section – Parker/Shiozaki, Boys, BHR-HF (in order of increasing value) – predict, under a superexchange model, a magnitude of electronic coupling in SF that is less than k_BT (298 K) ranging from 3-11 meV (ours is 4.4 meV) when using ΔE_{CT} = 1000 meV as per the high-level calculations by Parker and Shiozaki of a Tc dimer imbedded in a point-charge super-cell to mimic aspects of the crystalline environment.[210] It should be pointed out that even the most accurate Parker/Shiozaki model cannot accommodate charge delocalization or polarization of the crystal environment to the new charge distribution, and as such the estimate of ΔE_{CT} may still be too high. Electro-absorption studies suggest the CT states to be in the range of 2.7 – 3.1 eV[239] suggesting ΔE_{CT} in a range of 400 – 800 meV above the singlet exciton state of 2.32 eV.[240] If we choose for purposes of comparison the median case of ΔE_{CT} = 600 meV, the range of electronic couplings being discussed shifts to 5 meV – 18 meV with our prediction using the Boys methodology at 7.3 meV. Although shifted to higher values, the individual values within this range remain less than k_BT and notably less than recent calculations (varying values of ΔE_{CT}).[211,214] Further investigation will be needed to ascertain the source of this discrepancy.

7.3.2. Coupling Gradients and the Role of Vibrations

We now return to the BT1 dimer. The matrix elements t_{HL} and t_{LH} are calculated to be zero for the molecule in its ground state structure with C_{2v} point group symmetry. This is the expected result obtained by invoking the Longuet-Higgins-Roberts[224,240] (or Mulliken[241,242]) approximation stating that matrix elements of the type $\left\langle \phi_A | \hat{F} | \phi_B \right\rangle$ are proportional to the overlap integral $\langle \phi_A | \phi_B \rangle$. Here, orbital symmetry arguments are useful in that either localized HOMO orbital h_A or h_B is anti-symmetric with respect to a reflection plane passing through both Tc units, while either LUMO l_A or l_B is symmetric. Thus HOMO/LUMO overlaps (from A to B or from B to A) must be zero. It stands to reason,

then, that certain molecular vibrations, specifically those that break the plane of symmetry in the molecule, should impact electronic coupling through non-zero values of t_{HL} and t_{LH}. To explore this, we have calculated gradients $\frac{d_t}{dq_i}$ for all of the inter-chromophore orbital couplings t_{HH}, t_{LL}, t_{HL}, and t_{LH}, where q_i refers to each of the 183 normal modes of motion for BT1. Each gradient was calculated by performing a finite difference calculation according to Eq. 7.10

$$\frac{dt}{dq_i} \approx \frac{t\left(\mathbf{r}_0 + \mathbf{h}_i\right) - t\left(\mathbf{r}_0 - \mathbf{h}_i\right)}{2\left|\mathbf{h}_i\right|} \tag{7.10}$$

where $\mathbf{r}_0$ is the reference geometry, and $\mathbf{h}_i$ represents a geometric perturbation in the direction of normal mode q_i, with $|\mathbf{h}_i| = 0.0001$ Å. A separate calculation was needed to generate the couplings for each perturbed geometry, so that the total number of single point calculations necessary to approximate the coupling gradients was 366.

Certain patterns emerge in these calculated coupling gradients (all values are listed in Table 7.5) that can be linked to the irreducible representations of the C_{2v} point group assigned to each normal mode of motion. Examples are illustrated in Fig. 7.28, where coupling gradients for the lowest frequency A_1, A_2, B_1, and B_2 modes are shown. For purposes of assignment, it is assumed that the C_2 symmetry axis of the molecule is aligned with the Cartesian z-axis, that the Cartesian xz plane bisects the molecule through both Tc units of the dimer, and that the function x transforms as the irreducible representation B_1. For all B_1 modes, all coupling gradients are zero. For all A_1 modes, the gradients $\frac{dt_{\mathrm{HH}}}{dq_i}$ and $\frac{dt_{\mathrm{LL}}}{dq_i}$ are finite with different magnitudes (either can be either sign) but these are ultimately irrelevant in the context of SF because $\frac{dt_{\mathrm{HL}}}{dq_i}$ and $\frac{dt_{\mathrm{LH}}}{dq_i}$ equal zero. This latter point is the expected result because normal motions classified with the A_1 irreducible representation (and with B_1 as well) are symmetrical with respect to symmetry operation of reflection through the xz plane ($\hat{\sigma}_{xz}$) and cannot facilitate coupling between antisymmetrical HOMOs with symmetrical LUMOs. Thus, these results suggest A_1 and B_1 vibrations play no role in SF for BT1.

This leaves motions belonging to the A_2 and B_2 irreducible representations. Both induce

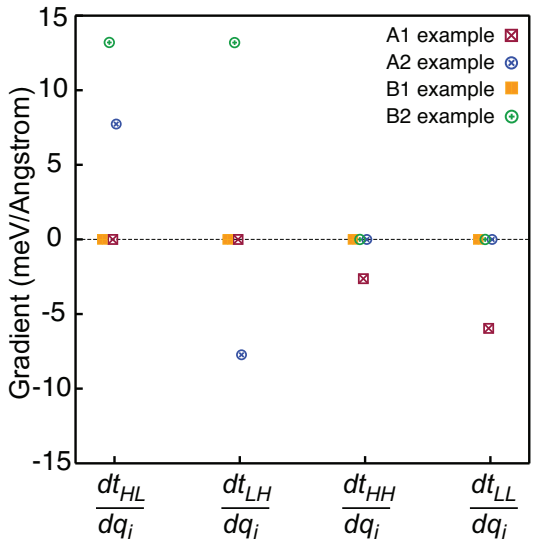

Figure 7.28: Examples of patterns in the one-electron coupling gradients (in meV/Å) for each type of vibrational mode according to its irreducible representation (A_1, A_2, B_1, and B_2; relevant for the C_{2v} point group symmetry of the molecule). Those shown correspond to the lowest-frequency instances of each: A_1 at 21 cm^{-1}, A_2 at 81 cm^{-1}, B_1 at 44 cm^{-1}, and B_2 at 72 cm^{-1}. Of note, only A_2 and B_2 modes have non-zero values for $\frac{dt_{\rm HL}}{dq_i}$ and $\frac{dt_{\rm LH}}{dq_i}$. In all B_2 modes these have the same sign whereas in all A_2 modes these have opposite signs.

no change in coupling between HOMOs or between LUMOs of the two chromophoric units of the molecule; i.e., $\frac{dt_{\rm HH}}{dq_i} = \frac{dt_{\rm LL}}{dq_i} = 0$. More importantly, the HOMO/LUMO coupling gradients $\frac{dt_{\rm HL}}{dq_i}$ and $\frac{dt_{\rm LH}}{dq_i}$ are non-zero. In the case of all B_2 modes, both gradients are of equal magnitude and equal sign (but can be either positive or negative). In the case of all A_2 modes, both gradients are again of equal magnitude but take on opposite signs. It is noted that the absolute sign for any of these coupling gradients for either A_2 or B_2 modes is somewhat arbitrary as it will flip in the $--q_i$ direction. However, as discussed below the sign difference between $\frac{dt_{\rm HL}}{dq_i}$ and $\frac{dt_{\rm LH}}{dq_i}$ for A_2 modes compared to its similarity in B_2 modes is important.

As noted above, all coupling gradients are listed in Table 7.5; but for illustrative purposes, we plot just $\frac{dt_{\rm LH}}{dq_i}$ in Fig. 7.29. Of note, there is a single B_2 normal mode at 1772 cm^{-1} (mode no. 159) that is dominant in its impact on $\frac{dt_{\rm LH}}{dq}$ (and by inference $\frac{dt_{\rm HL}}{dq}$) relative to other modes. In terms of the magnitude $|\frac{dt_{\rm LH}}{dq}|$, its value of 721 meV/Å is a factor of 2.7

larger than the next largest (267 meV/Å) occurring at 1765 cm^{-1} for an A_2 mode (mode no. 158).

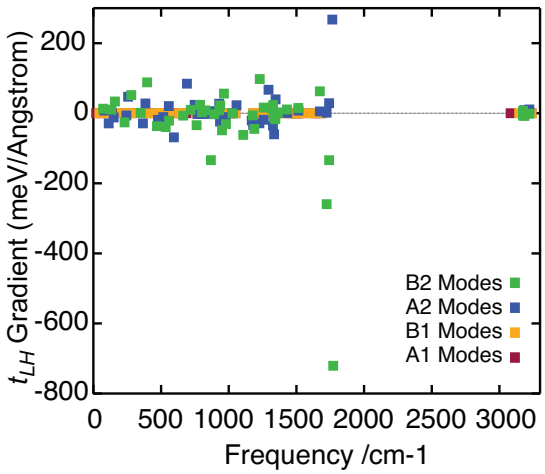

Figure 7.29: Coupling gradient $\frac{dt_{\mathrm{LH}}}{dq}$ shown for all frequencies and according to the irreducible representation of each mode: A_1 (red), A_2 (blue), B_1 (orange), and B_2 (green). For each frequency the corresponding gradient $\frac{dt_{\mathrm{HL}}}{dq}$ can be inferred using the pattern according to Fig. 7.28.

In Fig. 7.30 (a) is plotted a cartoon of this normal mode (no. 159) with projection vectors as well as an exaggerated view of the molecule at its vibrational turning points. The perspective in these pictures is in the positive z direction with the central methylene group at the apex of the molecule in the background. The impact on electronic coupling between the Tc chromophores in the dimer is clearly a result of distortions derived from C-C stretching localized significantly to the norbornyl bridging unit and nearest phenyl rings where through-bond and through-space interactions between $l_A$and h_B (or vice versa) are largest. Focusing on through-space interactions, a qualitative explanation is provided that focuses on only a piece of the orbital phase for $l_A$and h_B at the norbornyl bridge with phase information inferred from Fig. 7.26 (left). In the center of Fig. 7.30(b) the molecule is captured in its static C_{2v} structure where, by the symmetry arguments described above, there is no net overlap between $l_A$and h_B and t_{LH} is zero. Using an exaggerated distortion in this B_2 direction (left), it is shown that inter-orbital energy coupling can develop as inferred by

an increase in overlap (green double arrow) of regions of l_A and h_B that are in-phase concomitant with a decrease (black double arrow) of out-of-phase overlap. In the $-q$ direction (right) a similar process happens but it results–due to phase – in a coupling matrix element of opposite sign. As shown in Fig. 7.31 (b), an analogous qualitative argument applied to h_A and l_B (as opposed to l_A and h_B as discussed above) explains how $\frac{dt_{HL}}{dq_i}$ and $\frac{dt_{LH}}{dq_i}$ have the same sign for B_2 motions.

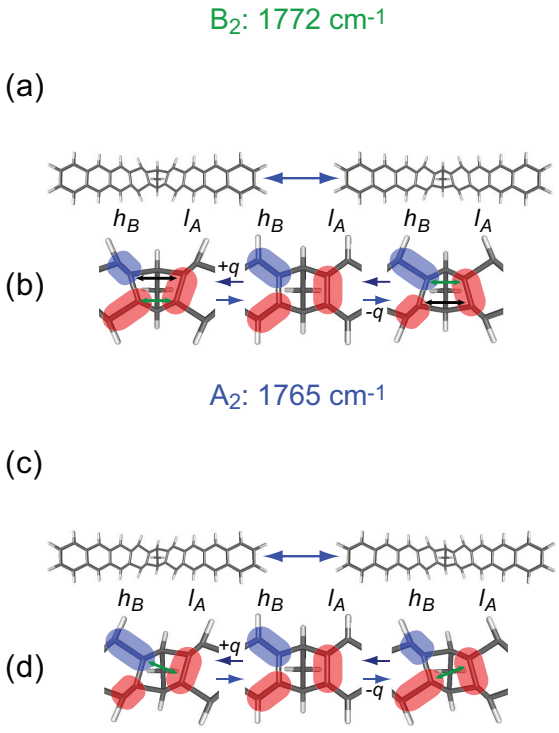

Figure 7.30: (a) Depiction of 1772 cm^{-1} B_2 normal mode of motion (no. 159) that has the highest magnitude coupling gradient $\frac{dt_{LH}}{dq}$. The viewpoint is in the $+z$ direction such that the central methylene group of the molecule is headed into the paper. (b) Cartoon rationalizing how t_{LH} coupling develops during this motion (in both $+q$ and $-q$ directions) with the focus on only part of the orbital (phase inferred from Fig. 7.26) for l_A and h_B (see text for details). (c) Depiction of A_2 1765 cm^{-1} normal mode of motion (no. 158) that has the second highest magnitude coupling gradient $\frac{dt_{LH}}{dq}$. (d) Cartoon rationalizing how t_{LH} coupling develops during this motion (in both $+q$ and $-q$ directions) with the focus on only part of the orbital for l_A and h_B (again, see text for details).

The A_2 mode (1765 cm^{-1}; no. 158) that has the second largest magnitude of coupling gradient $\frac{dt_{LH}}{dq_i}$ (and again by inference $\frac{dt_{HL}}{dq_i}$) also involves distortions largely localized to

the norbornyl bridge and nearest phenyl rings (Fig. 7.30 (c)). Here it can be seen that inter-orbital coupling can develop as the vibration proceeds as inferred from l_A to h_B orbital overlap diagonally across the bridge (Fig. 7.30 (d)). The magnitude of the coupling gradient $\frac{dt_{LH}}{dq_i}$ in this case is understandably smaller (the factor of 2.7 mentioned above) than the 1772 cm^{-1} B_2 mode (no. 159) where coupling develops via l_A to h_B π overlap directly across the bridge.

In order to calculate coupling values as opposed to coupling gradients – given that t_{LH} (and t_{HL}) equal zero for the static C_{2v} structure – we rely on an estimation of the deviation in position that may be expected to occur at a given temperature for any of the normal modes of motion q_i. With Eq. 7.11, an average vibrational level occupation number $\langle n_i \rangle$ is first calculated (for what follows, 298 K is used). With this, the root-mean-squared (RMS) deviation in the q_i^{th} direction ($\sqrt{\langle q_i^2 \rangle}$) is then evaluated using Eq. 7.12. In these equations, ω_i and μ_i refer to the frequency and reduced mass of the i^{th} normal mode. Finally we calculate coupling at this RMS deviation using Eq. 7.13. These data are compiled in Table 7.6.

$$\langle n_i \rangle = \frac{1}{e^{\hbar\omega_i / k_B T} - 1} \tag{7.11}$$

$$\sqrt{\langle q_i^2 \rangle} = \sqrt{\frac{\hbar}{2\mu_i \omega_i} \left(2\langle n_i \rangle + 1\right)} \tag{7.12}$$

$$\Delta t_{AB} = \frac{dt_{AB}}{dq_i} \sqrt{\langle q_i^2 \rangle} \tag{7.13}$$

Given the relatively high frequency of the two modes discussed above (1772 cm^{-1} and 1765 cm^{-1}), the average occupation number at room temperature is 0.00, i.e., the vibrational ground state. This leads to a 0.035 Å RMS deviation for both modes and coupling values ($t_{LH} + \Delta t_{LH}$) equal to 9.45 meV (1765 cm^{-1}; A_2) and -25 meV (1772 cm^{-1}; B_2). While the magnitudes of these coupling contributions vary substantially, their impact on SF is expected to be quite similar by coincidence. This originates in the difference of terms (products of one-electron matrix elements) central to the electronic coupling expressions in Eqs. 7.4 and 7.5 (e.g., $t_{HL}t_{LL} - t_{LH}t_{HH}$). As seen in the Fock matrix following localization

and rediagonalization in Fig. 7.26 (right), the quantities t_{HH} and t_{LL} have a common sign for this molecular system. This confluence means that A_2 modes, where there is a sign difference between Δt_{LH} and Δt_{HL} (Table 7.6), will fare better due to a constructive interference of pathways than B_2 modes where Δt_{LH} and Δt_{HL} have a common sign. That the B_2 modes have any role in SF relies on the fact that the hole-transfer and electron-transfer pathways for donor-acceptor interactions between the two chromophores (i.e., t_{HH} and t_{LL}) have differing importance in this system (vide supra).41 Using the value of ΔE_{CT} = 659 meV determined previously by the Damrauer group for BT1,[5] we calculate the coupling relevant for rate expressions such as Eq. 7.1 according to either Eq. 7.14 ($S_0S_1 \rightarrow {}^1\mathrm{TT}$) or Eq. 7.15 ($S_1S_0 \rightarrow {}^1\mathrm{TT}$) below and find a remarkably similar 3.589 meV for the A_2 mode (1765 cm^{-1}; no. 158) versus 3.594 meV for the B_2 mode (1772 cm^{-1}; no. 158). In this system electronic coupling for either $S_0S_1 \rightarrow {}^1\mathrm{TT}$ or $S_1S_0 \rightarrow {}^1\mathrm{TT}$ is identical because in all cases (modes) $|t_{\mathrm{HL}}| = |t_{\mathrm{LH}}|$.

$$\mathrm{coupling}_{S_0S_1 \rightarrow {}^1\mathrm{TT}} = \Delta E_{\mathrm{CT}}^{-1}\sqrt{3/2}\,|(t_{\mathrm{HL}} + \Delta t_{\mathrm{HL}})\,(t_{\mathrm{LL}} + \Delta t_{\mathrm{LL}}) - (t_{\mathrm{LH}} + \Delta t_{\mathrm{LH}})\,(t_{\mathrm{HH}} + \Delta t_{\mathrm{HH}})| \tag{7.14}$$

$$\mathrm{coupling}_{S_1S_0 \rightarrow {}^1\mathrm{TT}} = \Delta E_{\mathrm{CT}}^{-1}\sqrt{3/2}\,|(t_{\mathrm{LH}} + \Delta t_{\mathrm{LH}})\,(t_{\mathrm{LL}} + \Delta t_{\mathrm{LL}}) - (t_{\mathrm{HL}} + \Delta t_{\mathrm{HL}})\,(t_{\mathrm{HH}} + \Delta t_{\mathrm{HH}})| \tag{7.15}$$

The identical procedure applied to all modes results in a set of coupling values shown in Fig. 7.32 and listed in Table 7.6. In general, it can be seen that A_2 modes feature prominently as may be expected from the pathway interference issues discussed above. Of these, the 113.5 cm^{-1} vibration (no. 6) is notable with a coupling value of 3.31 meV ranking it third amongst all modes and 92% of the maximum at 3.59 meV. While the gradient magnitude for this mode $\left|\frac{dt_{\mathrm{LH}}}{dq}\right|$ (or $\left|\frac{dt_{\mathrm{HL}}}{dq}\right|$) is not insignificant, it nonetheless ranks 11^{th} amongst A_2 modes and 28^{th} overall. The significant coupling arises in large part due to its low frequency, which permits an average population of higher quantum states and with that a larger RMS deviation in position. Here, via Eq. 7.11, $\langle n \rangle = 1.37$, to be compared with the $\langle n \rangle = 0.00$ described above for the 1772 cm^{-1} and 1765 cm^{-1} modes, and to $\langle n \rangle = 0.41$ for a more

modestly higher frequency 257 cm^{-1} A_2 mode (no. 16). The resulting RMS deviation (Eq. 7.12) for the 113.5 cm^{-1} vibration is $\sqrt{\langle q^2 \rangle} = 0.30$ Å, making it nearly an order of magnitude larger than the 1772 cm^{-1} and 1765 cm^{-1} vibrations (vide supra) and twice as large as the 257 cm^{-1} A_2 mode where $\sqrt{\langle q^2 \rangle} = 0.15$ Å.

7.3.3. Evaluation of the two-electron coupling contribution

As has been discussed, the electronic coupling for mediated SF evaluated using either Eq. 7.14 or 7.15 ignores two-electron repulsion integrals that are, for example, shown in Eq. 7.2. Although these integrals are time-consuming to numerically evaluate, we have considered several cases for purposes of comparison. First, within Eq. 7.2, all integrals (two-electron or one-electron) associated with the terms $\left\langle {}^1\mathrm{TT}|\hat{H}_{\mathrm{el}}|{}^1\mathrm{CA} \right\rangle$ or $\left\langle {}^1\mathrm{TT}|\hat{H}_{\mathrm{el}}|{}^1\mathrm{AC} \right\rangle$ vanish with C_{2v} symmetry. We consider, then, four cases involving RMS deviation along two high-frequency modes (nos. 158 and 159: 1765 cm^{-1} (A_2) and 1772 cm^{-1} (B_2)) and along two low-frequency modes (nos. 4 and 6: 72 cm^{-1} (B_2) and 113.5 cm^{-1} (A_2)). Expressions inclusive of two-electron integral terms that are analogous to Eqs. 7.14 and 7.15 are shown in Eqs. 7.16 and 7.17. Because of symmetry, only one of these needs to be evaluated and we have considered the integrals relevant for Eq. 7.17 (i.e., for $S_1S_0 \rightarrow {}^1\mathrm{TT}$). We find relatively small deviations in couplings calculated with or without the two-electron integrals. For the 1772 cm^{-1} B_2 mode, the magnitude of coupling is calculated to be 3.81 meV (including two-electron integrals) as compared with 3.59 meV (one-electron integrals) representing a very modest 6% difference. Similarly for the 1765 cm^{-1} A_2 mode, we find a 6.5% difference (3.84 meV (two-electron) versus 3.589 (one-electron)). For the lower frequency modes we find slightly larger, although still small, deviations. At 72 cm^{-1} (B_2) the relative error is 8% (0.95 meV (two-electron) versus 1.03 meV (one-electron)) while at 113.5 cm^{-1} the relative error is 11% (2.98 meV (two-electron) versus 3.31 meV (one-electron)). These results, while not complete for all A_2 and B_2 modes, nonetheless appear to justify using the simpler one electron coupling expressions (Eqs. 7.14 or 7.15) particularly in computationally expensive

scenarios such as during explorations of dynamics.

$$\begin{aligned}
\text{Coupling}_{\mathrm{S_1S_0}\rightarrow{}^1\mathrm{TT}} =& \frac{1}{\Delta E_{\mathrm{CT}}} \left| \left\langle {}^1\mathrm{TT} \right| \hat{H}_{\mathrm{el}} \left| {}^1\mathrm{AC} \right\rangle \left\langle {}^1\mathrm{AC} \right| \hat{H}_{\mathrm{el}} \left| \mathrm{S_1S_0} \right\rangle + \left\langle {}^1\mathrm{TT} \right| \hat{H}_{\mathrm{el}} \left| {}^1\mathrm{CA} \right\rangle \left\langle {}^1\mathrm{CA} \right| \hat{H}_{\mathrm{el}} \left| \mathrm{S_1S_0} \right\rangle \right| \\
=& \frac{1}{\Delta E_{\mathrm{CT}}} \left| \sqrt{\frac{3}{2}} \left[(t_{\mathrm{HL}} + \Delta t_{\mathrm{HL}}) + (\langle \mathrm{l_B l_A} | \mathrm{h_A l_A} \rangle + \Delta \langle \mathrm{l_B l_A} | \mathrm{h_A l_A} \rangle) \right. \right. \\
& - (\langle \mathrm{l_B h_B} | \mathrm{h_A h_B} \rangle + \Delta \langle \mathrm{l_B h_B} | \mathrm{h_A h_B} \rangle)] [(t_{\mathrm{LL}} + \Delta t_{\mathrm{LL}}) \\
& + 2 (\langle \mathrm{h_B l_B} | \mathrm{l_A h_B} \rangle + \Delta \langle \mathrm{h_B l_B} | \mathrm{l_A h_B} \rangle) - (\langle \mathrm{h_B l_B} | \mathrm{h_B l_A} \rangle + \Delta \langle \mathrm{h_B l_B} | \mathrm{h_B l_A} \rangle)] \\
& + \sqrt{\frac{3}{2}} [(t_{\mathrm{LH}} + \Delta t_{\mathrm{LH}}) + (\langle \mathrm{l_A l_B} | \mathrm{h_B l_B} \rangle + \Delta \langle \mathrm{l_B l_B} | \mathrm{h_B l_B} \rangle) \\
& - (\langle \mathrm{l_A h_A} | \mathrm{h_B h_A} \rangle + \Delta \langle \mathrm{l_A h_A} | \mathrm{h_B h_A} \rangle)] [- (t_{\mathrm{HH}} + \Delta t_{\mathrm{HH}}) \\
& \left. + 2 (\langle \mathrm{h_B l_B} | \mathrm{l_B h_A} \rangle + \Delta \langle \mathrm{h_B l_B} | \mathrm{l_B h_A} \rangle) - (\langle \mathrm{h_B l_B} | \mathrm{h_A l_B} \rangle + \Delta \langle \mathrm{h_B l_B} | \mathrm{h_A l_B} \rangle)] \right|
\end{aligned} \tag{7.16}$$

$$\begin{aligned}
\text{Coupling}_{\mathrm{S_1S_0}\rightarrow{}^1\mathrm{TT}} =& \frac{1}{\Delta E_{\mathrm{CT}}} \left| \left\langle {}^1\mathrm{TT} \right| \hat{H}_{\mathrm{el}} \left| {}^1\mathrm{CA} \right\rangle \left\langle {}^1\mathrm{CA} \right| \hat{H}_{\mathrm{el}} \left| \mathrm{S_0S_1} \right\rangle + \left\langle {}^1\mathrm{TT} \right| \hat{H}_{\mathrm{el}} \left| {}^1\mathrm{AC} \right\rangle \left\langle {}^1\mathrm{AC} \right| \hat{H}_{\mathrm{el}} \left| \mathrm{S_0S_1} \right\rangle \right| \\
=& \frac{1}{\Delta E_{\mathrm{CT}}} \left| \sqrt{\frac{3}{2}} \left[(t_{\mathrm{LH}} + \Delta t_{\mathrm{LH}}) + (\langle \mathrm{l_A l_B} | \mathrm{h_B l_B} \rangle + \Delta \langle \mathrm{l_A l_B} | \mathrm{h_B l_B} \rangle) \right. \right. \\
& - (\langle \mathrm{l_A h_A} | \mathrm{h_B h_A} \rangle + \Delta \langle \mathrm{l_A h_A} | \mathrm{h_B h_A} \rangle)] [(t_{\mathrm{LL}} + \Delta t_{\mathrm{LL}}) \\
& + 2 (\langle \mathrm{h_A l_A} | \mathrm{l_B h_A} \rangle + \Delta \langle \mathrm{h_A l_A} | \mathrm{l_B h_A} \rangle) - (\langle \mathrm{h_A l_A} | \mathrm{h_A l_B} \rangle + \Delta \langle \mathrm{h_A l_A} | \mathrm{h_A l_B} \rangle)] \\
& + \sqrt{\frac{3}{2}} [(t_{\mathrm{HL}} + \Delta t_{\mathrm{HL}}) + (\langle \mathrm{l_B l_A} | \mathrm{h_A l_A} \rangle + \Delta \langle \mathrm{l_B l_A} | \mathrm{h_A l_A} \rangle) \\
& - (\langle \mathrm{l_B h_B} | \mathrm{h_A h_B} \rangle + \Delta \langle \mathrm{l_B h_B} | \mathrm{h_A h_B} \rangle)] [- (t_{\mathrm{HH}} + \Delta t_{\mathrm{HH}}) \\
& \left. + 2 (\langle \mathrm{h_A l_A} | \mathrm{l_A h_B} \rangle + \Delta \langle \mathrm{h_A l_A} | \mathrm{l_A h_B} \rangle) - (\langle \mathrm{h_A l_A} | \mathrm{h_B l_A} \rangle + \Delta \langle \mathrm{h_A l_A} | \mathrm{h_B l_A} \rangle)] \right|
\end{aligned} \tag{7.17}$$

For completeness we have also considered the magnitude of electronic coupling for direct $\mathrm{S_1S_0}$ (or $\mathrm{S_0S_1}$) $\rightarrow {}^1\mathrm{TT}$ SF, which as described earlier, also depends on two electron repulsion integrals. In the frontier orbital basis, the direct electronic coupling matrix element $\left\langle {}^1\mathrm{TT} | \hat{H}_{\mathrm{el}} | {}^1\mathrm{S_1S_0} \right\rangle$ (or $\left\langle {}^1\mathrm{TT} | \hat{H}_{\mathrm{el}} | {}^1\mathrm{S_0S_1} \right\rangle$) is given as a difference between two two-electron integrals[2,6,243] (see Eq. 7.2) that also vanish with the $\mathrm{C_{2v}}$ symmetry of this system. Evaluation of these integrals at RMS deviation along the four modes discussed above leads to direct electronic coupling magnitudes that are less than 1 meV just as is seen in crystalline pentacene.[2] To be precise, the exact magnitudes we calculate – that would augment the mediated couplings discussed above – are 0.37 meV (no. 4; 72 $\mathrm{cm^{-1}}$; $\mathrm{B_2}$), 0.37 meV (no.

6; 113.5 cm^{-1}; A_2), 0.60 meV (no. 158; 1765 cm^{-1}; A_2), and 0.50 meV (no. 159; 1772 cm^{-1}; B_2). For modes 6, 158, and 159 – where coupling for mediated SF is significant at RMS deviation in position – ignoring the direct mechanism amounts to underestimating coupling with a small error of order 12%. For the lower frequency B_2 mode (no. 4; 72 cm^{-1}) – where the mediated coupling magnitude is small (1.03 meV; one-electron terms) – the error incurred is modestly larger and of order 26%. It can be inferred from these sets of calculations that one-electron terms do a reasonable job capturing the magnitude of the electronic coupling for SF in this system.

7.3.4. Calculation of the SF rate and effective total coupling

Our final goal in this chapter is to calculate an overall effective singlet fission coupling value by applying a procedure similar to that proposed by Stuchebrukhov et al.[244] for determining the rate of inelastic tunneling in a fluctuating medium. Under this model, we consider BT1 a two-level system weakly coupled to a bath of harmonic oscillators (i.e., its vibrational modes), with the model Hamiltonian given by Eq. 7.18.

$$\begin{aligned}\hat{H} =& E_{\mathrm{S}_1} \left|\mathrm{S}_1\mathrm{S}_0\right\rangle \left\langle \mathrm{S}_1\mathrm{S}_0\right| + E_{^1\mathrm{TT}} \left|{}^1\mathrm{TT}\right\rangle \left\langle {}^1\mathrm{TT}\right| \\ &+ \sum_{\alpha} \left[c_\alpha \hat{\sigma}_x + \sum_{i=\mathrm{S}_1, {}^1\mathrm{TT}} g_{i,\alpha} |i\rangle\langle i| \right] \left(\hat{a}_\alpha^\dagger + \hat{a}_\alpha \right) + \frac{1}{2}\hbar\omega_\alpha \hat{a}_\alpha^\dagger \hat{a}_\alpha \end{aligned} \tag{7.18}$$

In this expression, $\hat{a}_\alpha^\dagger$ and $\hat{a}_\alpha$ are creation and annihilation operators of bath mode α, $g_{i,\alpha} = \sqrt{\hbar/2m_\alpha\omega_\alpha}\left(\frac{\partial E_i}{\partial q_\alpha}\right)$ is proportional to the energy gradient of electronic state i with respect to mode α, and $\hat{\sigma}_x = \left|\mathrm{S}_1\mathrm{S}_0\right\rangle \left\langle {}^1\mathrm{TT}\right| + \left|{}^1\mathrm{TT}\right\rangle \left\langle \mathrm{S}_1\mathrm{S}_0\right|$. Critical to Eq. 7.18 in terms of the general findings of this work is the term c_α, which is proportional to the electronic coupling gradient with respect to mode α. The c_α term is determined using Eq. 7.19 below, for which we use $\Delta E_{\mathrm{CT}} = 659$ meV.[5]

$$c_\alpha = \frac{1}{\Delta E_{\mathrm{CT}}} \sqrt{\frac{3\hbar}{4m_\alpha\omega_\alpha}} \left[\left(\frac{dt_{\mathrm{HL}}}{dq_\alpha} \right) t_{\mathrm{LL}} + t_{\mathrm{HL}} \left(\frac{dt_{\mathrm{LL}}}{dq_\alpha} \right) - \left(\frac{dt_{\mathrm{LH}}}{dq_\alpha} \right) t_{\mathrm{HH}} - t_{\mathrm{LH}} \left(\frac{dt_{\mathrm{HH}}}{dq_\alpha} \right) \right] \tag{7.19}$$

As previously noted, due to molecular orbital symmetry, the normal modes of BT1 either change the energy of the frontier orbitals (A_1 and B_1 modes) or the coupling between them (A_2 and B_2 modes), but not both. Thus, for a given mode, either $c_\alpha \neq 0$ or $g_\alpha \neq 0$, but never both. To clarify the distinction, from this point A_2 and B_2 modes will only be indexed by α, while A_1 and B_1 modes will only be indexed by β.

For the spin boson-like Hamiltonian in Eq. 7.18, following Stuchebrukhov et al.,[244] we solve for the golden rule rate, making the following substitution and assumptions. First, the reorganization energy (λ) of the SF reaction is given by the following expression:

$$\lambda = \sum_\beta \frac{\left(g_{^1\mathrm{TT},\beta} - g_{\mathrm{S_1S_0},\beta}\right)^2}{\hbar\omega_\beta} \tag{7.20}$$

Second, we assume we are in the Marcus nonadiabatic limit, in which the effective coupling is the smallest parameter in the Hamiltonian. It has been suggested that similar systems may actually fall within the adiabatic Marcus limit[211] or the Redfield limit.[1,2] Third, the system is taken to be in the thermal activation limit where Eq. 7.21 below holds.

$$\sum_\beta \left(g_{^1\mathrm{TT},\beta} - g_{\mathrm{S_1S_0},\beta}\right)^2 \frac{\langle n_\beta \rangle}{\left(\hbar\omega_\beta\right)^2} \gg 1 \tag{7.21}$$

Fourth, the A_1 and B_1 modes are assumed to be in the classical limit, so that $\langle n_\beta \rangle = k_\mathrm{B}T/\hbar\omega_\beta$. This fourth assumption is a weak requirement compared to the second and third assumptions, and can be generalized easily. With these assumptions, the resulting rate expression is given by Eq. 7.22. For the purposes of our calculations, we take $E_{^1\mathrm{TT}} - E_{\mathrm{S_1S_0}}$ to be 30 meV.[5]

$$\begin{aligned} k_{^1\mathrm{TT}\leftarrow\mathrm{S_1S_0}} = \frac{1}{\hbar}\sqrt{\frac{\pi}{k_\mathrm{B}T\lambda}} \sum_\alpha c_\alpha^2 \Bigg[\langle n_\alpha \rangle \exp\left(-\frac{(E_{^1\mathrm{TT}} - E_{\mathrm{S_1S_0}} + \hbar\omega_\alpha - \lambda)^2}{4k_\mathrm{B}T\lambda}\right) \\ + \left(\langle n_\alpha \rangle + 1\right) \exp\left(-\frac{(E_{^1\mathrm{TT}} - E_{\mathrm{S_1S_0}} - \hbar\omega_\alpha - \lambda)^2}{4k_\mathrm{B}T\lambda}\right)\Bigg] \end{aligned} \tag{7.22}$$

The rate constants (k) obtained from Eq. 7.22 can then be used as a parameter in the

classical-limit Marcus non-adiabatic rate equation (Eq. 7.23) to solve for the effective total coupling V_{eff} as a function of the reorganization energy. The resulting possible values for V_{eff} are shown in Fig. 7.33.

$$k_{^1\text{TT}\leftarrow \text{S}_1\text{S}_0} = \frac{|V_{\text{eff}}|^2}{\hbar}\sqrt{\frac{\pi}{k_{\text{B}}T\lambda}}\exp\left(-\frac{(E_{^1\text{TT}} - E_{\text{S}_1\text{S}_0} - \lambda)^2}{4k_{\text{B}}T\lambda}\right) \tag{7.23}$$

According to Fig. 7.33, we are able to calculate an effective coupling for BT1 for a range of reorganization energies. For large enough λ, the effective coupling approaches 5.9 meV, but is never smaller than 5.1 meV. For small reorganization energy, we note that our coupling estimate is less reliable, as the assumption of the thermal activation limit is no longer valid. However, under the assumptions detailed here, our results show a robust coupling of 5-6 meV.[5] [209]

Interestingly, it is clear from Fig. 7.33, that the effective coupling $|V_{\text{eff}}|$ converges as λ becomes large. In the limit where $\lambda \gg |E_{^1\text{TT}} - E_{\text{S}_1\text{S}_0}|$, the square of the effective coupling becomes simply a weighted sum of the squares of the vibrationally-induced couplings (Eq. 7.24).

$$|V_{\text{eff}}|^2 = \sum_{\alpha} c_{\alpha}^2 \text{csch}\left(\frac{\hbar\omega_{\alpha}}{2k_{\text{B}}T}\right) \tag{7.24}$$

It would be interesting to investigate $|V_{\text{eff}}|$ for other cases where zero diabatic coupling for SF is expected for static structures such as in in facially stacked pentacene [220] or in other symmetrical covalent dimer systems. [7,222]

7.4. Conclusions

The search for new molecular and material platforms for SF demands inexpensive but effective computational tools that not only predict state energetics but also allow for facile exploration of key sources of electronic coupling in this multi-electron photoreaction including the role played by intra- and inter-molecular vibrations. In this current work we

[5] It would be interesting to construct an effective coupling through more rigorous rate theories for singlet fission, e.g. Ref. 209.

have discussed the simplest approach possible to calculate couplings between diabatic one-electron wavefunctions localized to chromophores within intramolecular or intermolecular dimeric systems. These couplings are critical ingredients in approximate theoretical treatments of SF mediated by virtual charge transfer states.

In summary, one starts with the relevant subset of canonical (adiabatic) molecular orbitals (here, HOMO-1, ..., LUMO+1) accessed through a typical electronic structure calculation such as DFT. Application of a unitary transformation based on the localization scheme of Boys, leads to pairs of orbitals that separately occupy space on each of the two chromophores A and B of the dimer. A rediagonalization procedure66 reveals the HOMO/LUMO pair localized to each of the two chromophores A and B as well as the desired diabatic couplings t_{AB}: t_{HH}, t_{LL}, t_{HL}, and t_{LH}. This procedure avoids reliance on more expensive multi-reference calculations, has zero marginal cost relative to a DFT calculation, is entirely blackbox, and can be applied to covalently or noncovalently linked systems. The method was tested first on a dimer of Tc monomers in a geometry relevant for the molecular crystal. The calculated t_{AB} couplings are in good agreement with those inferred from reported high level calculations,[210] and those determined using the methods of Berkelbach and coworkers.[1,2]

We now turn to the main system focus of this manuscript: the norbornyl-bridged tetracene dimer BT1.[5] In the ground state optimized geometry (C_{2v} point group), the elements t_{LH} and t_{HL}, that are essential for mediated SF, vanish by symmetry. This suggests value in considering the role played by molecular vibrations that can impact molecular symmetry. In this vein, we calculated the coupling gradients $\frac{dt_{\mathrm{HH}}}{dq_i}$, $\frac{dt_{\mathrm{LL}}}{dq_i}$, $\frac{dt_{\mathrm{HL}}}{dq_i}$, and $\frac{dt_{\mathrm{LH}}}{dq_i}$ for all 183 normal modes of motion.

On the one hand, we find that for motions transforming as the A_1 or B_1 irreducible representations, the non-horizontal terms t_{HL} and t_{LH} remain zero because a plane of symmetry running through the long axis of the molecule (xy plane; see Fig. 1) is preserved during vibration. On the other hand, A_2 and B_2 motions do impact these non-horizontal terms and orbital phase plays a particularly interesting role in this context. For B_2 motions, the

coupling gradients $\frac{dt_{\mathrm{HL}}}{dq_i}$ and $\frac{dt_{\mathrm{LH}}}{dq_i}$ have a common sign whereas for A_2 motions the signs are opposite. These patterns ultimately highlight whether SF pathways through two different virtual CT states (^{1}AC versus ^{1}CA) interfere destructively (B_2) or constructively (A_2). Ultimately, although this point is somewhat nuanced by coupling gradient magnitudes, A_2 motions are found to play a more prominent mechanistic role in BT1 due to this quantum interference phenomenon.

We have identified three normal modes in BT1 with the highest impact on electronic coupling for SF: mode 6 at 113.5 cm^{-1} (A_2), mode 158 at 1765 cm^{-1} (A_2), and mode 159 at 1772 cm^{-1} (B_2). Mode 6 does not stand out in the magnitude of its gradients $\frac{dt_{\mathrm{HL}}}{dq_i}$ and $\frac{dt_{\mathrm{LH}}}{dq_i}$. Rather, it achieves prominence due to constructive interference of CT pathways as well as its low frequency that enables substantial RMS deviations in position at room temperature. The two higher frequency modes 158 and 159 have insignificant RMS deviation and must exploit larger values of $\frac{dt_{\mathrm{HL}}}{dq_i}$ and $\frac{dt_{\mathrm{LH}}}{dq_i}$ made possible by motions that strongly impact the norbornyl bridge and its two proximal phenyl rings. For mode 159 (B_2), these coupling gradients are the largest we have seen but the CT pathways destructively interfere. For mode 158 (A_2) the coupling gradient magnitudes are diminished by a factor of 2.7 (relative to mode 159) but the system can take advantage of the constructive interference.

Finally, by application of a model Hamiltonian [244] that incorporates our coupling gradients, we can back out a range of effective coupling magnitudes $|V_{\mathrm{eff}}|$ for SF as a function of possible values of the reorganization energy (λ) of the SF reaction in BT1 at room temperature. For values of λ that range from 100 meV (expected to be relevant for crystalline systems [211]) to 1000 meV (expected to be more relevant when solvent is included) the effective coupling is robust and spans a range from 5.4 meV to 5.8 meV. For comparative purposes, it is worthwhile to return to the noncovalent Tc dimer in which, as discussed previously, we calculated (based on t_{HH}, t_{LL}, t_{HL}, and t_{LH}) a value for electronic coupling for SF ($S_0S_1 \rightarrow {}^1$TT) of 7.3 meV under conditions where $\Delta E_{\mathrm{CT}} = 600$ meV. On the one hand, this would suggest that future calculations of SF should and must investigate the possibility of

non-Condon effects; fluctuations in diabatic couplings might be as large the ground-state geometry coupling itself. On the other hand, if non-Condon effects are larger in BT1 than in Tc, and we suppose that BT1 and Tc have fairly similar frequencies and reorganization energies, one might speculate that BT1 might also allow for observable SF efficiencies (e.g, the efficiency of SF in crystalline Tc is 200%). We are also intrigued going forward by the notion of using experimental protocols based on laser-pulse shaping to create non-equilibrium vibrational conditions as a means of controlling SF rates and more importantly of identifying those most strongly correlated with the photophysical mechanism. In the end, we believe the simple procedure discussed here can be used to explore and identify new dimer designs that avoid key symmetries impeding SF.

7.5. Acknowledgements

NHD gratefully acknowledges support from the Chemical Sciences, Geosciences, and Biosciences Division, Office of Basic Energy Science, U.S. Department of Energy through grant DE-FG02-07ER15890. NHD would like to thank Dr. Timothy Berkelbach for very helpful correspondences and for calculating (and sharing) certain one-electron coupling matrix elements that we used for comparison purposes in the manuscript. NHD would also like to thank Dr. Shane Parker for very helpful correspondences and for sharing certain unpublished diabatic state couplings cast in a Frenkel exciton basis. JES thanks Seogjoo Jang for very interesting discussions and acknowledges support from NSF CAREER Grant No. CHE-1150851 and a David & Lucile Packard Fellowship.

Mode	Freq. (cm^{-1})	Irr. Rep.	$\frac{dt_{HL}}{dq_i}$	$\frac{dt_{LH}}{dq_i}$	$\frac{dt_{HH}}{dq_i}$	$\frac{dt_{LL}}{dq_i}$
1	20.9	A_1	0	0	-2.6	-6
2	44	B_1	0	0	0	0
3	64.3	A_1	0	0	-11.3	-19.4
4	72.2	B_2	13.1	13.1	0	0
5	81.1	A_2	-7.7	7.7	0	0
6	113.5	A_2	28.9	-28.9	0	0
7	114.6	B_1	0	0	0	0
8	133.2	B_2	10.3	10.3	0	0
9	141.6	A_1	0	0	-25.5	-32.8

10	150.3	A_2	12	-12.1	0	0
11	159.4	B_2	33.7	33.7	0	0
12	214.4	B_1	0	0	0	0
13	224.5	A_1	0	0	15	-2.8
14	230.2	B_2	-26.1	-26.1	0	0
15	243.8	A_2	6.2	-6.2	0	0
16	256.7	A_2	-47.3	47.3	0	0
17	268.1	B_1	0	0	0	0
18	277.1	A_1	0	0	-34.8	-35.9
19	280.4	B_2	51.9	51.9	0	0
20	306.5	B_1	0	0	0	0
21	350.2	B_2	0.9	0.9	0	0
22	366.2	A_2	29	-29	0	0
23	384.5	A_2	-27.9	27.9	0	0
24	386.2	A_1	0	0	-40.3	4.6
25	389	B_1	0	0	0	0
26	397.5	B_2	88.1	88.1	0	0
27	451.9	A_1	0	0	-13.9	-9.6
28	460.1	B_1	0	0	0	0
29	470.2	B_2	-36.8	-36.8	0	0
30	477.4	A_2	18.8	-18.8	0	0
31	500.8	B_1	0	0	0	0
32	501.6	A_1	0	0	-28.7	42.1
33	511.3	B_1	0	0	0	-0.1
34	511.5	A_1	0	0	-1.1	10.3
35	514.9	B_1	0	0	0.1	-0.1
36	514.9	A_1	0	0	-10.3	5.1
37	516.8	A_2	10.8	-10.8	0	0
38	534.5	B_2	-39.5	-39.5	0	0
39	557.1	A_2	-20.5	20.6	0	0
40	558.8	B_2	-21.2	-21.2	0	0
41	564.9	B_1	0	0	0	0
42	592.6	A_1	0	0	-93.9	-49.4
43	595.1	A_2	68.7	-68.7	0	0
44	634	A_1	0	0	54.6	14.6
45	636.7	B_1	0	0	0	0
46	652.3	A_1	0	0	-13.2	-12.5
47	653.4	B_1	0	0	0	0
48	663.6	B_2	-6.7	-6.7	0	0
49	691	A_2	-84.4	84.5	0	0
50	720	B_2	9.8	9.8	0	0
51	736.3	A_1	0	0	-33.2	-39.5
52	748.3	A_2	-24	24	0	0
53	757.6	B_1	0	0	0	0
54	763	B_2	-34.2	-34.2	0	0

55	769.3	A_2	2.2	-2.2	0	0
56	781.4	A_1	0	0	-2.4	5.5
57	782.6	B_1	0	0	0	0
58	787.7	A_1	0	0	-6.6	29.7
59	788.3	B_2	24	24	0	0
60	789	A_2	0.8	-0.8	0	0.1
61	789.2	A_1	0	0	3.4	1.3
62	789.3	B_1	0	0	0	0
63	803.1	B_2	3.1	3.1	0	0
64	803.3	A_2	0.8	-0.8	0	0
65	819	B_1	0	0	0	0
66	829.1	B_2	8.2	8.2	0	0
67	842.4	A_2	2	-2	0	0
68	862.8	A_1	0	0	33.9	43.3
69	868.6	B_2	-133.9	-133.9	0	0
70	892.8	A_2	-5.9	6	0	0
71	892.8	B_2	-3.1	-2.8	0	0
72	895.5	B_1	0	0	0	0
73	901.2	A_1	0	0	8.5	-13.7
74	910.2	A_1	0	0	-19.4	-1.2
75	914	B_1	0	0	0	0
76	929.1	A_1	0	0	-18.5	-28.2
77	929.4	A_2	-27.2	27.2	0	0
78	929.8	B_2	8.1	8.2	0	0
79	935.7	A_2	24	-24	0	0
80	936.7	B_2	22.3	22.3	0	0
81	938.8	B_1	0	0	0	0
82	948.3	A_1	0	0	11.9	-6.2
83	950.5	B_2	-48.7	-48.7	0	0
84	956.4	A_2	19.2	-19.2	0	0
85	964.9	B_2	56.2	56.2	0	0
86	974.1	B_1	0	0	0	0
87	976.7	A_2	10.9	-10.9	0	0
88	978.4	A_1	0	0	-3.8	5.1
89	979.4	B_2	-31	-31	0	0
90	1012.1	B_1	0	0	0	0
91	1012.2	A_1	0	0	-0.7	1.1
92	1015.8	B_1	0	0	0	0
93	1028.1	A_2	-0.3	0.3	0	0
94	1028.1	B_2	0	-0.1	0	0
95	1048.8	A_1	0	0	-0.3	1.8
96	1049	B_1	0	0	0	0
97	1057.6	A_2	-22.9	22.9	0	0
98	1107.3	B_2	-61.8	-61.8	0	0
99	1169.8	A_2	20.5	-20.5	0	0

100	1178	B_2	-6.1	-6.1	0	0
101	1180.7	A_2	33.5	-33.5	0	0
102	1180.9	B_1	-0.1	0.1	0	0
103	1182.6	A_1	0	0	24.6	32.2
104	1189.3	B_2	-44.6	-44.6	0	0
105	1199.2	B_1	0	0	0	0
106	1218.3	A_1	0	0	0	-14
107	1222.6	B_1	0	0	0	0
108	1222.8	A_1	0	0	5.5	13.2
109	1226.9	A_2	28.5	-28.6	0	0
110	1229.2	B_2	97.6	97.6	0	0
111	1258.2	A_2	18.8	-18.7	0	0
112	1258.5	B_2	16.3	16.3	0	0
113	1264.8	B_1	0	0	0	0
114	1266.5	A_1	0	0	1.1	2.9
115	1294.2	A_2	-67.2	67.2	0	0
116	1303.9	B_1	0	0	0	0
117	1313.4	A_1	0	0	27.2	19.1
118	1313.8	B_2	14.1	14.1	0	0
119	1326.7	A_2	35.1	-35.1	0	0
120	1327.9	B_2	23.7	23.6	0	0
121	1332.5	B_2	-11.2	-11.1	0	0
122	1335.4	A_2	60.1	-60.1	0	0
123	1344.3	B_2	-17	-17	0	0
124	1346.2	A_2	-39.8	39.8	0	0
125	1353.2	B_1	0	0	0	0
126	1354.1	A_1	0	0	-36.8	-94.3
127	1362.5	B_2	1	1	0	0
128	1368.7	A_2	-1.9	1.9	0	0
129	1408.7	B_1	0	0	-0.6	-1.1
130	1408.9	A_1	0	0	42.3	83.6
131	1430.4	B_2	10.8	10.8	0	0
132	1433.1	A_2	-0.8	0.8	0	0
133	1458.3	B_1	0	0	0	0
134	1459.4	A_1	0	0	35.3	76.4
135	1485	A_1	0	0	-7.5	-15.9
136	1485	B_1	0	0	-0.4	-0.8
137	1492.9	A_1	0	0	-0.8	24
138	1499.7	B_1	0	0	0	0
139	1503.4	A_1	0	0	26	96.5
140	1506.6	B_1	0	0	0	0
141	1513.9	B_2	15.2	15.2	0	0
142	1514.8	A_2	-7.7	7.7	0	0
143	1519.9	A_1	0	0	-19.8	-61.7
144	1541.7	A_1	0	0	-2.4	-27

145	1541.9	B_1	0	0	0	-0.3
146	1618.4	A_1	0	0	-14.8	-36.8
147	1618.6	B_1	0	0	0	0
148	1645	A_1	0	0	63.7	130.7
149	1645.1	B_1	0	0	1.9	3.9
150	1673	A_2	-5	5.2	0	0
151	1673.2	B_2	62.7	62.6	0	0
152	1679.6	B_1	0	0	0	0
153	1685.7	A_1	0	0	-108.9	-174.2
154	1723.5	A_2	-4.3	1.5	0	0
155	1723.6	B_2	-259.5	-259.5	0	0
156	1741.3	A_2	-27.7	28.6	0	0
157	1741.5	B_2	-134.1	-133.9	0	0
158	1765.1	A_2	-267.3	267.4	0	0
159	1771.9	B_2	-720.9	-720.9	0	0
160	3082	A_1	0	0	0.4	-20.8
161	3145.8	B_1	0	0	0	0
162	3174	B_2	-6.3	-6.5	0	0
163	3174	A_2	4.3	-4.1	0	0
164	3174.3	B_2	7.1	7	0	0
165	3174.9	A_2	-1.8	1.8	0	0
166	3175.3	A_1	0	0	-0.8	8.3
167	3175.3	B_1	0.1	-0.1	0	0.1
168	3176	B_2	0.6	0.6	0	0.1
169	3176.6	A_1	0	0	3.4	-7.6
170	3178.7	A_1	0	0	-0.9	-9.5
171	3178.7	B_1	0	0	0.1	0.9
172	3183.7	B_2	-4	-4	0	0
173	3183.9	A_2	1.5	-1.4	0	0
174	3184.4	A_2	-8.7	8.8	0	0
175	3184.8	B_2	-7.8	-7.7	0	0
176	3185.8	B_1	0	0	0	0.2
177	3186	A_1	0	0	-1.7	-13.5
178	3187.4	A_1	0	0	-0.1	-1.8
179	3187.6	B_1	0	0	0	0
180	3221.4	A_2	-8.1	10.9	0	0
181	3221.4	B_2	7.4	-1.4	0	0
182	3236.7	A_1	0	0	-1.9	-1.7
183	3237.4	B_1	0	0	0	0

Table 7.5: Coupling gradients for all normal modes of BT1, given in meV/Å.

Mode	Freq. (cm^{-1})	Irr. Rep.	$\langle n_i \rangle$	$\sqrt{\langle q_i^2 \rangle}$	Δt_{HL}	Δt_{LH}	Δt_{HH}	Δt_{LL}

1	20.9	A_1	9.294	1.472	0	0	-4.01	-8.81
2	44	B_1	4.219	0.728	0	0	0	0
3	64.3	A_1	2.752	0.506	0	0	-5.64	-9.78
4	72.2	B_2	2.392	0.543	7.09	7.09	0	0
5	81.1	A_2	2.084	0.497	-3.78	3.78	0	0
6	113.5	A_2	1.37	0.302	8.72	-8.72	0	0
7	114.6	B_1	1.354	0.297	0	0	0	0
8	133.2	B_2	1.108	0.301	3.11	3.11	0	0
9	141.6	A_1	1.02	0.238	0	0	-6.08	-7.83
10	150.3	A_2	0.938	0.273	3.27	-3.27	0	0
11	159.4	B_2	0.863	0.245	8.26	8.26	0	0
12	214.4	B_1	0.551	0.175	0	0	0	0
13	224.5	A_1	0.511	0.15	0	0	2.25	-0.41
14	230.2	B_2	0.49	0.178	-4.66	-4.66	0	0
15	243.8	A_2	0.445	0.17	1.06	-1.06	0	0
16	256.7	A_2	0.408	0.149	-7.04	7.04	0	0
17	268.1	B_1	0.378	0.152	0	0	0	0
18	277.1	A_1	0.356	0.133	0	0	-4.62	-4.76
19	280.4	B_2	0.348	0.149	7.73	7.73	0	0
20	306.5	B_1	0.295	0.129	0	0	0	0
21	350.2	B_2	0.226	0.123	0.1	0.1	0	0
22	366.2	A_2	0.206	0.121	3.53	-3.53	0	0
23	384.5	A_2	0.185	0.111	-3.09	3.09	0	0
24	386.2	A_1	0.183	0.124	0	0	-4.98	0.57
25	389	B_1	0.18	0.129	0	0	0	0
26	397.5	B_2	0.172	0.115	10.1	10.1	0	0
27	451.9	A_1	0.127	0.085	0	0	-1.17	-0.81
28	460.1	B_1	0.122	0.113	0	0	0	0
29	470.2	B_2	0.115	0.097	-3.58	-3.58	0	0
30	477.4	A_2	0.111	0.093	1.75	-1.75	0	0
31	500.8	B_1	0.098	0.107	0	0	0	0
32	501.6	A_1	0.097	0.109	0	0	-3.14	4.59
33	511.3	B_1	0.093	0.116	0	0	0	0
34	511.5	A_1	0.092	0.117	0	0	-0.13	1.21
35	514.9	B_1	0.091	0.115	0	0	0	0
36	514.9	A_1	0.091	0.115	0	0	-1.19	0.6
37	516.8	A_2	0.09	0.081	0.89	-0.89	0	0
38	534.5	B_2	0.082	0.073	-2.89	-2.89	0	0
39	557.1	A_2	0.073	0.096	-1.97	1.99	0	0
40	558.8	B_2	0.072	0.098	-2.07	-2.07	0	0
41	564.9	B_1	0.07	0.099	0	0	0	0
42	592.6	A_1	0.061	0.069	0	0	-6.46	-3.39
43	595.1	A_2	0.06	0.07	4.83	-4.83	0	0
44	634	A_1	0.049	0.067	0	0	3.65	0.98
45	636.7	B_1	0.048	0.07	0	0	0	0

46	652.3	A_1	0.045	0.064	0	0	-0.83	-0.8
47	653.4	B_1	0.045	0.064	0	0	0	0
48	663.6	B_2	0.042	0.063	-0.43	-0.43	0	0
49	691	A_2	0.037	0.056	-4.7	4.7	0	0
50	720	B_2	0.032	0.058	0.57	0.57	0	0
51	736.3	A_1	0.029	0.062	0	0	-2.07	-2.47
52	748.3	A_2	0.028	0.066	-1.58	1.58	0	0
53	757.6	B_1	0.026	0.066	0	0	0	0
54	763	B_2	0.026	0.064	-2.2	-2.2	0	0
55	769.3	A_2	0.025	0.071	0.15	-0.15	0	0
56	781.4	A_1	0.024	0.067	0	0	-0.16	0.36
57	782.6	B_1	0.023	0.071	0	0	0	0
58	787.7	A_1	0.023	0.072	0	0	-0.47	2.12
59	788.3	B_2	0.023	0.073	1.75	1.75	0	0
60	789	A_2	0.023	0.076	0.06	-0.06	0	0
61	789.2	A_1	0.023	0.131	0	0	0.46	0.18
62	789.3	B_1	0.023	0.13	0	0	0	0
63	803.1	B_2	0.021	0.082	0.25	0.25	0	0
64	803.3	A_2	0.021	0.082	0.07	-0.07	0	0
65	819	B_1	0.02	0.08	0	0	0	0
66	829.1	B_2	0.019	0.06	0.49	0.49	0	0
67	842.4	A_2	0.017	0.063	0.12	-0.12	0	0
68	862.8	A_1	0.016	0.081	0	0	2.74	3.49
69	868.6	B_2	0.015	0.067	-8.96	-8.96	0	0
70	892.8	A_2	0.014	0.12	-0.72	0.72	0	0
71	892.8	B_2	0.014	0.12	-0.36	-0.33	0	0
72	895.5	B_1	0.013	0.122	0	0	0	0
73	901.2	A_1	0.013	0.114	0	0	0.96	-1.55
74	910.2	A_1	0.013	0.09	0	0	-1.75	-0.1
75	914	B_1	0.012	0.085	0	0	0	0
76	929.1	A_1	0.011	0.074	0	0	-1.38	-2.1
77	929.4	A_2	0.011	0.121	-3.28	3.28	0	0
78	929.8	B_2	0.011	0.114	0.93	0.93	0	0
79	935.7	A_2	0.011	0.057	1.38	-1.38	0	0
80	936.7	B_2	0.011	0.064	1.42	1.42	0	0
81	938.8	B_1	0.011	0.114	0	0	0	0
82	948.3	A_1	0.01	0.111	0	0	1.33	-0.69
83	950.5	B_2	0.01	0.103	-4.99	-4.99	0	0
84	956.4	A_2	0.01	0.113	2.15	-2.15	0	0
85	964.9	B_2	0.01	0.104	5.84	5.84	0	0
86	974.1	B_1	0.009	0.109	0	0	0	0
87	976.7	A_2	0.009	0.107	1.16	-1.16	0	0
88	978.4	A_1	0.009	0.109	0	0	-0.41	0.56
89	979.4	B_2	0.009	0.106	-3.27	-3.27	0	0
90	1012.1	B_1	0.008	0.112	0	0	0	0

91	1012.2	A_1	0.008	0.112	0	0	-0.09	0.12
92	1015.8	B_1	0.007	0.098	0	0	0	0
93	1028.1	A_2	0.007	0.114	-0.03	0.03	0	0
94	1028.1	B_2	0.007	0.114	0	0	0	0
95	1048.8	A_1	0.006	0.083	0	0	-0.02	0.13
96	1049	B_1	0.006	0.083	0	0	0	0
97	1057.6	A_2	0.006	0.087	-1.99	1.99	0	0
98	1107.3	B_2	0.005	0.055	-3.38	-3.38	0	0
99	1169.8	A_2	0.004	0.099	2.02	-2.02	0	0
100	1178	B_2	0.003	0.086	-0.54	-0.54	0	0
101	1180.7	A_2	0.003	0.092	3.06	-3.06	0	0
102	1180.9	B_1	0.003	0.088	0	0	0	0
103	1182.6	A_1	0.003	0.089	0	0	2.18	2.86
104	1189.3	B_2	0.003	0.093	-4.17	-4.17	0	0
105	1199.2	B_1	0.003	0.083	0	0	0	0
106	1218.3	A_1	0.003	0.08	0	0	0	-1.14
107	1222.6	B_1	0.003	0.11	0	0	0	0
108	1222.8	A_1	0.003	0.11	0	0	0.6	1.44
109	1226.9	A_2	0.003	0.081	2.33	-2.33	0	0
110	1229.2	B_2	0.003	0.088	8.55	8.55	0	0
111	1258.2	A_2	0.002	0.096	1.8	-1.8	0	0
112	1258.5	B_2	0.002	0.096	1.56	1.56	0	0
113	1264.8	B_1	0.002	0.085	0	0	0	0
114	1266.5	A_1	0.002	0.084	0	0	0.09	0.25
115	1294.2	A_2	0.002	0.092	-6.2	6.2	0	0
116	1303.9	B_1	0.002	0.091	0	0	0	0
117	1313.4	A_1	0.002	0.092	0	0	2.5	1.75
118	1313.8	B_2	0.002	0.093	1.32	1.32	0	0
119	1326.7	A_2	0.002	0.089	3.11	-3.11	0	0
120	1327.9	B_2	0.002	0.083	1.97	1.97	0	0
121	1332.5	B_2	0.002	0.086	-0.96	-0.96	0	0
122	1335.4	A_2	0.002	0.068	4.08	-4.08	0	0
123	1344.3	B_2	0.002	0.064	-1.08	-1.08	0	0
124	1346.2	A_2	0.002	0.083	-3.32	3.32	0	0
125	1353.2	B_1	0.001	0.06	0	0	0	0
126	1354.1	A_1	0.001	0.059	0	0	-2.15	-5.53
127	1362.5	B_2	0.001	0.088	0.1	0.1	0	0
128	1368.7	A_2	0.001	0.085	-0.16	0.16	0	0
129	1408.7	B_1	0.001	0.069	0	0	-0.04	-0.08
130	1408.9	A_1	0.001	0.069	0	0	2.91	5.73
131	1430.4	B_2	0.001	0.08	0.88	0.88	0	0
132	1433.1	A_2	0.001	0.082	-0.07	0.07	0	0
133	1458.3	B_1	0.001	0.043	0	0	0	0
134	1459.4	A_1	0.001	0.04	0	0	1.4	3.03
135	1485	A_1	0.001	0.069	0	0	-0.51	-1.09

136	1485	B_1	0.001	0.067	0	0	-0.02	-0.05
137	1492.9	A_1	0.001	0.094	0	0	-0.08	2.26
138	1499.7	B_1	0.001	0.053	0	0	0	0
139	1503.4	A_1	0.001	0.056	0	0	1.47	5.43
140	1506.6	B_1	0.001	0.056	0	0	0	0
141	1513.9	B_2	0.001	0.053	0.8	0.8	0	0
142	1514.8	A_2	0.001	0.053	-0.4	0.4	0	0
143	1519.9	A_1	0.001	0.058	0	0	-1.16	-3.6
144	1541.7	A_1	0.001	0.067	0	0	-0.17	-1.82
145	1541.9	B_1	0.001	0.068	0	0	0	-0.02
146	1618.4	A_1	0	0.047	0	0	-0.69	-1.74
147	1618.6	B_1	0	0.047	0	0	0	0
148	1645	A_1	0	0.039	0	0	2.5	5.13
149	1645.1	B_1	0	0.039	0	0	0.07	0.15
150	1673	A_2	0	0.042	-0.2	0.22	0	0
151	1673.2	B_2	0	0.042	2.6	2.6	0	0
152	1679.6	B_1	0	0.037	0	0	0	0
153	1685.7	A_1	0	0.037	0	0	-3.99	-6.38
154	1723.5	A_2	0	0.039	-0.17	0.05	0	0
155	1723.6	B_2	0	0.039	-10.2	-10.2	0	0
156	1741.3	A_2	0	0.04	-1.11	1.14	0	0
157	1741.5	B_2	0	0.04	-5.37	-5.35	0	0
158	1765.1	A_2	0	0.035	-9.45	9.46	0	0
159	1771.9	B_2	0	0.035	-25.04	-25.04	0	0
160	3082	A_1	0	0.072	0	0	0.04	-1.49
161	3145.8	B_1	0	0.069	0	0	0	0
162	3174	B_2	0	0.07	-0.44	-0.46	0	0
163	3174	A_2	0	0.07	0.3	-0.28	0	0
164	3174.3	B_2	0	0.07	0.49	0.49	0	0
165	3174.9	A_2	0	0.07	-0.13	0.13	0	0
166	3175.3	A_1	0	0.07	0	0	-0.06	0.57
167	3175.3	B_1	0	0.07	0	0	0	0
168	3176	B_2	0	0.07	0.04	0.04	0	0
169	3176.6	A_1	0	0.07	0	0	0.25	-0.53
170	3178.7	A_1	0	0.07	0	0	-0.06	-0.66
171	3178.7	B_1	0	0.07	0	0	0	0.06
172	3183.7	B_2	0	0.07	-0.28	-0.28	0	0
173	3183.9	A_2	0	0.07	0.09	-0.09	0	0
174	3184.4	A_2	0	0.07	-0.61	0.61	0	0
175	3184.8	B_2	0	0.07	-0.55	-0.53	0	0
176	3185.8	B_1	0	0.07	0	0	0	0.02
177	3186	A_1	0	0.07	0	0	-0.11	-0.93
178	3187.4	A_1	0	0.07	0	0	0	-0.13
179	3187.6	B_1	0	0.07	0	0	0	0
180	3221.4	A_2	0	0.069	-0.57	0.75	0	0

181	3221.4	B_2	0	0.069	0.51	-0.09	0	0
182	3236.7	A_1	0	0.069	0	0	-0.13	-0.11
183	3237.4	B_1	0	0.069	0	0	0	0

Table 7.6: One-electron couplings calculated at RMS deviation of the normal modes of BT1 at 298 K.

Exchange type	t_{HH}	t_{LL}	t_{HL}	t_{LH}
PBE	-50.9	106.6	-3.9	3.9
B3LYP	-56.5	122.3	-5.3	5.3
ωB97X-D	63.5	140.8	-9	-9
HF	-76.5	176.7	-9.8	9.8

Table 7.7: Couplings for BT1 using a geometry perturbed from the ωB97X-D minimum energy by 0.1 Å along mode 26. All couplings in meV. Note the monotonic increase in the coupling magnitudes with the portion of exact exchange included in the exchange-correlation functional.

Exchange type	t_{HH}	t_{LL}	t_{HL}	t_{LH}
PBE	-72.5	-63.5	-35.5	-51.5
B3LYP	-78.5	-70.7	-47.3	-66.7
ωB97X-D	-91	-83.5	-73.9	-107
HF	-114.7	-104	-74.5	-125.5

Table 7.8: Couplings for tetracene dimer using a geometry perturbed from the ωB97X-D minimum energy by 0.1 Å along mode 26. All couplings in meV. Note the monotonic increase in the coupling magnitudes with the portion of exact exchange included in the exchange-correlation functional.

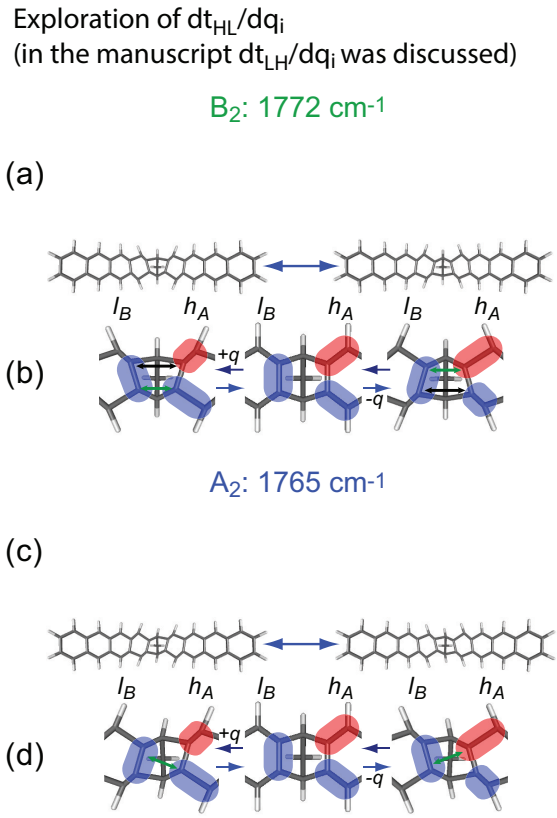

Figure 7.31: This figure is analogous to Fig. 7.30 from the manuscript but works with h_A and l_B as opposed to l_A and h_B. (a) Depiction of 1772 cm^{-1} B_2 normal mode of motion (no. 159) that has the highest magnitude coupling gradient $\frac{dt_{HL}}{dq}$ (and $\frac{dt_{LH}}{dq}$). The viewpoint is in the $+z$ direction such that the central methylene group of the molecule is headed into the paper. (b) Cartoon rationalizing how t_{HL} coupling develops during this motion (in both $+q$ and $-q$ directions) with the focus on only part of the orbital (phase inferred from Fig. 7.26) for h_A and l_B. Note that the sign of the coupling that develops is the same here as it was in Fig. 7.30 which considered l_A and h_B. This similarity in sign is true of all B_2 motions. (c) Depiction of A_2 1765 cm^{-1} normal mode of motion (no. 158) that has the second highest magnitude coupling gradient $\frac{dt_{HL}}{dq}$ (and $\frac{dt_{LH}}{dq}$). (d) Cartoon rationalizing how t_{HL} coupling develops during this motion (in both $+q$ and $-q$ directions) with the focus on only part of the orbital for h_A and l_B (again, see text for details). Note here that the sign of the coupling that develops is the opposite of what it in Fig. 7.30 which considered l_A and h_B. This difference in sign is true of all A_2 motions.

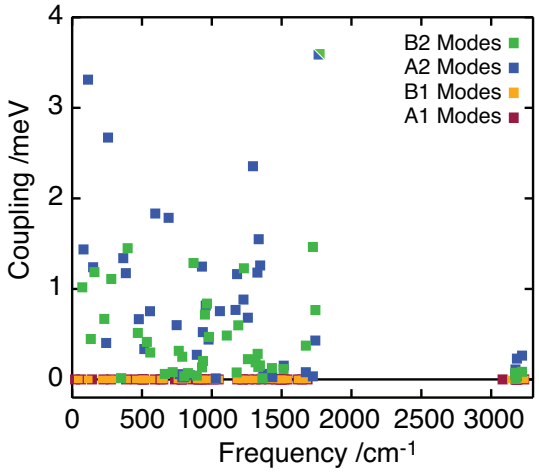

Figure 7.32: Electronic coupling (S_0S_1 to ^{1}TT; mediated via virtual CT states) calculated (Eq. 7.14) at RMS deviation in position (298 K) for each normal mode and plotted as a function of frequency and according to irreducible representation (A_1 (red), A_2 (blue), B_1 (orange), and B_2 (green)). The value for ΔE_{CT} is 659 meV as determined in previous work by the Damrauer group.[5]

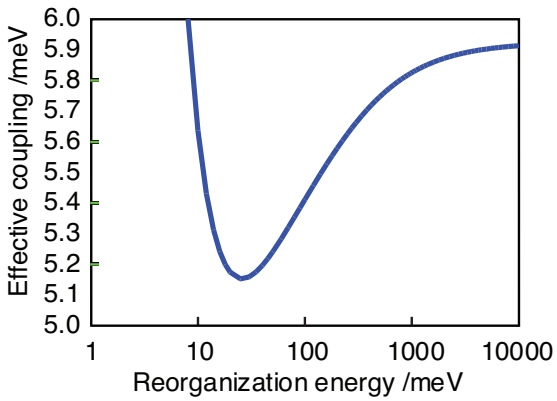

Figure 7.33: Effective SF coupling in BT1 for a range of reorganization energies as determined by the Stuchebrukhov formalism, for which we equate Eq. 7.22 with Eq. 7.23 and solve for $|V_{\text{eff}}|$, using $E_{^1\text{TT}} - E_{S_1S_0} = 30$ meV and $\Delta E_{CT} = 659$ meV.[5] The SF coupling terms c_α are inversely proportional to ΔE_{CT} within the frontier orbital model (cf. Eq. 7.19).

CHAPTER 8 : Conclusion and future work

We have introduced a number of methods that can be applied to the study of excited state dynamics. In chapter 3 we proposed an extension to localized diabatization algorithms with the CIS framework that allows the ground electronic state to be considered in the same footing as excited states, enabling more accurate modelling of charge recombination processes. In chapter 4 we described a new localized diabatization method that can take solvent conditions and state energies into account, reducing the need for manual rediagonalization and potentially extending the range of systems for which localized diabatization is applicable. In chapter 5, we applied our groups previously-derived analytic expression for BoysOV diabatic derivative couplings to an intramolecular triplet-triplet energy transfer system, demonstrating that the localized diabatic states maintain small derivative couplings near an avoided crossing. We also proposed a useful approximation which allows for the accurate calculation of diabatic energy gradients at minimal computational cost. In chapter 6 we derived an accurate, stable analytical expression for the derivative coupling between TDHF states, an essential step in modelling nonadiabatic dynamics within the TDHF formalism. Finally, in chapter 7, we used orbital localization methods to construct a basis for a frontier orbital description of singlet fission in two molecular systems, and elucidated a model that describes the effect of molecular vibrations on the singlet fission coupling.

There are many projects that could follow from the research described here. It would be useful to extend localized diabatization methods to encompass the spin-flip XCIS [99–101] description of electronic states, which would provide a more accurate platform for modelling charge recombination. A number of algorithms have been made possible by the advent of inexpensive diabatic gradient quantities, including diabatic state minimization and low-energy avoided crossing optimization. Finally, there is the open question of how to accurately propagate nonadiabatic dynamics on a diabatic potential energy surface: although nonadiabatic dynamics methods such as fewest-switches surface hopping [127] can, in principle, be performed using any electronic representation, it is not yet clear how to handle

momentum conservation and manage the frequency of frustrated hops. Hopefully the work collected here will inform and inspire more original work in this exciting area of research.

APPENDIX

A.1. Overview of the spin boson model

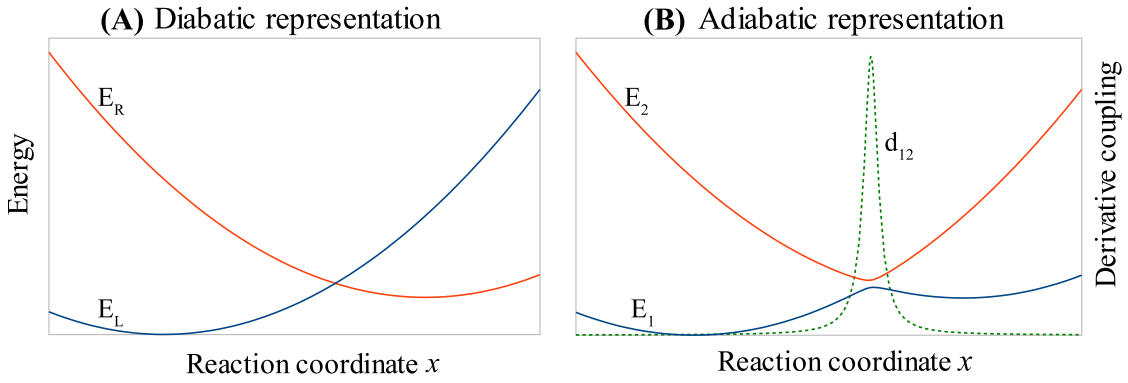

Figure 34: **(A)** Potential energy surfaces of a spin boson system in the diabatic representation. The derivative coupling between the two diabatic states is zero by assumption, but the diabatic coupling (not pictured) is constant with respect to the reaction coordinate x. **(B)** Potential energy surfaces in the adiabatic representation. The two energy surfaces no longer cross, and the diabatic coupling is now zero. The derivative coupling (d_{12}) is small except for a peak near the avoided crossing.

The spin boson model is a one-dimensional, two-level system that can be used to model electron and energy transfer. We will use it here as an idealized illustration of the difference between the adiabatic and strictly diabatic representations, and give insight into the nature of derivative couplings. The energy levels of the two states are given by two shifted parabolas with identical curvatures (ω), referred to here as either the left ($|\Xi_L\rangle$) or right ($|\Xi_R\rangle$) states, as depicted in Fig. 34A. The diabatic coupling (V) between the states is taken to be constant as a function of the single reaction coordinate (x), so that the full Hamiltonian in atomic units is given by

$$H = T + W = \frac{p^2}{2}\begin{pmatrix} 1 & 0 \\ 0 & 1 \end{pmatrix} + \begin{pmatrix} \frac{1}{2}\omega^2 x^2 + Mx & V \\ V & \frac{1}{2}\omega^2 x^2 - Mx + \epsilon_0 \end{pmatrix}, \tag{A.1}$$

where p is the momentum operator, $M > 0$ defines the separation between the states in coordinate space, and $\epsilon_0 \geq 0$ is a 'driving force' that defines the energy difference between

the minima associated with the two states. This system is defined in the strictly diabatic basis, so the derivative coupling ($d_{RL}(x) = \langle \Xi_L(x) | \frac{\partial}{\partial x} | \Xi_R(x) \rangle$) is zero by assumption.

One can obtain the adiabatic representation of this system, depicted in Fig. 34B, by diagonalizing the potential matrix W. The resulting eigenvalue energies are given by

$$E_1(x) = \frac{1}{2}\omega^2 x^2 + \frac{\epsilon_0}{2} - \sqrt{(\frac{\epsilon_0}{2} - Mx)^2 + V^2} \tag{A.2}$$

and

$$E_2(x) = \frac{1}{2}\omega^2 x^2 + \frac{\epsilon_0}{2} + \sqrt{(\frac{\epsilon_0}{2} - Mx)^2 + V^2}. \tag{A.3}$$

The corresponding adiabatic wavefunctions are given by

$$|\Phi_1(x)\rangle = \begin{pmatrix} \sqrt{\frac{1}{2} - \frac{1}{2}\frac{Mx - \epsilon_0/2}{\sqrt{(Mx-\epsilon_0/2)^2+V^2}}} \\ \sqrt{\frac{1}{2} + \frac{1}{2}\frac{Mx - \epsilon_0/2}{\sqrt{(Mx-\epsilon_0/2)^2+V^2}}} \end{pmatrix} \tag{A.4}$$

and

$$|\Phi_2(x)\rangle = \begin{pmatrix} \sqrt{\frac{1}{2} + \frac{1}{2}\frac{Mx - \epsilon_0/2}{\sqrt{(Mx-\epsilon_0/2)^2+V^2}}} \\ \sqrt{\frac{1}{2} - \frac{1}{2}\frac{Mx - \epsilon_0/2}{\sqrt{(Mx-\epsilon_0/2)^2+V^2}}} \end{pmatrix} \tag{A.5}$$

The derivative coupling between the two adiabatic states can then be found through direct differentiation,

$$d_{12}(x) = \left\langle \Phi_1(x) \left| \frac{\partial}{\partial x} \right| \Phi_2(x) \right\rangle = \frac{1}{2}\frac{MV}{(Mx - \epsilon_0/2)^2 + V}. \tag{A.6}$$

It is trivial to show that in the adiabatic basis, the avoided crossing at which the energy difference $E_2(x) - E_1(x)$ is minimized corresponds with the point at which the derivative coupling is maximized.

A.2. Generalization of BoysOV

While the Boys representation is defined in terms of the excitation dipole matrix, X_{AB}, the BoysOV representation is defined in terms of partitions of the this matrix, including the occupied component X_{AB}^{occ}, and the virtual component X_{AB}^{virt}, such that their sum equals the full excitation dipole matrix, $X_{AB} = X_{AB}^{\text{occ}} + X_{AB}^{\text{virt}}$. This partitioning is trivially defined for CIS and TD-DFT/TDA because both of these methods involve only single excitations from a reference ground state (see Eqs. 5.7 and 5.8). For any more sophisticated wavefunction ansatz, however, the partitioning process is not as clear.

Although it may not always be physical, a reasonable partitioning of the dipole matrix can be defined, provided there is a single determinant reference ground state. For example, one can write state dipole matrix elements in the molecular orbital basis,

$$X_{AB} = \sum_{r,s} X^{rs} D_{AB}^{rs} \tag{A.7}$$

for some excitation density matrix $\mathbf{D}$. The density matrix can be split into occupied and virtual components, $D_{AB}^{rs} = D_{AB}^{rs,\text{occ}} + D_{AB}^{rs,\text{virt}}$ as follows:

$$D_{AB}^{rs,\text{occ}} = \begin{cases} D_{AB}^{rs} & \text{if } r,s \in \text{ occ}, \\ \frac{1}{2} D_{AB}^{rs} & \text{if } r \in \text{ occ and } s \in \text{ virt, or } s \in \text{ occ and } r \in \text{ virt, and} \\ 0 & \text{if } r,s \in \text{ virt}, \end{cases} \tag{A.8}$$

with $D_{AB}^{rs,\text{virt}}$ defined in an analogous manner. The occupied and virtual components of the dipole matrix can then be written as

$$X_{AB}^{\text{occ}} = \sum_{r,s} X^{rs} D_{AB}^{rs,\text{occ}} \tag{A.9}$$

and

$$X_{AB}^{\text{virt}} = \sum_{r,s} X^{rs} D_{AB}^{rs,\text{virt}}. \tag{A.10}$$

A.3. Calculation of finite difference derivative couplings within the CIS formalism

The central difference approximation to the derivative of a function $f(x)$ is given by

$$\left.\frac{df(x)}{dx}\right|_{x_0} \approxeq \frac{f(x_0+h)-f(x_0-h)}{2h} \tag{A.11}$$

for some small h. In the case of derivative couplings, we wish to approximate the quantity $d_{IJ}^{[Q]}(\mathbf{x}) = \langle \Phi_I(\mathbf{x}) | \frac{\partial}{\partial x_Q} \Phi_J(\mathbf{x}) \rangle$ for some nuclear degree of freedom x_Q, which we approximate by the expression

$$d_{IJ}^{[Q]}(\mathbf{x}) \approxeq \frac{\langle \Phi_I(\mathbf{x}) | \Phi_J(\mathbf{x}+\mathbf{h}_Q) \rangle - \langle \Phi_I(\mathbf{x}) | \Phi_J(\mathbf{x}-\mathbf{h}_Q) \rangle}{2|\mathbf{h}_Q|}. \tag{A.12}$$

The challenge of calculating this quantity lies mainly in obtaining the overlap between CIS states at different nuclear geometries, $\langle \Phi_I | \Phi'_J \rangle$, where $|\Phi\rangle$ and $|\Phi'\rangle$ denote CIS states belonging to two distinct but similar nuclear geometries. Each CIS state–either adiabatic or localized diabatic–is a linear combination of singly-excited determinants of the reference state,

$$|\Phi_I\rangle = \sum_{i,a} t_i^{Ia} |\Phi_i^a\rangle \tag{A.13}$$

so that the total overlap between CIS states can be written

$$\langle \Phi_I | \Phi'_J \rangle = \sum_{ijab} t_i^{Ia} t_j^{Jb\prime} \langle \Phi_i^a | \Phi_j^{b\prime} \rangle. \tag{A.14}$$

To further expand this expression, we first note that because the two determinants are associated with different nuclear geometries, they are comprised of non-orthogonal MOs. Consequently, every possible combination of the $N!$ terms that comprise each determinant must be considered. We must also keep track of the sign of each of the overlap contributions.

This expression reduces to a determinant of overlaps, and is given in Eq. A.15.

$$\begin{aligned}\langle\Phi_i^a|\Phi_j^{b\prime}\rangle &= \frac{1}{N!}\left(\sum_\sigma \mathrm{sgn}(\sigma)\prod_{k=1}^{N}\langle\phi_{f(k)}(\sigma(k))|\right)\left(\sum_\sigma \mathrm{sgn}(\sigma)\prod_{l=1}^{N}|\phi'_{g(l)}(\sigma(l))\rangle\right)\\ &= \sum_\sigma \mathrm{sgn}(\sigma)\prod_{k=1}^{N}\langle\phi_{f(k)}|\phi'_{g(\sigma(k))}\rangle\\ &= \det\begin{pmatrix} \langle\phi_{f(1)}|\phi'_{g(1)}\rangle & \langle\phi_{f(1)}|\phi'_{g(2)}\rangle & \cdots & \langle\phi_{f(1)}|\phi'_{g(N)}\rangle \\ \langle\phi_{f(2)}|\phi'_{g(1)}\rangle & \langle\phi_{f(2)}|\phi'_{g(2)}\rangle & \cdots & \langle\phi_{f(2)}|\phi'_{g(N)}\rangle \\ \vdots & \vdots & \ddots & \vdots \\ \langle\phi_{f(N)}|\phi'_{g(1)}\rangle & \langle\phi_{f(N)}|\phi'_{g(2)}\rangle & \cdots & \langle\phi_{f(N)}|\phi'_{g(N)}\rangle \end{pmatrix}.\end{aligned} \tag{A.15}$$

Here, $|\phi_k(l)\rangle$ is the k$^{\text{th}}$ MO occupied by the l$^{\text{th}}$ electron. σ indexes a set of $N!$ permutation operators that act on the MO indices that describe each of the possible arrangements of the N electrons into N orbitals. These in turn are acted upon by the sign function (sgn), which returns either 1 if σ is even or -1 if σ is odd. Finally, the functions f and g are excitation operators associated with the states $|\Phi_i^a\rangle$ and $|\Phi_j^{b\prime}\rangle$, respectively. The function f is defined by its action upon the MO indices as follows:

$$f(k) = \begin{cases} a & k = i \\ k & k \neq i \end{cases}, \tag{A.16}$$

and similarly,

$$g(k) = \begin{cases} b & k = j \\ k & k \neq j \end{cases}. \tag{A.17}$$

The MO overlap terms from the determinant, $\langle\phi_r|\phi'_s\rangle$, are obtained from the expression

$$\langle\phi_r|\phi'_s\rangle = \sum_{\mu\nu} C_{r\mu} S'_{\mu\nu} C'_{\nu s}, \tag{A.18}$$

where $C_{r\mu}$ is a MO coefficient, and $S'_{\mu\nu} = \langle\chi_\mu|\chi'_\nu\rangle$ is a cross-geometry AO overlap.

Several practical concerns must be addressed when calculating these overlaps. The first is:

how can the most fundamental quantity, the cross-geometry AO overlap $\langle\mu|\nu'\rangle$ be obtained? The simplest solution[1] is to begin a single point calculation using nuclear coordinates from both geometries. In the Q-CHEM electronic structure package,[102,158] the overlap matrix $S_{\mu\nu}$ is calculated and saved to disk before the program inevitably crashes due to the unphysical proximity of the nuclei from the two configurations. This data can be recovered and used for a second set of calculations, in which the MOs and CIS amplitudes at the two distinct geometries are calculated separately.

Another concern is the cost of such a calculation: for a derivative coupling calculation involving n CIS states, $n \times N_{\text{occ}} \times N_{\text{virt}}$ determinants must be calculated from overlap matrices with dimensions $N \times N$. This can become a very time-consuming calculation for large systems. Fortunately, there are several levels of approximation. The first is to simply ignore the change in MOs, and describe the cross-geometry overlap of CIS states only in terms of the CIS excitation amplitudes as in Eq. 4.14. A more accurate description can be achieved by including only the product of the diagonal of the overlap matrix in Eq. A.15, instead of the full overlap determinant. Assuming the geometry difference is small, the MOs should not be dramatically different between the two geometries, so the product along the diagonal can be expected to be the dominant contribution to the full overlap determinant.

A.4. Calculation of the self-interaction term

In this chapter, when describing ER-ε diabatization, we slightly modify the definition of the R_{AAAA} tensor as compared with Ref. 63. Previously, we had defined

$$R_{IJKL} = \int \mathrm{d}\mathbf{r}_1 \int \mathrm{d}\mathbf{r}_2 \frac{\langle\Phi_I|\hat{\rho}(\mathbf{r}_1)|\Phi_J\rangle\langle\Phi_K|\hat{\rho}(\mathbf{r}_2)|\Phi_L\rangle}{|\mathbf{r}_1 - \mathbf{r}_2|} \tag{A.19}$$

$$= \sum_{pqrs} D^{IJ}_{pq}(pq|rs)D^{KL}_{rs}, \tag{A.20}$$

[1] Provided to us by Yihan Shao of Q-Chem, Inc.

where $(pq|rs)$ is the two-electron Coulomb integral

$$(pq|rs) = \int \mathrm{d}\mathbf{r}_1 \int \mathrm{d}\mathbf{r}_2 \phi_p^*(\mathbf{r}_1)\phi_q(\mathbf{r}_1)\frac{1}{|\mathbf{r}_1 - \mathbf{r}_2|}\phi_r^*(\mathbf{r}_2)\phi_s(\mathbf{r}_2), \tag{A.21}$$

for molecular orbitals ϕ, and the density matrix D for CIS states is

$$D_{pq}^{IJ} = \langle \Phi_I | c_p^\dagger c_q | \Phi_J \rangle \tag{A.22}$$

$$= \begin{cases} \sum_i t_i^{I,p} t_i^{J,q}, & \text{if } p,q \text{ are virtual} \\ -\sum_a t_q^{I,a} t_p^{J,a} + \delta_{pq}\delta_{IJ}, & \text{if } p,q \text{ are occupied,} \end{cases} \tag{A.23}$$

where $c^\dagger$ and c are creation and annihilation operators, respectively, and t is a CIS amplitude. In this chapter, when calculating R_{IJKL} in the context of ER-ε diabatization, we neglect the term $\delta_{pq}\delta_{IJ}$. Our rationale for doing so is that this term corresponds to the stationary unexcited (negatively charged) electrons, whose electric field is largely canceled by the background of (positively charged) nuclei. Of course, the same assumption could be made in the calculation of ER diabatic states, but doing so would not affect the ER algorithm at all. Because the trace of a matrix is invariant unitary transformation, it is easy to show that the resultant ER diabatic states are entirely independent of the $\delta_{pq}\delta_{IJ}$ term.

A.5. The Jacobi method applied to diabatization function optimization

The Jacobi sweeps algorithm, originally used for orbital localization algorithms,[61,62,245] is also commonly used to optimize localized diabatization functions.[63,64] Briefly, the Jacobi algorithm is used in this context to optimize a diabatization function f of a $n \times n$ adiabatic-to-diabtic rotation matrix $\mathbf{U}$, where n is the number of states considered in the calculation. It does so by iterating over pairs of states $\{A, B\}$ and finding the optimum value of f as only a functon of those two states; in other words, for each pair of states, f is optimized for a 2×2 matrix $\mathbf{U}_2$, which only describes mixing between states A and B. This iteration over state pairs is performed until convergence is achieved.

For Boys an ER localization, which are both quartic functions of the unitary adiabatic-to-diabatic transformation matrix $\mathbf{U}$, the Jacobi algorithm offers rapid convergence because the two-state case has a simple analytic solution.[61] For more complex functions of $\mathbf{U}$, such as for ER-ε diabatization, no such analytic solution is available. However, because n is usually small, the efficiency of the two-state optimization is usually unimportant in the context of the electronic structure calculation that preceeds diabatization. For a two-state unitary mixing, the adiabatic-to-diabatic rotation matrix is given by

$$U_2 = \begin{pmatrix} \cos(\theta) & -\sin(\theta) \\ \sin(\theta) & \cos(\theta) \end{pmatrix}, \tag{A.24}$$

where θ is the so-called 'mixing angle' which only need be considered on the interval $[0, \frac{\pi}{4}]$, as other values will produce the same states (up to a sign). Given this small search space, it is possible to use even crude optimization methods that do not even require first derivatives of the diabatization function. One such approach is to calculate $f(\mathbf{U}_2) = f(\theta)$ at some small number (e.g., 10) of evenly-spaced values of the mixing angle, $0 \leq \theta \leq \frac{\pi}{4}$. This search will result in a bracket around the global optimum value of f, which can be refined using the golden section search or similar algorithm.

A.6. The equivalence of the Hellmann-Feynman and direct differentiation DCs

The derivative coupling expression in the current work is derived from a modified Hellmann-Feynman approach (starting from Eq. 6.39, we obtain Eqs. 6.65 and 6.66). In Ref. 181 we start with Eq. 6.38 to obtain the final result. By inspection, these two expressions agree– with the exception of the antisymmetric AO overlap gradient terms. Thus, to explicitly show that these two DC expressions are fully equivalent, we must reconcile only the apparent differences between the $S^{A[Q]}$ terms given in the current work by $G^{IJ} = G^{\mathrm{A},IJ} + G^{\mathrm{B},IJ}$, the sum of Eqs. 6.50 and 6.64, and in Eq. 50 in Ref. 181.

To show that these expressions are equivalent, we will transform our results into those of

Ref. 181. We first note that several terms in G are symmetric under exchange of μ and ν. The trace of these contributions with the antisymmetric $S^{A[Q]}$ must therefore be zero and so these terms can be discarded. Second, we note that following directly from the TDHF eigenvalue equations (Eq. 2.44), we must have

$$\sum_{jb} \left(\Pi_{ibaj} X_j^{Ib} + \Pi_{abij} Y_j^{Ib} \right) = \left(E_I + \varepsilon_i - \varepsilon_a \right) X_i^{Ia} \tag{A.25}$$

and

$$\sum_{jb} \left(\Pi_{ibaj} Y_j^{Ib} + \Pi_{abij} X_j^{Ib} \right) = \left(-E_I + \varepsilon_i - \varepsilon_a \right) Y_i^{Ia}. \tag{A.26}$$

Making use of these expressions in the context of the remaining terms of G, we arrive at

$$\begin{aligned} G_{\mu\nu} = \frac{1}{E_J - E_I} \Bigg[& \sum_{ijabc} C_{\mu c} C_{\nu a} \left[\left(E_I + \varepsilon_i \right) X_i^{Ia} X_i^{Jc} + \left(E_J + \varepsilon_i \right) X_i^{Ic} X_i^{Ja} \right] \\ & - \sum_{ijkab} C_{\mu i} C_{\nu k} \left[\left(E_I - \varepsilon_a \right) X_i^{Ia} X_k^{Ja} + \left(E_J - \varepsilon_a \right) X_k^{Ia} X_i^{Ja} \right] \\ & + \sum_{ijabc} C_{\mu c} C_{\nu a} \left[\left(-E_I + \varepsilon_i \right) Y_i^{Ia} Y_i^{Jc} + \left(-E_J + \varepsilon_i \right) Y_i^{Ic} Y_i^{Ja} \right] \\ & - \sum_{ijkab} C_{\mu i} C_{\nu k} \left[\left(-E_I - \varepsilon_a \right) Y_i^{Ia} Y_k^{Ja} + \left(-E_J - \varepsilon_a \right) Y_k^{Ia} Y_i^{Ja} \right] \Bigg]. \end{aligned} \tag{A.27}$$

By writing

$$C_{\mu c} C_{\nu a} = \frac{1}{2} \left(C_{\mu c} C_{\nu a} + C_{\nu c} C_{\mu a} \right) + \frac{1}{2} \left(C_{\mu c} C_{\nu a} - C_{\nu c} C_{\mu a} \right), \tag{A.28}$$

we can partition the first term of Eq. A.27 into two components: one that is symmetric under exchange of μ and ν, and one that is antisymmetric under such an exchange. By using this transformation to selectively eliminate symmetric (non-contributing) terms and rearrange the MO indices on the amplitudes, we obtain our final expression

$$G_{\mu\nu} = -\sum_{iab} C_{\mu b} C_{\nu a} \left(X_i^{Ia} X_i^{Jb} - Y_i^{Ia} Y_i^{Jb} \right) - \sum_{ija} C_{\mu j} C_{\nu i} \left(X_i^{Ia} X_j^{Ja} - Y_i^{Ia} Y_j^{Ja} \right) \tag{A.29}$$

in which the energy difference denominator is eliminated in a manner similar to that achieved for the analogous term in the CIS derivative coupling expression (cf. Eq. A25 of Ref. 67). Thus we have explicitly shown that Eq. A.29 is equivalent to the $S^{A[Q]}$ term derived in Eq. 50 of Ref. 181.

BIBLIOGRAPHY

[1] Berkelbach, T. C.; Hybertsen, M. S.; Reichman, D. R. *The Journal of Chemical Physics* **2013**, *138*.

[2] Berkelbach, T. C.; Hybertsen, M. S.; Reichman, D. R. *The Journal of Chemical Physics* **2013**, *138*.

[3] Zeng, T.; Hoffmann, R.; Ananth, N. *Journal of the American Chemical Society* **2014**, *136*, 5755–5764.

[4] Werner, H.-J.; Meyer, W. *The Journal of Chemical Physics* **1981**, *74*, 5802–5807.

[5] Vallett, P. J.; Snyder, J. L.; Damrauer, N. H. *The Journal of Physical Chemistry A* **2013**, *117*, 10824–10838.

[6] Smith, M. B.; Michl, J. *Chemical Reviews* **2010**, *110*, 6891–6936.

[7] Smith, M. B.; Michl, J. *Annual Review of Physical Chemistry* **2013**, *64*, 361–386.

[8] Hanwell, M. D.; Curtis, D. E.; Lonie, D. C.; Vandermeersch, T.; Zurek, E.; Hutchison, G. R. *Journal of Cheminformatics* **2012**, *4*, 17.

[9] Holmes, D.; Kumaraswamy, S.; Matzger, A. J.; Vollhardt, K. P. C. *Chem.–Eur. J.* **1999**, *5*, 3399–3412.

[10] Fatehi, S.; Alguire, E.; Subotnik, J. E. *The Journal of Chemical Physics* **2013**, *139*, 124112.

[11] Closs, G. L.; Piotrowiak, P.; MacInnis, J. M.; Fleming, G. R. *Journal of the American Chemical Society* **1988**, *110*, 2652–2653.

[12] Szabo, A.; Ostlund, N. *Modern Quantum Chemistry*; McGraw-Hill: New York, 1996; pp 39–107.

[13] Ben-Nun, M.; Martnez, T. J. *Chemical Physics Letters* **1998**, *298*, 57 – 65.

[14] Boys, S. F. *Proceedings of the Royal Society of London A: Mathematical, Physical and Engineering Sciences* **1950**, *200*, 542–554.

[15] Taketa, H.; Huzinaga, S.; O-ohata, K. *Journal of the Physical Society of Japan* **1966**, *21*, 2313–2324.

[16] Živković, T.; Maksić, Z. B. *The Journal of Chemical Physics* **1968**, *49*, 3083–3087.

[17] McMurchie, L. E.; Davidson, E. R. *Journal of Computational Physics* **1978**, *26*, 218 – 231.

[18] Pople, J. A.; Hehre, W. J. *Journal of Computational Physics* **1978**, *27*, 161 – 168.

[19] Obara, S.; Saika, A. *The Journal of Chemical Physics* **1986**, *84*, 3963–3974.

[20] Gill, P. M. W.; Pople, J. A. *International Journal of Quantum Chemistry* **1991**, *40*, 753–772.

[21] Krylov, A. I. *Chemical Physics Letters* **2001**, *338*, 375 – 384.

[22] Krylov, A. I. *Chemical Physics Letters* **2001**, *350*, 522 – 530.

[23] Krylov, A. I.; Sherrill, C. D. *The Journal of Chemical Physics* **2002**, *116*, 3194–3203.

[24] Bene, J. E. D.; Ditchfield, R.; Pople, J. A. *The Journal of Chemical Physics* **1971**, *55*, 2236–2241.

[25] Cave, R. J. In *Modern Electronic Structure Theory and Applications in Organic Chemistry*; Davidson, E. R., Ed.; World Scientific: Singapore, 1997; pp 197–256.

[26] Dreuw, A.; Weisman, J. L.; Head-Gordon, M. *The Journal of Chemical Physics* **2003**, *119*, 2943–2946.

[27] Subotnik, J. E. *The Journal of Chemical Physics* **2011**, *135*, 071104.

[28] Dirac, P. A. M. *Mathematical Proceedings of the Cambridge Philosophical Society* **1930**, *26*, 376–385.

[29] Bohm, D.; Pines, D. *Phys. Rev.* **1951**, *82*, 625–634.

[30] Pines, D.; Bohm, D. *Phys. Rev.* **1952**, *85*, 338–353.

[31] Bohm, D.; Pines, D. *Phys. Rev.* **1953**, *92*, 609–625.

[32] McLachlan, A. D.; Ball, M. A. *Rev. Mod. Phys.* **1964**, *36*, 844–855.

[33] Dreuw, A.; Head-Gordon, M. *Chemical reviews* **2005**, *105*, 4009–4037.

[34] Baer, M. *Chemical Physics Letters* **1975**, *35*, 112 – 118.

[35] Top, Z. H.; Baer, M. *The Journal of Chemical Physics* **1977**, *66*, 1363–1371.

[36] Halász, G. J.; Vibók, A.; Suhai, S.; Baer, M. *The Journal of Chemical Physics* **2007**, *127*, 244101.

[37] Mead, C. A.; Truhlar, D. G. *The Journal of Chemical Physics* **1982**, *77*, 6090–6098.

[38] Van Voorhis, T.; Kowalczyk, T.; Kaduk, B.; Wang, L.-P.; Cheng, C.-L.; Wu, Q. *Annual Review of Physical Chemistry* **2010**, *61*, 149–170.

[39] Baer, M. *Molecular Physics* **1980**, *40*, 1011–1013.

[40] Thiel, A.; Köppel, H. *The Journal of Chemical Physics* **1999**, *110*, 9371–9383.

[41] Köppel, H.; Gronki, J.; Mahapatra, S. *The Journal of Chemical Physics* **2001**, *115*, 2377–2388.

[42] Pacher, T.; Cederbaum, L. S.; Köppel, H. *The Journal of Chemical Physics* **1988**, *89*, 7367–7381.

[43] Pacher, T.; Cederbaum, L. S.; Köppel, H. In *Adiabatic and Quasiadiabatic States in a Gauge Theoretical Framework*; Prigogine, I., Rice, S. A., Eds.; Advances in Chemical Physics; Wiley, 1993; Vol. 84; pp 293–391.

[44] Ruedenberg, K.; Atchity, G. J. *The Journal of Chemical Physics* **1993**, *99*, 3799–3803.

[45] Atchity, G. J.; Ruedenberg, K. *Theoretical Chemistry Accounts: Theory, Computation, and Modeling (Theoretica Chimica Acta)* **1997**, *97*, 47–58.

[46] Nakamura, H.; Truhlar, D. G. *The Journal of Chemical Physics* **2001**, *115*, 10353–10372.

[47] Nakamura, H.; Truhlar, D. G. *The Journal of Chemical Physics* **2002**, *117*, 5576–5593.

[48] Wu, Q.; Van Voorhis, T. *Phys. Rev. A* **2005**, *72*, 024502.

[49] Wu, Q.; Van Voorhis, T. *The Journal of Physical Chemistry A* **2006**, *110*, 9212–9218.

[50] Wu, Q.; Voorhis, T. V. *The Journal of Chemical Physics* **2006**, *125*, 164105.

[51] Wu, Q.; Van Voorhis, T. *Journal of Chemical Theory and Computation* **2006**, *2*, 765–774.

[52] Voityuk, A. A.; Rösch, N. *The Journal of Chemical Physics* **2002**, *117*, 5607–5616.

[53] Hsu, C.-P.; You, Z.-Q.; Chen, H.-C. *The Journal of Physical Chemistry C* **2008**, *112*, 1204–1212.

[54] Chen, H.-C.; You, Z.-Q.; Hsu, C.-P. *The Journal of Chemical Physics* **2008**, *129*, 084708.

[55] Cave, R. J.; Newton, M. D. *Chemical Physics Letters* **1996**, *249*, 15 – 19.

[56] Cave, R. J.; Newton, M. D. *The Journal of Chemical Physics* **1997**, *106*, 9213–9226.

[57] Subotnik, J. E.; Yeganeh, S.; Cave, R. J.; Ratner, M. A. *The Journal of Chemical Physics* **2008**, *129*, 244101.

[58] Boys, S. F. *Rev. Mod. Phys.* **1960**, *32*, 296–299.

[59] Foster, J. M.; Boys, S. F. *Rev. Mod. Phys.* **1960**, *32*, 300–302.

[60] Boys, S. F. *Quantum Theory of Atoms, Molecules and the Solid State: A Tribute to John C. Slater*; Academic Press, 1966; pp 253–262.

[61] Edmiston, C.; Ruedenberg, K. *Rev. Mod. Phys.* **1963**, *35*, 457–464.

[62] Kleier, D. A.; Halgren, T. A.; John H. Hall, J.; Lipscomb, W. N. *The Journal of Chemical Physics* **1974**, *61*, 3905–3919.

[63] Subotnik, J. E.; Vura-Weis, J.; Sodt, A. J.; Ratner, M. A. *The Journal of Physical Chemistry A* **2010**, *114*, 8665–8675.

[64] Subotnik, J. E.; Cave, R. J.; Steele, R. P.; Shenvi, N. *The Journal of Chemical Physics* **2009**, *130*, 234102.

[65] Alguire, E.; Subotnik, J. E. *The Journal of Chemical Physics* **2012**, *137*, 194108.

[66] Yarkony, D. *Journal of Physical Chemistry A* **1998**, *102*, 8073–8077.

[67] Fatehi, S.; Alguire, E.; Shao, Y.; Subotnik, J. E. *The Journal of Chemical Physics* **2011**, *135*, 234105.

[68] Alguire, E.; Subotnik, J. E. *The Journal of Chemical Physics* **2011**, *135*, 044114.

[69] Newton, M. D. *Chemical Reviews* **1991**, *91*, 767–792.

[70] Newton, M. D. *International Journal of Quantum Chemistry: Quantum Chemistry Symposium* **1980**, *14*, 363–391.

[71] Logan, J.; Newton, M. D. *The Journal of Chemical Physics* **1983**, *78*, 4086–4091.

[72] Newton, M. D. *The Journal of Physical Chemistry* **1986**, *90*, 3734–3739.

[73] Newton, M. D. *The Journal of Physical Chemistry* **1988**, *92*, 3049–3056.

[74] Cave, R. J.; Baxter, D. V.; III, W. A. G.; Baldeschwieler, J. D. *The Journal of Chemical Physics* **1987**, *87*, 926–935.

[75] Broo, A.; Larsson, S. *Chemical Physics* **1990**, *148*, 103 – 115.

[76] Braga, M.; Broo, A.; Larsson, S. *Chemical Physics* **1991**, *156*, 1 – 9.

[77] Rosso, K. M.; Smith, D. M. A.; Dupuis, M. *The Journal of Physical Chemistry A* **2004**, *108*, 5242–5248.

[78] Farazdel, A.; Dupuis, M.; Clementi, E.; Aviram, A. *Journal of the American Chemical Society* **1990**, *112*, 4206–4214.

[79] Di Bella, S.; Lanza, G.; Fragal, I.; Yitzchaik, S.; Ratner, M. A.; Marks, T. J. *Journal of the American Chemical Society* **1997**, *119*, 3003–3006.

[80] Smith, F. T. *Phys. Rev.* **1969**, *179*, 111–123.

[81] O'Malley, T. F. *Diabatic States of Molecules– Quasistationary Electronic States*; Advances in Atomic and Molecular Physics; Academic Press, 1971; Vol. 7; pp 223–249.

[82] Hendeković, J. *Chemical Physics Letters* **1982**, *90*, 193–197.

[83] Pavlović, M.; Kučar, J.; Hendeković, J. *International Journal of Quantum Chemistry* **1987**, *32*, 705–710.

[84] Nakamura, H.; Truhlar, D. G. *The Journal of Chemical Physics* **2003**, *118*, 6816–6829.

[85] Hsu, C.-P. *Accounts of Chemical Research* **2009**, *42*, 509–518.

[86] Kawatsu, T.; Coropceanu, V.; Ye, A.; Bredas, J.-L. *The Journal of Physical Chemistry C* **2008**, *112*, 3429–3433.

[87] You, Z.-Q.; Shao, Y.; Hsu, C.-P. *Chemical Physics Letters* **2004**, *390*, 116 – 123.

[88] Yang, C.-H.; Hsu, C.-P. *The Journal of Chemical Physics* **2006**, *124*, 244507.

[89] Henderson, T. M.; Cave, R. J. *The Journal of Chemical Physics* **1998**, *109*, 7414–7423.

[90] Miller, N. E.; Wander, M. C.; Cave, R. J. *The Journal of Physical Chemistry A* **1999**, *103*, 1084–1093.

[91] Iordanova, N.; Dupuis, M.; Rosso, K. M. *The Journal of Chemical Physics* **2005**, *122*, 144305.

[92] Iordanova, N.; Dupuis, M.; Rosso, K. M. *The Journal of Chemical Physics* **2005**, *123*, 074710.

[93] Blancafort, L.; Voityuk, A. A. *The Journal of Physical Chemistry A* **2006**, *110*, 6426–6432.

[94] W. Domcke, H. K., D. R. Yarkony, Ed. *Conical Intersections: Electronic Structure, Dynamics and Spectroscopy*; Advanced Series in Physical Chemistry; World Scientific, 2004; Vol. 15.

[95] Cederbaum, L. S. *Conical Intersections: Electronic Structure, Dynamics and Spectroscopy*; Advanced Series in Physical Chemistry; World Scientific, 2004; Vol. 15; pp 3–40.

[96] Baer, M. *Beyond Born-Oppenheimer: Electronic Nonadiabatic Coupling terms and Conical Intersections*; Wiley, 2006.

[97] Creutz, C.; Newton, M. D.; Sutin, N. *Journal of Photochemistry and Photobiology A: Chemistry* **1994**, *82*, 47 – 59.

[98] Shao, Y.; Head-Gordon, M.; Krylov, A. I. *The Journal of Chemical Physics* **2003**, *118*, 4807–4818.

[99] Casanova, D.; Head-Gordon, M. *The Journal of Chemical Physics* **2008**, *129*, 064104.

[100] Casanova, D.; Slipchenko, L. V.; Krylov, A. I.; Head-Gordon, M. *The Journal of Chemical Physics* **2009**, *130*, 044103.

[101] Casanova, D.; Head-Gordon, M. *Phys. Chem. Chem. Phys.* **2009**, *11*, 9779–9790.

[102] Shao, Y. et al. *Phys. Chem. Chem. Phys.* **2006**, *8*, 3172–3191.

[103] Kahn, L. R.; Hay, P. J.; Shavitt, I. *The Journal of Chemical Physics* **1974**, *61*, 3530–3546.

[104] Botter, B.; Kooter, J.; Mulder, J. *Chemical Physics Letters* **1975**, *33*, 532 – 534.

[105] Charles W. Bauschlicher, J.; Langhoff, S. R. *The Journal of Chemical Physics* **1988**, *89*, 4246–4254.

[106] Varandas, A. J. C. *The Journal of Chemical Physics* **2009**, *131*, 124128.

[107] Lappe, J.; Cave, R. J.; Newton, M. D.; Rostov, I. V. *The Journal of Physical Chemistry B* **2005**, *109*, 6610–6619.

[108] Cave, R. J.; Edwards, S. T.; Kouzelos, J. A.; Newton, M. D. *The Journal of Physical Chemistry B* **2010**, *114*, 14631–14641.

[109] Braga, M.; Larsson, S. *Chemical Physics Letters* **1992**, *200*, 573 – 579.

[110] Cembran, A.; Song, L.; Mo, Y.; Gao, J. *Journal of Chemical Theory and Computation* **2009**, *5*, 2702–2716.

[111] Prezhdo, O. V.; Kindt, J. T.; Tully, J. C. *The Journal of Chemical Physics* **1999**, *111*, 7818–7827.

[112] You, Z.-Q.; Hsu, C.-P. *The Journal of Chemical Physics* **2010**, *133*, 074105.

[113] Ratner, M.; Schatz, G. *Quantum Mechanics in Chemistry*; Dover Publications: Mineola, NY, 2002.

[114] Nitzan, A. *Chemical Dynamics in Condensed Phases*; Oxford University Press: New York, 2006.

[115] Jasper, A. W.; Nangia, S.; Zhu, C.; Truhlar, D. G. *Accounts of Chemical Research* **2006**, *39*, 101–108.

[116] Herman, M. F. *The Journal of Chemical Physics* **1999**, *110*, 4141–4151.

[117] Herman, M. F. *The Journal of Chemical Physics* **1999**, *111*, 10427–10435.

[118] Yeganeh, S.; Voorhis, T. V. *The Journal of Chemical Physics* **2011**, *135*, 104114.

[119] Gehlen, J. N.; Chandler, D.; Kim, H. J.; Hynes, J. T. *The Journal of Physical Chemistry* **1992**, *96*, 1748–1753.

[120] Wang, H.; Thoss, M.; Miller, W. H. *The Journal of Chemical Physics* **2001**, *115*, 2979–2990.

[121] Holstein, T. *Annals of Physics* **1959**, *8*, 325 – 342.

[122] Holstein, T. *Annals of Physics* **1959**, *8*, 343 – 389.

[123] Hammond, J. R.; Kowalski, K.; deJong, W. A. *The Journal of Chemical Physics* **2007**, *127*, 144105.

[124] Rizzo, A.; Cappelli, C.; Jansík, B.; Jonsson, D.; ek, P. S.; Coriani, S.; gren, H. A. *The Journal of Chemical Physics* **2004**, *121*, 8814–8830.

[125] Ritchie, G. L.; Watson, J. N. *Chemical Physics Letters* **2000**, *322*, 143 – 148.

[126] Humphrey, W.; Dalke, A.; Schulten, K. *Journal of Molecular Graphics and Modelling* **1996**, *14*, 33–38.

[127] Tully, J. C. *The Journal of Chemical Physics* **1990**, *93*, 1061–1071.

[128] Ben-Nun, M.; Martinez, T. J. *The Journal of Chemical Physics* **1998**, *108*, 7244–7257.

[129] Ben-Nun, M.; Quenneville, J.; Martinez, T. J. *The Journal of Physical Chemistry A* **2000**, *104*, 5161–5175.

[130] Ben-Nun, M.; Martinez, T. J. *Advances in Chemical Physics*; John Wiley & Sons, Inc., 2002; pp 439–512.

[131] Evenhuis, C.; Martinez, T. J. *The Journal of Chemical Physics* **2011**, *135*, 224110.

[132] Alguire, E. C.; Fatehi, S.; Shao, Y.; Subotnik, J. E. *The Journal of Physical Chemistry A* **2014**, *118*, 11891–11900.

[133] Matsika, S.; Krause, P. *Annual Review of Physical Chemistry* **2011**, *62*, 621–643.

[134] Sadygov, R. G.; Yarkony, D. R. *The Journal of Chemical Physics* **1998**, *109*, 20–25.

[135] Zhu, X.; Yarkony, D. R. *The Journal of Chemical Physics* **2010**, *132*, 104101.

[136] Yarkony, D. *Journal of Chemical Physics* **1999**, *110*, 701–705.

[137] Kryachko, E. S.; Yarkony, D. R. *International Journal of Quantum Chemistry* **2000**, *76*, 235–243.

[138] Granucci, G.; Persico, M.; Toniolo, A. *The Journal of Chemical Physics* **2001**, *114*, 10608–10615.

[139] Plasser, F.; Granucci, G.; Pittner, J.; Barbatti, M.; Persico, M.; Lischka, H. *The Journal of Chemical Physics* **2012**, *137*, 22A514.

[140] Kapral, R.; Ciccotti, G. *The Journal of Chemical Physics* **1999**, *110*, 8919–8929.

[141] Ben-Nun, M.; Martínez, T. J. *The Journal of Chemical Physics* **2000**, *112*, 6113–6121.

[142] Ananth, N.; Venkataraman, C.; Miller, W. H. *The Journal of Chemical Physics* **2007**, *127*, 084114.

[143] Closs, G. L.; Johnson, M. D.; Miller, J. R.; Piotrowiak, P. *Journal of the American Chemical Society* **1989**, *111*, 3751–3753.

[144] Lengsfield, B. H.; Yarkony, D. R. *Journal of Chemical Physics* **1986**, *84*, 348.

[145] Saxe, P.; Yarkony, D. R. *Journal of Chemical Physics* **1987**, *86*, 321.

[146] Lengsfield, B. H.; Yarkony, D. R. *Advances in Chemical Physics* **1992**, *82*, 1–71.

[147] Yarkony, D. R. *Conical Intersections in Electron Photodetachment Spectroscopy: Theory and Applications*; Advanced Series in Physical Chemistry; World Scientific, 2004; Vol. 15; pp 129–174.

[148] Lengsfield, B. H.; Saxe, P.; Yarkony, D. R. *The Journal of Chemical Physics* **1984**, *81*, 4549–4553.

[149] Saxe, P.; III, B. H. L.; Yarkony, D. R. *Chemical Physics Letters* **1985**, *113*, 159 – 164.

[150] Lischka, H.; Dallos, M.; Shepard, R. *Molecular Physics* **2002**, *100*, 1647–1658.

[151] Lischka, H.; Dallos, M.; Szalay, P. G.; Yarkony, D. R.; Shepard, R. *The Journal of Chemical Physics* **2004**, *120*, 7322–7329.

[152] Dallos, M.; Lischka, H.; Shepard, R.; Yarkony, D. R.; Szalay, P. G. *The Journal of Chemical Physics* **2004**, *120*, 7330–7339.

[153] Jørgensen, P.; Simons, J. *The Journal of Chemical Physics* **1983**, *79*, 334–357.

[154] Helgaker, T. U.; Almlöf, J. *International Journal of Quantum Chemistry* **1984**, *26*, 275–291.

[155] Page, M.; Saxe, P.; Adams, G. F.; Lengsfield, B. H. *The Journal of Chemical Physics* **1984**, *81*, 434–439.

[156] Shepard, R. *International Journal of Quantum Chemistry* **1987**, *31*, 33–44.

[157] Shepard, R.; Lischka, H.; Szalay, P. G.; Kovar, T.; Ernzerhof, M. *The Journal of Chemical Physics* **1992**, *96*, 2085–2098.

[158] Krylov, A. I.; Gill, P. M. W. *WIREs Comput. Mol. Sci.* **2013**, *3*, 317–326.

[159] Alguire, E. C.; Ou, Q.; Subotnik, J. E. *The Journal of Physical Chemistry B* Available online.

[160] Berry, R. S. *The Journal of Chemical Physics* **1957**, *27*, 1288–1295.

[161] Ewing, J. J.; Milstein, R.; Berry, R. S. *The Journal of Chemical Physics* **1971**, *54*, 1752–1760.

[162] Tavernelli, I.; Curchod, B. F. E.; Laktionov, A.; Rothlisberger, U. *The Journal of Chemical Physics* **2010**, *133*, 194104.

[163] Hu, C.; Sugino, O.; Watanabe, K. *The Journal of Chemical Physics* **2014**, *140*, 054106.

[164] Ou, Q.; Fatehi, S.; Alguire, E.; Shao, Y.; Subotnik, J. E. *The Journal of Chemical Physics* **2014**, *141*.

[165] Chernyak, V.; Mukamel, S. *The Journal of Chemical Physics* **2000**, *112*, 3572–3579.

[166] Tommasini, M.; Chernyak, V.; Mukamel, S. *International Journal of Quantum Chemistry* **2001**, *85*, 225–238.

[167] Hu, C.; Hirai, H.; Sugino, O. *The Journal of Chemical Physics* **2007**, *127*, 064103.

[168] Hu, C.; Hirai, H.; Sugino, O. *The Journal of Chemical Physics* **2008**, *128*, 154111.

[169] Hu, C.; Sugino, O.; Tateyama, Y. *The Journal of Chemical Physics* **2009**, *131*, 114101.

[170] Hu, C.; Sugino, O.; Hirai, H.; Tateyama, Y. *Phys. Rev. A* **2010**, *82*, 062508.

[171] Tapavicza, E.; Tavernelli, I.; Rothlisberger, U. *Phys. Rev. Lett.* **2007**, *98*, 023001.

[172] Tavernelli, I.; Tapavicza, E.; Rothlisberger, U. *The Journal of Chemical Physics* **2009**, *130*, 124107.

[173] Tavernelli, I.; Curchod, B. F. E.; Rothlisberger, U. *The Journal of Chemical Physics* **2009**, *131*, 196101.

[174] Tavernelli, I.; Tapavicza, E.; Rothlisberger, U. *Journal of Molecular Structure: {THEOCHEM}* **2009**, *914*, 22 – 29, Time-dependent density-functional theory for molecules and molecular solids.

[175] Send, R.; Furche, F. *The Journal of Chemical Physics* **2010**, *132*, 044107.

[176] Li, Z.; Liu, W. *The Journal of Chemical Physics* **2014**, *141*, 014110.

[177] Casida, M. E. In *Recent Advances in Density Functional Methods*; Chong, D. P., Ed.; World Scientific: Singapore, 1995; Chapter 5, pp 155–192.

[178] Pulay, P. *Molecular Physics* **1969**, *17*, 197–204.

[179] Thorson, W. R.; Delos, J. B. *Phys. Rev. A* **1978**, *18*, 117–134.

[180] Tretiak, S.; Mukamel, S. *Chemical Reviews* **2002**, *102*, 3171–3212.

[181] Ou, Q.; Alguire, E. C.; Subotnik, J. E. *The Journal of Physical Chemistry B* **2014**, Available online.

[182] Ring, P.; Schuck, P. *The Nuclear Many-Body Problem*; Springer-Verlag: New York, NY, USA, 1980; Chapter 8, pp 280–397.

[183] Gerratt, J.; Mills, I. M. *The Journal of Chemical Physics* **1968**, *49*, 1719–1729.

[184] Pople, J. A.; Krishnan, R.; Schlegel, H. B.; Binkley, J. S. *International Journal of Quantum Chemistry* **1979**, *16*, 225–241.

[185] Pauli, W. In *Handbuch der Physik*; Geiger, H., Scheel, K., Eds.; Springer: New York, 1933; Vol. 24.

[186] Furche, F. *The Journal of Chemical Physics* **2001**, *114*, 5982–5992.

[187] Furche, F.; Ahlrichs, R. *The Journal of Chemical Physics* **2002**, *117*, 7433–7447.

[188] Alguire, E. C.; Subotnik, J. E.; Damrauer, N. H. *The Journal of Physical Chemistry A* **2015**, *119*, 299–311.

[189] Green, M. *Third Generation Photovoltaics*; Springer Series in Photonics; Springer-Verlag: Berlin, 2003; Vol. 12.

[190] Shockley, W.; Queisser, H. J. *Journal of Applied Physics* **1961**, *32*, 510–519.

[191] Hanna, M. C.; Nozik, A. J. *Journal of Applied Physics* **2006**, *100*, –.

[192] Burdett, J. J.; Bardeen, C. J. *Accounts of Chemical Research* **2013**, *46*, 1312–1320.

[193] Roberts, S. T.; McAnally, R. E.; Mastron, J. N.; Webber, D. H.; Whited, M. T.; Brutchey, R. L.; Thompson, M. E.; Bradforth, S. E. *Journal of the American Chemical Society* **2012**, *134*, 6388–6400.

[194] Walker, B. J.; Musser, A. J.; Beljonne, D.; Friend, R. H. *Nat Chem* **2013**, *5*, 1019–1024.

[195] Busby, E.; Berkelbach, T. C.; Kumar, B.; Chernikov, A.; Zhong, Y.; Hlaing, H.; Zhu, X.-Y.; Heinz, T. F.; Hybertsen, M. S.; Sfeir, M. Y.; Reichman, D. R.; Nuckolls, C.; Yaffe, O. *Journal of the American Chemical Society* **2014**, *136*, 10654–10660.

[196] Kolata, K.; Breuer, T.; Witte, G.; Chatterjee, S. *ACS Nano* **2014**, *8*, 7377–7383.

[197] Wilson, M. W. B.; Rao, A.; Ehrler, B.; Friend, R. H. *Accounts of Chemical Research* **2013**, *46*, 1330–1338.

[198] Mastron, J. N.; Roberts, S. T.; McAnally, R. E.; Thompson, M. E.; Bradforth, S. E. *The Journal of Physical Chemistry B* **2013**, *117*, 15519–15526.

[199] Lee, J.; Bruzek, M. J.; Thompson, N. J.; Sfeir, M. Y.; Anthony, J. E.; Baldo, M. A. *Advanced Materials* **2013**, *25*, 1445–1448.

[200] Johnson, J. C.; Nozik, A. J.; Michl, J. *Journal of the American Chemical Society* **2010**, *132*, 16302–16303.

[201] Schrauben, J. N.; Ryerson, J. L.; Michl, J.; Johnson, J. C. *Journal of the American Chemical Society* **2014**, *136*, 7363–7373.

[202] Johnson, J. C.; Nozik, A. J.; Michl, J. *Accounts of Chemical Research* **2013**, *46*, 1290–1299.

[203] Ryerson, J. L.; Schrauben, J. N.; Ferguson, A. J.; Sahoo, S. C.; Naumov, P.; Havlas, Z.; Michl, J.; Nozik, A. J.; Johnson, J. C. *The Journal of Physical Chemistry C* **2014**, *118*, 12121–12132.

[204] Wang, C.; Tauber, M. J. *Journal of the American Chemical Society* **2010**, *132*, 13988–13991.

[205] Dillon, R. J.; Piland, G. B.; Bardeen, C. J. *Journal of the American Chemical Society* **2013**, *135*, 17278–17281.

[206] Eaton, S. W.; Shoer, L. E.; Karlen, S. D.; Dyar, S. M.; Margulies, E. A.; Veldkamp, B. S.; Ramanan, C.; Hartzler, D. A.; Savikhin, S.; Marks, T. J.; Wasielewski, M. R. *Journal of the American Chemical Society* **2013**, *135*, 14701–14712.

[207] Congreve, D. N.; Lee, J.; Thompson, N. J.; Hontz, E.; Yost, S. R.; Reusswig, P. D.; Bahlke, M. E.; Reineke, S.; Van Voorhis, T.; Baldo, M. A. *Science* **2013**, *340*, 334–337.

[208] Lee, J.; Jadhav, P.; Reusswig, P. D.; Yost, S. R.; Thompson, N. J.; Congreve, D. N.; Hontz, E.; Van Voorhis, T.; Baldo, M. A. *Accounts of Chemical Research* **2013**, *46*, 1300–1311.

[209] Teichen, P. E.; Eaves, J. D. *The Journal of Physical Chemistry B* **2012**, *116*, 11473–11481.

[210] Parker, S. M.; Seideman, T.; Ratner, M. A.; Shiozaki, T. *The Journal of Physical Chemistry C* **2014**, *118*, 12700–12705.

[211] Yost, S. R. et al. *Nat Chem* **2014**, *6*, 492–497.

[212] Havenith, R. W.; de Gier, H. D.; Broer, R. *Molecular Physics* **2012**, *110*, 2445–2454.

[213] Beljonne, D.; Yamagata, H.; Brédas, J. L.; Spano, F. C.; Olivier, Y. *Phys. Rev. Lett.* **2013**, *110*, 226402.

[214] Casanova, D. *Journal of Chemical Theory and Computation* **2014**, *10*, 324–334.

[215] Mirjani, F.; Renaud, N.; Gorczak, N.; Grozema, F. C. *The Journal of Physical Chemistry C* **2014**, *118*, 14192–14199.

[216] Zimmerman, P. M.; Musgrave, C. B.; Head-Gordon, M. *Accounts of Chemical Research* **2013**, *46*, 1339–1347.

[217] Akimov, A. V.; Prezhdo, O. V. *Journal of the American Chemical Society* **2014**, *136*, 1599–1608.

[218] Chan, W.-L.; Berkelbach, T. C.; Provorse, M. R.; Monahan, N. R.; Tritsch, J. R.; Hybertsen, M. S.; Reichman, D. R.; Gao, J.; Zhu, X.-Y. *Accounts of Chemical Research* **2013**, *46*, 1321–1329.

[219] Renaud, N.; Sherratt, P. A.; Ratner, M. A. *The Journal of Physical Chemistry Letters* **2013**, *4*, 1065–1069.

[220] Feng, X.; Luzanov, A. V.; Krylov, A. I. *The Journal of Physical Chemistry Letters* **2013**, *4*, 3845–3852.

[221] Zeng, T.; Ananth, N.; Hoffmann, R. *Journal of the American Chemical Society* **2014**, *136*, 12638–12647.

[222] Müller, A. M.; Avlasevich, Y. S.; Schoeller, W. W.; Müllen, K.; Bardeen, C. J. *Journal of the American Chemical Society* **2007**, *129*, 14240–14250.

[223] Wang, L.; Olivier, Y.; Prezhdo, O. V.; Beljonne, D. *The Journal of Physical Chemistry Letters* **2014**, *5*, 3345–3353.

[224] Greyson, E. C.; Vura-Weis, J.; Michl, J.; Ratner, M. A. *The Journal of Physical Chemistry B* **2010**, *114*, 14168–14177.

[225] Berkelbach, T. C.; Hybertsen, M. S.; Reichman, D. R. *The Journal of Chemical Physics* **2014**, *141*.

[226] Kuhlman, T. S.; Kongsted, J.; Mikkelsen, K. V.; Møller, K. B.; Sølling, T. I. *Journal of the American Chemical Society* **2010**, *132*, 3431–3439.

[227] Zimmerman, P. M.; Bell, F.; Casanova, D.; Head-Gordon, M. *Journal of the American Chemical Society* **2011**, *133*, 19944–19952.

[228] Zimmerman, P. M.; Zhang, Z.; Musgrave, C. B. *Nat Chem* **2010**, *2*, 648–652.

[229] Grumstrup, E. M.; Johnson, J. C.; Damrauer, N. H. *Phys. Rev. Lett.* **2010**, *105*, 257403.

[230] Wilson, M. W. B.; Rao, A.; Johnson, K.; Glinas, S.; di Pietro, R.; Clark, J.; Friend, R. H. *Journal of the American Chemical Society* **2013**, *135*, 16680–16688.

[231] Burdett, J. J.; Gosztola, D.; Bardeen, C. J. *The Journal of Chemical Physics* **2011**, *135*.

[232] Tayebjee, M. J. Y.; Clady, R. G. C. R.; Schmidt, T. W. *Phys. Chem. Chem. Phys.* **2013**, *15*, 14797–14805.

[233] Johnson, J. C.; Akdag, A.; Zamadar, M.; Chen, X.; Schwerin, A. F.; Paci, I.; Smith, M. B.; Havlas, Z.; Miller, J. R.; Ratner, M. A.; Nozik, A. J.; Michl, J. *The Journal of Physical Chemistry B* **2013**, *117*, 4680–4695.

[234] Scholes, G. D.; Ghiggino, K. P.; Oliver, A. M.; Paddon-Row, M. N. *Journal of the American Chemical Society* **1993**, *115*, 4345–4349.

[235] Havlas, Z.; Michl, J. Unpublished calculations.

[236] Chai, J.-D.; Head-Gordon, M. *Phys. Chem. Chem. Phys.* **2008**, *10*, 6615–6620.

[237] Paddon-Row, M. N.; Wong, S. S. *Chemical Physics Letters* **1990**, *167*, 432 – 438.

[238] Jordan, K. D.; Paddon-Row, M. N. *Chemical Reviews* **1992**, *92*, 395–410.

[239] Kistler, K. A.; Spano, F. C.; Matsika, S. *The Journal of Physical Chemistry B* **2013**, *117*, 2032–2044.

[240] Sebastian, L.; Weiser, G.; Bssler, H. *Chemical Physics* **1981**, *61*, 125 – 135.

[241] Longuet-Higgins, H. C.; de V. Roberts, M. *Proceedings of the Royal Society of London A: Mathematical, Physical and Engineering Sciences* **1954**, *224*, 336–347.

[242] Mulliken, R. S. *J. Chim. Phys. Phys.-Chim. Biol.* **1949**, *46*, 497–542.

[243] Ayed, O.; Bernard, E.; Silvi, B. *Journal of Molecular Structure: {THEOCHEM}* **1986**, *135*, 159 – 168.

[244] Jortner, J.; Rice, S. A.; Katz, J. L.; Choi, S. *The Journal of Chemical Physics* **1965**, *42*, 309–323.

[245] Subotnik, J. E.; Shao, Y.; Liang, W.; Head-Gordon, M. *The Journal of Chemical Physics* **2004**, *121*, 9220–9229.